PHYSICAL MEASUREMENTS ASSOCIATED WITH THERMOLUMINESCENCE DATING.

By

H.E. JENSEN, B.Sc. (HONS).

A Thesis
presented for the degree of
DOCTOR OF PHILOSOPHY
at the
UNIVERSITY OF ADELAIDE
(Physics Department)

June 1982.

C O N T E N T S

Contents Continued.....

Contents Continued.....

Contents Continued....

Contents Continued.....

STATEMENT

To the best of the author's knowledge and belief, this thesis contains no material previously published or written by another person, except where due reference is made in the text. It contains no material which has been submitted or accepted for the award of any other degree or diploma in any University.

H. E. Jensen.
Adelaide
June 1982..

ACKNOWLEDGEMENTS

I would like to acknowledge the continuing advice and encouragement of my supervisor, Professor John Prescott, throughout the course of this work. Thanks are also due to Dr Mike Barbetti and Dr Alan Gregory, for their supervision while Professor Prescott was on study leave.

Invaluable technical assistance with the electronics was provided by Neville Wild, Brian Fuller and John Smith.

The members of the mechanical workshop must also be thanked for their help and advice, particularly, David Fearnside, Bill Old, Graham Eames and Peter Schebella. Other members of the Physics Department have also provided useful assistance. Discussions with Richard Johnson, Barnaby Smith and Dr Gillian Robertson have at times been very stimulating.

I would also like to thank the staff of the Physics Division of the Australian Atomic Energy Commission for their help and collaboration, particularly Terrence Wall, Peter Duerden and David Cohen. Thanks are also due to Dr Keith Norrish and Paul Rogers, of CSIRO, Division of Soils, Adelaide, for their help in the preparation of glass-discs for alpha counting.

Thanks are also extended to Pat Coe for the efficient typing of this thesis, and Judy Laing for helping to create some of the diagrams.

The author was in receipt of an Australian Commonwealth Post-Graduate Research Award.

Most importantly, however, I would like to thank my wife, Michele, for her continued support and encouragement throughout my candidature.

SUMMARY

The thesis begins with a brief account of the basic principles and development of the thermoluminescence (TL) dating method. The remainder of the thesis is in two parts : Part I deals with the low-level determination of uranium (U) and thorium (Th) in samples of archaeological and geological interest; and Part II is concerned with aspects associated with the measurement of TL emission spectra.

The most favoured technique in TL dating laboratories, for the determination of low-levels of U and Th in field samples, is thick-source alpha particle scintillation counting. An alpha counting system was commissioned for this purpose and this is described in Chapter II. A critical evaluation of the problems associated with the alpha-counting technique has been carried out by comparing the results obtained with those obtained by other methods available for the determination of low levels of U and Th. Other methods used included delayed neutron activation (DNA) analysis for U-235 and hence U-238, neutron activation analysis for Th-232 (using epi-thermal neutrons) and proton-induced X-ray emission (PIXE). Descriptions and discussions of these alternative methods are given in Chapter III.

Chapter IV is devoted to a comparison of the results obtained by alpha counting and those expected on the basis of neutron activation (DNA and NAA) measurements for a variety of field samples. From this comparison it was seen that for the majority of samples the agreement between expected and observed alpha count rates was good. However, on some samples the observed count rates were much higher than those expected. Some of the probable causes of alpha overcounting are outlined, as are possible solutions to the problem.

An alternative alpha counting sample preparation technique , which removes the possibility of overcounting, is presented in Chapter V. In this method the sample grains are fused into glass discs using lithium tetraborate as a flux. Using this glass-disc sample preparation method, alpha overcounting was eliminated in all of the troublesome samples so far encountered.

The Sixth Chapter commences Part II of this thesis. This Chapter outlines the physical principles associated with TL measurements and some of the more important TL characteristics which can contribute to errors and uncertainties in the application of the TL dating method. It is by no means intended to be a comprehensive or detailed treatment, but rather a means of obtaining an insight to the necessity of being able to measure TL emission spectra.

The basic problems with instruments previously constructed for the purpose of studying TL emission spectra (i.e. sensitivity) are discussed ; and possible methods for improving instrument efficiency is discussed in Chapter VII. The basic principles and advantages of a Michelson interferometer for this purpose are outlined.

Chapter VIII is devoted to the theoretical aspects of Fourier transform spectroscopy with a Michelson interferometer. A full description of the design, setting up and development of a Michelson interferometer is given in Chapter IX. The instrument constructed has the facility to measure both conventional glow-curves and TL emission spectra.

The computational procedures involved with obtaining spectra and some preliminary results are given in Chapter X. Also included is an

evaluation of the performance of the existing apparatus and suggestions for further improvements.

CHAPTER I

THERMOLUMINESCENCE DATING : INTRODUCTION

1.1 A Brief Account of the Development of the Thermoluminescence Dating Method.

Thermoluminescence (TL) was first reported by Sir Robert Boyle over 300 years ago, when noting a glimmering of "Mr. Clayton's diamond" as it was subjected to heat (Boyle, 27 October 1663), but it has been a well recognized phenomenon only since the early part of the present century.

Urbach (1930) and Randall and Wilkins (1945) obtained glow curves of TL in which the intensity of light was plotted against the temperature, or the time of heating with constant rate of increase of temperature; they also attempted to interpret the glow curves theoretically. The Randall and Wilkins theory is what researchers today describe as the "first order approximation"; this theory will be outlined in some detail in Chapter 6 of this thesis.

It was soon realized that the phenomenon of TL was extremely complicated as it exhibited a very large variety of behaviours, depending on the different physical systems under consideration, each of these physical systems having its own unique crystal lattice, impurities and other lattice defects. Very broadly speaking one may say that TL involves the radiative recombination of holes and electrons liberated from trapping sites by thermal activation. These transitions occur among levels within the energy gap of the dielectric crystal under consideration, see Figure 1.1.

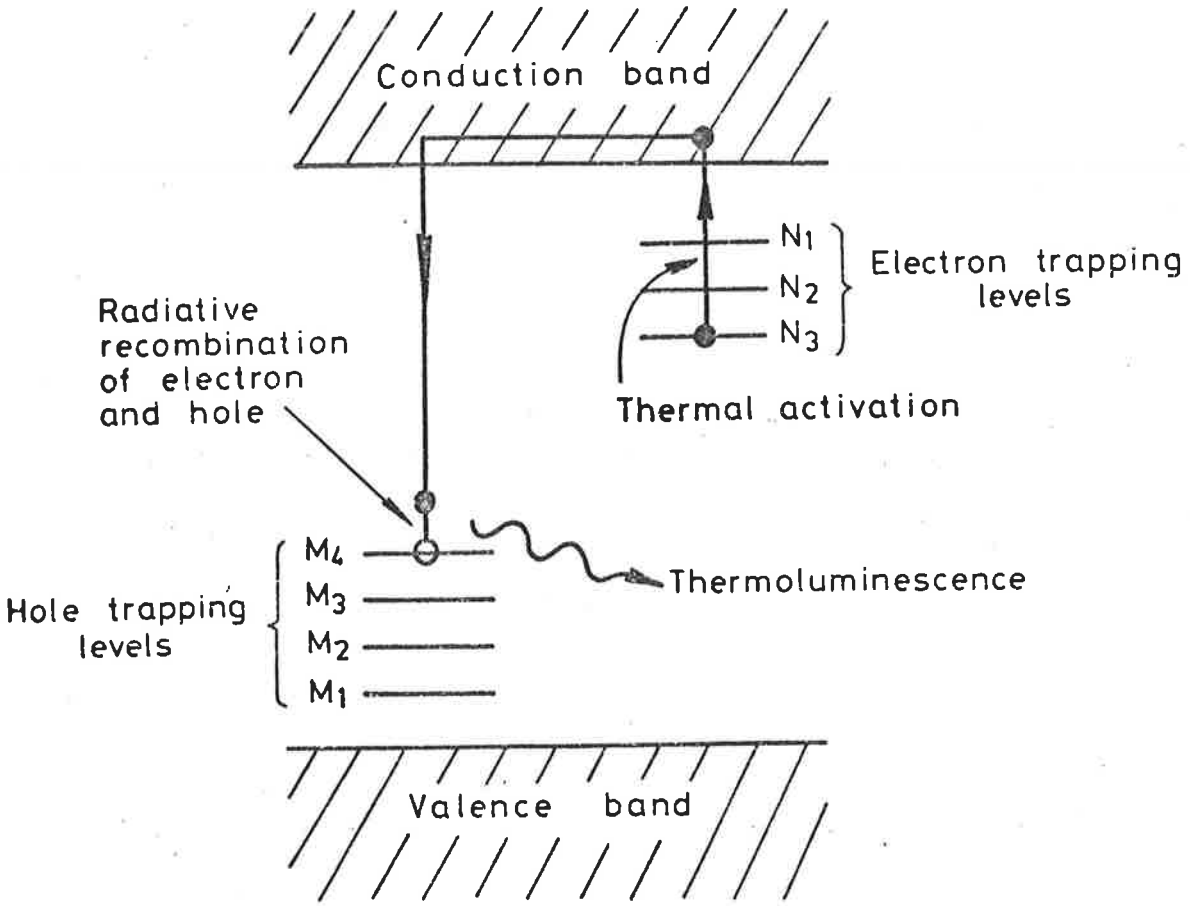

Figure 1.1 Schematic representation of the radiative recombination of electrons and holes.

It is radiation passing through a sample which gives rise to the initial separation of the electrons and holes in the crystal lattice. The amount of charge separation depends both on the chemical constituents of the sample and the type of radiation. The ionization per unit length produced by an alpha particle is about 100 times that for a beta particle and 10,000 times that for a gamma ray. One should point out that it is only a small fraction of the ionized electrons which are trapped at defects in the crystal lattice structure, the majority recombining with parent atoms.

It was Daniels *et al* (1953) who realized the possibility of applying the concept of TL to dating; the amount of light observed when heating a sample being a measure of time since the sample was last heated. Initial work on meteorites was done by Houtermans *et al* (1957), who estimated a value for the time the meteorites had been exposed to cosmic radiation in interplanetary space. A systematic study of TL on already dated archaeological pottery samples was carried out by Kennedy and Knopff (1960); the ages obtained all being relative to each other. The results were very encouraging as the ages of all of the samples were confirmed to within an error of about twenty percent. A more general test of the validity of TL as a method of age determination was performed by Tite and Waine (1962). Their results were very similar to those obtained by Kennedy and Knopff; even though they studied on extremely varied selection of pottery ranging in provenance from Egypt to England and in age from around 6000 B.C. to about 1300 A.D.

Fremlin and Srirath (1964) studied photographs of radiation-induced TL for a variety of pottery sherds; their results indicated that the distribution of TL for many sherds was non-uniform. From this observation they deduced that the radiation received by these samples

did not come from a uniformly distributed source and indeed there was therefore no reason to expect that radiation received by similar samples should be uniformly distributed. This implied that reliable dating of individual pieces of pottery by the TL method would be more difficult than had been forecast initially. They did however point out certain special cases in which this non-uniformity of TL would not spoil the results. The first case was one where the size of the grains used for TL studies were all small compared with the range of alpha particles in the sample. The second was the case where the radioactive content of the pottery itself was negligible for, by avoiding the outermost layers, one could deduce a dose-rate by examination of the site alone.

Up till that time (1964) the TL dating method was considered to be a relative one which required calibration with samples of known ages. Absolute ages independent of other chronology were first obtained at the Oxford TL Laboratory by Fleming in 1966; the technique used was what today is generally known as the "quartz-inclusion" method. As the name implies it is only concerned with large crystalline inclusions of quartz, typically of the order of 100 microns in size.

In 1967, Zimmerman, who was also working at the Oxford laboratory, proposed a technique in which only the grains in the range 1-8 microns were used, the so-called "fine-grain" technique. One may note that both the quartz-inclusion and the fine grain techniques had to some degree been suggested by Fremlin and Srirath in 1964 while critically analyzing their results.

A variant of the inclusion technique was introduced by Mejdahl in 1969; the "feldspar inclusion" technique. This uses grains in the range 0.3 to 0.5 mm and, as the name implies, it includes the feldspar which is not present in the standard inclusion technique developed by

Fleming.

Zimmerman (1971) introduced a new radioactive inclusion technique which follows the same principles as the previous techniques except for the fact that the TL measurements are made on highly radioactive grains of zircon (he also mentioned the possibility of using the mineral apatite). Zircon grains of a few tens of microns grain size are orders of magnitude more radioactive than the surrounding burial soil, thus nearly all of the natural radiation dose received is from internal alpha particles so that no burial information is required.

Fleming and Stoneham (1973) combined the fine grain and quartz inclusion techniques by subtraction of their respective total accummulated doses, therefore naming it the "subtraction" technique. As the environmental doses are subtracted out, one does not require any burial information.

The techniques mentioned so far all rely on getting enough TL emission in the 350°C - 450°C temperature region, and are not ideal for dating young samples, since the TL intensity is unsufficient. Fleming (1973) developed a "pre-dose" technique which utilizes the sensitivity enhancement of the 110°C glow curve peak of quartz after having given the quartz grains a dose of radiation and then heating to 500°C. This enhancement of sensitivity Fleming attributes to "defect creation" produced by the combined effects of dosage and heating.

One may note that all of the above-mentioned techniques involve TL studies on various grain sizes; i.e. the bulk sample has been separated into grains. Certain samples such as burnt flint show spurious results when studies are made on grains. Göksu and Fremlin, (1972) devised a thin-slice method whereby the spurious effects (regeneration TL and triboluminescence) could be reduced, they did TL

studies on slices which had a thickness of about 0.5 mm. Using this technique, Wintle and Aitken (1977) have assigned a TL date of about two hundred thousand years to burnt flint material from the palaeolithic site of Terra Amata. One may note that this is about four times older than any other TL date ever obtained previously for flint.

More recently it has been shown that ultraviolet light can reset the TL clock in the same way that heating does. This means that sediments can be dated by TL as the sample grains have previously been subjected to sunlight. TL dating of sediments is still in the early stages of development. Several Russian publications have appeared in the literature (Dreimanis *et al*, 1978; Hutt *et al*, 1979); however, the most significant advances have been reported by Wintle and Huntley (1979, 1980, 1982). A good review on the application of TL dating to non-pottery materials is given by Wintle (1980).

One should point out that TL dating of archaeological ceramics or geological events almost always employs either the fine grains or the quartz inclusion techniques.

1.2 The Thermoluminescence Age Equation

Each of the various TL dating techniques has essentially the same basis; that is, the time elapsed since the specimen was last heated is given by

$$\text{Age (years)} = \frac{\text{Total archaeological TL acquired}}{(\text{TL per unit dose of radiation}) \times (\text{Dose per year})} \qquad (1.1)$$

The total archaeological TL acquired (often referred to as the natural TL) refers to the TL acquired by the sample since it was last heated. The TL per unit dose is the sensitivity of the sample for acquiring TL and

is measured by exposing the sample to a known dose of nuclear radiation from a calibrated radioisotope source and then noting the level of TL at the same temperature as the natural TL. The Dose per year is the average annual dose of radiation received by the sample throughout its burial time; the radiation coming from the sample itself and its immediate surroundings and from cosmic rays.

1.3 Determination of the Annual Dose-Rate

The TL field samples possess a mixture of TL sensitive minerals such as quartz, calcite and various feldspars, each mineral having its own sensitivity to radiation. The origin of this radiation lies with three main groups of naturally occurring radioactive elements: (a) the uranium series, (b) the thorium series and (c) potassium-40. These supply a steady source of radiation dose. The most common method employed to determine the annual dose-rate from the uranium and thorium series is thick-source alpha particle scintillation counting.

1.4 Measurement of Thermoluminescence

The most common technique employed in the TL study of archaeological or geological samples is to measure the total light emitted as a function of temperature as the sample is heated in an oven. The emitted light is usually detected by a photomultiplier tube, and a plot of phototube output versus sample temperature is obtained - the so-called glow-curve. While this method of measuring TL is quite adequate for dating or authenticating many of the samples encountered, it has become increasingly apparent that it would often be advantageous to have a better understanding of the actual TL processes involved, before the accuracy of TL dating can be further improved. Some of the problems which limit both the accuracy and the range of datable samples include spurious-TL, anomalous fading, optical bleaching, light-induced

TL, non-linearity in the acquisition of TL at low levels of radiation dose and a change in the TL sensitivity after the natural TL has been removed by heating; these phenomena will be outlined in Chapter 6. Among useful results that can be obtained from a glow-curve is the determination for each peak of the kinetic parameters: activation energy, pre-exponential factor and trapped charge concentration; these will also be discussed in Chapter 6. Ordinary glow-curves are, however, not always suitable for kinetic analysis unless it can be demonstrated that the measured phototube current is proportional to the number of kinetic processes occurring per unit time (Levy *et al*, 1971; McKeever, 1980). As Levy *et al* (1971) point out, the information required to do a proper kinetic analysis of a particular sample is the wavelength emission spectrum. This type of measurement, in which the photomultiplier output is recorded as a function of both temperature and wavelength, is commonly referred to as a "3-D" glow-curve.

1.5 Scope of Thesis

The objectives of this work were two-fold. Firstly, to design, construct and commission an alpha-particle counting system to be used for determining low levels of uranium and thorium in archaeological and geological samples, and then to carry out a critical evaluation of the problems associated with the thick-source alpha-particle scintillation counting technique. Secondly, to design, construct and develop an instrument for measuring both conventional 2-D TL glow-curves and 3-D TL emission spectra. The basic problem with the instruments previously constructed for the purpose of studying TL emission spectra is the lack of sensitivity needed for archaeological TL. After considering the rather poor efficiency of the conventional grating or

prism type spectrometers, it was decided to develop a Michelson-type interferometer for the measurement of TL emission spectra. The overall design specifications sought was to cover the spectral range 300-650 nm with a modest resolution, of about 20 nm. One of the basic design requirements was that the interferometer needs to be interfaced to a conventional TL oven. A further requirement was that the instrument should be computer controlled.

Chapters II, III, IV and V deal with thick-source alpha-particle counting and some of the other methods used for determining low levels of uranium and thorium. The spectrometer and the theory of Fourier transform spectroscopy are discussed in Chapters VII, VIII, IX and X.

PART I

DETERMINATION OF URANIUM AND THORIUM IN SAMPLES OF ARCHAEOLOGICAL AND GEOLOGICAL INTEREST.

CHAPTER II

URANIUM AND THORIUM DETERMINATION BY ALPHA COUNTING

2.1 Introduction

It is well known that most of the radiation dose received by baked materials, buried in some soil, comes from radioactive elements in the material in question and its immediate surroundings. The common naturally-occurring elements are uranium, thorium (and their corresponding decay chains), potassium-40 and to a small extent rubidium - 87; typical concentrations are 3 $\mu g g^{-1}$, 10 $\mu g g^{-1}$, 2% and 100 $\mu g g^{-1}$ respectively.

Uranium has two main contributing parent isotopes; namely U-238 (99.28%) and U-235 (0.72%). In both of their decay series, as well as the Th-232 decay series, we get emission of alpha, beta and gamma rays. Potassium-40 decays in 89.3% of cases by emission of a beta particle and in the remaining 10.7% of cases by electron capture followed by gamma ray emission. Rubidium-87 decays by beta decay to strontium-87.

The uranium and thorium decay series together provide approximately 70% of the dose effective in producing fine grain TL (Bowman, 1976), potassium 25%, and the remaining 5% is provided by rubidium (1-2% contribution) and cosmic radiation.

This Chapter is concerned with a critical evaluation of the determination of uranium and thorium content by the method most commonly employed in the various TL laboratories; namely, thick source alpha particle scintillation counting. In spite of the simplicity of the

technique, sufficient queries were being raised at the time this work was begun to justify a re-examination of some of the problems encountered.

2.2 Basic Principles of Alpha Counting

To assess the total uranium and thorium content of a sample, one can employ thick source scintillation alpha particle counting. The basic theory of this counting technique is well known for the case in which the alpha emitters are homogeneously distributed throughout the sample. This case has been discussed by numerous authors; probably the best reference to early work in this field is Finney and Evans in 1935. Other very useful treatments have since then been given by Keevil and Grasham (1943), Nogami and Hurley (1948), Beharrell (1949), Kulp *et al* (1952), Turner *et al* (1958) and Cherry (1963, 1965). The earliest reference to the use of the technique, as far as obtaining radiation doses for TL dating, is that of Tite and Waine (1962). Some more recent references on the use of alpha counting in relation to TL dating are Aitken (1974) and Huntley and Wintle (1978, 1981).

The basic equation for thick source alpha particle counting can quite easily be derived by simple geometric considerations as

$$\alpha = \tfrac{1}{4} A \quad C \sum_{i=1}^{n} N_i \quad (R_i \rho) \qquad (2.1)$$

see for example, Turner *et al* (1958), where α represents the total number of alphas counted per unit time, N_i is the disintegration rate

per gram of the ith alpha emitting isotope, $R_i\rho$ is the range of alpha particles from the ith isotopic component (cm) and ρ is the sample density ($g.cm^{-3}$), A is the counting area in cm^2 and C is a counting efficiency factor. In the derivation of this basic equation one assumes, as already mentioned, that the alpha activity is distributed homogeneously throughout the sample volume.

Using Equation 2.1 one can in principle estimate the disintegration rates of the uranium and thorium parents, if the relative Th/U ratio is known and if the decay series are all in equilibrium and the appropriate range values for the particular sample are known.

2.3 The Alpha Counting Apparatus

To measure the alpha activity of a sample, the apparatus illustrated diagrammatically in Figure 2.1 is used. A layer of crushed sample a few millimetres thick is spread in direct contact with a zinc sulphide (ZnS) scintillation screen, this screen being placed at the bottom of a perspex cell, which is then positioned on top of a 5 cm diameter photomultiplier tube (type EMI - 6097B), which detects the scintillations produced by the alpha particles in the ZnS. The ZnS screens (discs) are punched from commercial sheets of ZnS phosphor deposited on a plastic material (see Section 2.4.5 for more details on these screens). ZnS is very inefficient for the detection of gamma-rays and electrons, hence making it an ideal scintillator for the detection of alpha particles. The photomultiplier pulses are fed through a preamplifier, which is situated in the same light-tight housing as the photomultiplier. From there the pulses are amplified by an Ortec 471 amplifier and then fed through a single channel

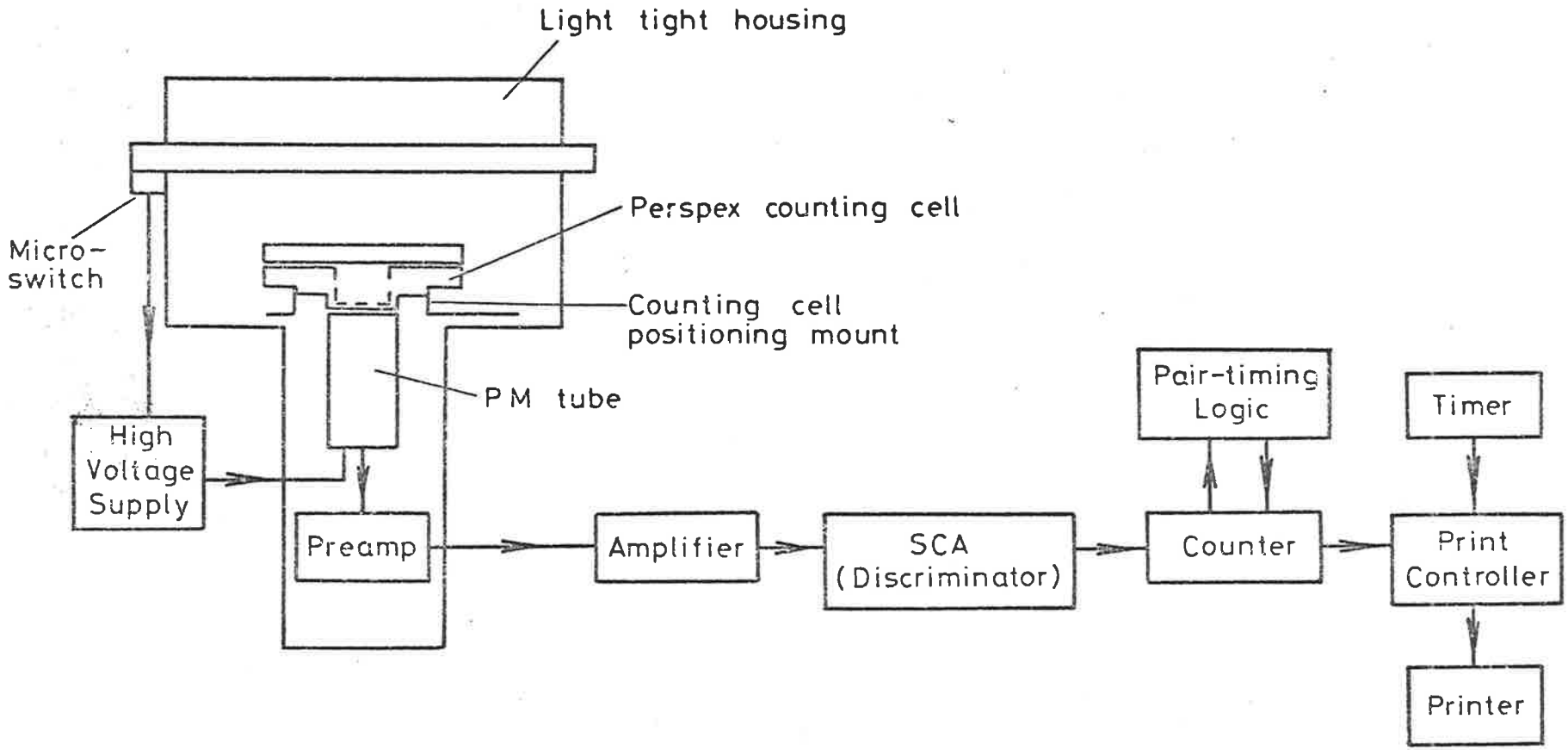

Figure 2.1 Schematic Illustration of Alpha Counting Apparatus.

analyser (Ortec 406A), which is used as a lower level discriminator (see Section 2.4.5 for the details on how the gain of the amplifier and the lower level threshold of the discriminator are set). The pulses coming from the single channel analyser are then counted by a slightly modified Ortec 772 counter. As well as counting alpha particles, one is also interested in counting alpha pairs (see Section 2.4.1), this is done by counting alphas emitted within about 0.2s of each other. A specially designed pair timing logic unit, which enables alpha's within this period (or any other period up to about 0.5s) to be counted, has also been incorporated. As soon as a pair has been registered this pair timer is reset and hence is ready to accept the next pair. The six digit Ortec counter has been modified so that the number of pairs is displayed in the first two digits and the remaining four digits are then used to count normal alphas ; this means that a separate pairs counter is not required. One still has the option of using all the six digits available to handle the total alpha count if one is not interested in the pairs count or if one is counting radioactive standards where the alpha count rate is high. An Adler 121P printer has also been incorporated so that one obtains hard copy of the results. An Ortec 719 timer and a print controller are also included so that one can preset the interval between printouts; unless one is counting highly radioactive standards this is usually set at 1 ks.

In the design of an alpha counting system it is important to make sure that the surfaces exposed close to the scintillation screen produce a low background. The counting cells used are very similar to those used in other TL laboratories (see for example, Bowman, 1976;

Bell, 1978). A 42 mm internal diameter aluminium ring is positioned on top of the ZnS screen to act as a spacer, as well as to accurately define the counting area. Figure 2.2 is a diagrammatic illustration of the standard counting cell used (drawn in section). On top of the aluminium spacing ring is placed a split stainless steel retaining ring; the main purpose of this ring is to keep the aluminium ring in direct contact with the ZnS screen. Once the ZnS screen and the two rings are in position one can pour the sample into the counting cell; the usual procedure is then to position a perspex disc on top of the sample. One usually deposits a few grams of sample on to the ZnS screen, although only about 0.1g of sample is actually counted due to the fact that the average alpha particle range is only about 25 μm or so. For a typical sample grain size of 100 μm only a mono-layer of grains on top of the 13.85 cm^2 ZnS screen are actually counted, this corresponds to approximately 10,000 grains.

Having positioned the sample in the counting cell it is possible to count the sample with the cell either sealed or unsealed (see Section 2.4.2 for further discussion of this aspect). A gas cell was constructed to the design of Aitken (1978) and is illustrated in Figure 2.3. In this counting cell only the indirect alpha particles can possibly be detected by the ZnS screen. The only alpha particles reaching the scintillation screen are those from radon (see Section 2.4.2) that has escaped from the sample or radon daughters which have been deposited on the walls and the screen from escaped radon. However, in none of the TL field samples so far studied in this laboratory, which include pottery samples, oven stones and soils from Australia and the South Pacific region, has there been any need for its use. For this reason

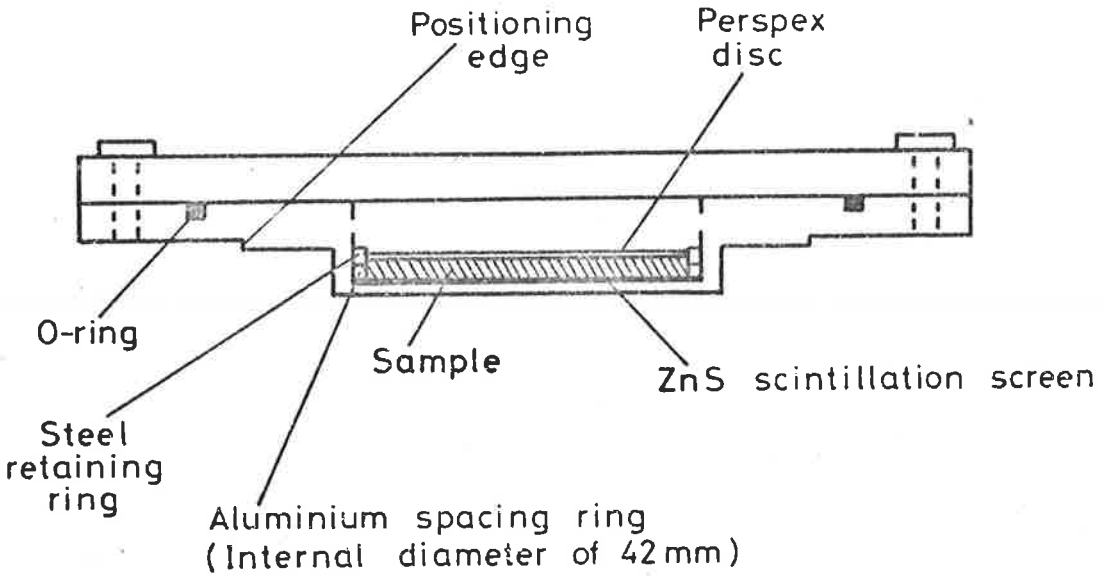

Figure 2.2 Standard Alpha Particle Counting Cell.

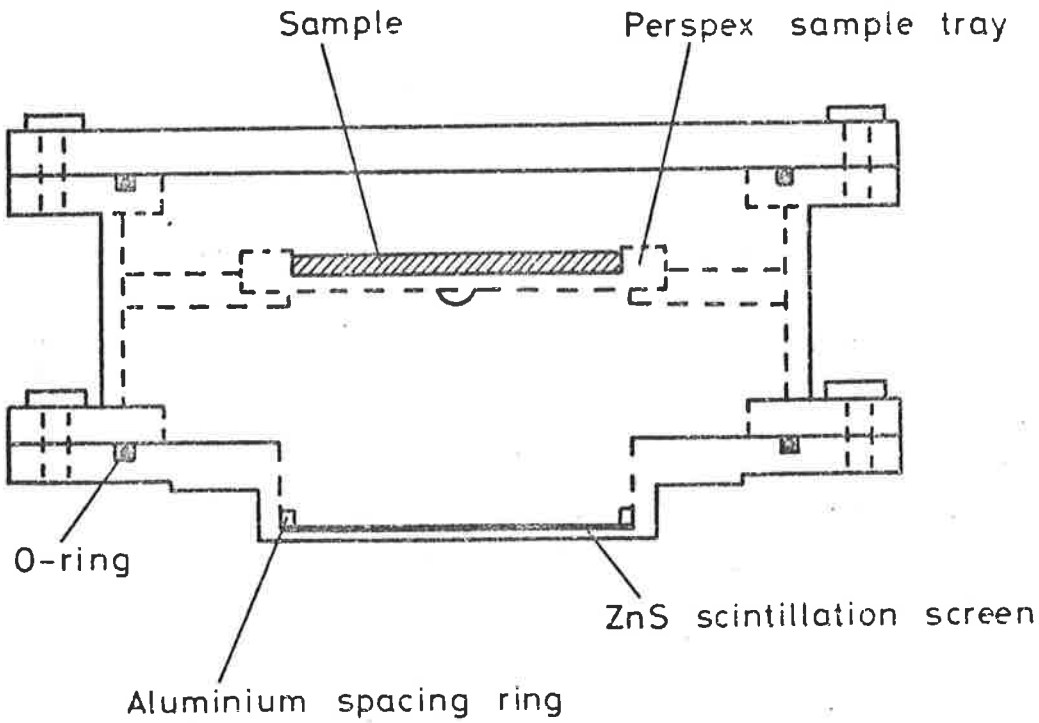

Figure 2.3 Indirect Alpha Particle Counting Cell (Gas-Cell).

no performance data on this gas cell are available. A photograph of the overall alpha counting apparatus is shown in Figure 2.4.

2.4 Problems Encountered in Alpha Counting

The alpha counting method gives us a total alpha count rate from the three radioactive series, uranium - 238, uranium - 235 and thorium - 232. From this one must then calculate the doses. In order to do this one needs their relative concentrations by weight. The U-235/U-238 ratio is well established and constant at 0.72%; however the Th/U ratio varies with sample geochemistry and hence a separate estimate of this is required for each individual sample. If this ratio is not actually measured by some means, it is then necessary to assume a value. A frequent assumption is that the alpha activity of Th-232 is equal to the combined activities of U-238 and U-235, this corresponds to a Th/U ratio of 3.16 by weight (Bowman, 1976).

Bowman correctly states that this assumption does not lead to gross errors. Nevertheless, it adds an automatic uncertainty to the obtained age. Sasidharan *et al* (1978a) have examined the validity of the above assumption; they estimated that the error component in a TL age estimate due to this assumption would never exceed 5% and in the majority of cases would be less than about 2%. Bowman states that the alpha dose is virtually independent of the Th/U ratio, but the beta and gamma doses could be in error by up to 10%. One way to reduce this uncertainty is to employ the " pairs technique"; this method will be described and discussed in Section 2.4.2.

In evaluating the dose-rate one also has to know the degree

Figure 2.4 Photograph of the Overall Alpha-Counting Apparatus.

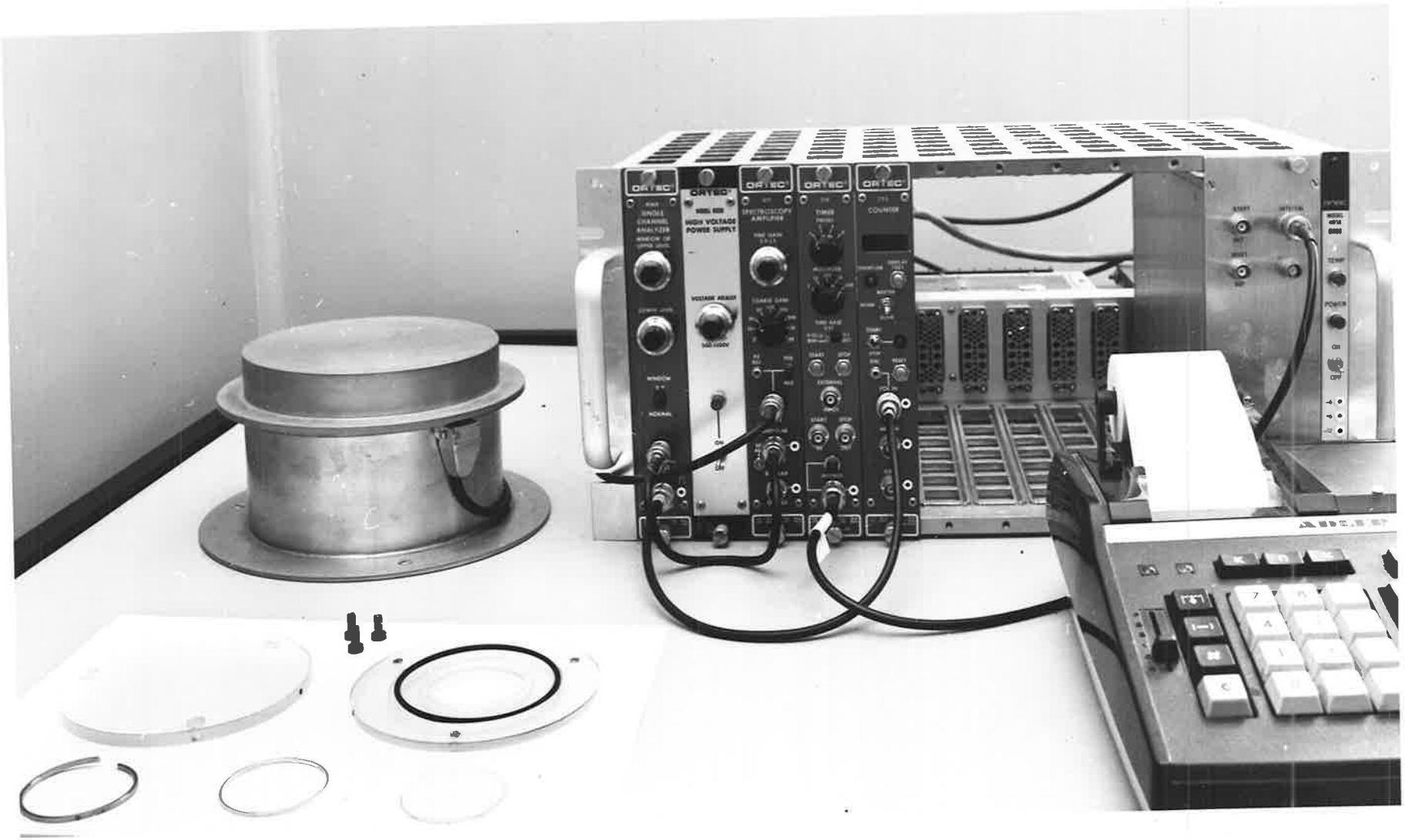
ORTEC
HIGH VOLTAGE
POWER SUPPLY
SPECTROSCOPY
AMPLIFIER
TIMER
COUNTER

of secular equilibrium in the decay chains. The favourite assumption is that the activity (rate of decay) of each member of the series is precisely the same as that of any other member; that is, secular equilibrium has been reached. This assumption may not always be true (see for example, Szöghy *et al* 1978; Meakins *et al* 1979; Megumi, 1979). The uranium decay chains, in particular U-238, contain daughter elements which have either long half-lives or are relatively mobile, thus making it possible for the elements in the decay series to exist in other than their equilibrium condition. One might for example expect some geochemical fractionation of some of the long half-life elements, as well as diffusion of the gaseous element Rn-222, the radon half-life being about 3.8 days. One usually assumes that the thorium decay chain is always close to equilibrium as all decay products have relatively short half-lives, the only gas being thoron (Rn-220) with a half-life of about 55 seconds.

The problem of radioactive disequilibrium as related to alpha counting and TL dating in general will be further discussed in Section 2.4.3.

As has already been mentioned, one also has to have a knowledge of the alpha particle ranges in the sample which is to be counted. Cherry (1963) have discussed the problems involved with the determination of $R\rho$ (see Equation 2.1) as have many other authors, i.e. Glasson (1922), Turner *et al* (1958), Bowman (1976).

The Bragg-Kleeman relation (1905),

$$R\rho = 3.2 \times 10^{-4} \; A^{\frac{1}{2}} \; R_o \; gm.cm^{-2} \qquad (2.2)$$

is often used; in this equation, R_o is the range in cm of an alpha particle of the same energy in air and A is the atomic weight (calculated on the atomic fraction basis). Glasson replaced $A^{\frac{1}{2}}$ by $Z^{\frac{2}{3}}$, where Z is the atomic number; this was also adopted by Turner *et al* (1958) and Tite and Waine (1962).

Tite and Waine measured the effective value of Z on six random pottery samples and found it to vary by up to 17%, thus indicating the variations in R that are likely when counting pottery samples. They adopted a value for $Z^{\frac{2}{3}}$ of 4.82 (that of brick dust) and used this when calculating the alpha activity of pottery samples. Aitken and Bowman (1975) and Bell (1976, 1977, 1979) have calculated dose-rate conversion tables using A = 21.4 (this also corresponds to $Z^{\frac{2}{3}} = 4.82$), and assumed proportionality to $A^{\frac{1}{2}}$. They obtained alpha particle range values of 6.94 $mg.cm^{-2}$ and 5.84 $mg.cm^{-2}$ for the thorium and uranium series respectively. These values were obtained by interpolating between the known values for neon (A = 20.2) and sodium (A = 23.0); which had been derived by Northcliffe and Schilling in 1970 and Williamson *et al* (1966). Using these dose-rate conversion tables it is possible to convert the measured alpha count rates (counts $cm^{-2}ks^{-1}$) into alpha, beta and gamma dose rates (mrad yr^{-1}) as long as the degree of equilibrium and the Th/U ratio are known. These dose-rates can also be converted into uranium and thorium concentration levels ($\mu g g^{-1}$)

In order to utilize these dose-rate conversion tables one must also have a knowledge of the atomic weight of the sample, this is particularly so if the deviation from A = 21.4 (that of the mineral illite) is significant. The accuracy in using the $A^{\frac{1}{2}}$ dependence on

a range of atomic weights, in the alpha particle energy range around 5 MeV, will be discussed in Section 2.4.5.

One of the basic assumptions used by Tite and Waine was that the reflectivity of each sample for the light emitted by the ZnS screen is the same, i.e. that the alpha count rate obtained is independent of the sample colour. Several TL researchers have found that the alpha pulse height spectral shapes are very much dependent on the sample colour (see for example, Huntley, 1977; 1978). Bowman (1976) states that Aitken, at the Oxford TL Laboratory, has found that white samples produce pulses which can be up to twice as large as those from black samples. Aitken (1978) also states that the effect on the actual alpha count rate is not a strong one, unless exceptionally white or black samples are being counted. In Section 2.4.4 the effect of varying sample reflectances on the observed alpha count rate is discussed and put on a quantitative basis.

The different aspects involved with the absolute calibration of the alpha counter will be discussed in Section 2.4.5. One of the assumptions used in deriving the basic alpha counting equation (Equation 2.1) is that the alpha activity is distributed homogeneously throughout the sample volume. The validity of this assumption will be discussed in Section 2.4.6.

2.4.1 The Pairs Counting Technique

Normally one uses pairs counting to see whether there is any gross deviation from the assumed Th/U ratio of 3.16. This technique makes use of two consecutive alpha transitions in the thorium decay

chain. The alpha emitter Po-216 follows Rn-220 with a half-life of only 0.15s (Ward 1942; Diamond and Gindler, 1963). The number of pairs occurring within an interval of, say, 0.2s is recorded by an electronic coincidence circuit and hence the number of pairs per unit time will be proportional to the Po-216 concentration. If radioactive equilibrium exists in the thorium decay chain one obtains a measure of the concentration of the head member of the chain, namely Th-232 (Hurley and Shorey, 1952; Turner *et al*, 1958). Together with the total alpha count rate from the three different decay series the pairs count rate gives one a relative measure of the Th/U ratio. This method is not normally used for accurate estimations of the Th/U ratio because the actual fraction of pairs is small, typically one pair in fifty alphas; hence long counting times are required in order to obtain good statistics. The pairs technique nevertheless gives a Th/U ratio which is better than that obtained using the already mentioned assumption of equal activities in the thorium and uranium decay chains. Any actual measurement is always better than even an educated guess!

A couple of days counting time is usually enough to obtain a reasonable estimate of the Th/U ratio; to get the statistical accuracy of the ratio below 10% one would have to count for a week or two (see for example, Sasidharan *et al*, 1978a).

In order to obtain the true alpha pairs rate for a particular sample, one first has to subtract the number of random coincidence pairs from the observed pairs; by random coincidence pairs, sometimes referred to as spurious pairs, one means the pairs that are due to chance coincidences. Furthermore, one has to have an accurate conversion from

the true pairs rate to the thorium activity.

Turner *et al* (1958), who were the first to describe the successful application of the pairs technique in any detail, found the random coincidence pairs rate by calculating the probability that two pulses would occur within a time τ equal to the gating time of the coincidence circuit. Cherry (1963) states the random coincidence rate as being equal to the observed total alpha count rate multiplied by the probability of a single pulse occurring within a time τ. Cherry's assumption seems to be in agreement with our experimental situation, so this adoption will also be used here. Assuming a Poisson distribution then gives the coincidence pairs rate C_p by the formula

$$C_p = \alpha^2 \tau \exp(-\alpha\tau), \qquad (2.3)$$

where α is the total observed alpha count rate and τ the gating time. As Cherry correctly states, the random coincidence pairs rate evaluated by Equation 2.3 is twice as high as that calculated by Turner *et al*. This means that in general the correct coincidence pairs formula depends on the characteristics of the counting system in question. For normal alpha pairs counting on TL field samples the alpha count rate is generally low, which means that the exponential term in Equation 2.3 is close to unity. Hence we have

$$C_p \simeq \alpha^2 \tau \quad (\alpha \lesssim 50\ ks^{-1}) \qquad (2.4)$$

A variety of uranium and thorium counting standards has been supplied to us by the United States Department of Energy (USDOE). The uranium standards contain no thorium but the thorium standards all contain small, but known, amounts of uranium. Some of the uranium standards

have been used to test the random coincidence pairs rate formula; this assumes that the true pairs from the uranium decay chains are negligible. The only other half-life between two alpha emitters that is short enough to contribute pairs is the 1.78 ms half-life of Po-215 in the U-235 decay chain (see Appendix A); however, since the relative abundance of U-235 in natural uranium is low and constant (0.72%), the contribution to the pairs count rate is small and correctable. A small delay of about 20 ms or so will also circumvent the problem of counting Po-215 pairs, without having to make any appreciable correction to the pairs counting efficiency.

Table 2.1 shows that for uranium standards, in the concentration range up to 0.1%, the number of observed pairs agree well with those predicted by Equation 2.3. One notes that the random pairs coincidence formula holds well for count rates up to at least 1500 counts ks^{-1}.

Following the geometric argument given by Turner *et al.*, with minor modifications to allow for the different ranges of the two alpha particles involved (the values used were calculated from the data supplied by Aitken and Bowman (1975) and from Bowman (1976), where ranges were estimated using a value of 21.4 for the atomic weight), it can be shown that for a typical TL field sample the true pairs fraction is given by :

$$(P/\alpha)_{Thorium} = 0.0627 \left[1 - \exp(-\ell n2 \ (\tau/\tau_{\frac{1}{2}})) \right] \qquad (2.5)$$

TABLE 2.1

RANDOM COINCIDENCE PAIRS DATA (URANIUM STANDARDS)

Sample	Uranium Concentration ($\mu g g^{-1}$)	Effective counting time	Total No. of observed pairs	α ks^{-1}	Expected No. of pairs
NBL 105	10 ± 1	200 ks	21 ± 9	20.1 ± 0.6	16 ± 1
NBL 104	103 ± 4	200 ks	908 ± 60	148 ± 2	851 ± 23
NBL 103	470 ± 10	7.8 ks	748 ± 55	756 ±20	764 ± 40
NBL 102	1010 ± 10	2.8 ks	967 ± 62	1587 ±80	1028 ± 104

NOTES :

1. The errors shown are 95% confidence limits.

2. The given alpha particle count rates are not absolute as there has been no correction made for sample atomic weight and scintillator screen efficiency (see Sections 2.4.3 and 2.4.5.)

(see Appendix B for the derivation of this equation) where the term in square brackets represents the half-life correction factor (i.e. only a certain fraction of pairs of half-life $\tau_{\frac{1}{2}}$ occur in the time period τ), P is the number of true pairs observed and α is the corresponding number of thorium alpha particles in the same counting time.

There are only three references in the literature to measured values of the Po-216 half-life; namely, Moseley and Fajans (1911), Ward (1942) and Diamond and Gindler (1963). The values quoted are 0.145 ± 0.002s, 0.158 ± 0.008s and 0.145 ± 0.002 respectively. The most recent value of 0.145 ± 0.002s will be used here. Hence, for our counting system Equation (2.5) becomes

$$(P/\alpha)_{\text{thorium}} = 0.039 \pm 0.001 \qquad (2.6)$$

In calculating the error in Equation (2.6) no error has been assumed in the alpha range values. This pairs fraction ratio is in good agreement with Aitken and Allared (1972); they use a value of 0.035 ± 0.01. On the common assumption of a Th/U ratio of 3.16 by weight (which corresponds to 48.1% of the alphas above threshold being from the thorium chain and 51.9% from the uranium chains, under equilibrium conditions), the expected pairs fraction would be 0.019 ± 0.001.

Having already verified the random coincidence pairs formula, a range of thorium standards was counted in order to check Equation (2.6). Table 2.2 shows that for the standards NBL-110 and NBL-109; which corresponds to about 10 $\mu g g^{-1}$ and 100 $\mu g g^{-1}$ of thorium respectively, there is a good agreement between the experimental and theoretical value for the pairs fraction. On sample NBL-108 (about 500 $\mu g g^{-1}$ thorium) the agreement is not quite so good. However, one can certainly conclude

TABLE 2.2

EXPERIMENTAL VALUES FOR (P/α) (Thorium Standards)

Sample	Thorium Concentration ($\mu g g^{-1}$)	Uranium Concentration ($\mu g g^{-1}$)	Measured (P/α)	Corrected (P/α) (Thorium)
NBL 110	9.8 ± 0.6	.35	.034 ± .004	.038 ± .004
NBL 109	104 ± 3	3.7	.034 ± .002	.038 ± .002
NBL 108	520 ± 10	18	.030 ± .001	.034 ± .001

NOTES :

1. The errors shown are the 95% confidence limits.
2. The uranium concentrations have been calculated using the known Th/U ratio of monazite.
3. The corrected (P/α) values are obtained by subtracting the fraction of alpha's that are from the uranium from the measured alpha's.

that in thorium concentration range up to about 100 $\mu g g^{-1}$ there is good agreement between the experimental and theoretical value for the pairs fraction as long as the random coincidence formula given by Equation 2.3 is used. This more than covers thorium concentration levels which are likely to be encountered in TL field samples.

Having verified the estimate for the true pairs fraction on thorium standards one is in a better position to test the relation for a variety of Th/U ratios; that is, in the presence of both uranium and thorium. Several substandards were prepared by mixing known amounts of the NBL-104 uranium standard (about 100 $\mu g g^{-1}$) with known amounts of the NBL-109 thorium standard (about 100 $\mu g g^{-1}$); these mixtures were thoroughly homogenized prior to alpha counting. The results obtained on these substandards are shown in Table 2.3 where the expected Th/U ratios, calculated from the known concentration and weight ratios of the standards, are compared with those obtained by pairs counting. In addition, the expected relative alpha count rates are also compared with the measured relative alpha count rates. From the data obtained on these substandards one can conclude that by using the pairs counting technique one obtains Th/U ratios which are in good agreement with the correct values. The estimation of the relative error in the Th/U ratio, when employing the alpha pairs technique, is discussed in Appendix C.

One should point out that both the random coincidence (Equation 2.3) and the true pairs fraction formulae (Equation 2.5) depend on the characteristics of the pairs counter. Huntley and Wintle (1978, 1981) have discussed the use of commercially available nim modules. They mention the fact that on these modules there is generally

TABLE 2.3

ALPHA PAIRS COUNTING ON STANDARDS OF VARYING Th/U RATIOS

SAMPLE NO.	$\frac{\text{NBL-109}}{\text{NBL-104}}$ (weight)	$(Th/U)_{calculated}$	$(Th/U)_{\alpha\text{-P}}$	Normalised Expected Relative α-count-rate	Normalised Measured Relative α-count-rate
ADL-56	1.0	1.0 ± 0.1	1.1 ± 0.5	1.00 ± 0.03	1.00 ± 0.01
ADL-57	3.0	2.7 ± 0.2	2.4 ± 1.1	0.75 ± 0.03	0.74 ± 0.01
ADL-58	6.0	5.0 ± 0.3	4.7 ± 1.5	0.64 ± 0.02	0.62 ± 0.01
ADL-59	9.0	6.4 ± 0.4	5.9 ± 1.6	0.60 ± 0.02	0.62 ± 0.01

NOTES :

The errors shown are 95% confidence limits.

an unwanted delay in opening the pairs gate, the delay being effectively random between 0 and 0.1s. They also describe a 3 MHz crystal controlled clock which is sometimes available on these timers, by using this option they obtained a pairs gating delay of about 18 ms.

2.4.2 Radioactive Disequilibrium in the Uranium and Thorium Decay Chains : Discussion.

One has to have a knowledge of the degree of equilibrium in the uranium and thorium decay chains in order to accurately estimate annual dose-rates from the measured alpha count rates. As already mentioned, the main problem of disequilibrium exists in the uranium decay chains. Radon emanation has for some time now been recognized as a potential cause of disequilibrium in the U-238 decay chain. Several researchers have been trying to get around the problem of radon escape or at the very least trying to measure the extent of escape. One assumption, proposed by Desai and Aitken (1974) was that the degree of radon retention by a sample buried in the ground is proportional to its water content; this assumption was later shown to be incorrect by Aitken (1976, 1978). Aitken states that the radon escape is not always suppressed by wetness and indeed may actually be enhanced. The present technique, used at the Oxford TL laboratory, is first to alpha count the sample in a normal manner ("unsealed"), let this count rate be α_0. The lid of the counting cell is then sealed and the 'immediate' sealed count rate, α_1, during the ensuing 24 hours is noted. If α_1 exceeds α_0 by more than 10% then a special gas cell technique has to be employed; otherwise α_1 is used for dose-rate calculations. This gas cell technique is fully described by Aitken (1978).

An important point to note regarding disequilibrium in a given decay chain is that once a given amount of one of the elements in the chain has disappeared, the decrease in alpha count rate is not only that corresponding to the loss of that particular element alone but also that corresponding to the loss of the same fraction of the daughters following that element in the chain.

Having gross disequilibrium in the uranium decay chains does not always mean that the corresponding total alpha count rate is low. One may plausibly expect some enrichment in one or more of the elements in the U-238 decay chain; in which case one may observe an increase rather than a decrease in the total alpha count rate. Recently Murray and Aitken (1980) have observed Ra-226/U-238 ratios of as much as 4:1 in their analysis on various sherds and soils. They also observed some degree of disequilibrium in the thorium decay chain due to losses of the gaseous element Rn-220; this cause of disequilibrium will of course never be as severe as possible radon losses because of its much shorter half-life (55s compared with 3.8d).

To study disequilibria in the radioactive series it is sufficient to determine the abundance of selected key elements; hence the decay chains may be simplified into groups within which one can assume secular equilibrium to exist (see for example, Rosholt, 1959). One way of doing this is to measure the intensity of the gamma-rays which they emit. NaI gamma-ray scintillators have for some time now been used by geophysicists as a means of detecting the high energy gamma-rays emitted by Bi-214 (1.764 MeV) which is in the lower half of the U-238 chain (see for example, Hurley, 1956). The Tℓ-208 gamma-ray (2.614 MeV) can also be used to measure the activity in the Th-232 chain. The method has several weaknesses. First of all a

separate method is needed for the analysis of U-238, and secondly if gross disequilibrium exists then the method does not indicate exactly where in the decay chain it occurs, it could for example, occur because of radon diffusion, radium leaching, or possibly both. Meakins *et al* (1978) employed such a γ-ray detector in relation to TL dating studies. They state that the only daughters of U-238 above Bi-214 which can undergo chemical leaching or deposition are U-234 and Ra-226. By using a mass spectrometer to measure the U-234/U-235 isotopic ratio they determined the relative abundances of the U-238 daughters for a variety of sherds and soils.

Recent advances in solid state technology, particularly in the field of Ge(Li) detectors, have greatly improved the quality of γ-ray spectrometry. Much greater resolution can be achieved with the use of a Ge(Li) detector as compared with a NaI detector, thus permitting the resolution of selected low energy peaks (Lewis, 1974; Szöghy and Kish, 1978). With such a system the U-238 concentration can be measured using either the 63 or 93 keV gamma rays produced in the decay of Th-234 to Pa-234, thus removing the need for separate U-238 analysis. Szöghy and Kish measured γ-ray spectra in the energy range 40-250 keV and established the degree of equilibrium by the measurement of the relative abundances of U-238, Pa-231, Ra-226, Rn-222 and Pb-210. Recently, Murray and Aitken (1980) at the Oxford TL laboratory have made use of a Ge(Li) detector for the study of disequilibria. In this way they can detect γ-rays with energies from about 40 keV to about 1470 keV, with an absolute efficiency of about

60% at 120 keV; thus making it an extremely useful instrument as far as disequilibrium studies are concerned.

Several other methods have been employed when studying discquilibrium in the uranium decay chains. For example, radon escape during burial of the sample can be estimated by alpha spectrometric analysis on Po-210 (Aitken, 1978).

Having discussed some of the causes of disequilibrium as well as quantitative analysis methods on the various elements in the decay chains, one is in a much better position to relate the problem to alpha counting. One can easily see that if one were to use the alpha counting data to obtain α, β and γ dose rates for a particular sample which exhibited gross disequilibrium in the U-238 decay chain (due to the loss or gain of elements in the top half of the decay chain); then all of the three components would be in error, although to different extents. About 98% of the gamma dose-rate of the U-238 chain is from members below radon in the chain; thus making the reduction in gamma dosage particularly serious. Fortunately the U-238 chain supplies only about a quarter of the total gamma dosage from typical soil. The magnitude of the error in alpha and beta doses will be appreciably less than that of the gamma dose (see for example, Aitken, 1974, 1978); although certainly quite important if accurate dates are to be obtained. For a typical sample of pottery the alpha and beta dose-rates each contribute between 35 and 40% of the total effective dose (Aitken 1974).

Hence if possible, one should avoid the alpha counting technique to obtain beta and gamma dose-rates. As Aitken most correctly points out, one should measure beta rays (by for example, using beta-TLD) in order to obtain beta-doses and gamma rays in order to obtain gamma-doses; the alpha counting technique should really be used to obtain the

accumulated alpha dose only. An even better situation, as far as the use of alpha counting is concerned, is to separately measure the degree of disequilibrium of the decay chains in conjunction with obtaining the alpha count rate for a particular sample. It is, however, still possible that the degree of disequilibrium as measured in the laboratory today is not the same as that during the sample burial time. Aitken (1978) mentions the fact that with its 1600 year half-life Ra-226 it is a particularly worrying possibility. Charalambous and Papastefanou (1977, 1978) have studied the effects of Ra-226 leaching in fossil bones; they found that it is quite often a cause of disequilibrium in the U-238 decay chain.

2.4.3 Alpha Particle Range Dependence on Atomic Weight.

When comparing alpha count rates from one sample to another, one has to have an accurate estimate of how the alpha particle range, and hence the count rate, depends on the atomic weight of the sample. For normal alpha counting on samples used in a TL dating program, this problem may not be too serious as the effective atomic weights of the various samples do not deviate appreciably (Bowman, 1976).

In the calculation of the dose-rate conversion tables (Aitken and Bowman, 1975; Bell, 1976, 1977, 1978) the Bragg-Kleeman (B-K) rule has been used in preference to the previously used $Z^{\frac{2}{3}}$ dependence (Turner *et al*, 1958; Tite and Waine, 1962). Bowman states that in the energy range of interest; namely, 4.0 to 8.8 MeV (see Appendix A) the proportionality to $A^{\frac{1}{2}}$, rather than $Z^{\frac{2}{3}}$, provides better range predictions.

A search of the literature on alpha particle energy range data was made in order to verify Bowman's statement, as well as to quantitatively estimate the accuracy of the B-K rule. In Table 2.4 the alpha particle range data, at an alpha particle energy of 5 MeV, from Whaling (1958), Williamson *et al*, (1966), Northcliffe and Schilling (1970) and Ziegler (1977), are compared with the values calculated using the B-K rule, as well as those calculated using a $Z^{\frac{2}{3}}$ dependence. Using the more recent range values of Williamson *et al*, Northcliffe and Schilling and Ziegler, one can see that Bowman's conclusion regarding the $A^{\frac{1}{2}}$ and $Z^{\frac{2}{3}}$ dependence is correct. One may also point out that the earlier range values of Whaling are probably more consistent with a $Z^{\frac{2}{3}}$ dependence, hence justifying the choice made by the early researchers. Also shown in Table 2.4 are the quantitative percentage deviations between the B-K range values and the Williamson *et al* and Ziegler values, these are denoted A and B respectively. One can see that in the atomic weight range between 14 and 35 (which certainly covers the majority of TL field samples and alpha counting standards) the calculated B-K range values are in good agreement with both the Williamson *et al* and Ziegler values, the accuracy of the B-K rule being within about 3%. In the case of the Williamson *et al* data, there is an even better agreement in the atomic weight range between 16 and 27, the accuracy being within about 1%. Generally speaking it appears that the B-K rule gives range values which are slightly higher at atomic weights above about 20 and slightly lower in the atomic weight range from about 14 to 20. The B-K rule clearly gives range values which are too low in the lower atomic weight region, the inaccuracy increasing the smaller the atomic weight. As an example of

TABLE 2.4 COMPARISON OF ALPHA PARTICLE RANGE DATA FOR VARIOUS ELEMENTS AT AN ENERGY OF 5 MeV

Alpha Ranges ($mg.cm^{-2}$)

Element	A	Z	R_{B-K}	$R_{Z^{\frac{2}{3}}}$	$R_{Whaling}$	$R_{Williamson}$	R_{N-S}	$R_{Ziegler}$	% Dev A	% Dev B
He	4.00	2	2.23	1.78	3.16	3.27	3.16	2.96	- 32.9	- 24.7
Li	6.94	3	2.94	2.32	4.25	3.84	-	3.65	- 23.4	- 19.5
B	10.81	5	3.67	3.27	-	4.12	-	3.95	- 10.9	- 7.1
C	12.01	6	3.87	3.70	-	4.06	3.96	3.93	- 4.7	- 1.5
N	14.01	7	4.18	4.10	4.14	4.30	4.24	4.34	- 2.8	- 3.7
O	16.00	8	4.47	4.48	4.11	4.53	4.44	4.51	- 1.3	- 1.1
Ne	20.18	10	5.02	5.20	5.16	5.02	4.93	4.87	0	3.1
Na	22.99	11	5.35	5.54	-	5.41	-	-	- 1.1	-
Aℓ	26.98	13	5.80	6.20	6.63	5.79	5.92	5.79	0.2	0.2
Si	28.01	14	5.91	6.51	-	5.78	-	5.89	2.2	0.3
Cℓ	35.45	17	6.67	7.41	-	6.59	-	6.83	1.2	- 2.3
Ca	40.08	20	7.07	8.23	-	6.85	-	7.42	3.2	- 4.7

NOTES: The Bragg-Kleeman alpha particle ranges were estimated using the relation $R_O = 0.32 \quad A^{\frac{1}{2}} \quad R_o mg.cm^{-2}$, where R_o is the range in cm. of an alpha particle of the same energy in air.

this, for the element lithium the B-K range value is about 20% shorter than the Williamson *et al* and Ziegler values. However, as already mentioned this should not be a problem since the majority of minerals which are found in TL field samples, i.e., quartz (A = 20.3), hectorite (A = 20.8), illite (A = 21.4), calcium carbonate (A = 21.1) and feldspar (A = 21.3), have average atomic weights which are very close to about 20. A similar comparison of alpha particle ranges was also carried out at other energies. In this respect the data of Williamson *et al* is the most exhaustive. A comparison of their ranges with those predicted by the B-K equation for six different elements; namely lithium (A = 6.94), nitrogen (A = 14.01), neon (A = 20.18), sodium (A = 22.99), silicon (A = 28.01) and calcium (A = 40.08), with energies in the range from 4 to 9 MeV is shown in Table 2.5. One notes that for atomic weights around 20 (neon and sodium), there is good agreement between the Williamson *et al* and the B-K range values over the entire energy range 4 to 9 MeV, the accuracy of the B-K equation being within about 4%. Furthermore, there is an even better agreement in the energy range 4 to 6 MeV. This result is important, as the majority of the alpha's emitted by the U-238 and Th-232 decay chains have energies between 4 and 6 MeV (see Appendix A). Good agreement was also observed for the element nitrogen, with a general accuracy of about 3% over the entire energy range. For higher atomic weight elements (silicon and calcium) the B-K equation gives range values which are generally too high and the discrepancy increases with increasing energy. For lower atomic weight elements (lithium) the B-K equation gives ranges which are too low, with only a slight increase in the discrepancy as the energy is increased.

TABLE 2.5 COMPARISON OF THE WILLIAMSON *et al* AND BRAGG-KLEEMAN ALPHA PARTICLE RANGES FOR VARIOUS ELEMENTS : ENERGY RANGE FROM 4 TO 9 MeV

Alpha Ranges ($mg.cm^{-2}$)

Energy MeV	Li			N			Ne		
	W	B-K	% Dev	W	B-K	% Dev	W	B-K	% Dev
4	2.70	2.11	- 21.9	3.10	2.99	- 3.5	3.65	3.60	- 1.4
5	3.84	2.94	- 23.4	4.30	4.18	- 2.8	5.02	5.02	0
6	5.17	3.89	- 24.8	5.70	5.53	- 3.0	6.58	6.64	0.9
7	6.68	5.00	- 25.1	7.27	7.10	- 2.3	8.33	8.52	2.3
8	8.37	6.20	- 25.9	9.01	8.82	- 1.0	10.26	10.58	3.1
9	10.02	7.58	- 24.4	10.93	10.77	- 1.5	12.38	12.92	4.4

Energy MeV	Na			Si			Ca		
	W	B-K	% Dev	W	B-K	% Dev	W	B-K	% Dev
4	3.95	3.84	- 2.8	4.26	4.23	- 0.7	5.11	5.06	- 1.0
5	5.41	5.35	- 1.1	5.78	5.91	2.2	6.58	7.07	3.2
6	7.07	7.09	0.3	7.51	7.82	4.1	8.82	9.36	6.1
7	8.94	9.10	1.8	9.44	10.04	6.4	10.99	12.00	9.2
8	11.00	11.29	2.6	11.56	12.46	7.8	13.37	14.91	11.5
9	13.25	13.79	4.1	13.88	15.23	9.7	15.95	18.21	14.2

One can conclude that the B-K rule can be used to determine effective alpha particle range values for the majority of samples with an accuracy of a few percent. However, the use of actual range data is to be preferred, especially for cases of low or high A materials, e.g. the lithium tetraborate glass discussed in Chapter 5.

For a compound or mixture of minerals, the effective $A^{\frac{1}{2}}$ (or $Z^{\frac{2}{3}}$) value can be computed by the relation:

$$A^{\frac{1}{2}}_{\text{effective}} = \frac{\sum_{i=1}^{r} n_i A_i}{\sum_{i=1}^{r} n_i A_i^{\frac{1}{2}}} \qquad (2.7)$$

where n_i is the atomic fractions of the ith mineral as calculated on the atomic weight basis and A_i its corresponding atomic weight (see for example, Evans, 1955). Some of the uranium ore counting standards obtained from the USDOE are dunite based and some are quartz based. The average composition of the mineral dunite is shown in Table 2.6, also shown are the calculated atomic weights of the various compounds making up dunite. The effective atomic weight of dunite was calculated to be 21.8, certainly not far from the value of 21.4, which generally is used as an average value for TL field samples.

2.4.4 Alpha Count-Rate Dependence on Sample Reflectance

As already mentioned in Section 2.4, the alpha pulse height spectral shapes are very much dependent on sample colour. Figure 2.5 shows the normalized pulse height spectra obtained from various uranium and thorium counting standards. The uranium-ore standards NBL-42-1 and 42-2 are dark grey in colour (dunite based), whereas both NBL-101(U) and NBL-106(Th) are whitish in colour (quartz based); hence the

TABLE 2.6 AVERAGE COMPOSITION OF THE MINERAL DUNITE

	Mass (%)*	Atomic Weight
SiO_2	40.5	20.3
Al_2O_3	.9	20.7
Fe_2O_3	2.8	35.1
FeO	5.7	39.2
MgO	46.3	20.4
CaO	.7	29.4
H_2O	2.9	9.0
Others	0.2	20.3

Notes : Using Equation 2.7 this gives us an effective atomic weight of dunite of 21.8

* The mass fractions shown are from Spock (1961).

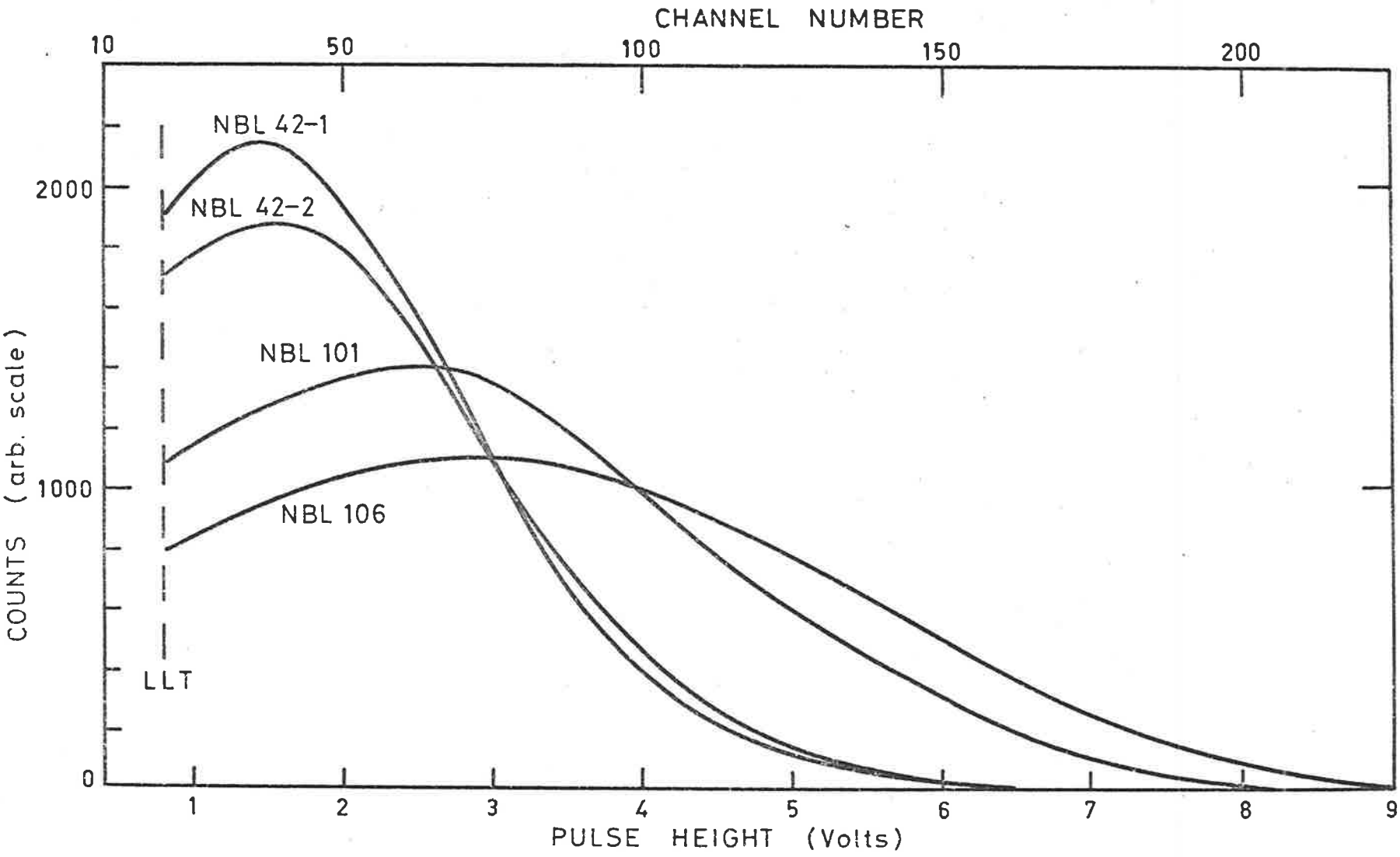

Figure 2.5 Normalized Pulse Height Spectra on some Uranium and Thorium Standards.

observed effect on spectral shape is a strong one. From these spectral shapes one can see that it is important to calibrate the alpha counter with standards which have colours typical of TL field samples, unless the reflectivity effect can be put on a quantitative basis. Huntley (1978) states that if one calibrates the counter using a white standard and then uses the counter to measure the count rate of a grey sample, the resulting count rate could be up to 20% too low. If this is true then the ideal solution to the problem would be to apply a quantitative correction to the observed count rate based on sample colour, as well as to avoid calibrating the counter using whitish counting standards.

Huntley (1978) has attempted such a quantitative experiment, to see how accurately the reflectivity effect can be predicted and hence corrected for. He measured the reflectance (R) of a variety of counting standards and determined the discriminator setting for each (85% thorium threshold, see Section 2.4.5). The data obtained was fairly consistent with the size of the light pulses being proportional to (1+R), although there was an appreciable scatter in the data. One of the main problems with this technique is that a separate reflectance measurement has to be made on each sample.

A much simpler method as an indicator of sample reflectance is to employ a soil colour chart such as the Munsell system; where each colour is described by three attributes of colour: "hue", "value" and "chroma". The hue represents the dominant spectral colour, the value represents the relative lightness of the hue colour and the chroma represents the relative purity or strength of the spectral colour.

The notation of value consists of numbers from 0 to 10 where the higher the number the lighter the colour; i.e. the higher the reflectivity. Hence by using the "value", notation one has a reflectivity scale from 0 to 10; each increment in value representing a successively lighter grey sample.

If one was to prepare a variety of accurately known counting standards varying in brightness from dark grey to white one should be able to obtain a sample reflectivity correction curve; that is a plot of sample brightness (reflectivity) versus alpha count rate - reflectivity correction factor. Various ways of preparing these standards can be suggested. One could for example mix a white counting standard (i.e. 1% U-NBL-101) with varying but accurately known amounts of a dark mixer (i.e. graphite (A $\sim$ 12), or alternatively mix a dark grey standard (i.e. 4% U-NBL-42-1) with varying amounts of a white mixer (i.e. Al_2O_3 (A $\sim$ 20.7)). As long as the concentration levels and atomic weights of the standards and mixers are well known it should be possible to obtain a sample reflectance factor for each mixed standard.

In order to obtain a quantitative measure of the possible magnitude of the reflectivity effect it was decided to compare the alpha count rates (above 85% thorium threshold) for a variety of NBL counting standards which vary in colour from completely white to dark grey. The pulse height spectra of some of these have already been discussed (see Figure 2.5). These standards all have accurately known uranium and thorium concentration levels. The results obtained are summarized in Table 2.7. The observed alpha count rates have been compared with the expected alpha count rates based on their accurately known concentrations. The uranium standards are all pure, that is, there is no thorium present.

TABLE 2.7 COMPARISON OF ALPHA COUNT RATES FOR A VARIETY OF STANDARDS

Sample (NBL)	Concentrations U	Th	Observed α-count rate ks^{-1}	α_u (ks^{-1})	α_{Th} (ks^{-1})	Measured Activity	Meas. Act. / Concentration	Sample Colour
42-1	4.04±.04%	-	54500	54500	-	3.22%	0.80	
42-2	1.99±.006%	-	26064	26064	-	1.54%	0.77	dark grey
42.3	1.07±.003%	-	14212	14212	-	.84%	0.79	
42-4	.52±.006%	-	6894	6894	-	.41%	0.79	
101	1.00±.01%	-	13115	13115		.77%	0.77	
102	.101±.001%	-	1316	1316		.078%	0.77	
103	470± 10μgg^{-1}	-	658	658		388μgg^{-1}	0.83	whitish
104	103± 4μgg^{-1}	-	142	142		84μgg^{-1}	0.82	
106	350μgg^{-1}	1.00±.01%	4218	449	3769	.76%	0.76	
107	35μgg^{-1}	.10±.004%	422	45	377	758μgg^{-1}	0.76	whitish
108	18μgg^{-1}	520 ± 10μgg^{-1}	236	23	213	429μgg^{-1}	0.83	
109	37μgg^{-1}	104 ± 3μgg^{-1}	475	4.7	42.8	86μgg^{-1}	0.83	

NOTE: Statistical counting error in the measured alpha count rates was negligible (certainly less than 1%).

The uranium-ore standards NBL-42-1 to 42-4 are all dunite based ($A \sim 21.8$, see Section 2.4.3) whereas the uranium standards NBL-101 to 104 and the thorium standards NBL-106 to 109 are all quartz based ($A \sim 20.4$). The thorium standards also contain small but known quantities of uranium, from which the alphas emitted have been subtracted from the observed count rate in order to get the true thorium count rate. If one ignores the fact that the standards have slightly different atomic weights then one gets an indication of the way in which the sample colour (reflectivity) affects the measured alpha count rate. The results displayed in Table 2.7 have been split into three groups. The first group consists of the four dunite based uranium ore standards. These standards are dark grey in colour, the darkness increasing with uranium concentration. The brightness "values" of these standards are all about 3 to 4. The second group consists of four quartz based uranium standards which are all extremely white in colour. The brightness "values" of these standards are about 9 to 10, with the lower concentration standards being the brightest. The third group consists of four quartz based thorium standards which also are extremely white in colour with the lower concentration again being the brightest.

A quantitative measure of the magnitude of the reflectivity effect on these various counting standards has been estimated by comparing the measured alpha activity with the expected activity (determined from the accurately known concentration levels, using Bell's dose-rate conversion tables). The variation in this ratio from one standard to the next reflects the magnitude of the reflectivity effect.

The results obtained are a bit surprising; the maximum discrepancy between any of the counting standards is about 9% and this is

between two white standards. The dunite based uranium standards have colours which are fairly typical of the ones encountered on field samples; on these the estimated ratios are fairly constant; the average value being 0.79 ± 0.01. For absolute alpha calibration purposes one should probably use one of these standards (see Section 2.4.5). If one takes the average values of this ratio on both the quartz based uranium and thorium standards then one also obtains a value quite close to 0.79. That is, the observed magnitude of the reflectivity effect in going from a very dark standard to a completely white standard is less than about ± 5%. The fact that there is no observable trend of the white standards having more counts than the grey standards suggests furthermore that the cause of the observed discrepancy may not even be that of varying sample reflectances. It is very interesting to note that although the spectral shapes of the various standards are markedly different; especially in going from a dark grey to a white standard (see Figure 2.5), the net change in alpha count rate above threshold is quite small. There is, for example, a drastic difference in the pulse height spectral shapes of the standards NBL-101 (1% uranium) and NBL-106 (1% thorium) as compared to the pulse height spectrum of the standard NBL-42-2 (2% uranium); although the net difference in alpha count rate above threshold between the three standards is negligible. That is, the increase in counts in the upper channels is compensated for by the decrease in counts in the lower channels.

As there is no observable reflectivity effect on the measured alpha count rate (above threshold) in going from a dark grey to a completely white standard, there is rather little point in trying to prepare a variety of different brightness standards which covers the

range white to dark grey more extensively.

2.4.5 Absolute Calibration of the Alpha Counter

The standard alpha counter calibration procedure, used in most of the TL dating laboratories, is to plot the count rate versus discriminator setting for a "well behaved" uranium (or thorium) standard; then to choose a fixed discriminator setting where the count rate is 82% (or 85%) respectively of the extrapolated zero threshold level (see for example, Huntley, 1978). The threshold is set at a level to make sure that the general background above this threshold is as low as possible. This background is due to beta particles and gamma radiation as well as photomultiplier dark noise. The 82% figure is used so that the dose-rate conversion factors of Aitken and Bowman (1975) and Bell (1978) may be used; assuming that extrapolation to zero threshold yields a 100% efficient count rate. By the term a "well behaved" standard one means a standard which is known to be close to secular equilibrium (see Section 2.4.2), one which has an accurately known atomic weight (see Section 2.4.3) and the sample colour should be typical of field samples (see Section 2.4.4). Figure 2.6 shows a plot of counting threshold versus count rate on a 4% uranium standard (NBL-42-1); which is known to be close to secular equilibrium. From the actual pulse height spectrum of this standard, shown in Section 2.4.4 (Figure 2.5), it is easy to see that the plot of threshold versus count rate (for a particular value of photomultiplier EHT) will not be a straight line over the entire threshold range, but a slightly curved one. Hence one must be careful when extrapolating to zero threshold. A plot of threshold versus count rate will only be a straight line on a flat part of the pulse height spectrum. To make sure that the counts recorded are all due to alpha's emitted by the sample standard, a

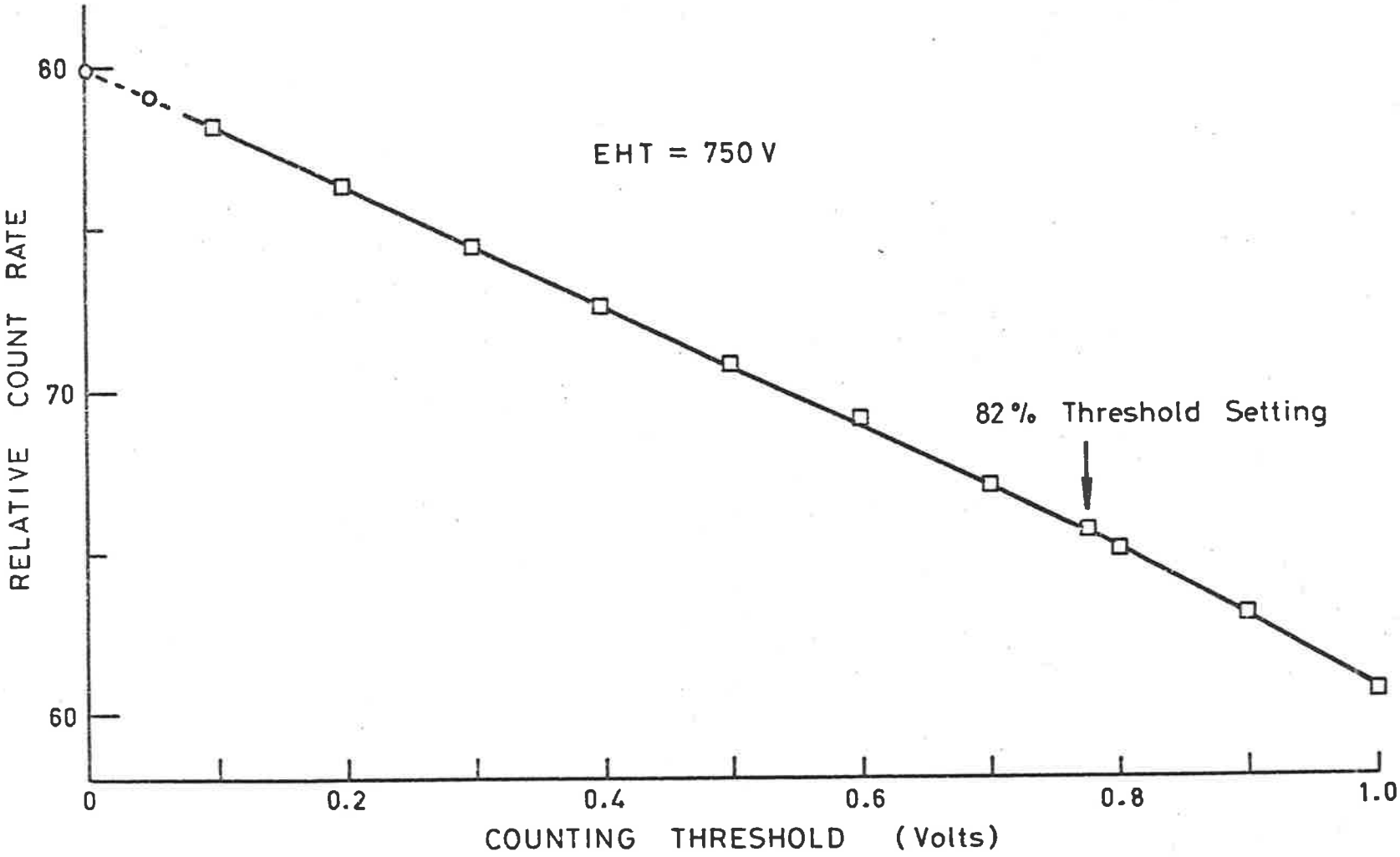

Figure 2.6 Counting Threshold versus Alpha Count Rate for Uranium Standard N3L 42-1.

measure of the general background under normal counting conditions as a function of threshold was obtained by inserting a 125 μm thick disc of acetate transparent film between the sample standard and the counting screen. This disc prevents all alpha's from the standard from reaching the counting screen while allowing most of the beta particles (and gamma radiation) to pass through. This measurement is of course different from the "normal background" measurement which is obtained without the sample present. For the 4% uranium standard, the general background was negligible above a threshold of about 0.1V. It was also found that in the region below 0.1V the sample count rate corrected for background agreed well with the linearly extrapolated count rates. From Figure 2.6 one can see that for the 4% uranium standard the plot of alpha count rate versus threshold (at an EHT of 750V) is very close to linear in the region between zero threshold and about 0.8V.

As well as determining the discriminator level one also has to set the gain of the amplifier and the high voltage (EHT) on the photo-multiplier tube. The amplifier gain is set so that on none of the standards, even the whitish ones, are there any counts with pulse heights above the upper level acceptable to the single channel analyzer (SCA). This is clearly demonstrated in Figure 2.5 where even the white standards NBL-101 and 106 do not exhibit any counts above a pulse height of 9V, the upper discriminator level being 10V. While this requirement is not strictly necessary under normal alpha counting conditions, where the SCA is used as a discriminator, and all counts above lower level threshold are registered, it is necessary when one wants to compare pulse height spectra using a single- or multichannel analyzer (MCA). The EHT is chosen so that the background count

rate above the lower level discriminator level is negligible. For a typical field sample one would want the background to contribute less than 1%. In Figure 2.7, the relative count rate versus threshold setting has been plotted for different values of applied EHT. One notes that for the different EHT values one obtains a constant extrapolated to zero threshold count rate; that is, the extrapolated count rate is independent of the EHT value. One can also see that plots of threshold versus count rate are not straight lines but curved. Furthermore, the curvature increases with decreasing EHT.

Having obtained the "correct" discriminator setting for a given photomultiplier EHT (750V), one is in a position to estimate the overall counting efficiency. The ZnS(Ag) screens used are obtained in 30.5 cm x 30.5 cm sheets from W.B. Johnson and Associates, Montville, New Jersey, U.S.A. Bowman (1976) has pointed out that the efficiency of these screens can vary from one batch to another. In order to check this variation in efficiency phenomenon a 4.2 cm diameter calibration standard ("hanstand") was made up. Hanstand was made by mixing 4% uranium (NBL-42-1) into a silicone rubber matrix and then placing the mixture in an aluminium holder which then could be positioned on top of the ZnS screen. The actual source does not touch the screen so there is no chance of contamination; the source holder is shown diagrammatically in Figure 2.8. Five batches of ZnS sheets have so far been tested for efficiency variations and the results obtained are summarized in Table 2.8. The ZnS screens from within the same batch were found to have the same efficiency, within counting statistics, in four out of the five batches. In the remaining batch (batch No. 2) a deviation of as much as 5% from the mean

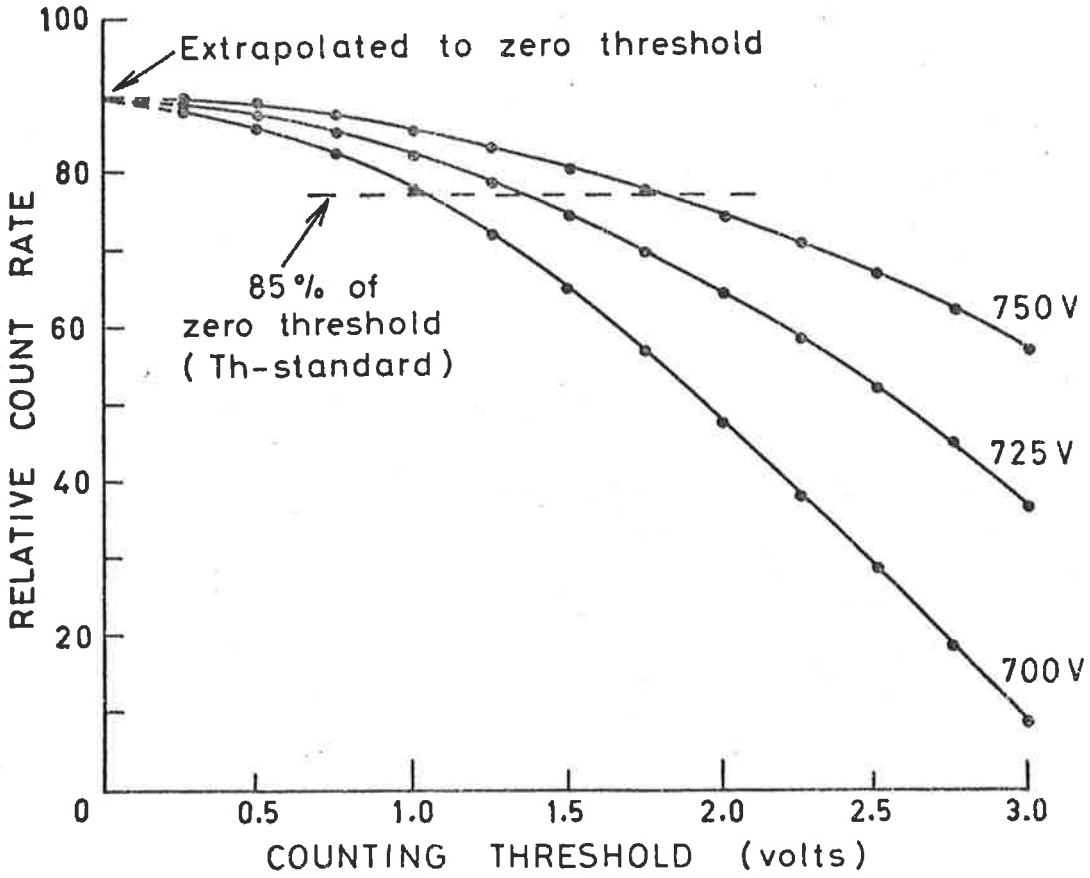

Figure 2.7 Counting Threshold versus Relative Alpha Count Rate as a Function of Applied EHT.

TABLE 2.8 BATCH TO BATCH VARIATION IN ALPHA COUNTING EFFICIENCY FOR ZnS SCREENS

	BATCH NO.				
	1	2	3	4	5
Date Received	Sept 1977	Nov 1977	Oct 1978	Dec 1979	Dec 1980
Counts/0.4 ks using Cu1	12300±110	10560±500	10260±100	10250±100	11720±120
Absolute Efficiency Factor	95±2%	81±2%	79±2%	79±2%	89±2%

NOTES: Both the counts/0.4 ks as well as the absolute efficiency factor were estimated at a constant threshold which was set on a screen from batch number 3 (82% of the extrapolated zero threshold value on a 4% uranium standard).

The counting standard CU1 is referred to in the text as "hanstand".

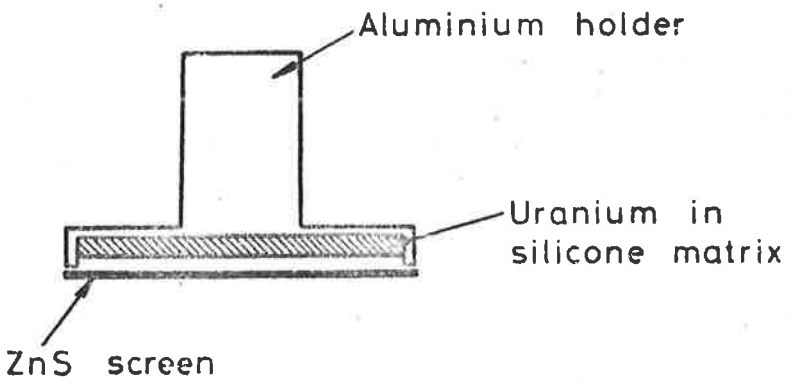

FIGURE 2.8 The ZnS Screen Calibration Standard-"Hanstand"

count rate was observed; in each case a total of 12 randomly chosen screens was examined. The batch to batch variation in efficiency was found to be as large as 20%; although batches 3 and 4 showed no batch variation and no screen to screen variation. Batches 3 and 4 are suspected of coming from the same production run; the manufacturers tell us that several hundred feet of ZnS material is produced per run. Hence for routine alpha counting it is recommended that the screen to screen variation be tested as soon as a new batch of ZnS sheets has been received; while at the same time comparing the measured efficiency to the efficiency of the previous batch. This can be done by choosing screens at random from within the batch. If no screen to screen variation is found then there should be no need to test each individual screen prior to use. As a reference it is useful to retain a couple of screens from each of the batches received.

In obtaining Figure 2.6; where the threshold versus absolute count rate is plotted for a 4% uranium standard, the ZnS screen used came from batch 3. ZnS screens from batch 3 were also used in obtaining

the data in Table 2.6. Hence, the overall efficiency of the alpha counter, as measured using the 4% uranium standard on a ZnS screen from batch 3, is 80 ± 2%. That is, the extrapolation to zero threshold in Figure 2.6 does not yield a 100% count rate efficiency. Perhaps an even better estimate of this efficiency factor can be obtained by taking the average from those obtained on different counting standards, as well as by doing repeat measurements. If one takes the average efficiency factor on the grey counting standards NBL-42-1 to NBL-42-4 (see Table 2.7); then one obtains a value of 79 ± 2%. It is important to note that on these dunite based standards the atomic weight is close to the usually assumed value of 21.4 and hence less errors are likely to be introduced when applying the Bragg-Kleeman correction factor.

In principle, one should be able to obtain a 100% detection efficiency of the optimum EHT value if the ZnS screens have the correct thickness of ZnS (Ag) powder deposited on them. Graves and Dyson (1949) have measured the variation of the count rate of 5 MeV alpha particles, using a ZnS (Ag) screen viewed by an RCA 931A photomultiplier tube, as a function of phosphor screen thickness. The results, plotted in Figure 2.9, show that under their experimental conditions the count rate is constant, presumably corresponding to 100% detection efficiency, for a ZnS powder thickness from about 9 to 25 $mg.cm^{-2}$. At greater thicknesses the detection efficiency decreases due to the increased opacity of the screen, and at smaller thicknesses it decreases due to less energy being dissipated by the alpha particles and because of inhomogeneity of the screen. The ZnS screens which we use have a phosphor thickness of about 4.5 $mg.cm^{-2}$ and the manufacturers do state

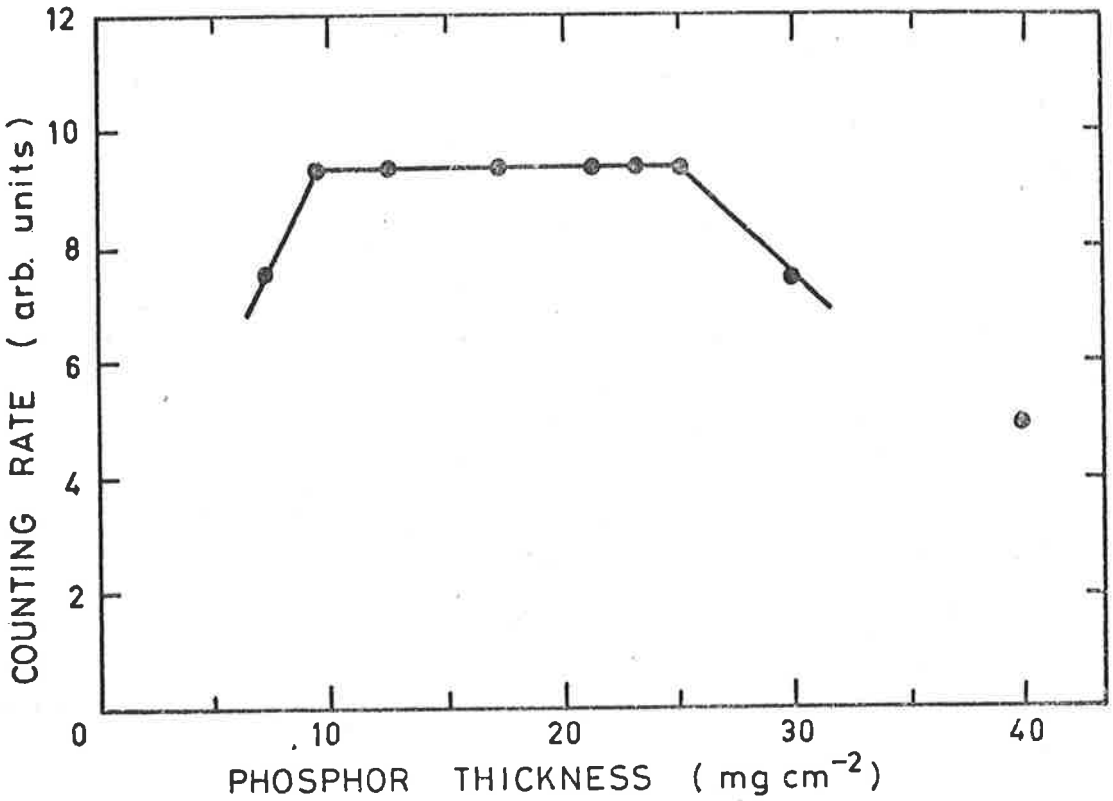

Figure 2.9 Alpha Count Rate as a Function of ZnS Screen Thickness (From Graves and Dyson, 1949).

that they are not 100% efficient. (see also, Fisenne and Keller, 1981). Figure 2.8 may explain the variation observed in ZnS screen efficiency from one batch to another; that is, a small variation in phosphor thickness may lead to quite an appreciable difference in the corresponding efficiency factor.

Having estimated the overall counting efficiency for a particular batch of ZnS screens one is in a position to use the already mentioned dose-rate conversion tables, as long as the background count rate has first been subtracted from the measured count rate. The background count rate varies somewhat from one run to the next, although it is generally less than 0.25 counts ks^{-1}. If the background exceeds 0.3 counts ks^{-1} then the ZnS screen is rejected and the perspex counting cell, aluminium spacer and steel retaining ring thoroughly cleaned in methanol. The background has been found to vary from one batch of ZnS screens to another. For the first three batches received the background was usually in the range 0.15 to 0.25 counts ks^{-1}; whereas for batches four and five the level was generally below 0.1 counts ks^{-1}. Huntley (1977) states that the background measured with a clean perspex disc laid on top of the ZnS screen is generally five times lower than that measured without the perspex disc. The experience with our counter is that even without the perspex disc the background is still generally below 0.25 counts ks^{-1}. Radon present in the counting chamber could explain the increase in background activity as measured by Huntley. For this reason one should not store active standards in the same room as the alpha counting equipment and one should certainly not count TL field samples in the same counting cells

as are used for standards. Quite often one may observe a higher level of background in the first few hours after having exposed the ZnS screen to normal light in the laboratory. This is due to phosphorescence from the phosphor which decays away within a few hours or so. Hence, the usual counting procedure is to avoid subjecting the ZnS screen to too much light prior to commencing a background or sample count and to always check the data obtained in the first few hours of counting. If excess counts occur in the first few hours then our usual procedure is to reject the first 30 ks of counting.

2.4.6 Possibility of "Overcounting"

One of the assumptions used in deriving the basic alpha counting equation (Equation 2.1) is that the alpha activity is distributed homogeneously throughout the sample volume. While this assumption generally holds for the counting standards it does not always hold for the large variety of TL field samples encountered. For an alpha count on a given field sample the possibility of "overcounting" (or "undercounting") must not be discounted. By the term "overcounting" one means that the measured count rate is higher than the true count rate. Furthermore, the effective atomic weight formula (Equation 2.7) will not apply to samples in which the alpha emitters are contained in crystalline structures within the aggregate in which the alpha ranges are widely different from the aggregate as a whole. Hurley (1950) gives an example in which an aggregate of ground quartz and feldspar has within it little crystals that contain all the alpha emitters in the aggregate as a whole. Even if this sample was not finely ground to the size of the small alpha emitting crystals, the overall alpha range

correction for the alpha count rate must lie between the range correction for the pure quartz-feldspar matrix and the range correction for a sample made up entirely of the alpha emitting crystals.

The possibility of overcounting was another reason why the uranium and thorium concentrations as obtained by alpha counting were to be compared to the uranium and thorium concentrations as obtained by other means (see Chapters 3, 4 and 5).

Preliminary investigations of the alpha inhomogeneity problem were carried out on a baked soil sample (Sc 3/3) which was giving abnormally high alpha count rates. First of all the bulk sample, which consisted of mainly quartz grains with a reddish coating on the surface, was sieved into various grain size groups; namely, less than 45 μm, 45-90 μm, 90-180 μm and 180-250 μm. The relative alpha count rates of these different grain size groups are shown in Table 2.9. One can see that the alpha activity is not distributed uniformly throughout the various grain sizes; for example, the less than 45 μm size fraction exhibits an alpha count rate which is appreciably higher than the bulk sample. In this particular sample the relative amounts of the various grain size fractions were fairly constant; perhaps the 45-180 μm size range was slightly predominant. The fact that the smaller grain sizes exhibit higher relative count rates indicates that the possibility of overcounting must be considered. The reason for this line of argument is that it is possible for the fine grains to work their way down into the gaps between the larger

TABLE 2.9 ALPHA COUNT-RATES ON SAMPLE Sc 3/3 AS A FUNCTION OF GRAIN SIZE AS WELL AS ETCHING TIME

	Grain-Size Range			
Treatment	< 45 μm	45-90 μm	90-180 μm	180-250 μm
None	30 ± 1.6	24.6 ± 1.0	17.4 ± 1.0	21.4 ± 1.0
10 Mins. Etch in 40% HF acid		* 41 ± 12	17.8 ± 1.0	10.5 ± 0.8
60 Mins. Etch in 40% HF acid			12.6 ± 0.8	

NOTES : Units of alpha count rates are ks^{-1}

* - Very inhomogeneous sample.

grains as they lie on the scintillation screen, or similarly in a sample container, these are then counted with a higher efficiency than the bulk sample. This overcounting phenomenon was actually seen to occur on the bulk sample.

Because of the reddish surface colour on the quartz grains; which is probably due to deposition of iron oxide, it was decided to check for any obvious alpha count surface effect. The various grain size fractions were first etched in 40% hydrofluoric acid for a period of 10 minutes; the relative changes in count-rates due to this surface etching are also shown in Table 2.9. The 45-90 μm size fraction exhibited a drastic increase in activity of about 65%, although the count rate was not very reproducible from one count to another. This count rate was very much dependent on exactly how the sample grains were deposited on to the ZnS screen. In contrast the 180-250 μm size fraction exhibited a drastic decrease of about 50% upon etching and the count rate on the 90-180 μm size fraction remained unchanged. A further 50 minutes etch was done on the 90-180 μm size fraction, the result of this was an approximate 25% reduction in count rate. Hence, for this particular sample, namely Sc 3/3, there is a non-uniform distribution of alpha activity both within the various grain sizes and within each individual sample grain. It was thought that the majority of the excess surface activity was caused by transportation of uranium containing minerals while the sample had been buried. This was verified by comparing the alpha pairs data obtained on the etched sample portions with those obtained on the untreated portions. The alpha pairs fractions (see Section 2.4.1) obtained are shown in Table

2.10. One can see that prior to etching the pairs fraction was more or less independent of grain size; with an average value of 0.011 ± 0.001 (this corresponds to a Th/U ratio of about 1.4). After a 10 minute etch, the pairs fraction had increased considerably, although it was still more or less independent of grain size. The average value was 0.020 ± 0.001, which corresponds to a Th/U ratio of about 3.5. These results clearly indicate that pairs counting on the bulk sample (Sc 3/3) does not give a correct indication of the true Th/U ratio, as the relative thorium activity is much less on the surface of the grains.

Other soil samples have been shown to exhibit alpha count rates which are very much grain size dependent. For example, sample EBla, which is a soil sample from the surrounds of a prehistoric Australian fireplace, exhibits a much higher alpha activity on the fine grains (less than 45 μm) than that of the rest of the sample (Prescott, private communication). On Ebla one obtains count rates varying from about 4 ks^{-1} to about 50 ks^{-1} depending on how the grains are deposited on to the ZnS screen.

Some of the possible causes of overcounting have already been discussed in the literature. Murray (1980) suggests that overcounting could also be due to radon which escapes from the mineral phase into the air spaces between the grains, but does then not diffuse any further. This radon activity is then counted with a higher efficiency than that retained in the solid phases, giving a higher count rate than expected. The magnitude of the overcount produced by this phenomenon would clearly depend on the relative amounts of uranium

TABLE 2.10 ALPHA PAIRS FRACTIONS ON SAMPLE Sc 3/3 AS A FUNCTION OF GRAINS SIZE AS WELL AS ETCHING TIME

Treatment	Grain-Size Range			
	< 45 μm	45-90 μm	90-180 μm	180-250 μm
None	.010±.001	.012±.001	.012±.001	.011±.001
10 Mins. Etch in 40% HF acid		.020±.002	.021±.002	.019±.002

NOTES : Above data represents average values obtained from several runs.

present in a given sample as well as on the packing density. Murray also mentions the possibility of a surface effect; if the average grain size is larger than the alpha range (about 25 μm), then counting geometries can be suggested which would give rise to over-counting.

2.5 Summary and Conclusions

In this chapter the basic principles of the thick source alpha particle counting method were discussed. The experimental alpha counting apparatus was described in some detail, as were some of the main problems encountered when using the method. The alpha pairs counting technique was shown to be a suitable method for estimating Th/U ratios. It was pointed out that, although the usual assumption of Th-232 having the same activity as that of U-238 and U-235 combined, which corresponds to a Th/U ratio of 3.16 by weight, does not lead to any gross errors in the obtained alpha dose, any reasonable measurement of the Th/U ratio is always better than even an educated guess!

The problem of radioactive disequilibrium in the uranium and thorium decay chains was also discussed. In the absence of any equilibrium information one should be careful in interpreting the significance of the measured alpha count rates. One should, if possible, always avoid calculating beta and gamma dose rates based solely on observed alpha count rates; the main problem being in the U-238 decay chain, where the bulk of the gamma dose-rate comes from members below radon. The ideal situation is to estimate the activity of each element

in the individual decay chains; this can be done by determining the abundance of some selected key elements. However, even if this is done, there is no guarantee that the degree of equilibrium has been constant during the sample's burial time.

By comparing alpha particle range values, at an energy of 5 MeV, it was found that the alpha ranges for varying atomic weights were in good agreement with those predicted by the B-K relation. For atomic weights in the range 14 to 35, which more than covers the range one is normally interested in, the accuracy of the B-K relation was found to be within about 3%. A similar comparison was also carried out for various elements in the energy range 4 to 9 MeV. In this case, the B-K relation was found to hold well for atomic weights around 20, the accuracy being within about 4%. This result is important as there has been some uncertainty about the accuracy of the B-K equation (Bowman, 1976; Huntley and Wintle, 1981). It means that for the majority of samples, which contain a mixture of minerals, the uncertainty in the absolute count rate can be reduced by applying the appropriate B-K correction factor. However, for higher atomic weight elements the B-K equation gives range values which are generally too high, with the discrepancy increasing as the energy increases. Also, for lower atomic weight elements the B-K equation gives ranges which are too low, although there is only a slight increase in the discrepancy as the energy increases.

It was also shown that although the alpha particle pulse height spectral shapes are highly dependent on sample colour (reflectance), the net effect on the observed alpha count rate above a fixed threshold is rather small. In trying to obtain a quantitative measure of

the reflectivity effect upon the alpha count rate, it was found that on examining a set of 12 counting standards, varying in colours from white to dark grey, the maximum deviation in count rate, presumably due to varying reflectivity, was less than 5%. Furthermore, it was found that on the average the alpha count rates obtained on the whitish standards agreed quite well with those obtained on much darker standards.

The absolute efficiency of the alpha counter was found to depend on the particular batch of ZnS screens used. Among 5 different batches a batch to batch variation in efficiency of up to 20% was observed. For batch number 3, the absolute alpha efficiency factor was estimated at 0.79 ± 0.02. It is recommended that upon receipt of a new batch of ZnS screens, the screen to screen variation be tested by choosing a number of screens at random, while also comparing the measured efficiency to the absolute efficiency of the previous batch.

It was also found that the alpha activity in some of the field samples is not distributed uniformly. On some of the soil samples, it was found that the finer grains exhibited alpha activities which were up to ten times higher than the bulk sample. This means that the observed alpha count rate may be highly dependent on the degree of crushing as well as homogenization prior to counting, it may also depend on exactly how the sample grains are deposited on to the ZnS screen. On one of the field samples, the alpha activity was also found to be inhomogeneous within the individual grains; the surface activity being appreciably higher than the bulk average, hence

producing a count rate which is higher than the true count rate ("overcounting").

The main problems with the use of the alpha counting method are hence, the possibility of disequilibrium in the decay chains, in particular the U-238 decay chain, and the possibility of overcounting. If one is to use the method to determine the archaeological alpha dose-rate for a particular TL field sample, then it is very important to make sure that the measured alpha count rate is correct; that is overcounting must be circumvented. This problem will be further discussed in Chapter 4 where some of the results obtained using alpha counting are compared with those obtained using neutron activation analysis for both uranium and thorium.

CHAPTER III

SOME OTHER METHODS FOR THE LOW LEVEL DETERMINATION OF URANIUM AND THORIUM

3.1 Introduction

The most favoured technique, in the different TL dating laboratories, for the determination of the archaeological radiation dose is, as already mentioned in Chapter 2, thick-source alpha particle scintillation counting. This technique is almost always used in order to obtain the archaeological dose due to alpha-particles.

Some of the problems associated with the use of this alpha counting technique were also discussed in the previous chapter, these included possible errors due to uncertain Th/U ratios, unknown degree of secular equilibrium in the decay chains and the possibility of overcounting. It was because of these uncertainties that it was decided to look at other methods for low level thorium and uranium determinations.

A research grant was obtained from the Australian Institute of Science and Engineering (AINSE) which enabled our research group to use the facilities at the Australian Atomic Energy Commission (AAEC), which is situated at Lucas Heights, near Sydney. The author participated personally in all of the procedures described in this chapter and, until recently, was responsible for carrying out this programme. Furthermore, unless otherwise indicated, the author is

responsible for the relevant results presented in this thesis.

At the AAEC one has available various techniques which can be used for the determination of low levels of uranium and thorium. This Chapter contains descriptions and discussions of the techniques employed in the quest for alternative means of determining uranium and thorium. In this Chapter the suitability of the methods (a) Delayed Neutron Activation Analysis for Uranium (Section 3.2), (b) Proton-Induced X-ray Emission Analysis for Uranium and/or Thorium, and/or Potassium (Section 3.3) and (c) Neutron Activation Analysis for Thorium (Section 3.4), are discussed. A thorough investigation of their suitability was carried out by testing the methods on well known uranium and thorium standards.

3.2 Delayed Neutron Activation Analysis for Uranium

Delayed neutron activation (DNA) analysis is a well established technique for the determination of low levels of U-235 and hence U-238, recalling that the U-235/U-238 ratio is constant at 0.72%. A very good review of the method is given by Binney and Scherpelz (1978). In brief, a known amount of sample to be analysed is placed inside a reactor where it is irradiated by thermal neutrons for a given period of time. For the reactor situated at Lucas Heights the neutron flux is about 1.2×10^{12} neutrons $cm^{-2}s^{-1}$ and the samples are usually irradiated for about 1 min. Some of the U-235 present in the sample undergoes fission after having been bombarded by the thermal neutrons, the efficiency of the reaction being a function of the incident neutron energy. The general fission equation may be

written, as follows :

$$\text{U-235} + n \rightarrow \text{Fission Products} + \text{approx. } 2\tfrac{1}{2} \text{ neutrons} + 200 \text{ MeV (approx)} \qquad (3.1)$$

Two fission fragments and either two or three neutrons, called "prompt neutrons", are produced in the reaction. Most of the neutron-rich fission products undergo beta decay, but in a few cases a decay product is produced in an excited state with sufficient energy to make possible the emission of a neutron, called a "delayed neutron". The fission products which emit neutrons have been found experimentally to fall into six groups, each characterised by a definite exponential decay rate (see for example, Wall, 1979). After having been irradiated with thermal neutrons the sample (in a polypropylene container), is rapidly transferred to a shielded counting station, remote from the irradiation position, where the delayed neutrons can be counted. The decay rates of these delayed neutrons are quite rapid with half-lives varying from 0.2s for Br-93 to 55.7s for Br-97. The mean rate of decay after applying the correct group weightings is about 9s (Wall, 1979). Figure 3.1 illustrates diagrammatically the DNA detection scheme.

The level of activity, measured as a count rate, is converted to a U-235 concentration by comparing it with that obtained from accurately known uranium standards. One usually also irradiates several blank samples in exactly the same manner in order to provide an accurate background correction to the observed count rate; this correction can however be made insignificant by a suitable choice of

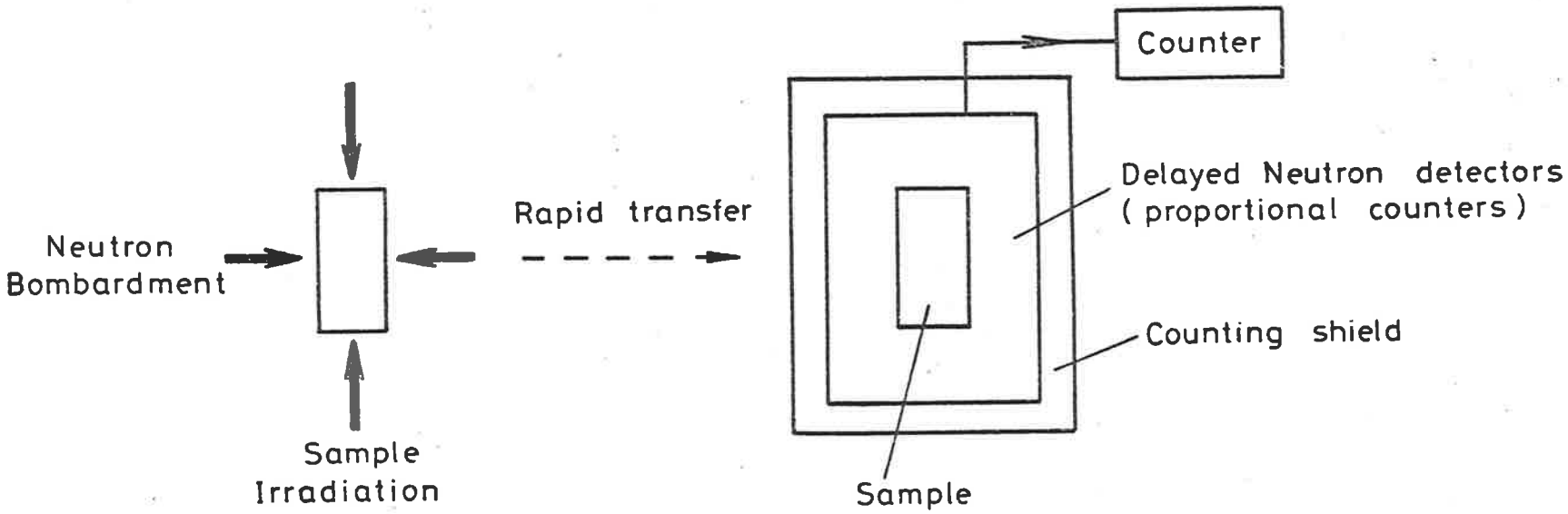

Figure 3.1 Diagrammatic Illustration of the Delayed Neutron Activation Detection Scheme.

sample containers and counter shield designs (Wall, 1979). The neutron counting assembly is a circle of $^{10}BF_3$ proportional counters surrounding the sample counting site in a 4π geometry arrangement. The assembly is immersed in graphite blocks and shielded from external neutron sources by cadmium foil. At the AAEC the transport of the samples into the nuclear reactor and then the movement to the activity measuring station is done on an automatic basis, at a rate of 50 samples, four standards and four blanks per hour. This procedure is all computer controlled. Hence, the method is quick, requiring only about 2 minutes for the analysis proper, excluding the time for sample crushing, weighing, encapsulation, data processing and recording. The method is very sensitive. The quoted sensitivity of the rig used at the AAEC is such that using a 10g sample one can determine uranium concentration levels down to 0.5 μgg^{-1} with an accuracy of 0.1 μgg^{-1}. The precision is increased to about ± 3% at the 5 μgg^{-1} uranium level.

One should point out that the method gives us only the uranium concentration and not those of its daughters; hence the method does not by itself throw any direct light on the problem of disequilibrium (see Section 2.4.2). However, if the results obtained using the DNA method are compared with other methods such as, for example, thick-source alpha particle counting or gamma-ray spectrometry using a NaI scintillator, one is in a much better position to assess the magnitude of any possible disequilibrium in the uranium decay chains.

Various uranium counting standards of accurately known

concentrations and all known to be close to secular equilibrium were analysed for uranium by DNA, the results obtained are shown in Table 3.1. One can conclude that by the use of the DNA method one obtains uranium concentrations, down to the $\mu g g^{-1}$ concentration level, which are in good agreement with the known concentrations.

3.3 The Proton-Induced X-ray Emission Analysis Technique

In the search for a reliable method for the low level thorium and/or Th/U ratio determinations we were first led to consider Proton-Induced X-ray Emission (PIXE). This technique has been developed during recent years as a method for low level trace elemental analysis (see for example, Johansson and Johansson, 1976; Cohen and Duerden, 1978). A PIXE experiment had just been set up at the AAEC prior to our introduction to it in 1977. The method is a multi-elemental analysis technique as is the possibly more familiar X-ray fluorescence (XRF) method. A good review article on the PIXE method has been presented by Folkmann (1975).

A brief introduction to the actual PIXE process, in particular the production of X-rays, will be given here prior to the description of the necessary equipment and a discussion of some of the results obtained.

The interaction between accelerated, heavy charged particles and target atoms may lead to the emission of characteristic X-rays. Consider Figure 3.2, the impact of the proton on one of the atoms of a sample may eject one of the inner shell electrons. The vacancy so formed would then be filled by one of the outer electrons. This would result in the emission of the energy gained by the transition in the

TABLE 3.1 DELAYED NEUTRON ACTIVATION ANALYSIS ON A VARIETY OF URANIUM COUNTING STANDARDS

Sample	Uranium Concentrations ($\mu g g^{-1}$) DNA	Standard Values
NBL-102	1000 ± 30	1010 ± 10
NBL-103	478 ± 14	470 ± 10
NBL-104	99 ± 3	103 ± 4
AAEC-1	101 ± 2	104 ± 3
DL-1	40 ± 1	41 ± 1
NBL-105	10.2 ± 0.3	10 ± 1
*NBL-109	4.3 ± 0.2	3.7 ± 0.5
**NBL-110	0.5 ± 0.1	0.4 ± 0.1

* In the presence of about 100 $\mu g g^{-1}$ thorium

** In the presence of about 10 $\mu g g^{-1}$ thorium

NOTE: The errors quoted are 95% confidence limits.

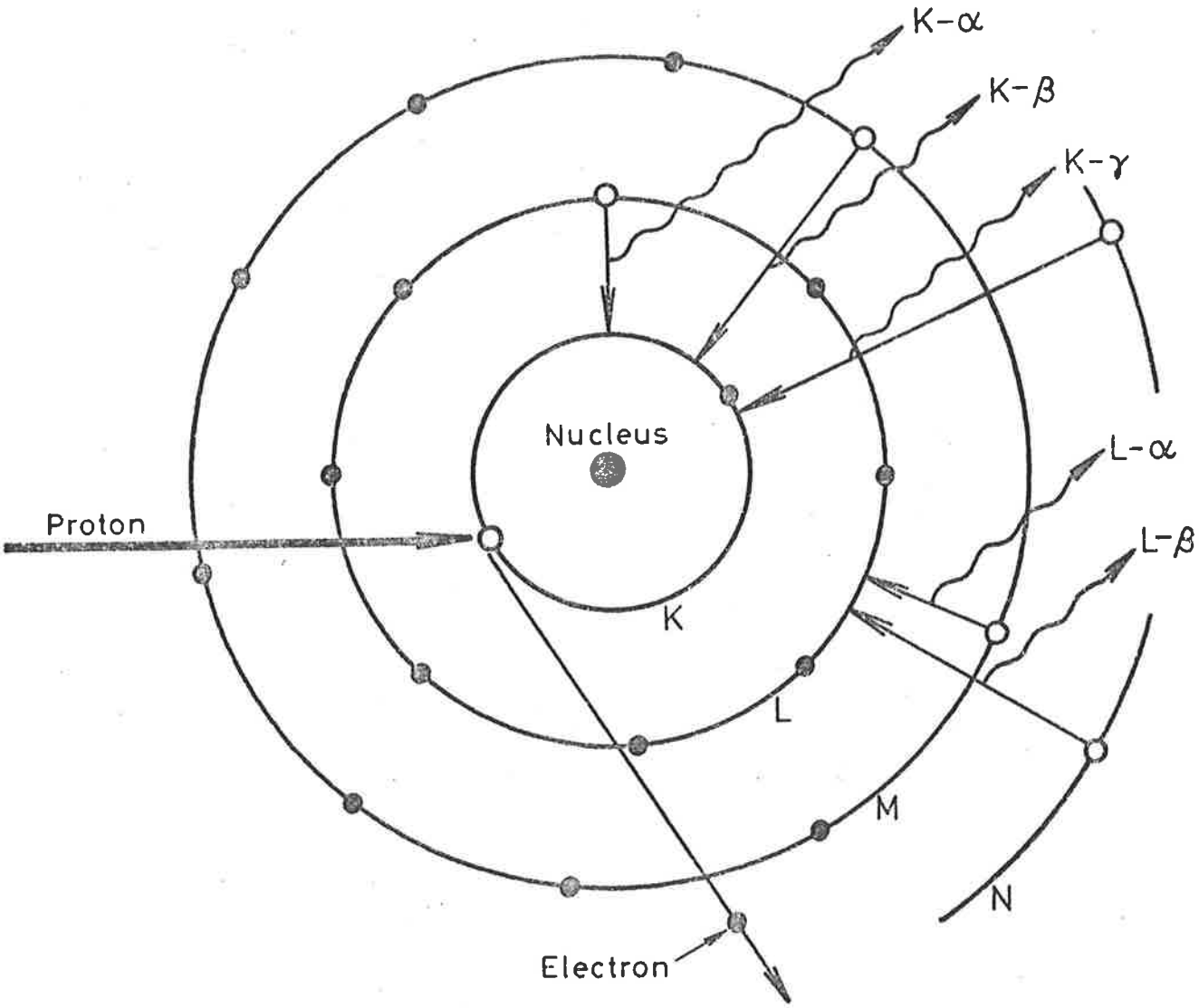

Figure 3.2 Schematic Diagram of the Proton-Induced X-Ray Emission Process.

form of a characteristic X-ray photon of energy dependent upon the atomic number Z of the bombarded atom. If the initial electron vacancy was in the K-shell then the photon emitted is described as a K X-ray, similarly an L X-ray would be emitted if the initial vacancy were in the L shell. A more detailed discussion of the possible electron transitions is given by Woldseth (1973).

In order to obtain the actual concentration of a particular element one first has to attribute a peak to the element in question (standard X-ray energy tables are available for this), integrating the number of counts in the peak then gives one a measure of the actual concentration level of that element. The technique is not an absolute method as one has to calibrate the system using accurately known standards. A comprehensive discussion on the various sources of background at the different energies has been given by Folkmann (1975).

Cohen and Duerden have described the principles behind the use of PIXE and the experimental set up at the AAEC (see for example, Cohen and Duerden, 1978; Cohen *et al*, 1980; Duerden *et al*, 1980); so only a brief description will be given here :

A schematic view of the PIXE chamber is shown in Figure 3.3 (from Cohen and Duerden, 1978). The 3 MeV Van de Graaff accelerator is used to produce protons with a typical energy of 2.3 MeV. These are steered through an energy analysing magnet and a diffusing quadrupole on to an aperture whose size can be varied from 0.1 to 9 mm diameter. The target chamber is insulated from the rest of the experiment and thus acts as a Faraday cup for charge collection and integration to give a total charge reaching the target; it is very important to obtain an

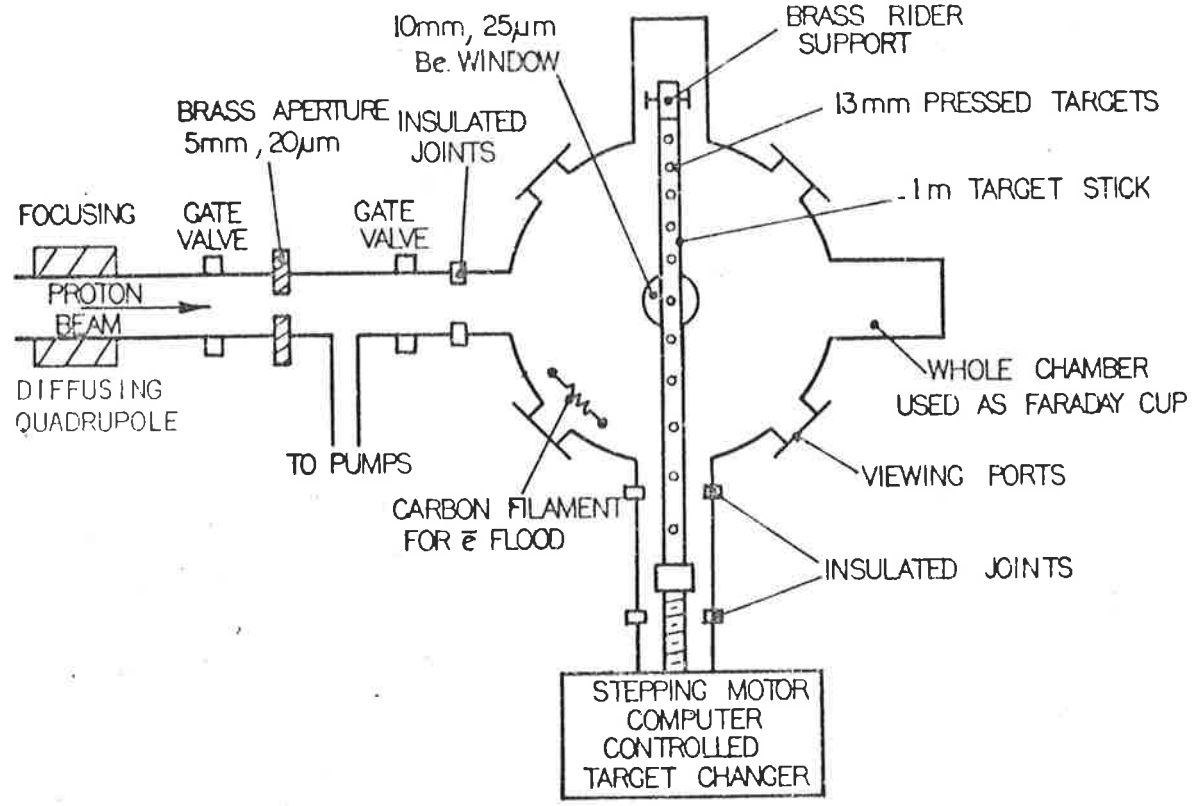

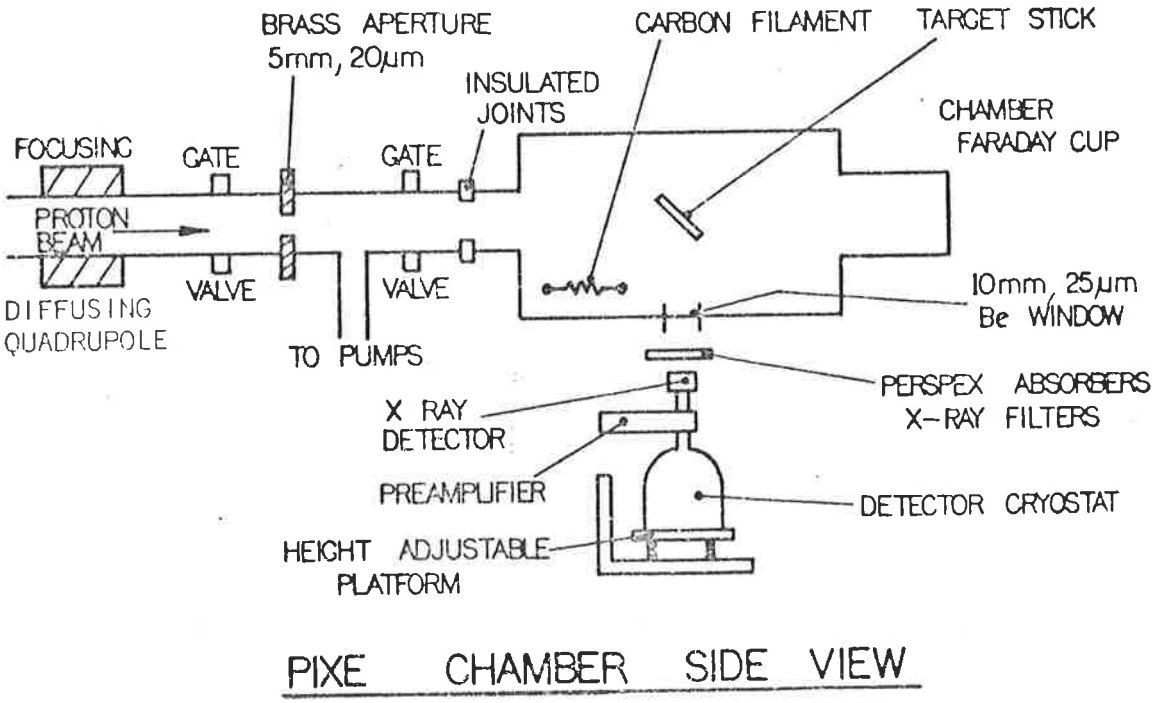

Figure 3.3 Schematic Diagram of the PIXE Experimental Arrangement.

accurate measure of the charge if one is to make comparisons from one run to the next. Up to 45 targets (pelletised samples in aluminium holders) can be placed on a metre long aluminium stick, whose position relative to the incident proton beam can be varied, to an accuracy of about 100 μm, by a computer controlled stepping motor. Lower energy X-rays (< 10 keV) produced in the target can be selectively absorbed by a perspex filter (6mm thick) placed between the bottom of the chamber and the detector. The detector sits on a platform of adjustable height, therefore the column of air (which also acts as a filter for low energy X-rays) between the chamber and the top of the detector can be varied from 20 cm down to a few mm. Prior to running, the target chamber is evacuated to a base pressure of about 0.5 mPa.

The detector used (GRUMPY 1) is an intrinsic hyperpure n-type silicon chip, built at the AAEC. It has an active area of 50 mm^2 and a depletion thickness of 5mm. Cohen *et al* (1980) have measured the full width at half maximum (fwhm) resolution as 313 eV at the thorium L-α peak which is at around 12.9 keV.

As far as PIXE analysis of thorium and uranium are concerned the dominant X-ray peaks are the L series lines; these all appear in the energy region between 11 and 21 keV (see for example, Cohen *et al*, 1980). The most dominant thorium and uranium peaks are the L-α lines which are at about 12.9 keV and 13.7 keV respectively. The corresponding peak areas of the L-β peaks are about 2-3 times smaller than the L-α peak areas.

Only a very small amount of sample is actually analysed during a PIXE run; the beam spot is usually a few mm in diameter and the proton penetration depth is only about 50 μm or so. This makes it very important to make sure that the rather small fraction of sample analysed is a good representation of the sample as a whole. The sample preparation technique used on our standards and TL field samples was to first thoroughly pulverize and homogenize the samples and then pour the powders into pure 99.9% aluminium caps (about 13mm in diameter) and then pelletise the powders at 2000 psi for about 60s. The pellets produced in this manner have very flat and well defined front surfaces as well as being a convenient size for mounting on the long target stick (see Figure 3.3).

Prior to taking any PIXE measurements on any of our TL field samples it was decided to first check the method on a variety of counting standards. Cohen and Duerden (PIXE researchers at the AAEC) had at that time not done much work on the application of PIXE towards obtaining thorium and uranium concentrations; mainly because of the interest shown in obtaining concentration levels or spectrum signatures on other elements. This meant that we were able to contribute to the development of the technique for uranium and thorium determinations. As we already have a technique for the measurement of U-238, namely DNA (see Section 2.3.2), we decided to first run a series of our thorium standards.

Figure 3.4 shows a typical pulse height spectrum as obtained on a 100 $\mu g g^{-1}$ thorium standard (NBL-109); some of the characteristic

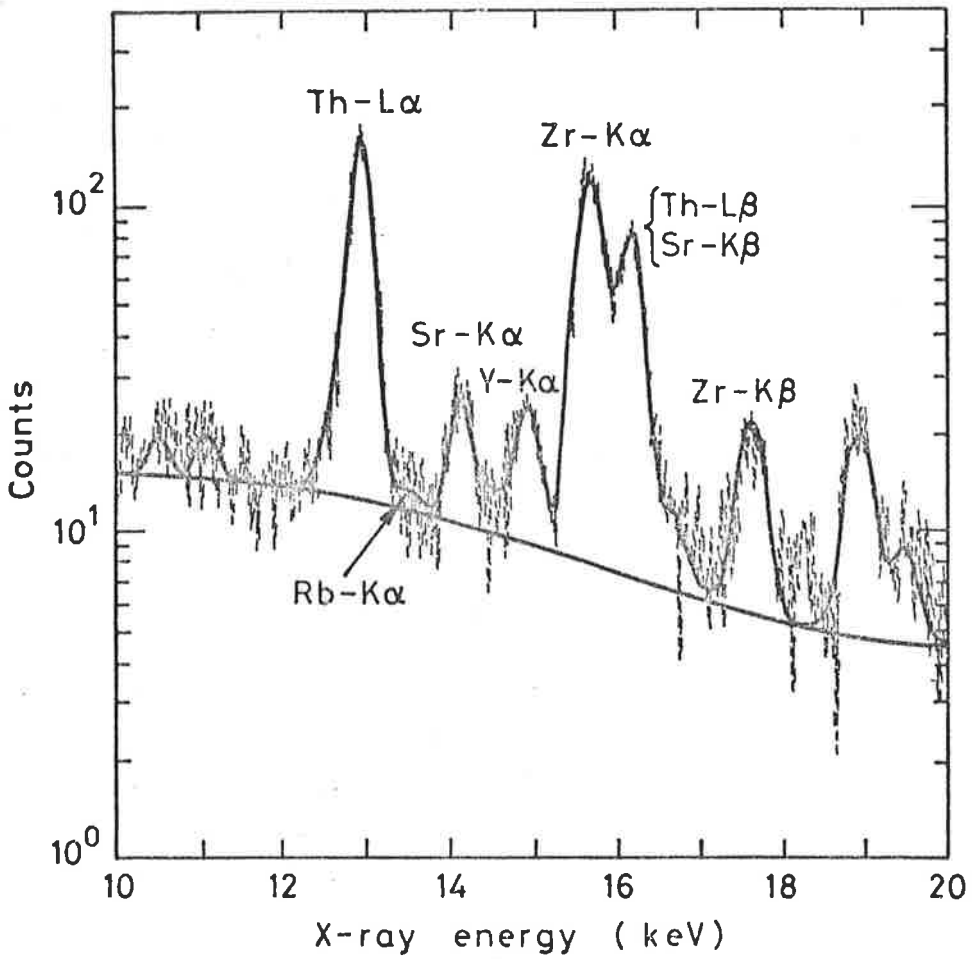

Figure 3.4 PIXE Spectrum obtained on a 100 $\mu g g^{-1}$ Thorium Standard.

X-ray peaks from various other elements present in the sample are also indicated. On top of the observed pulse height spectrum is fitted a theoretical spectrum, which has been derived by the use of a spectral computer fitting program (see Clayton *et al*, 1978; Cohen *et al*, 1980). We see that in this particular case the thorium L-α peak (12.9 keV) is easily resolved from other peaks in the same energy region; the only observable peaks in the vicinity of the thorium L-α peak are the rubidium and strontium K-α peaks. A thorium L-β peak is just observable at around 16 keV but this is masked somewhat by the presence of the zirconium K-α as well as the strontium K-β peaks.

Figure 3.5 shows a spectrum obtained on a 10 $\mu g g^{-1}$ thorium standard (NBL-110). In order to detect the thorium L-α peak at this concentration level (that is, above the background and resolved from neighbouring elements), the sample had to be subjected to the proton beam for about 45 min.

Cohen *et al* have since completed a comprehensive study on the accuracy of the PIXE method as far as the determination of thorium (and uranium) concentrations on standards are concerned (see Cohen *et al*, 1980). The results obtained are shown in Figure 3.6, where the thorium L-α peak areas for a large range of standards (ore matrix as well as carbon matrix) are plotted against the known thorium concentrations.

Some of the standards used in this study were supplied by the author; for example, the data point for the NBL-109 standard was derived from Figure 3.4. Good linearity is shown over four decades of thorium concentration levels (1 - 10^4 $\mu g g^{-1}$), similarly good

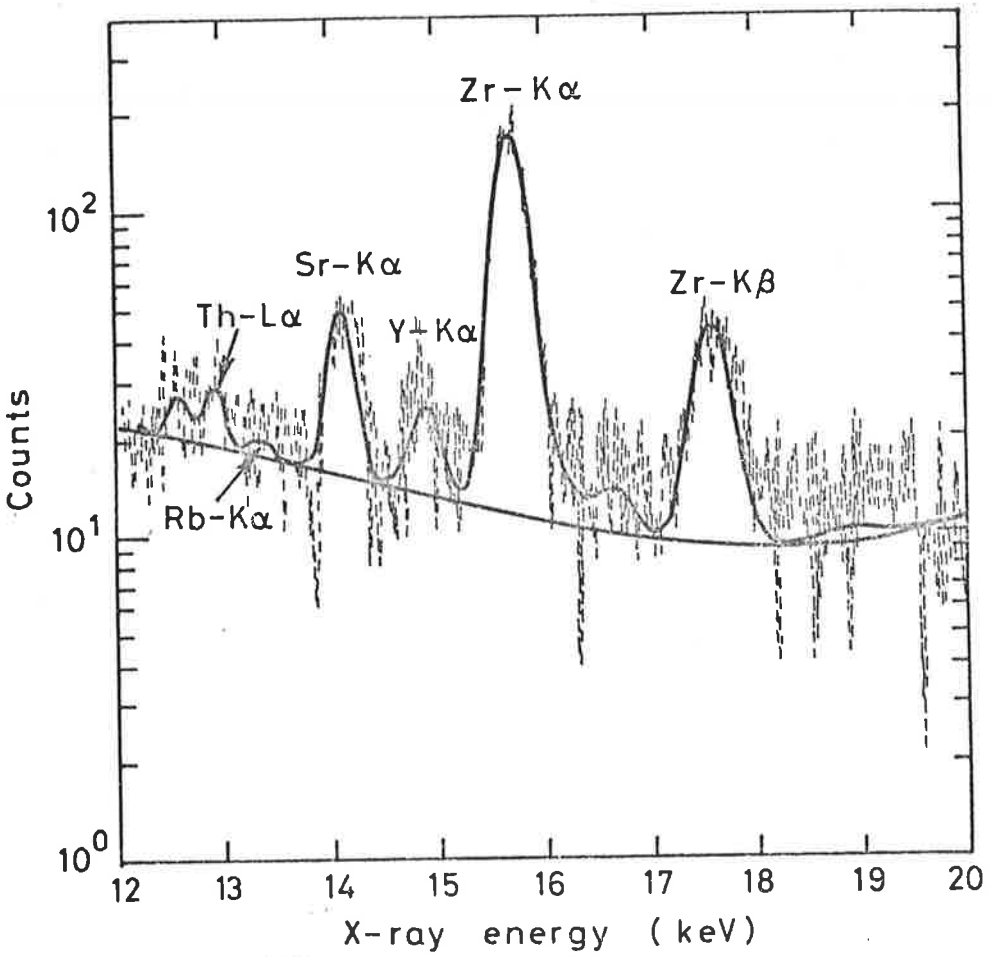

Figure 3.5 PIXE Spectrum obtained on a 10 $\mu g g^{-1}$ Thorium Standard.

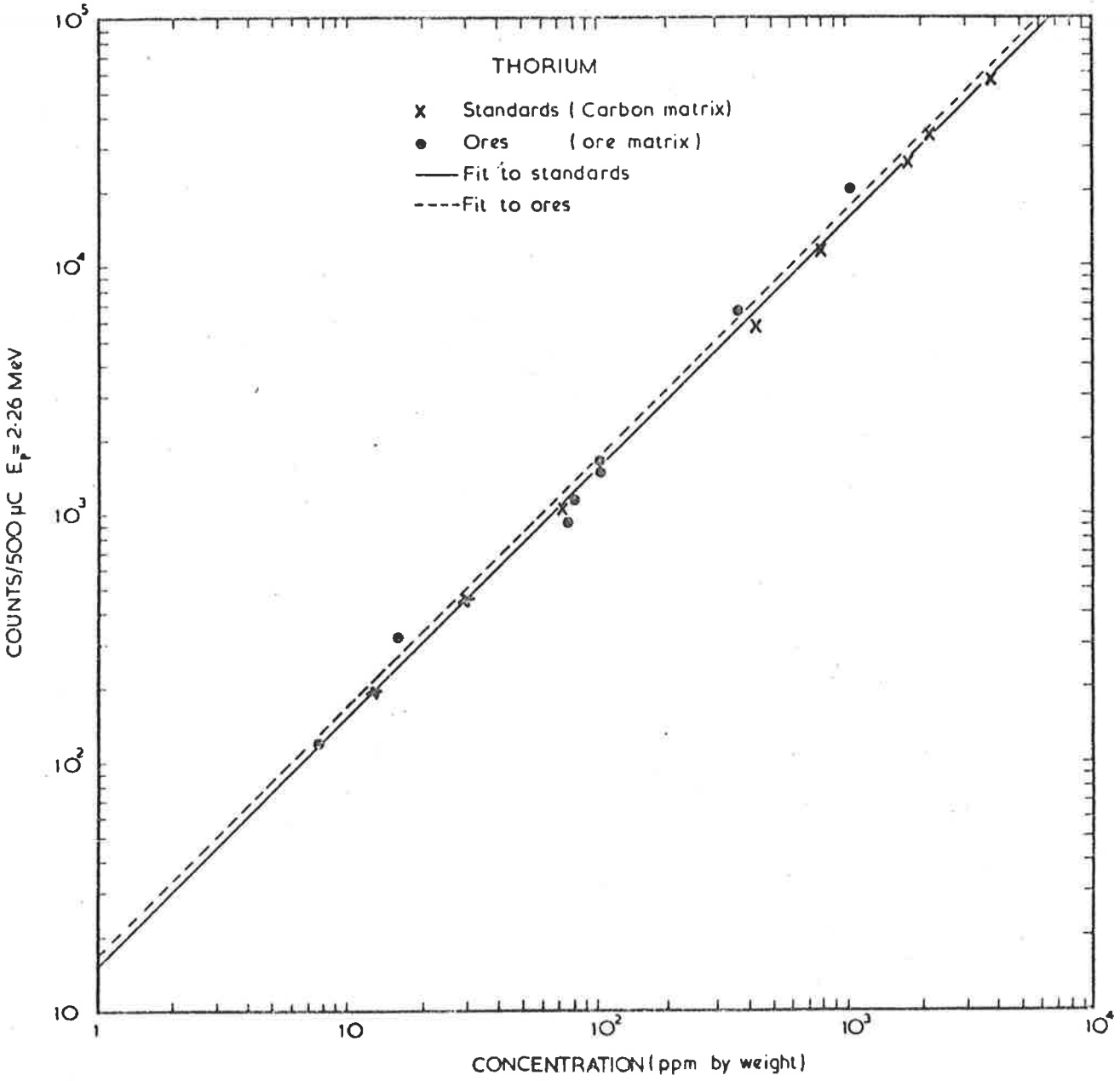

Figure 3.6 Thorium L-α Peak Area Versus Concentration.

linearity was observed using a variety of uranium standards.

Cohen *et al* quote a lower level thorium (and/or uranium) detection limit with no adjacent element interferences as 3-4 μgg^{-1} per 100 μC when using the detector GRUMPY 1 and a proton beam energy of 2.26 MeV. This detection limit may be improved upon if a higher resolution detector is used. The above-mentioned detection limit assumes a general background level of about 5 counts per channel. For standards containing large amounts of sodium and aluminium, the γ-ray induced background in the X-ray region of interest can be higher than 20 counts per channel. This will raise the lower level detection limit to 7 or 8 μgg^{-1} per 100 μC or greater. The ultimate thorium detection limit for a particular sample is clearly governed, among other factors, by the relative amounts of interfering elements. Cohen *et al* (1980) do state that their spectrum fitting routines can unfold the K-α series peaks (i.e. Rb, Sr) interfering with the thorium L-α peaks, provided that the low atomic number trace element concentration (i.e. Rb, Sr) do not exceed the corresponding thorium concentrations by a factor of 10-15. They also state that in the absence of rubidium and strontium, the thorium and uranium L-α lines can be resolved and spectra produced by thorium and uranium whose concentrations differ by as much as a factor of 50, can still be unfolded. Furthermore, the low energy tail present on all of the peaks indicates that small amounts of uranium can be analysed in larger amounts of thorium much more accurately than small amounts of thorium in larger amounts of uranium (this is so because the energy of the L-α uranium peak is just above the energy of the L-α thorium peak).

If the thorium (or uranium) L-α peaks are completely obscured by the Rb and Sr K-α peaks, then the thorium (or uranium) L-β peaks (around 16 keV) can be used and their known ratios to the L-α peak provide an estimate for the L-α peak area. In such a case, since the L-β peaks are 2-3 times smaller than the L-α peaks, only concentrations of Y, Sr and Zr less than 3-5 times that of thorium (or uranium) can be tolerated. In Figure 3.4 (100 $\mu g g^{-1}$ thorium standard) we saw that the thorium L-β peak was obscured due to the presence of larger amounts of Sr and Zr.

The measurements carried out on the various standards indicate that perhaps the PIXE method would be suitable for the determination of thorium concentration levels in our TL field samples, although as far as obtaining uranium concentration levels (or Th/U ratios) the method would not be suitable.

Numerous TL field samples were then studied by the PIXE process, but in none of the samples were we able to unfold the thorium L-α peak satisfactorily. In all of the samples studied there was an abundance of interfering elements, the most troublesome being Pb, Rb, Sr, Y and Zr. Figure 3.7 shows a PIXE spectrum obtained on a sample of baked sand which was collected for TL dating purposes. Using alpha pairs counting we know that this sample has about 20 $\mu g g^{-1}$ of thorium present which is in the upper range of usual thorium concentration levels in our field samples. In this case one notes that most of the thorium L-α peak is masked by the presence of a Rb K-α and a Pb L-β peak. One also notes that the thorium L-β peak (around 16 keV) is completely

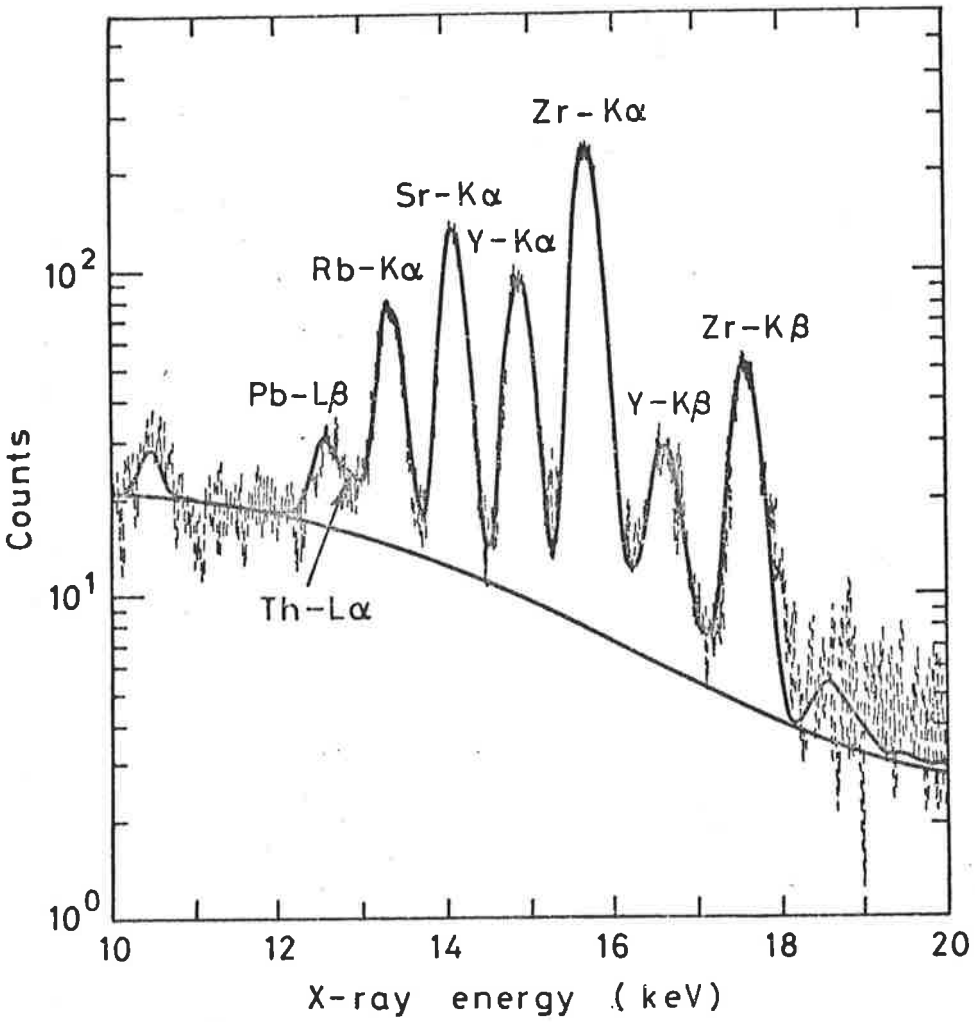

Figure 3.7 PIXE Spectrum obtained on TL Field Sample Sc 3/3.

obscured by the abundant presence of Zr and Y. Even with the aid of a good computer unfolding program, this interference makes it virtually impossible to obtain quantitative thorium concentrations in our TL field samples.

The only conclusion which can be drawn from the PIXE measurements on the large variety of field samples is that the method is unsuitable for the quantitative determination of thorium (and uranium) in these samples, the main problem being the presence of interfering elements such as Rb, Sr, Y and Zr in too large quantities.

As already mentioned in Section 2.1, Rb-87 contributes to the overall archaeological dose-rate by the process of beta decay to Sr-87. The actual Rb concentration levels in field samples are easily determined from PIXE measurements using the Rb K-α line around 13.5 keV; this was of course done in the process of looking for the thorium L-α peak contributions. In the 15 field samples studied; which consisted of 10 soil samples and 5 sherd/oven stones, the Rb concentration level varied from about 50 $\mu g g^{-1}$ to about 150 $\mu g g^{-1}$. Since the contribution of Rb-87 to the total β-dose rate is quite small (Warren, 1978), it is unlikely that an accurate estimate of the Rb concentration is warranted. Warren points out that in most rocks and soils there is a close geochemical association between rubidium and potassium and suggested that if potassium measurements are carried out then an estimate of the rubidium beta contribution can be calculated by assuming a potassium to rubidium concentration ratio of about 200:1.

In Section 2.1, it was pointed out that potassium-40 contributes significantly to the beta and gamma dose-rates; hence it is important

to be able to obtain potassium concentration levels quite accurately. This is not a problem since the usual potassium concentration in field samples is about 1%; the conventional analysis techniques used include flame photometry and X-ray fluorescence. In this laboratory we use the X-ray fluorescence facilities of the CSIRO Division of Soils which is situated in Adelaide. For comparisons we have also employed the PIXE method for potassium analysis on field samples using the 3.3 keV peak, the agreement with X-ray fluorescence measurements were generally quite good. However, in the absence of useful data for uranium and thorium, the PIXE technique is not justified for potassium analysis alone.

3.4 Neutron Activation Analysis for Thorium

Having discarded the PIXE method as far as thorium and/or Th/U ratio determinations are concerned, we turned to neutron activation analysis. In this method, Th-232; as well as U-235 and U-238 and anything else present, are exposed to thermal or epithermal neutrons. Nuclear gamma-rays from the products of neutron capture are then detected. This contrasts with the DNA process used for uranium determinations, viz. delayed neutron emission, following thermal neutron capture in U-235. The method requires less than 1g of pressed sample powder which is sealed in thin aluminium disc-shaped containers spaced by about 3mm of graphite. About 50 samples at a time can be loaded into the MOATA reactor at the AAEC; they are then irradiated for 7 hours at a flux level of 1.2×10^{12} neutrons $cm^{-2}s^{-1}$. The samples are then measured after a "cooling" period of 36 days (to allow the activity of other unwanted nuclear species to decay) using a

counting time of 10 minutes per sample. Thorium is detected by the 312 keV gamma-ray of Pa-233 using a 50 mℓ Ge(Li) detector, the detection limit being about 1 $\mu g g^{-1}$. Interference has been observed from other elements such as Co, Sc, Cr and Hf, but this is virtually eliminated if epithermal neutrons are used for the irradiation rather than the slower thermal neutrons. This technique has the advantage of requiring very little sample preparation; although very fine crushing and homogenization is required since only a small amount of sample is analysed (typically 0.3g). The 36-day waiting time between irradiation and the detection of gamma-rays constitutes the most serious drawback.

The method gives results generally in good agreement with other methods. In the absence of interfering activities we observed good agreement between this and the PIXE method for thorium concentrations above the 10 $\mu g g^{-1}$ level. Results obtained on a variety of thorium counting standards are shown in Table 3.2. One can see that the method shows fairly good agreement with the standard values, even at the 10 $\mu g g^{-1}$ or less. It can provide assays down to 1 $\mu g g^{-1}$ with a precision of $\pm$ 0.2 $\mu g g^{-1}$ at this level.

Even though one is only obtaining the activity of the head member of the thorium decay chain, namely Th-232, this method would have to be preferred to thick source alpha pairs counting as a means of obtaining thorium concentrations (see Section 2.4.1). This is so because it is unlikely that there is any gross disequilibrium in the thorium decay chain (see Section 2.4.2) and furthermore because of the

TABLE 3.2 NEUTRON ACTIVATION ANALYSIS ON A VARIETY OF THORIUM COUNTING STANDARDS

Sample	Thorium Concentrations ($\mu g g^{-1}$) NAA	Standard Values
NBL-107	1011 ± 20	1000 ± 40
NBL-108	504 ± 10	520 ± 10
NBL-109	108 ± 3	104 ± 3
NBL-110	11.4 ± 0.4	9.8 ± 0.6
AAEC-29	1.4 ± 0.2	1.4 ± 0.1
AAEC-30	1.4 ± 0.2	1.6 ± 0.1
AAEC-35	12.2 ± 0.4	13.6 ± 0.9

Note: The errors quoted are 95% confidence limits.

rather poor statistics involved with alpha pairs counting.

Having verified that both the DNA and NAA methods work well on uranium and thorium standards respectively, it was decided to check the methods on samples of varying Th/U ratios (that is in the presence of both uranium and thorium). Several samples were made up by mixing known amounts of the sample NBL-104 (about 100 $\mu g g^{-1}$ uranium standard) with known amounts of the sample NBL-109 (about 100 $\mu g g^{-1}$ thorium standard). These sample mixtures have already been used in order to check the alpha pairs counting method (see Section 2.4.1, Table 2.3). Table 3.3 shows the results obtained for the various Th/U ratios using both the DNA (see Section 3.1) and NAA methods. For comparisons the Th/U ratios obtained using the alpha pairs counting technique have also been included. As can be seen from Table 3.3 the combined use of the DNA and the NAA methods produce Th/U ratios which agree well with the calculated values as well as with those obtained by alpha pairs counting. One of course expects the agreement to be good as these Th/U mixtures are all known to be close to secular equilibrium.

TABLE 3.3 COMPARISON OF Th/U RATIOS AS OBTAINED BY NEUTRON ACTIVATION ANALYSIS AND ALPHA-PAIRS COUNTING FOR A VARIETY OF COUNTING STANDARDS.

Sample	$\frac{\text{NBL-109}}{\text{NBL-104}}$ (weight)	$(Th/U)_{calculated}$	$(Th/U)_{\substack{DNA \\ NAA}}$	$(Th/U)_{\alpha\text{-}P}$
ADL-56	1.0	1.0 ± 0.1	1.0 ± 0.1	1.1 ± 0.5
ADL-57	3.0	2.7 ± 0.2	2.8 ± 0.2	2.4 ± 1.1
ADL-58	6.0	5.0 ± 0.3	4.8 ± 0.4	4.7 ± 1.5
ADL-59	9.0	6.9 ± 0.4	6.3 ± 0.6	5.9 ± 1.6

NOTE : Both of the counting standards NBL-104 and NBL-109 are known to be close to secular equilibrium.

The errors quoted are 95% confidence limits.

CHAPTER IV

COMPARISON OF THE ALPHA COUNTING METHOD WITH THE NEUTRON ACTIVATION ANALYSIS METHODS FOR THE LOW LEVEL THORIUM AND URANIUM DETERMINATIONS

4.1 Introduction

In this chapter the results obtained, on a variety of TL field samples, using the alpha counting method are compared with those obtained by using the neutron activation analysis methods (DNA and NAA) for the low level determination of uranium and thorium. This comparison is presented in Section 4.2. The possible causes for discrepancies in the results obtained are discussed and in Section 4.3 the specific problem of alpha overcounting is dealt with. Possible methods for solving the alpha overcounting problem are discussed in Section 4.4.

4.2 Comparison of Data

A large number of field samples collected for dating purposes were alpha counted as well as analyzed for uranium and thorium by NAA. In Table 4.1 results are shown on a selection of soil samples. The expected alpha count rates have been estimated from the concentrations of uranium and thorium as measured by NAA. The expected count rates are compared with the observed rates; they are arranged roughly in order of decreasing goodness of rapport. To check the reproducibility of both of the neutron activation methods on field samples, several determinations were done on various portions of each individual sample. In the case of DNA for uranium the reproducibility from one run to the next was very good, which one expects since the determination is carried out on a bulk sample of about 5 to 10g. As far as thorium determinations are concerned one is only analyzing about 0.3g of sample; hence it is very important to thoroughly crush and homogenize the samples prior to analysis. Having done this, good reproducibility from one run to the next

TABLE 4.1 COMPARISON OF NEUTRON ACTIVATION ANALYSIS FOR URANIUM AND THORIUM WITH ALPHA COUNTING FOR A VARIETY OF SOIL SAMPLES

Sample Identifier	DNA U ($\mu g g^{-1}$)	NAA Th ($\mu g g^{-1}$)	α-expected (Ks^{-1})	α-observed (Ks^{-1})
F70a	0.9 ± 0.1	3.6 ± 0.3	3.3 ± 0.6	3.8 ± 0.2
F70b	0.9 ± 0.1	2.0 ± 0.2	2.5 ± 0.8	3.2 ± 0.2
F80a	0.9 ± 0.1	5.0 ± 0.3	4.0 ± 0.7	4.5 ± 0.2
F80b	1.1 ± 0.1	7.4 ± 0.4	5.5 ± 0.8	5.1 ± 0.2
OXH76	1.7 ± 0.1	8.2 ± 0.6	6.7 ± 0.9	7.5 ± 0.4
MG7Ca	2.0 ± 0.1	8.3 ± 0.6	7.5 ± 0.9	8.9 ± 0.4
EB1a	0.9 ± 0.1	5.8 ± 0.4	4.4 ± 0.8	
EB2sc	0.9 ± 0.1	6.5 ± 0.4	4.8 ± 0.8	4.1 → 48.4
EB2sd	0.7 ± 0.1	5.2 ± 0.4	3.8 ± 0.8	
ALD 22-50	0.9 ± 0.1	7.9 ± 0.3	5.5 ± 0.7	6.0 → 22.1
LF6	1.2 ± 0.1	7.2 ± 0.4	5.4 ± 0.8	8.9 ± 0.4

NOTE: The errors quoted are 95% confidence limits.

was observed. The thorium concentration levels given in Table 4.1 are all average values from at least three different determinations. The observed alpha count rates were all determined on samples which had been gently crushed in a mortar by a pestle (coarse grains). In all cases both "sealed" (α_1) and "unsealed" (α_0) count rates were determined (see Section 2.4.2); however, in none of the samples counted was there a discrepancy between the two. The observed count rates displayed in Table 4.1 are all average values from at least six different runs; the observed variations in count rate are indicated in the table.

Towards the top of the table the agreement between expected and observed count rates is quite good, certainly within counting statistics. However, in other cases the measured alpha count rates are much higher than those expected from neutron activation measurements. In particular samples EB1a, EB2sc and EB2sd, which are all soil samples from the South Australian Museum's Roonka excavation, have been observed to have count rates which can vary from one measurement to the next. On these soil samples the measured count rate is highly dependent upon how the samples grains are deposited on to the ZnS screens (see discussion in Section 2.4.6); variation in count rates by as much as a factor of 10 has been observed. A similar variation in count rate phenomenon was exhibited by sample ALD 22-50. Alpha overcounting was also exhibited by sample LF6; however, on this sample there is no drastic variation in count rate from one measurement to another. On none of the soil samples so far analysed have the measured alpha count rates been less than the expected count rates.

If, for a particular sample, there is gross disequilibrium in the uranium decay chains (see Section 2.4.2), one might expect discrepancies between neutron activation analysis (DNA and NAA) and alpha counting. This is because in DNA for uranium one detects only the uranium parent and not its daughters. However, most of the soil samples shown in Table 4.1 have relatively low uranium concentrations, typically around 1 $\mu g g^{-1}$, hence disequilibrium in the uranium chains is not likely to introduce count rates which are several times higher than expected. Furthermore, the effective atomic weights of the soil samples exhibiting this counting discrepancy are not unusually high; hence the observed discrepancy cannot be explained in such terms (see Section 2.4.3).

A similar comparison program has also been carried out on some of the pottery and sherd samples used in our TL dating program. Although samples Sc 3/3 and Sc 3/6 are strictly speaking soil samples, they are included in this comparison because they are datable by TL. The results obtained are shown in Table 4.2. On these samples the uranium concentration levels are generally higher than those obtained on the soil samples shown in Table 4.1 (3 to 4 $\mu g g^{-1}$ compared with about 1 $\mu g g^{-1}$). The observed alpha count rates on these samples were generally much more reproducible than the count rates on some of the soil samples, and in most cases the agreement between expected and observed count rates was good. However, alpha overcounting was observed on some of the samples. The problem with alpha overcounting on samples Sc 3/3 and Sc 3/6 has already been discussed in Section 2.4.6; the reason being higher than average uranium activity on the surface of the

TABLE 4.2 COMPARISON OF NEUTRON ACTIVATION ANALYSIS FOR URANIUM AND THORIUM WITH ALPHA PARTICLE COUNTING FOR A VARIETY OF FIELD SAMPLES

Sample Identifier	Description of Sample	DNA U ($\mu g g^{-1}$)	NAA Th ($\mu g g^{-1}$)	α-expected (Ks^{-1})	α-observed (Ks^{-1})
POM-T	Pompeii Tile	4.6 ± 0.3	16.7 ±0.6	16.2 ± 0.8	16.4 ± 1.0
LRF73 F314	Pottery	3.8 ± 0.2	17.2 ±0.6	15.1 ± 0.6	13.8 ± 0.6
Thai-26	Thai	1.7 ± 0.2	6.8 ± 0.3	6.3 ± 0.4	6.2 ± 0.4
Thai-46	Pottery	3.4 ± 0.3	14.1 ± 0.5	12.8 ± 0.5	13.6 ± 0.9
BS-SZ-8/203	Lapita Pottery	3.6 ± 0.2	1.3 ± 0.2	6.8 ± 0.4	6.7 ± 0.6
BS-RL-2/41		2.3 ± 0.2	0.4 ± 0.4	4.1 ± 0.5	18.9 ± 2.0
SU-MU-1-P4	"	27.4 ± 0.8	3.8 ± 0.3	48.5 ± 1.5	13.4 ± 1.0
Sc 3/3	Baked Sand	2.1 ± 0.2	16.7 ± 0.5	11.9 ± 0.6	39.7 ± 1.7
Sc 3/6		2.2 ± 0.2	15.1 ± 0.5	11.3 ± 0.6	36.5 ± 1.6
EB1	Aboriginal Hearthstone	1.1 ± 0.1	3.9 ± 0.4	3.8 ± 0.4	4.1 ± 0.2

NOTE: The errors quoted are 95% confidence limits.

sample grains. Some of the Lapita pottery samples collected from the South-West Pacific Islands region (see Prescott *et al*, 1982) also exhibit gross alpha overcounting. In particular, sample BS-RL-2/41, which comes from one of the Santa Cruz Islands, has an observed count rate which is 4 to 5 times greater than the expected count rate. The Lapita pottery sample SU-MU-1-P4 is included in Table 4.2 to give an example in which the expected count rate exceeds the observed count rate ("undercounting"). However, the uranium concentration level for this particular sample is unusually high (about 27.4 $\mu g g^{-1}$); this means that the observed discrepancy could be caused by a loss of some of the U-238 daughters.

Alpha pairs counting (see Section 2.4.1) was also carried out on the samples which were analysed by DNA and NAA. In Table 4.3 the Th/U ratios obtained by alpha pairs counting on a variety of field samples are compared with those obtained by neutron activation analysis. On most of the samples the agreement of Th/U ratios was quite good. Even on the samples EB1a, EB2sc and EB2sd, which can exhibit gross alpha overcounting, there is good agreement between the two methods. The range in Th/U ratios on the samples shown is not very large and the average value is between 4 and 5. The sample SU-MU-1-P4 exhibited a lower than usual alpha pairs Th/U ratio; however, this was also confirmed by the DNA and NAA measurements. In this particular case there is no doubt that an alpha pairs count yielding a Th/U ratio of 0.8 ± 1.0 is certainly a better estimate than the usually adopted value of 3.16 (see Section 2.4.1).

TABLE 4.3 COMPARISON OF (Th/U) RATIOS OBTAINED BY NEUTRON ACTIVATION ANALYSIS WITH THOSE OBTAINED BY ALPHA-PAIRS COUNTING.

Sample Identifier	Description of Sample	$(Th/U)_{NAA-DNA}$	$(Th/U)_{\alpha-P}$
F70a	Soil	4.0 ± 0.8	4.6 ± 3.0
F80a	Soil	5.6 ± 1.0	3.7 ± 2.4
F80b	Soil	6.7 ± 0.9	6.1 ± 3.4
EB1a	Soil	6.4 ± 1.2	7.5 ± 4.8
EB2sc	Soil	7.2 ± 1.2	5.3 ± 2.8
EB2sd	Soil	7.4 ± 1.6	5.3 ± 2.4
POM-T	Tile	3.6 ± 0.4	3.1 ± 1.3
LRF73F314	Pottery	4.5 ± 0.4	4.0 ± 1.3
SUMU1P4	Pottery	0.1 ± 0.1	0.8 ± 1.0
THAI-26	Pottery	4.0 ± 0.6	3.4 ± 0.7
THAI-48s	Soil	3.8 ± 0.4	2.1 ± 0.9
MG7Ca	Soil	4.2 ± 0.5	3.4 ± 1.2
		$(Th/U)_{ave}$ ~ 4.8	$(Th/U)_{ave}$ ~ 4.1

NOTE: The errors quoted are 95% confidence limits.

4.3 Probable Causes of Alpha Overcounting

Some of the possible causes of alpha overcounting have already been mentioned in Section 2.4.6. The main probable causes which can give rise to gross overcounting are :

1(a) The possibility of a large fraction of the alpha activity being distributed on the grain surfaces. If the average grain size is larger than the alpha particle range of the sample (~ 25 μm), then counting geometries which produce overcounting are possible. This has already been seen to be the cause of overcounting on sample Sc 3/3 (see Section 2.4.6).

(b) The possibility of the smaller sample grains exhibiting higher alpha activity then the rest of the sample. Overcounting is then possible if the counting screen sees more than its proper fraction of fine grains. This has been observed to be the reason why samples EB1a, EBsc and EB2sc exhibited gross overcounting. That is, the very active fine grains work their way down into the gaps between the larger grains as they are deposited on to the counting screen.

2. The possibility of radon being counted with a much higher efficiency than the other alpha emitters. Being a gas with a half-life of about 3.8d it is possible for the radon to travel through the airspaces between the grains and fissures within the individual grains. Overcounting can then occur because the sample is no longer a homogeneous alpha emitter; a large fraction of the radon activity detected by the ZnS screen comes from outside the expected alpha range. The possibility of this phenomenon actually occurring has already been discussed by Murray (1980).

Possibilities 1(a) and (b) are quite similar in the respect that both are due to the inhomogeneous distribution of alpha activity throughout the sample volume , one being the preferential segregation of uranium and/or thorium on the smaller grain sizes and the other being the non-uniform distribution of alpha activity within each individual grain. Possibility (2) is of course quite different as it deals only with the excess activity of radon in the vicinity of the counting screen. One should point out that the alpha attenuation in the airspaces between the sample grains is much less than the attenuation in the solid phase. Hence, the alpha count rate may also depend on the degree of packing of sample grains on to the counting screen. It may well be that for a particular sample, which exhibits gross overcounting, the actual discrepancy is caused by a combination of the above listed possibilities.

One should also point out that possibilities 1(a) and (b) can also explain "undercounting". That is, there is no reason why the alpha activity on the surface of the larger grains or that of the finer grains could not be less than that of the bulk sample.

4.4 Solutions to the Problem of Alpha Overcounting

In the absence of alternative methods for uranium and thorium determinations one is not in a position to distinguish between the samples which exhibit alpha overcounting and the ones which do not. That is, unless there is an obvious variation in alpha count rate from one portion of the sample to another. If the alpha counting method is the only method available, which is the case in some of the TL laboratories,

then it is important to be able to distinguish samples exhibiting overcounting from the others. Furthermore, one would want to be able to quantitatively correct for this counting discrepancy, or perhaps remove the overcount completely.

Murray (1980) attempted to remove the overcount by mixing the sample grains with a polyester resin. The purpose of this experiment was to replace the air in the sample cavities with the resin and hence make it impossible for the radon to diffuse towards the counting screen. Murray found that in the majority of the samples studied overcounting was drastically reduced. The experiment was, however, not very quantitative as the atomic weight of the resin was not accurately known and no great care was taken to homogenize the samples prior to mixing. In order to apply the alpha particle range correction factor (Equation 2.7) it is important that the sample mixtures are homogeneous in nature and, furthermore, the grain sizes must be small compared to the average alpha particle range. However, the purpose of Murray's experiment was not to make a quantitative correction for overcounting, but rather to demonstrate that the retention of radon in the sample cavities was one of the causes of overcounting. Murray states that the fact that overcounting was drastically reduced, after mixing the samples into a resin, supports the radon retention model. One should also point out that mixing the sample with a resin would also remove the possibility of the more active fine grains working their way towards the counting screen. Mixing the sample with a resin would, however, not remove the possibility

of alpha overcounting due to preferential segregation of alpha activity within some of the individual grains, that is, unless the sample is thoroughly crushed and homogenized prior to mixing it with resin.

The phenomenon of mineralogical and radioactive inhomogeneities in rocks and soils is well recognized by field geologists. Mineralogical assaying techniques such as XRF, NAA and PIXE (see Chapter 3) are all based on the premise that the sample is of uniform mineralogical composition, thus making it essential to homogenize the samples thoroughly prior to analysis. There are basically two different sample preparation techniques, that are familiar to us, which overcome this inhomogeneity problem. One of them has already been mentioned in connection with PIXE analysis and NAA. In these analytical methods it is important to homogenize the samples to micron diameter size prior to analysis. If it is necessary to make the analysis on solids rather than powders then the powders can easily be pelletised. The other method is to fuse the samples into a solid solution. Both methods have been described in detail by Norrish and Hutton (1969) in connection with XRF analysis of soils. The fusion method not only solves the problem of sample inhomogeneity (possibilities 1(a) and (b) in Section 4.3) but also prevents the possibility of alpha overcounting due to radon retention. Hence, for the purpose of removing overcounting in all of the troublesome field samples, it appears that the sample fusion homogenization method is better suited than the more conventional crushing procedure. However, the method of counting homogenized powders might well be sufficient for some of the troublesome field samples. By thoroughly crushing and homogenizing the samples one may well reduce the

degree of overcounting due to the smaller grains being more active than the rest of the sample. However, one would not expect the method to completely remove overcounting for all of the troublesome samples encountered; particularly samples having an excess of alpha activity on the grain surfaces. Nevertheless, a selection of field samples were crushed and homogenized by a Siebtechnik mill using a tungsten carbide crushing vessel. The powdered samples were alpha counted and a selection of the results obtained is shown in Table 4.4. For comparisons the count rates obtained on the coarse grains and those expected on the basis of DNA and NAA measurements have also been included. The outcome was that overcounting was drastically reduced in all of the troublesome samples; furthermore, the count rates for the powdered samples were all reproducible from one measurement to the next. For the soil samples LF6 and EB1a the count rates obtained are in good agreement with the expected count rates; that is, for these two samples overcounting seems to have been completely eliminated. For the other troublesome samples, Sc 3/6 still has a count rate which exceeds the expected count rate by more than a factor of 2, sample ALD-22-50 has a count rate which is slightly less than that expected and sample BS-RL-2/41 has a count rate which is consistent with that observed on the coarse grains. Samples POM-T, LRF73F314 and F80-a have also been included in the comparison to show that the homogenization procedure also works for the "well behaved" samples.

The details of the fusion sample preparation method together with its application on uranium and thorium standards and a selection of field samples will be discussed in Chapter 5.

TABLE 4.4 COMPARISON OF ALPHA COUNT RATES OBTAINED ON HOMOGENIZED POWDERS WITH THE COUNT RATES OBTAINED ON COARSE GRAINS AND THOSE EXPECTED ON THE BASIS OF DNA AND NAA MEASUREMENTS FOR VARIOUS FIELD SAMPLES

Sample Identifier	Description of Sample	$\alpha_{coarse\text{-}grain}$ (ks^{-1})	$\alpha_{expected}$ (ks^{-1})	α_{powder} (ks^{-1})
LF6	Soil	8.9 ± 0.4	5.4 ± 0.8	6.1 ± 0.3
EB1a	Soil	4.1 → 48.4	4.4 ± 0.8	5.0 ± 0.3
ALD-22-50	Soil	6.0 → 22.1	5.5 ± 0.7	3.8 ± 0.4
F80-a	Soil	4.5 ± 0.2	4.0 ± 0.7	4.6 ± 0.2
Sc 3/6	Baked Sand	36.5 ± 1.6	11.3 ± 0.6	27.7 ± 1.4
POM-T	Tile	16.4 ± 1.0	16.2 ± 0.8	16.2 ± 1.0
LRF73F314	Pottery	13.8 ± 0.6	15.1 ± 0.6	13.4 ± 0.5
BS-RL-2/41	Lapita Pottery	18.9 ± 2.0	4.1 ± 0.5	18.1 ± 0.6

NOTE: The errors quoted are 95% confidence limits.

CHAPTER V

ALPHA COUNTING USING GLASS DISCS

5.1 Introduction

In XRF analysis of rocks and soils, one of the standard sample preparation techniques is to produce glass discs with the aid of fusion using a lithium borate mixture as the flux (Norrish and Hutton, 1964; 1969). Norrish and Hutton use a lithium borate-lanthanum oxide fusion mixture consisting of accurately and predetermined proportions of anhydrous lithium tetraborate, lithium carbonate and lanthanum oxide. The borate flux produced is then mixed with a known amount of sample, the usual mixing ratio being 1.50g of flux to 0.28g of powdered sample. A small amount of sodium nitrate (0.02g) is also added to ensure oxidizing conditions during the fusion process.

In producing glass discs for alpha counting there are several requirements which have to be met : The flux mixture matrix must be well known so that an alpha particle range correction factor can be calculated. The flux mixture alpha activity must be negligible compared with the sample activity. The actual decrease in alpha activity in going from sample grains to glass discs must be kept at a minimum, that is, one wants the sample-to-flux mixing ratio to be as high as possible and the area of the discs to be as large as possible (while still fitting inside the standard size counting cell).

5.2 Glass Disc Sample Preparation Method

After some initial experimentation using a variety of flux mixtures and sample to flux ratios we arrived at the following preparation recipe : Mix 4g of anhydrous lithium tetraborate ($Li_2B_4O_7$, code 1882, supplied by Allied Chemicals) with 2g of finely ground sample; the lithium tetraborate having been dried at 550° C before weighing. Heat the mixture in a large gold-platinum crucible with a lid at about 1050-1100° C, in an electric furnace, for about 15-20 min, after which time the mixture has completely dissolved (the melting point of lithium tetraborate being at 915° C). The melt may be stirred or swirled around in the crucible, but this is usually not necessary as effervescence, accompanying solution, and convection currents ensure mixing. Norrish and Hutton have found that the most satisfactory crucibles are a gold-platinum alloy (5% gold) that are available commercially. These crucibles are not wetted by the melt and successive samples can be made without cleaning the crucible. The melt is then poured onto a gold-platinum mould which has an internal diameter of 40mm. This mould is initially kept at a temperature of about 1000° C and after a decrease in temperature glass discs are formed on the tray. To ensure that the glass discs so produced do not crack it is then positioned between two clean asbestos mats on another hot plate at about 200° C. After a few minutes the mats may be removed from the plate to allow the glass disc to cool slowly. If more than one disc is being prepared, the mats can be retained on the second hot plate until the last sample is poured, then all of the discs may be cooled together.

As a precautionary means to make sure that there is no sample loss during fusion (i.e. due to moisture etc.,) the crucibles are weighed by themselves prior to analysis and then re-weighted (plus sample) after fusion. That is, the sample plus flux was first fused, then cooled down to allow for weighing and then re-heated to allow the mixture to be poured.

After cooling, the glass discs are put in labelled envelopes and can be kept indefinitely. To avoid surface moisture the discs are then stored in a desiccator until use. The glass discs are 40mm diameter and have a thickness of about 1.5mm.

5.3 Alpha Counting on Glass Discs Made From Uranium and Thorium Standards

In order to calibrate the glass disc alpha counting procedure, it was decided to count a variety of glass discs made from well known uranium and thorium standards. Ten glass disc standards were prepared, consisting of six uranium standards, three thorium standards and a blank glass disc (pure lithium tetraborate). The counting standards used to prepare the glass disc standards varied in concentration from about 2% down to about 500 $\mu g g^{-1}$. In none of the glass disc preparations was there any measurable sample weight loss during fusion. These glass disc standards were first alpha counted about 20 hours after the sample preparation. The alpha count rate of the pure lithium tetraborate glass disc was not measurable above the background of about 0.1 counts ks^{-1}. In Table 5.1 the observed count rates of the uranium and thorium glass discs have been compared with the count rates observed on the corresponding granular standards. The count rate

TABLE 5.1 COMPARISON OF ALPHA COUNT-RATES FOR VARIOUS URANIUM AND THORIUM GLASS DISC STANDARDS AS A FRACTION OF THE COUNT-RATES OBSERVED ON THE GRAIN STANDARDS : MEASUREMENTS TAKEN APPROXIMATELY 20 HOURS AND 50 HOURS AFTER PREPARATION

Sample Standard		(Glass-Disc/Grain) Alpha Count Rate Fraction	
		20 hours	50 hours
42-2		0.14 ± 0.01	0.17 ± 0.01
42-3		0.14 ± 0.01	0.17 ± 0.01
42-4		0.13 ± 0.01	0.16 ± 0.01
101	U	0.14 ± 0.01	0.18 ± 0.01
102		0.14 ± 0.01	0.17 ± 0.01
103		0.14 ± 0.01	0.17 ± 0.01
106		0.31 ± 0.01	0.31 ± 0.01
107	Th	0.29 ± 0.01	0.30 ± 0.01
108		0.30 ± 0.01	0.30 ± 0.01

NOTES: (1) The errors quoted are 95% confidence limits.

(2) NBL-42-2, 42-3 and 42-4 are all dunite based standards, whereas the remaining are quartz based.

dilution factor was observed to be fairly constant for both the uranium and thorium standards. At about 20 hours after fusion, the uranium standards have an average glass-disc/grain count rate dilution factor of 0.14 ± 0.01, while the corresponding thorium ratio is 0.30 ± 0.01. In order to quantitatively discuss this difference it is necessary to consider the relevant decay characteristics of the U-238 and Th-232 decay chains, these have been summarized in Figures 5.1 and 5.2 respectively. (see also Appendix A, Tables A1 and A2). In the U-238 decay chain the gaseous element Rn-222, which is removed during the fusion process, has a half-life of about 3.8 days. This is followed by the alpha emitters Po-218 and Po-214 both of which decay within a few hours after fusion. The remaining alpha emitter below radon is Po-210 ($\tau_{\frac{1}{2}} \sim 138.4$ days); this is however, not lost during fusion due to the 21.3 year beta half-life of its parent Pb-210. It is fortunate that the half-lives of the elements between Po-218 and Pb-210 are so short and the half-life of Pb-210 is so long compared with the half-life of Rn-222. Hence as a good approximation, the alphas lost during (and just after) the fusion process will grow back according to the 3.8 day half-life of Rn-222. In the Th-232 decay chain the gaseous element Rn-220 has a half-life of only 55 seconds. The other elements below Rn-220 also have relatively short half-lives, the longest by far being the 10.6 hour beta half-life of Pb-212. This means that only the alphas from Rn-220 and Po-216 are lost during the fusion process. These then grow back within a few minutes and equilibrium is again reached in the thorium decay chain.

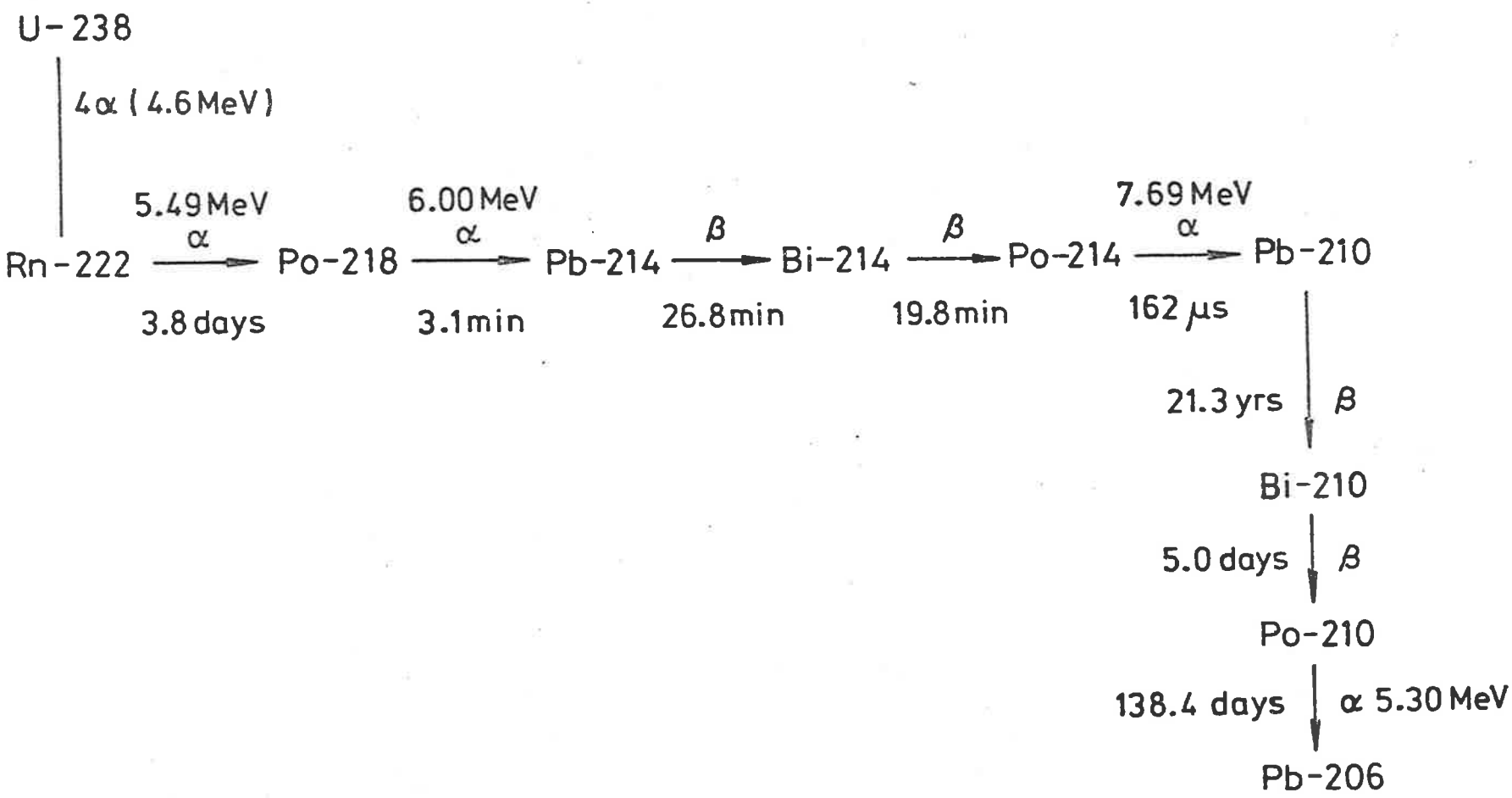

Figure 5.1 Some Relevant Decay Characteristics of the U-238 Decay Series.

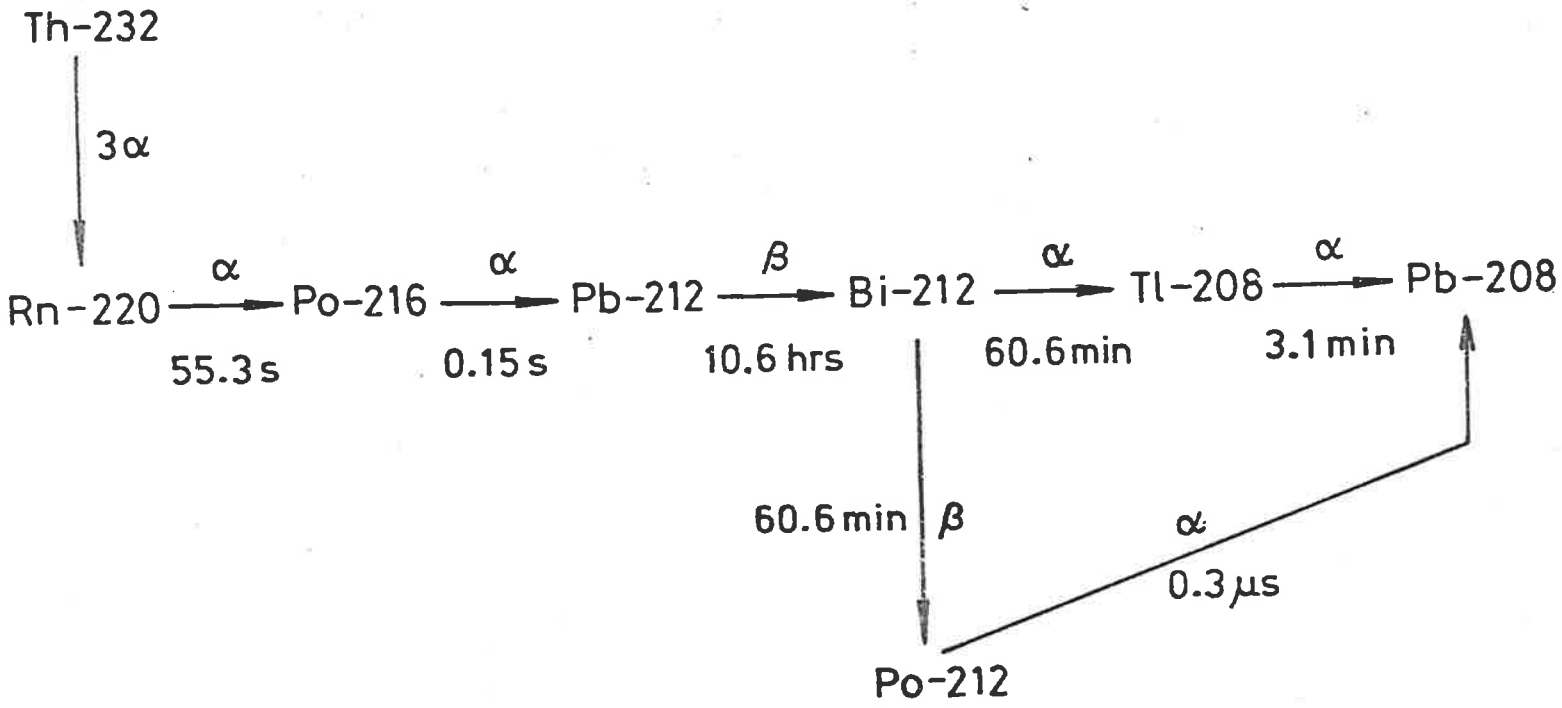

Figure 5.2 Some Relevant Decay Characteristics of the Th-232 Decay Series.

The alpha counting data in Table 5.1 agree quite well with the above-mentioned decay characteristics. For comparison the glass-disc/grain alpha count rate fractions observed a period of about 50 hours after fusion are also shown in Table 5.1. Alpha activity growth curves were measured on all of the six uranium glass disc standards. Figure 5.3 shows the growth curve, up to about five radon half-lives, as measured on the NBL-42-4 glass disc standard (0.5% uranium ore in glass). The general shape of the uranium growth curve can be approximated by the relationship

$$\alpha(\tau) = C(1 - e^{-\lambda\tau}) + \alpha(0), \qquad (5.1)$$

where $\alpha(\tau)$ represents the total alpha count rate at a time τ after fusion, $\alpha(0)$ represents the alpha count rate immediately after fusion, C is a constant alpha count rate determined by the value of $\alpha(0)$ and $(1-e^{-\lambda\tau})$ is the half-life correction factor, where λ is the decay constant of Rn-222. After a 19-day wait, which corresponds to about 5 radon half-lives, one expects about 97% of the lost alphas to have grown back into the glass discs. The glass-disc/grain count rate ratios of the six uranium standards obtained a period of 19 days after fusion are shown in Table 5.2. Although the agreement between the different uranium standards is good the average uranium glass-disc/grain count rate ratio of 0.27 ± 0.01 is slightly lower than that observed on the thorium standards (0.30 ± 0.01).

The glass-disc/grain count rate fractions can also be determined theoretically by applying the following effective correction factor (glass-disc/grain count rate dilution factor)

$$R_{eff} = R_1 \; R_2 \; R_3 \; (1 - R_4) \; R_5, \ldots\ldots \qquad (5.2)$$

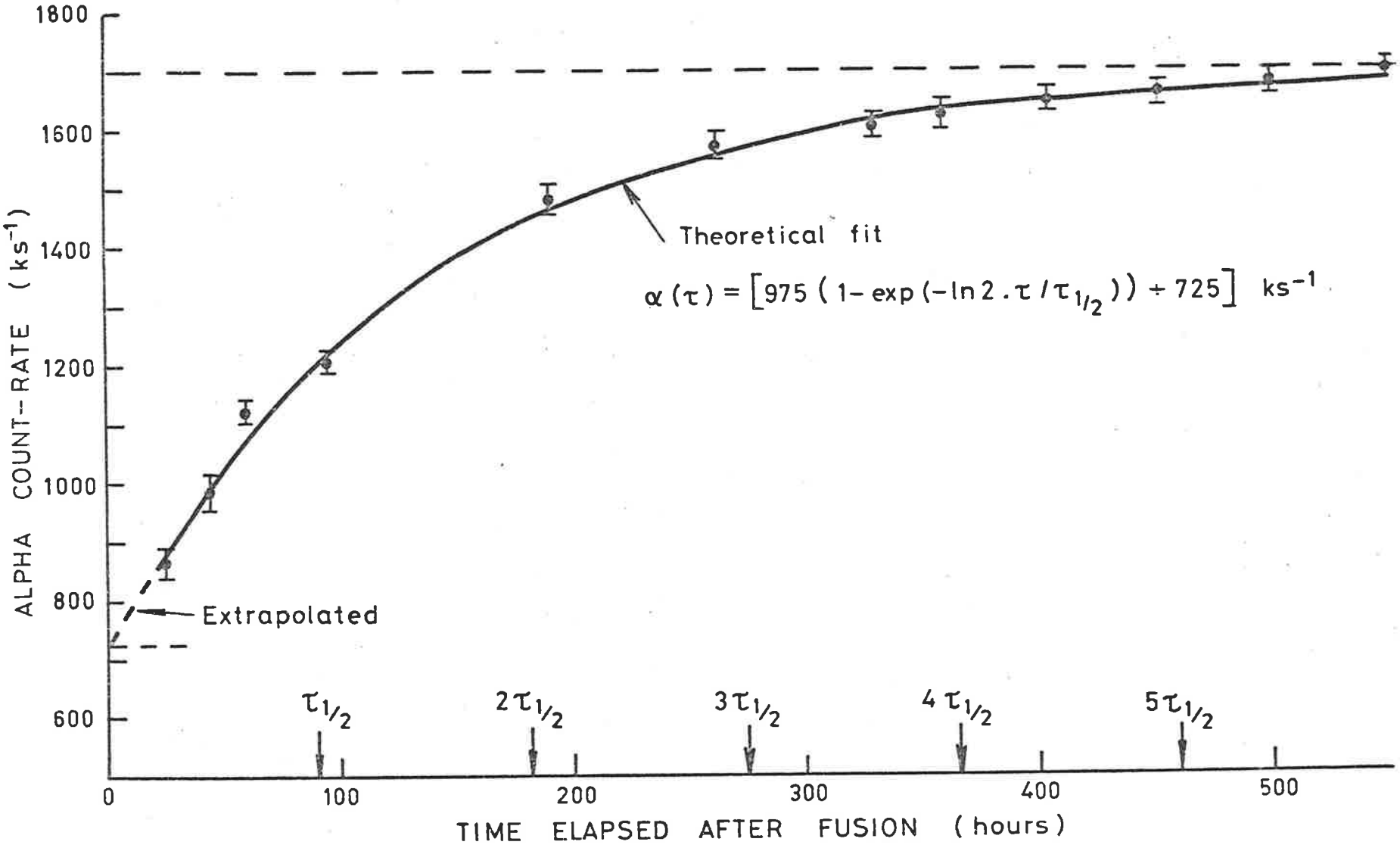

Figure 5.3 Alpha Activity Growth-Curve of Uranium Glass-Disc Standard (NBL-42-4).

TABLE 5.2 COMPARISON OF ALPHA COUNT-RATES FOR VARIOUS URANIUM AND THORIUM GLASS DISC STANDARDS AS A FRACTION OF THE COUNT-RATES OBSERVED ON THE GRAIN STANDARDS : MEASUREMENTS TAKEN APPROXIMATELY 19 DAYS AFTER PREPARATION.

Sample Standard (NBL)		(Glass Disc/Grain) Alpha Count-Rate Fraction 19 days after fusion
42.2		0.27 ± 0.01
42.3		0.26 ± 0.01
42.4		0.26 ± 0.01
101	U	0.27 ± 0.01
102		0.27 ± 0.01
103		0.27 ± 0.01
106		0.31 ± 0.01
107	Th	0.30 ± 0.01
108		0.30 ± 0.01

NOTE: The errors quoted are 95% confidence limits.

where R_1 represents the weight dilution factor, R_2 the reduction in counting area factor, R_3 the B-K atomic weight correction factor, R_4 the sample weight loss during fusion factor and R_5 the reduction in count rate due to the loss of radon factor (which is time dependent, see Equation 5.1). The factor R_4 is in Equation 5.2 as a precautionary measure. In none of the standards prepared was there any measurable weight loss during fusion. This may however, not always be the case on TL field samples.

One reason for the slight difference in alpha count rates for the uranium and thorium glass disc standards (as measured at least 19 days after fusion) could be the inadequacy of the B-K correction factor (R_3). It has already been shown that the B-K equation gives alpha particle ranges which are too short for the lower atomic weight elements (Section 2.4.3). This means that the B-K correction factor for lithium tetraborate ($Li_2B_4O_7$), and hence the glass discs, will also be too low. However, for the lower atomic weight elements there is only a slight increase in the B-K discrepancy as the energy of the alphas increases (see Table 2.5). For completeness, a comparison of the Williamson *et al* and B-K alpha ranges for the elements lithium, boron and oxygen is given in Table 5.3. For lithium and boron the discrepancy of the B-K ranges is about 24% and 11% respectively, whereas for oxygen there is agreement (within about 1%). A comparison of the B-K ranges with some of the other range tables produced quite similar results (see Table 2.4). The fact that the B-K discrepancy is almost independent of energy for lithium, boron and oxygen in the energy range 4 to 9 MeV means that, although R_3 will be too low, it will be much the same irrespective of whether one is counting uranium or thorium glass disc standards. Using the Williamson *et al* alpha range data one finds that the B-K alpha ranges

TABLE 5.3 COMPARISON OF THE WILLIAMSON *et al* AND BRAGG-KLEEMAN ALPHA PARTICLE RANGES FOR LITHIUM, BORON AND OXYGEN : ENERGY RANGE FROM 1 TO 9 MeV.

	Alpha Ranges ($mg.cm^{-2}$)		
Energy (MeV)	W	B-K	% Dev
	Lithium		
4	2.70	2.11	- 21.9
6	5.17	3.89	- 24.8
9	10.02	7.58	- 24.4
	Boron		
4	2.93	2.63	- 10.2
6	5.50	4.86	- 11.6
9	10.70	9.46	- 11.6
	Oxygen		
4	3.28	3.20	- 2.4
6	5.98	5.91	- 1.2
9	11.39	11.51	1.1

for lithium tetraborate are about 7 to 8% too low, depending on the energy of the alpha particle in question.

If one assumes that the thorium standard matrices are purely quartz, one obtains an effective standard plus lithium tetraborate (A = 13.27) atomic weight of 15.82, this gives a value of R_3 of 0.88. Corrected for the B-K range discrepancy, this value becomes 0.92. This gives an effective theoretical correction factor (R_{eff}) for the thorium glass discs of 0.28 ± 0.01. For a period of 19 days after fusion the theoretical effective correction factor for the quartz based uranium standards is also 0.28 ± 0.01, whereas for the dunite based standards the factor is slightly lower at 0.27 ± 0.01. These theoretical predictions are in very good agreement with the correction factors observed on the uranium standards. Although the thorium glass-disc/grain count rate ratios are consistently slightly higher than the corresponding uranium ratios, there is (within the errors) also good agreement with the theoretical value.

Comparing the data from Tables 5.1 and 5.2, one notes that the uranium glass disc/grain count rate factor 20 hours after fusion is approximately half of the value observed after the radon has almost fully grown back. That is, during the fusion process there is more than a 50% loss in alpha activity even though only three out of the eight alpha emitters in the U-238 decay chain are missing. The reason for this is that the alpha particle energies (ranges) of the missing alpha's (average value of 6.4 MeV) are appreciably higher than the remaining alpha energies (average value of 4.7 MeV).

For glass-discs made from TL field samples (average $A \sim 21.4$, see Section 2.4.3) the alpha count rate calibration factor can be estimated from the values obtained on the uranium and thorium standards. For a wait of 19 days or longer after fusion this calibration factor is between 0.27 and 0.30 depending on the Th/U ratio of the sample. The accuracy of the alpha count rate dilution factor depends on how well the Th/U ratio of the particular sample is known. However, it is unlikely that the uncertainty in the calibration factor is greater than about 5% for any field sample. Hence the glass disc counting procedure outlined in Section 5.2 is certainly suitable for the detection and correction of gross alpha overcounting. Furthermore, in order to obtain the best counting statistics the glass-discs should be alpha counted a period of at least 19 days after preparation.

5.4 Alpha Counting on Glass Discs Made From A Variety of Field Samples

Having calibrated the glass disc counting procedure with standards, glass discs were made up from a variety of TL field samples. Seven discs were prepared, consisting of four samples normally exhibiting alpha overcounting (LF6, EB1a, ALD-22-50 and Sc 3/6) and three "well behaved" samples (F80a, POM-T and LRF-73-F314). Figure 5.4 is a colour photograph of a selection of glass discs made from standards and field samples. In none of the seven preparations was there any measurable weight loss during fusion. The glass discs were all alpha counted at regular periods of time after preparation in order to check any abnormal behaviour in the alpha "growth-curve" (see

Figure 5.4 Colour Photograph of a Selection of Glass-Discs made from Standards and Field Samples.


MM
1
2
3
4
5
6
7
8
9
10

Section 5.3). The corrected glass disc count rates were calculated by using the count rates obtained a period of at least 19 days after preparation and the appropriate correction factors (see Equation 5.2). The results obtained have been summarized in Table 5.4, where the corrected glass disc count rates are compared with the expected count rates as well as the count rates obtained on the coarse-grain field samples (see also Tables 4.1 and 4.2). Also included in the table are the corresponding alpha count rates obtained on powdered samples (see Section 4.4, Table 4.4). The results indicate that the count rates observed on the glass discs are generally in good agreement with the count rates expected on the basis of DNA and NAA measurements. Overcounting was certainly eliminated on the soil samples LF6, EB1a and ALD-22-50. Furthermore, the glass disc count rates for the three "well behaved" field samples also came out as expected. Overcounting was also drastically reduced on sample Sc 3/6, even more so than was the case when counting the homogenized sample powder. However, the glass disc count rate was still about 80% higher than that expected on the basis of DNA and NAA measurements. An excess in concentration of some of the U-238 daughters would explain this discrepancy. This was confirmed by Lioutas (1981) who carried out gamma-ray NaI scintillation measurements on this sample. By measuring the Bi-214 and Tℓ-208 gamma rays (see Section 2.4.2), Lioutas determined the concentration levels to be $12.8 \pm 1.6\ \mu g g^{-1}$ and $19.5 \pm 3.4\ \mu g g^{-1}$ respectively, the errors quoted being at 95% confidence limits. One notes that while the Tℓ-208 concentration is in reasonably good agreement with the NAA measurements on Th-232

TABLE 5.4 COMPARISON OF ALPHA COUNT RATES OBTAINED ON GLASS DISCS WITH THOSE OBTAINED ON SAMPLE GRAINS AND THOSE EXPECTED ON THE BASIS OF DNA AND NAA MEASUREMENTS FOR VARIOUS TL FIELD SAMPLES.

Sample Identifier	Description of Sample	$\alpha_{coarse\text{-}grain}$ (ks^{-1})	α_{powder} (ks^{-1})	$\alpha_{glass\text{-}disc}$ (ks^{-1})	$\alpha_{expected}$ (ks^{-1})
F80-a	Soil	4.5 ± 0.2	4.6 ± 0.2	4.6 ± 0.5	4.0 ± 0.7
LF6	Soil	8.9 ± 0.4	6.1 ± 0.3	6.3 ± 0.2	5.4 ± 0.8
EB1-a	Soil	4.1 → 48.4	5.0 ± 0.3	4.5 ± 0.8	4.4 ± 0.8
ALD-22-50	Soil	6.0 → 22.1	3.8 ± 0.4	5.2 ± 0.7	5.5 ± 0.7
POM-T	Tile	16.4 ± 1.0	16.2 ± 1.0	16.6 ± 1.4	16.2 ± 0.8
LRF73F314	Pottery	13.8 ± 0.6	13.4 ± 0.6	14.8 ± 1.2	15.1 ± 0.6
Sc 3/6	Baked Sand	36.5 ± 1.6	27.7 ± 1.4	20.3 ± 1.4	11.3 ± 0.6

NOTES: (1) The errors quoted are 95% confidence limits.

(2) Included in the Table are the alpha count rates obtained on powdered (thoroughly crushed and homogenized) samples.

(i.e. 19.5 ± 3.4 $\mu g g^{-1}$ compared with 15.1 ± 0.5 $\mu g g^{-1}$), the Bi-214 concentration is about 6 times that determined by DNA measurements on U-238 (i.e. 12.8 ± 1.6 $\mu g g^{-1}$ compared with 2.2 ± 0.2 $\mu g g^{-1}$). This is consistent with the observed glass disc alpha count rate of 20.3 ± 1.4 ks^{-1}. However, an accurate comparison can only be made if the relative abundances of some of the other key elements in the U-238 decay chain are determined (see Section 2.4.2). For this sample the glass-disc alpha count rate gives the best estimate of the present day alpha activity.

5.5 Summary and Conclusion

In this Chapter a sample preparation technique for producing glass disc samples for alpha counting has been described. This sample preparation method was utilized in order to remove the possibility of alpha overcounting. The method was calibrated by counting accurately-known uranium and thorium glass disc standards. The alpha count rates obtained on these standards were in good agreement with the theoretically expected values. Although the number of TL field samples exhibiting overcounting is relatively small, overcounting was eliminated in all of the troublesome samples so far encountered.

Having removed the possibility of alpha overcounting one is in a much better position to compare the measured alpha activity with that predicted on the basis of DNA and NAA measurements. Observed discrepancies must then be caused by disequilibrium in the uranium decay chains. Of the samples so far encountered, only Sc 3/6 has been found to have the U-238 decay chain in gross disequilibrium.

PART II

ASPECTS ASSOCIATED WITH MEASUREMENTS OF THERMOLUMINESCENCE SPECTRA.

CHAPTER VI

PHYSICAL PRINCIPLES AND RELEVANT CHARACTERISTICS OF THERMOLUMINESCENCE

6.1 Introduction

A very brief description of the TL phenomenon as well as a historical development of the TL dating method has already been given in Chapter 1. In this Chapter a more detailed account will be given. It is important that one understands the basic physical principles of TL if one is to interpret TL measurements correctly.

Before commencing a discussion on the actual TL kinetic processes it is necessary to outline the interpretation of TL in terms of basic band theory of solids. In a perfect crystal lattice the electrons fill up the available states in the valence band with an energy gap to the conduction band which would normally be free from electrons. The presence of lattice imperfections, such as impurities or structural defects, modifies this band model by creating additional energy levels mostly in the gap between the valence and conduction bands. These energy levels can be categorized as either electron traps or hole traps; these hole traps can be further subdivided into luminescent centres and non-luminescent ("killer") centres. The types of trap and centre responsible for trapping in archaeological samples are rarely known; identification is difficult even when dealing with pure substances containing known impurities. The band structure energy level representation illustrated in Figure 6.1 is of great utility in discussing TL. The incoming ionizing radiation may detach an electron from its parent atom or ion, this electron is then free to diffuse

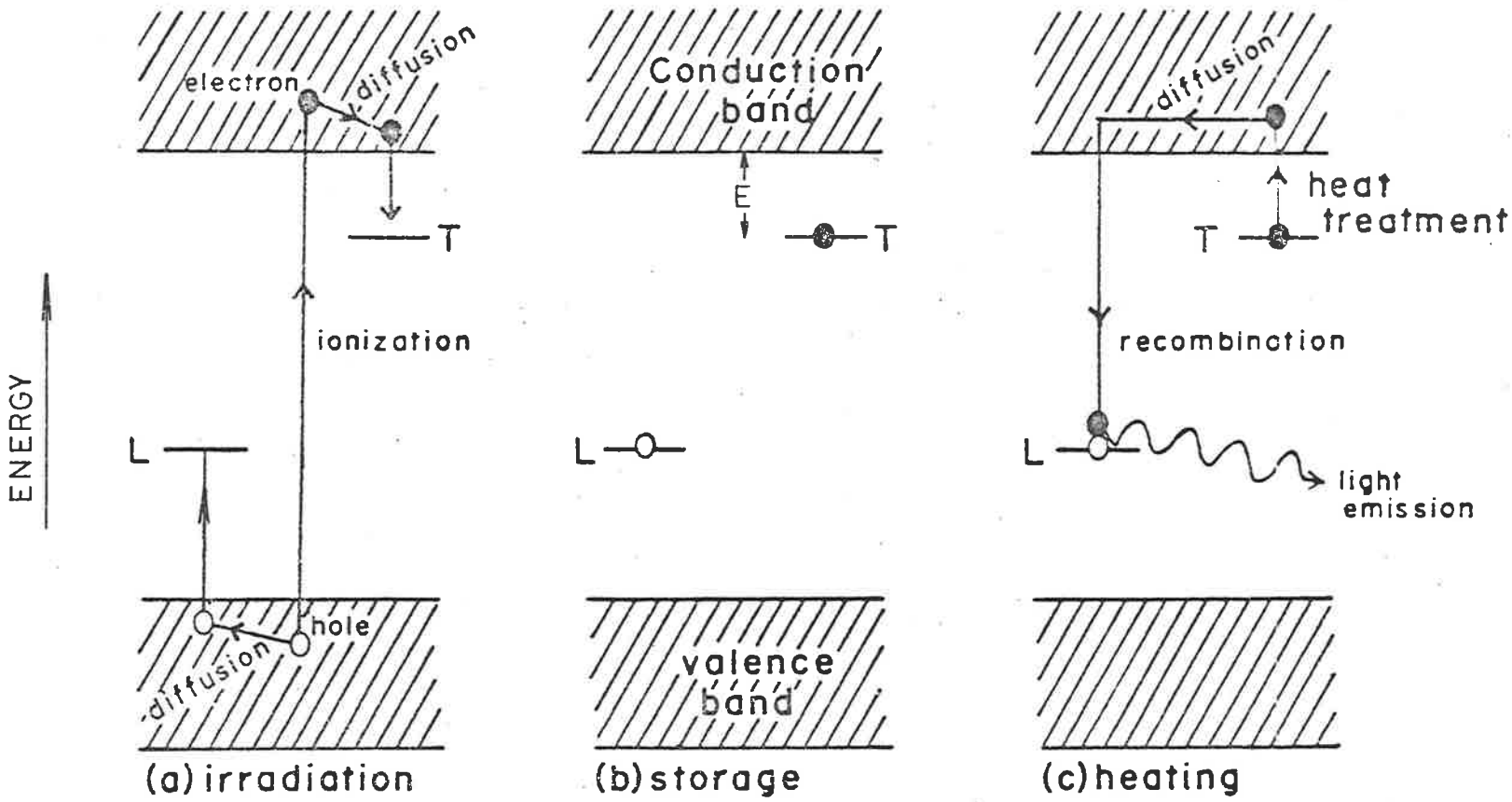

Figure 6.1 Schematic band structure energy level representation of the thermoluminescence process.

about in the conduction band until it is trapped in the energy gap at a defect T. Similarly, the hole left in the valence band can diffuse until it is trapped at a centre L (Figure 6.1(a)). The lifetime of the electron in trap T depends on the depth E below the conduction band; the larger the depth the longer one expects the lifetime to be. This aspect is important as far as TL dating of ancient objects are concerned, one can only consider trap depths which allow negligible escape at ambient temperatures over the archaeological period; this will be further discussed in Section 6.2.

When the sample is subsequently heated one reaches a temperature at which thermal excitation of the crystal lattice is sufficient to allow the electron to escape from the trap into the conduction band. The electron diffuses until it recombines with a hole at a luminescent centre, hence producing the TL which is observed (Figure 6.1(c)). The wavelength of the light emitted is determined by the atom or ion forming the luminescence centre and not by the depth of T below the conduction band. One should also note that it is possible for the electron to recombine at a non-luminescent centre where, instead of the emission of light, the available energy is dissipated by non-radiative lattice interactions, or be recaptured ("retrapped") by an even deeper trap.

To summarize Figure 6.1, we see that the TL process is one of charging empty electron and hole-trapping centres with their respective charge carriers; then storage of these carriers at the centres over an appreciable period of time after which, upon heating the sample, the charge carriers are released from the centres and one observes the associated emission of TL.

It was early realized that the processes governing the emission of TL can be quite complex, each individual sample studied having a variety of impurities and lattice defects as well as possible recombination processes. In Section 6.2, an attempt is made to provide some sort of formalism upon which the work in this part of the thesis is based.

6.2 First and Second Order Kinetics

The wide variety of materials used in TL studies makes a complete theoretical study of the phenomenon rather complicated, although in some cases theory has been quite successful. Randall and Wilkins (1945) were among the first to investigate TL theoretically. They proposed the so-called first-order ("monomolecular") kinetic theory, where one has for a single glow curve peak the relationship

$$\frac{dn}{dt} = - ns \exp(- E/kT) \qquad (6.1)$$

$\frac{dn}{dt}$ being the number of charges released per unit time, t the time, n the trap charge concentration at time t, s the "attempt to escape" frequency, k the Boltzmann's constant, T the absolute temperature in degrees K and E the activation energy for thermal charge release. This model is very simple as it only considers a single electron trap and a luminescent centre with no provision for a particular charge carrier to be trapped more than once. Randall and Wilkins then assumed that the intensity of the emitted light, I, for a given peak is proportional to the number of charges released per unit time. That is, the intensity is given by

$$I = -\frac{dn}{dt} = ns \exp(-E/kT) \qquad (6.2)$$

One hence obtains an intensity which decays exponentially with a half-life given by

$$\tau_{\frac{1}{2}} = \frac{\ell n 2}{s} \exp(E/kT) \qquad (6.3)$$

this half-life is of paramount importance in TL dating as the use of a particular glow peak depends on whether it has a half-life at the ambient temperature which is very much longer than the TL age of the sample in question.

If a sample is heated at a constant heating rate, $\beta = dT/dt$, then the solution of Equation (6.1) can be shown to be

$$n = n_o \exp\left(-\int_{T_o}^{T} \frac{s}{\beta} \exp\left(-\frac{E}{kT'}\right) dT'\right) \qquad (6.4)$$

where T_o is the initial temperature.

The actual shape of the predicted peak is given by

$$I(T) = C\, n_o s \exp\left(-\frac{E}{kT}\right) \left[\exp\left(-\int_{T_o}^{T} \frac{s}{\beta} \exp\left(-\frac{E}{kT'}\right) dT'\right)\right] \qquad (6.5)$$

where C is a constant which, without loss of generality, may be set to unity. From this equation we see that initially the intensity rises exponentially with increasing temperature; the concentration of trapped charges is reduced and the intensity, after reaching a maximum at a certain temperature T_m, begins to fall and reaches zero when all the traps have been emptied. A relation giving the peak temperature in terms of E, s and β can be obtained by differentiating Equation (6.5) at $T = T_m$. That is by setting

$$\left(\frac{dI}{dT} \right)_{T=T_m} = 0 \qquad (6.6)$$

one obtains the relationship

$$\frac{E}{kT_m^2} = \left(\frac{s}{\beta} \right) \exp\left(- \frac{E}{kT_m} \right) \qquad (6.7)$$

This equation cannot be solved analytically as neither E nor s is usually known.

The physical interpretation of this model is straightforward, at time t there are n trapped charges, each of them vibrating back and forth in a trap with frequency s. The exponential term in Equation (6.1) is the well known Boltzmann factor expressing the probability that the charge will escape each time it encounters a potential barrier. However, from the Equations given one can see that, the computation of the kinetic parameters E, s and n can be quite complicated. From Equation (6.7) one sees that E is an implicit function of the peak temperature T_m, the relation between them being defined by the parameter β/s. The equation can be evaluated numerically with an accuracy of better than 1% and one can write (Curie, 1963).

$$E(eV) = \frac{T_m\ (^\circ K) - T_o\ (\beta/s)}{K\ (\beta/s)} \qquad (6.8)$$

where the functions T_o and K may be obtained graphically for different values of the parameter β/s and then used for calculating E. In order to get an estimate of the magnitudes of the trap depths as a function of the peak temperature it is useful to consider the Urbach formula (see Urbach, 1946; Curie, 1963), which states that for

$s \sim 10^9 s^{-1}$ an approximate value for the trap depth is given by the relation

$$E(eV) \sim \frac{T_m\ (^\circ K)}{500} \qquad (6.9)$$

Curie (1963) found that using this approximation one obtains trap depths which are generally of the right order of magnitude as long as the heating rate is not too low. For higher values of s the temperature required to release trapped charges at a given trap depth is lowered; if $s \sim 10^{13} s^{-1}$ then one may write

$$E(eV) \sim \frac{T_m\ (^\circ K)}{350} \qquad (6.10)$$

On the basis of Equations (6.9) and (6.10) the half-lives (at $20^\circ C$), given by Equation (6.3) and corresponding to various values of T_m, have been estimated and are tabulated in Table 6.1. One notes that these approximate values are quite consistent with the experimental observation that in a natural glow curve from an ancient sherd there is not usually any observable TL below about $250^\circ C$. A basic assumption in the general TL dating method is that the relevant traps are deep enough to retain the charge carriers without leakage over archaeological time. For the quartz inclusion technique the glow curve obtained consists, in the higher temperature ($300 - 400^\circ C$) region, of two broad overlapping peaks at about $325^\circ C$ and $375^\circ C$ respectively (see Figure 6.2(a)), the lifetime as well as trap depths corresponding to these peaks can be estimated by experimental determination of the relevant kinetic parameters, this aspect will subsequently be discussed in more detail. However, in the fine-grain technique the sample consists of a mixture of unidentified minerals and a variety of glow-

TABLE 6.1 ESTIMATION OF THE HALF-LIVES OF TL GLOW PEAKS AS A FUNCTION OF TEMPERATURE

T^*	100° C	200° C	300° C	400° C	500° C
a: $\tau_{\frac{1}{2}}$	2h	230d	1800 years	5×10^6 years	1.5×10^{10} years
b: $\tau_{\frac{1}{2}}$	3d	600 years	5×10^7 years	4×10^{12} years	4×10^{17} years

NOTES: (1) The half-lives were estimated at 20° C

(2) The first row of half-lives (a) are calculated using Equations 6.9 and 6.3 ($s \sim 10^9 s^{-1}$) and the second row (b) are calculated using Equations 6.10 and 6.3 ($s \sim 10^{13} s^{-1}$).

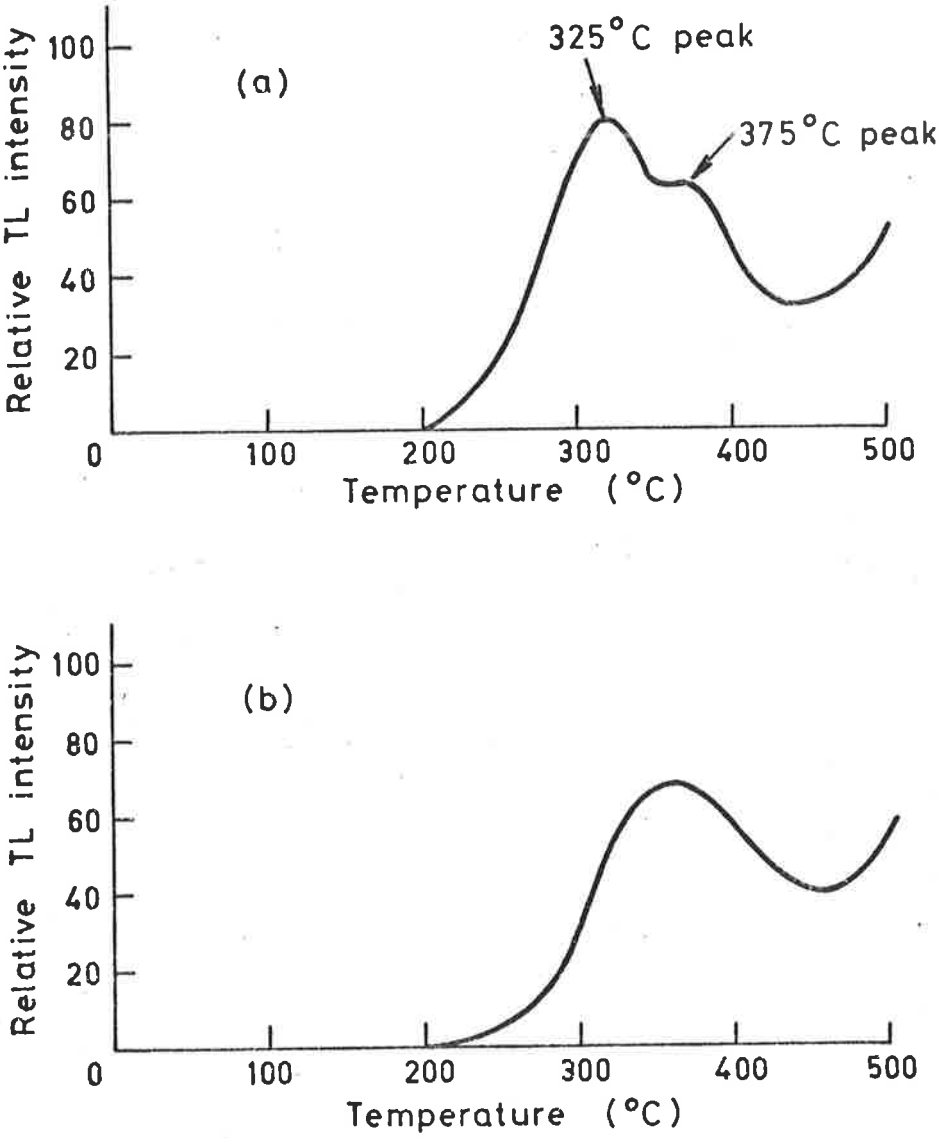

Figure 6.2 Typical Natural TL Glow-Curves from an Archaeological Sample

(a) Obtained from quartz grains extracted from the sample.

(b) Obtained from fine grains extracted from the sample.

curve shapes are generally obtained, such as that shown in Figure 6.2(b). It is usually not possible to resolve the glow curve into peaks suitable for kinetic studies but fortunately a check on the stability of traps can be obtained by applying the "plateau" test (see Section 6.3).

Another model which describes the shape of a glow peak was proposed by Garlick and Gibson in 1948; their model is said to be of "second order" ("bimolecular"). This model differs from the first order model in that it allows charge carriers to be trapped more than just once ("retrapping"). For this model, the intensity given by Equation (6.2) for no retrapping must be modified by the probability of recombination, which then gives the relation

$$I = \frac{-dn}{dt} = \frac{sn^2}{N_o} \exp(-E/kT) \qquad (6.11)$$

where N_o represents the total number of electron traps. This gives an isothermal decay of trap population which is no longer a simple exponential, but rather given by

$$n = \frac{n_o}{1 + (\frac{n_o}{N_o})st \exp(-E/kT)} \qquad (6.12)$$

where n_o is the total number of traps filled prior to heating. Solving this equation for a constant heating rate, β, then gives one the second order peak intensity distribution

$$I(T) = \frac{sn_o^2 \exp(-E/kT)}{N_o \left[1 + \frac{n_o}{N_o} \int_{T_o}^{T} \frac{s}{\beta} \exp(-\frac{E}{kT'}) dT' \right]^2} \qquad (6.13)$$

Theoretical first and second order glow peaks using Equations (6.5)

and (6.13) have been computed by numerous authors (see for example, Garlick and Gibson, 1948; Levy, 1978). Levy (1978) computed both first and second order glow peaks using commonly occurring values of E and s for various values of initial trapped charge concentration, the results obtained are illustrated in Figures 6.3(a) and (b) respectively. From the intensity Equations one can see that the most significant difference between second and first order kinetics is that for a second order peak the shape and peak temperature are both functions of the initial trap charge concentrations, whereas for a first order peak they are not. From Figures 6.3(a) and (b) one sees that the shape of the glow peaks depends on whether one has second or first order kinetics; that is, whether there is retrapping or not. Hence, in principle it should be possible to differentiate between the two kinetics by comparing the measured glow peak with theoretical first and second order peaks.

If the temperature under consideration is appreciably less than the peak temperature, T_m, then the first and second order intensity equations become similar. Equation (6.5) becomes

$$I \equiv n_o s \exp(- E/kT) \quad \text{(first order)} \tag{6.14}$$

similarly, Equation (6.13) becomes

$$I \equiv \left(\frac{n_o^2}{N_o} \right) s \exp(- E/kT) \quad \text{(second order)} \tag{6.15}$$

This is so because in both Equations (6.5) and (6.13) the term in square brackets becomes more or less constant if $T \ll T_m$. This provides us with a simple means for calculating the activation energy

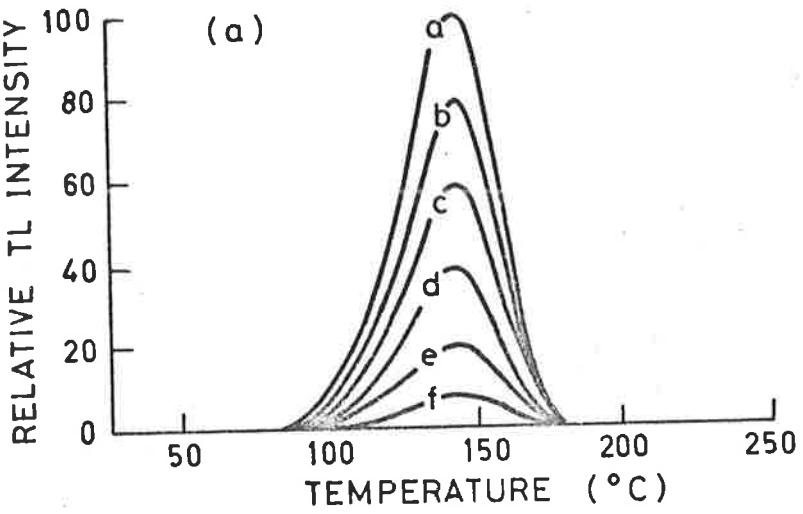

Figure 6.3(a) Theoretically computed first order glow peaks with E = 1.0 eV, $s = 10^{10}\,sec^{-1}$ and $\beta = 10^{\circ}C\ min^{-1}$. The initial trapped charge concentrations from (a) to (f) are 1.0, 0.8, 0.6, 0.4, 0.2 and 0.05 x $10^{16}\,cm^{-3}$ respectively. (From Levy, 1978).

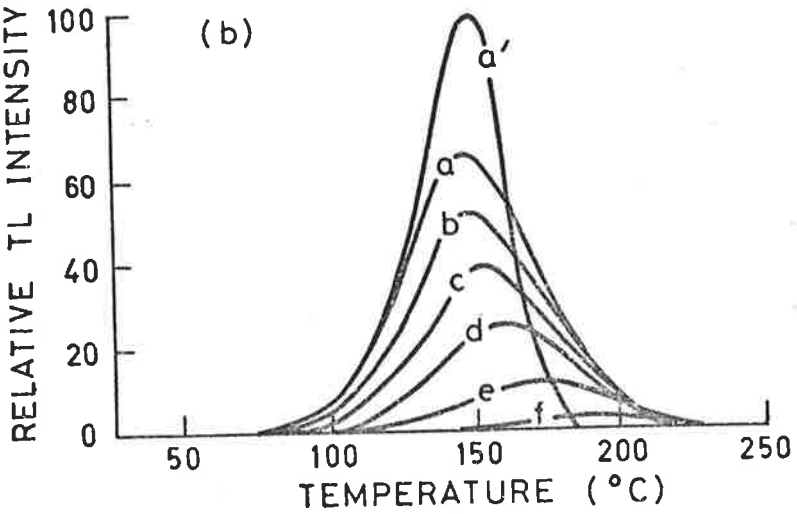

Figure 6.3(b) Theoretically computed second order glow peaks with E = 1.0 eV, $s = 10^{10}\,sec^{-1}$ and $\beta = 10^{\circ}C\ min^{-1}$. The initial trapped charge fractions from (a) to (f) are 1.0, 0.8, 0.6, 0.4, 0.2 and 0.05 respectively. The curve labelled (a)' is the first order peak labelled (a) from Figure 6.3(a). (From Levy, 1978).

from the slope derived from a plot of ℓnI versus $1/T$ in this initial temperature rise region. It is important to note that by using this initial rise method there is no need to know the complete shape of the glow peak in order to obtain an estimate of the activation energy. Bräunlich (1967) gives a good discussion on the use of the initial rise method for determination of trap depths; he clearly points out what the method can and cannot do and cases where the method should not be used. One of the main disadvantages with using the initial rise method is that by the measurements taken one cannot conclusively deduce whether one is dealing with first or second order kinetics. However, recalling Figure 6.3(b) we note that for second order kinetics the glow peak temperature is very much dependent on the dose delivered, the peak shifting to lower temperatures as the dose is increased; the effect being stronger the lower the dose. This may well be an important phenomenon when studying natural TL as the archaeologically accumulated doses are usually rather small.

Using the initial rise method, Fleming (1969) (see also Aitken and Fleming, 1972) carried out kinetic studies on Norwegian α-quartz. He deduced that the $110^{\circ}C$ peak exhibited almost pure first order kinetics, whereas studies of the peak position with trap filling indicate that the $325^{\circ}C$ and $375^{\circ}C$ peaks obey mainly first order kinetics but do exhibit some second order behaviour. Quoted is an example on the $375^{\circ}C$ peak where filling the associated traps from 5% to 100% shifts the peak position some $8^{\circ}C$ lower; whereas for pure second order kinetics the corresponding theoretical shift is about $50^{\circ}C$ and for pure first order kinetics no shift is expected.

One does not yet have a general operational method for calculating trap depths, which is based on the shape of the glow peaks. The first and second order approximations are however, fairly good ones, for the majority of experimentally found peaks. Many of the methods described in the literature are based on either of these two assumptions. However, some researchers have found it useful to consider a "general" order kinetics (see for example, May and Partridge, 1964; Chen, 1976) , for which one has the expression

$$I = \left(\frac{s}{N_o}\right) n^b \exp(-E/kT) \qquad (6.16)$$

where b is the order of the kinetics.

The majority of the methods used for calculating trap depths are based on measurements of T_m, T_1 and T_2; where T_1 and T_2 refers to the first and second half intensity temperatures. The formulaes derived for the determination of trap depths usually contain one of the following factors

(a) $\tau = T_m - T_1$, the half-width of the low temperature side of the peak

(b) $\delta = T_2 - T_m$, the half-width of the high temperature side of the peak

or (c) $w = T_2 - T_1$, the total half-width.

These factors are illustrated digrammatically in Figure 6.4. By assuming that the area of the half peak toward the fall-off is equal to the area of a triangle having the same height and half-width, Lushchik (1955) showed that for first order kinetics one has

$$E = \frac{kT_m^2}{\delta} \qquad (6.17)$$

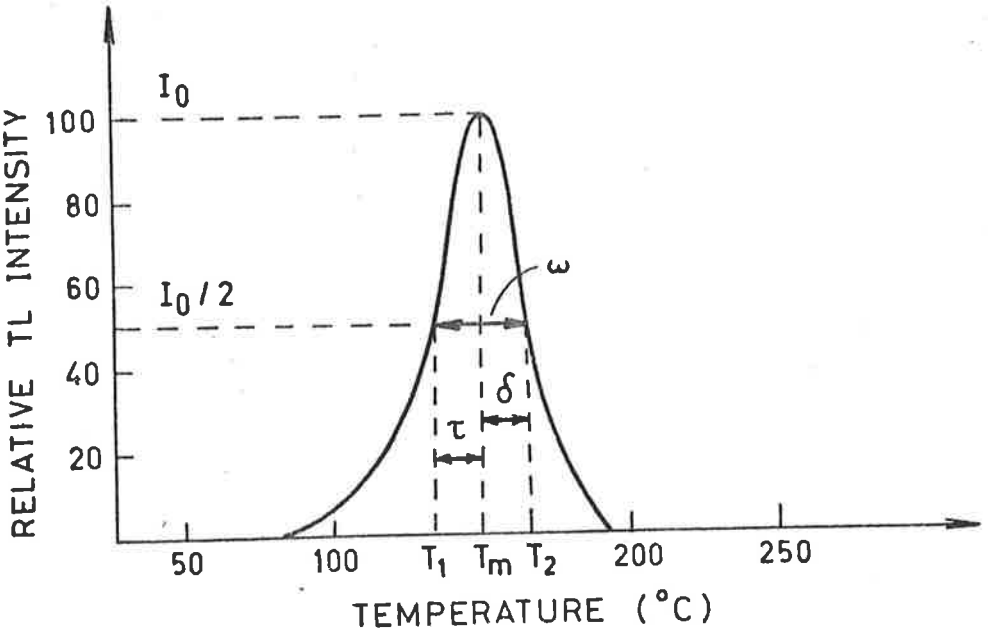

Figure 6.4 Diagrammatic Illustration showing some of the Parameters which determine the shape of a Glow Peak.

Similarly, he showed that for second order kinetics one obtains

$$E = \frac{2kT_m^2}{\delta} \qquad (6.18)$$

which is exactly twice that for first order kinetics.

These equations, based on the Luchchik assumption, were modified by Chen (1969) to give better accuracy

$$E = \frac{0.978\ T_m^2}{\delta} \quad \text{(first order)} \qquad (6.19)$$

$$E = \frac{1.706\ T_m^2}{\delta} \quad \text{(second order)} \qquad (6.20)$$

Halperin and Braner (1960) defined a symmetry factor U_g given by

$$U_g = \frac{T_2 - T_m}{T_m - T_1} \qquad (6.21)$$

This factor can be a very useful parameter when deciding on the type of kinetics involved. They decided that for first order kinetics one has

$$U_g \lesssim \left(\frac{1 + 2k\ T_m/E}{e}\right) \qquad (6.22)$$

whereas for second order kinetics one has

$$U_g \gtrsim \left(\frac{1 + 2k\ T_m/E}{2}\right) \qquad (6.23)$$

Once the type of kinetics for a given peak is known, an estimate of the activation energy can be estimated by Chen's equations (Equations (6.19) and (6.20)).

One should point out that many other methods have been suggested for the determination of the type of kinetics involved. Several good review papers have appeared in the literature, including Chen, 1969; 1976 and Shalgaonkar and Narlikar, 1972.

Some researchers use computerized best-fit routines in order to determine the kinetic parameters for a given glow peak (see for example, Fairchild *et al*, 1974; Levy, 1978; McKeever, 1980). McKeever described a procedure in which a theoretical glow peak is computed for initially assumed values of E,s and n, using the appropriate kinetic intensity equation. The computed glow peak is then compared to the experimental glow peak and the values of E,s and n are sequentially varied until a "best-fit" between the two is obtained.

From the discussion given we see that one of the most useful results which can be obtained from TL glow curves is the determination for each peak of the kinetic parameters: activation energy, attempt-to-escape frequency factor and trapped charge concentration. However, one has to be extremely careful in selecting the raw glow curve data as the measured glow peak intensity must be strictly proportional to the number of kinetic processes occurring per unit time. This is a requirement upon which both the first and second order intensity equations were derived and one which is often ignored by researchers when calculating kinetic parameters (see for example, Levy *et al* 1971; Levy, 1978). Levy points out that in many instances a curve of photo-tube current versus temperature, which shall be referred to as the 2-D glow curve, is not proportional to the number of photons emitted per unit time. Thus, the kinetic parameters obtained by analyzing 2-D glow

curves may well be incorrect or meaningless. In order to add understanding regarding this important point, Levy considered some of the possibilities which exists when studying the rather complex 2-D TL glow curves produced by certain minerals. It is, for example, possible that one has a particular emission centre contributing to a given glow peak while two or more centres contribute to another glow peak, with each of the emission centres present having their own characteristic emission spectrum. This difference in the contribution of emission centres to glow peaks would not be apparent by analyzing a conventional 2-D glow curve. Levy also points out the fact that the phototube sensitivity changes somewhat with wavelength which means that, when more than one emission centre is involved with a particular glow curve, the measured relative light intensities of the various peaks would be incorrect. The information extracted from a 2-D glow curve would only be suitable for kinetic analysis if all the glow peaks arise from a single emission centre, that is, the glow curve obtained is measured at close to a constant wavelength. When more than one emission centre is operative for a given TL exhibiting mineral, then the information which is required in place of the 2-D glow curve is the wavelength emission spectrum, corrected for instrumental reponse, as a function of the temperature; this will be referred to as a 3-D glow curve. The single glow peaks obtained as a function of both temperature and wavelength would, after the appropriate corrections, be entirely suitable for kinetic analysis.

6.3 Some Relevant TL Characteristics

This Section describes briefly some of the more important TL characteristics which may contribute to errors and uncertainties in the application of the TL dating method. It is by no means intended to be a comprehensive or detailed treatment, but rather a means of obtaining an insight to some of the more important problems involved with the method.

6.3.1 The Plateau Test - Kinetic Models

In the previous Section it was shown that the lifetime of charge carriers in traps of different depths, at ambient temperature, can vary over many orders of magnitude. Some of the shallow traps experiencing drainage of part or all of their stored TL, even over archaeological time, thus making them quite unsuitable for normal dating purposes. When dealing with a mixture of unidentified minerals, as is often the case in the fine-grain technique, it is necessary to check whether the peaks of interest exhibit any thermal fading. This can conveniently be done by means of the "plateau" test (see for example, Aitken *et al*, 1963). In this test the shape of the natural TL (TLN) glow curve is compared with that of a corresponding radiation induced (TLA) glow curve; a plot is done of the ratio of light outputs against glow curve temperature. The principle is illustrated in Figure 6.5 where some typical natural and artificial glow curves for fine grains extracted from pottery are compared. The ratio is effectively zero below about 250°C but at higher temperatures the ratio rises and quickly reaches a constant level, the onset of the plateau usually occurs at about 350°C. The presence of the plateau

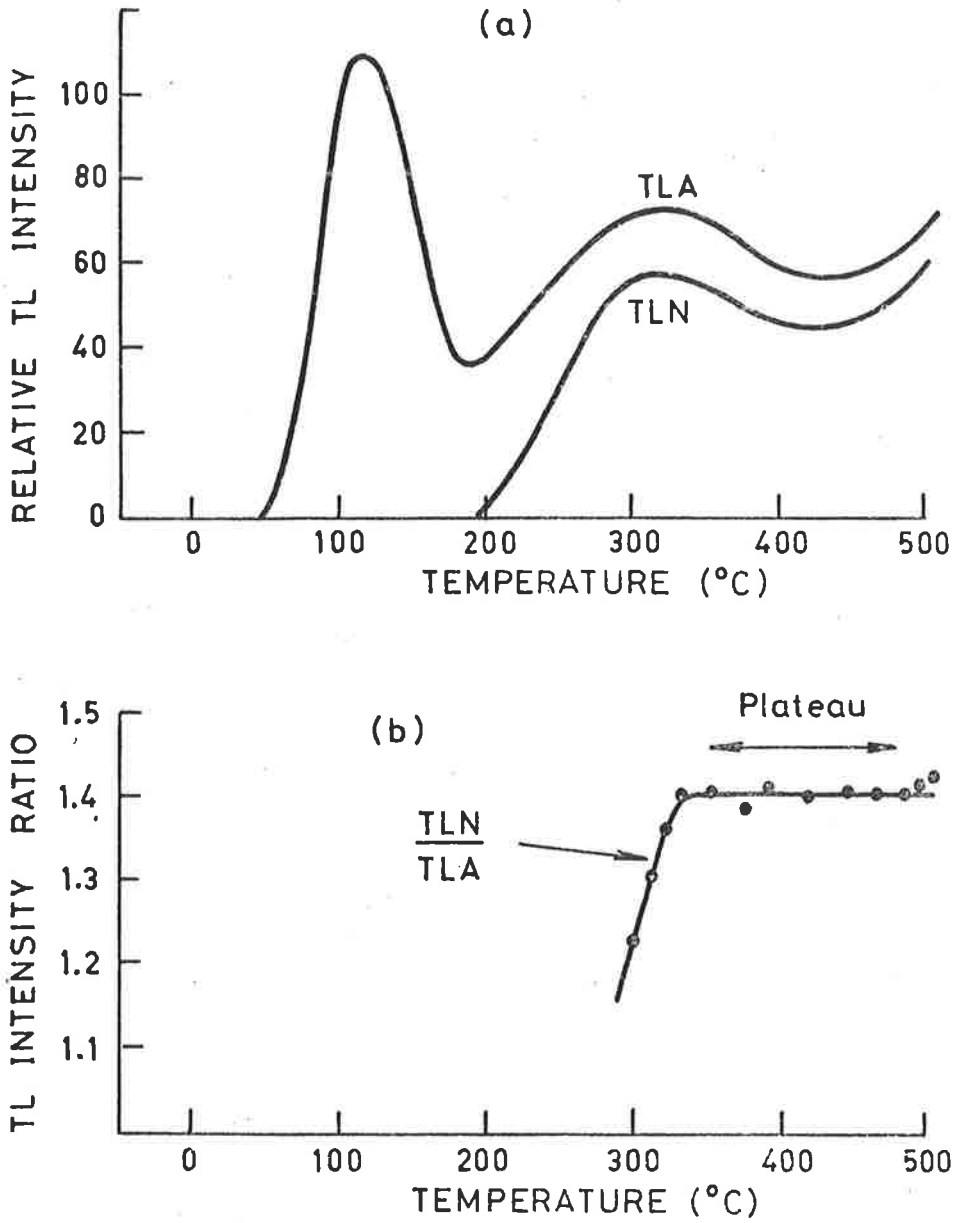

Figure 6.5

(a) Typical glow curves for fine-grains extracted from pottery : curve labelled TLN is the natural TL and the curve labelled TLA is the artificial TL.

(b) "Plateau" test of TL storage stability over archaeological time; the value at each temperature equals TLN/TLA.

indicates the absence of thermal fading of the TL emitted in this plateau region, that is, the corresponding traps are stable in this region. In practice it has been found that a plot of the ratio TLN/TLA as a function of temperature sometimes produce poor plateaux, or even fails to produce a plateau at all. One of the reasons for this is a change in the TL sensitivity induced in a sample which has already been heated prior to being given an artificial radiation dose; this phenomenon and some of the other reasons will be discussed in more detail in Section 6.3.5. To get around this problem the procedure most commonly used is to artificially irradiate a second, previously undrained, portion of the sample. A glow curve corresponding to the artificial plus natural TL (TL(A + N)) is then recorded. The plateau test is then carried out by plotting the ratio TLN/(TL(A + N) - TLN) against glow curve temperature (see for example, Aitken and Fleming, 1972).

In the previous Section, it was seen that a TL peak exhibiting purely first order kinetics will always appear at the same temperature irrespective of the dose delivered to the sample, whereas a peak governed by second order kinetics would shift to lower temperatures as the dose is increased. This phenomenon is clearly very relevant as far as the plateau test is concerned, as peaks exhibiting non-first order kinetics may not produce a good plateau. If only a single peak is involved than one can make appropriate allowances by simply shifting the peak; this may, however, not be possible when one is dealing with a number of peaks of unknown kinetics. This important phenomenon has been discussed by McKeever (1979) who

produced graphical examples illustrating this point. McKeever concluded that for glow curves in which some of the high temperature peaks exhibit non-first order kinetics, a good plateau is only obtained if the artificial dose is close to the natural dose. Recent work by Sunta and Kathuria (1978) suggests that in some minerals, including quartz, the order of kinetics of the given peaks depends on the dose delivered to the sample. This change of kinetics as a function of dose delivered has not been suggested previously. If this phenomena does actually occur it is essential that the artificial dose is close to the natural dose when doing the plateau test.

Although Sunta and Kathuria suggests that the glow peaks of quartz do not always exhibit first order kinetics, it is the general consensus of other researchers that both the 325°C and 375°C peaks exhibit close to first order kinetics (see for example, Aitken and Fleming, 1972; Levy, 1978). This is very fortunate as quartz is probably the most commonly used mineral in TL dating. When studying a combination of various TL emitting minerals, as is the case in the fine grain method, the situation is not always this simple. By studying the cathodoluminescence of about 200 fine grains, extracted from ceramics, Singhvi and Zimmerman (1978) found that about 45% of the grains were quartz, 36% K-feldspar, 15% plagioclase, 4% apatite and less than 1% were zircon; it is quite plausible that some of these minerals exhibit non-first order kinetics. Not much has been published on the

kinetics of feldspars, although Levy (1978) found that the mineral albite exhibits second order kinetics which tends to suggest that perhaps other feldspars may also follow second order kinetics.

6.3.2 Spurious TL

One of the more serious problems associated with taking TL glow curve measurements is the appearance of non-radiation-induced TL ("spurious TL"). Early researchers in the TL dating field (see for example, Tite and Waine, 1962) found that the radiation induced TL of archaeological samples (natural and artificial) was usually accompanied by a large proportion of spurious TL, predominantly occuring in the temperature region above 300° C. Aitken *et al* (1963) found that the magnitude of this spurious component was extremely variable from one sample to another, as well as from one measurement to the next, thus making it impossible to correct for it by simple subtraction. Aitken *et al* found that by surrounding the sample with an inert atmosphere of oxygen-free nitrogen, while the glow curve was being taken, the spurious component is dramatically reduced. Spurious TL had been reported prior to 1962, mainly in relation to TL studies of phosphors and geological minerals (see for example, Grögler and Stauffer, 1959; Schulman *et al*, 1960); however, because of the rather low light levels involved with archaeological TL it became important to find a cure.

Various experimental studies (see for example, Aitken

et al, 1967; 1968; Nash *et al*, 1967; Svarcer and Fowler, 1967; Bettinali and Ferraresso, 1968; Lewis, 1968) have established the broad phenomenological features of spurious TL, although the mechanisms involved still remain poorly understood. The various types of spurious TL encountered have been discussed in the literature (see for example, Aitken, 1968); these include spurious TL induced by pressure ("piezo-TL"), friction ("tribo-TL"), gas adsorption, as well as by chemical changes ("chemi-TL"). The existence of spurious TL resulting from gas adsorption on grain surfaces was first shown by Grögler and Stauffer as early as 1959. Since then it has been demonstrated by many other researchers including Bettinali and Ferraresso (1968) who studied adsorption TL of calcium carbonate. Lewis (1968) has demonstrated the effect of grinding on spurious TL for the minerals dolomite, calcite and halite. The majority of the above mentioned spurious TL producing effects are surface phenomenon, which is consistent with the fact that the observed spurious signals are generally much stronger in fine grains rather than in coarse grain samples.

Much effort has been devoted to ways of reducing, or even eliminating, the spurious TL component from a measured glow curve (see for example, Aitken *et al*, 1968; Aitken and Fleming, 1972; Sutton and Zimmerman, 1977; Debenham, 1978; Huxtable, 1978; Jensen and Prescott, 1979). Although the mechanisms involved are still not well understood, it has been possibly to drastically reduce the spurious TL component in a large range of fine grain samples. It is now the common view among TL researchers that in the majority of cases the spurious component arises from the presence of oxygen and water vapour in the ambient gas. In working on fine grains, extracted from pottery samples, Aitken and

Fleming (1972) found it necessary to flush the glow oven with nitrogen gas, having less than 5 ppm oxygen present, at a continual flow rate during heating of about 5 litres/min. They deduced that it was not enough to surround the sample with a static atmosphere of high purity nitrogen; presumably due to the desorption of oxygen from the sample grains as they are heated.

The fact that the spurious TL component varies unpredictably from one glow to the next and the fact that it predominates in the temperature region above 300°C, makes the plateau test mentioned in the previous Section very suitable for its detection. If a plateau exists, to within a few percent accuracy, then one can generally assume that the spurious TL component is negligible. The only problem with using the plateau test, as a criteria for the existence of spurious TL, is that failure to produce a plateau does not necessarily mean that the spurious TL component is significant (see Section 6.3.1).

Experience has shown that spurious TL is predominantly observed on very fine grain samples, this is the basic reason for rejecting the less than 1 μm diameter grain size fraction in the fine grain method. Huxtable (1978) has also found that fine grain samples in which calcium carbonate is present, which includes hearth stones and limestone, are usually the most troublesome; although the effect can be drastically reduced by washing the fine grains in 5% calgon and/or dilute acetic acid prior to measurement. A suitable fine grain sample preparation method has been outlined by Fleming (1979).

It is now generally accepted that the quenching of the spurious signal by controlling the environment of the sample during

heating is mainly due to the removal of oxygen and water vapour, rather than some active effect by the inert gas. An experiment has, however, been carried out on the use of chemically reducing atmospheres as a means of reducing the spurious TL (Jensen and Prescott, 1979). It was demonstrated that a nitrogen gas with about 5% hydrogen present (less than 10 ppm oxygen, less than 25 ppm moisture) was slightly better in reducing spurious TL than was a high purity argon gas (less than 6 ppm oxygen, 12 ppm moisture). Further investigations suggested that at times an even higher purity gas is required. We presently use a high purity nitrogen mixture which the manufacturers (Commonwealth Industrial Gases, Adelaide) claims has less than 2 ppm oxygen and less than 1 ppm moisture present.

However, on some of the fine grain samples encountered, efforts to eliminate the spurious TL component have been fruitless; this of course means that the fine grain method cannot be employed on these samples. On such troublesome samples it may well be that the spurious TL can be eliminated, or at least separated, by measurement of the wavelength emission spectrum (3-D) rather than the conventional 2-D glow curve; there is certainly no reason to suggest that the spurious TL emission spectrum is related to the true TL emission spectrum. Very little research has been done on the colour of spurious TL; although Fleming (1968a) obtained some broad characteristics by measurements on dosimeter phosphors. His studies showed that for the phosphors, LiF (TLD-100), CaF_2 (MBLE, natural fluorite) and CaF_2:Mn, the majority of the spurious TL (which he attributed to tribo-TL) was for all of the three phosphors in the wavelength region above 400 nm, predominating even more so above 500 nm; whereas the only phosphor to

exhibit radiation induced TL in this wavelength region was CaF_2:Mn. Both LiF(TLD-100) and CaF_2(MBLE) exhibited radiation induced TL in the wavelength region below about 450 nm. Also studied by Fleming was the spurious TL emission spectrum from fine grains extracted from a terracotta clay sample (with quartz present as the predominant TL mineral). He observed that, on this rather typical archaeological sample, the spurious TL emission spectrum was much the same as that measured on the phosphors.

Fleming's measurements confirm the opinion that by measuring wavelength emission spectra one may well be able to recognize the spurious TL component and hence eliminate it. Worthwhile discrimination against spurious TL can also be obtained by the use of appropriate colour filters (see for example, Aitken and Fleming, 1972; Fleming, 1979).

6.3.3 Anomalous Fading

We have already seen that the expected lifetimes of trapped charges corresponding to glow peaks above 300°C are of the order of 10^5 years or more (Section 6.2). Wintle (1971, 1973) has however, found that for certain minerals these traps are not as stable as expected from purely kinetic considerations. On the minerals fluorapatite and labradorite she observed a reduction of TL in the 300-400°C temperature region of about 40% within 15 hours after irradiation. This type of loss was appropriately termed "anomalous fading". Other minerals found to exhibit this anomalous phenomenon included sanidine, andensine, bytownite and zircon. Fortunately, Wintle found that the high temperature peaks of quartz and calcite did not

show any significant TL loss over periods of 2 years and 2 months respectively.

Although extensive studies have been carried out on the various minerals exhibiting anomalous fading (see for example, Wintle 1974; Whittle and Arnaud, 1975; Wintle, 1978; Sutton and Zimmerman, 1978a; Singhvi and Zimmerman, 1979; Singhvi, 1981), no satisfactory way of eliminating it has been found. On studies of recent volcanic lava, Wintle (1974) found that even samples that passed the plateau test exhibited significant anomalous fading. Wintle also found that on the minerals studied there was a rapid initial fading, in the first few hours, followed by a much slower loss of TL with time.

Presently there seems no better way of detecting anomalous fading than by long term storage tests. Such tests, ranging from a few hours to 2 months storage, have been employed by several researchers including Whittle and Arnaud (1975) and Huxtable *et al* (1976).

6.3.4 Optical Bleaching and Light-Induced TL

The exposure of a sample containing stored TL to a source of light may reduce the stored TL of the sample (Aitken *et al*, 1963); this phenomenon is usually referred to as optical bleaching. Alternatively, exposure to light may increase the measured TL signal, often producing a glow curve shape markedly different to the normal glow curve shape. Both of these effects have been found to be more predominant with light of short wavelengths (Aitken *et al*, 1963; Schayes *et al*, 1967). However, neither of these phenomena presents

serious problems in routine TL measurements, as long as all sample preparation and handling is conducted under subdued red light (Aitken and Fleming, 1972). As far as the sample preparation techniques are concerned it is routine procedure to remove the outer layer of a sample prior to the extraction of the quartz or fine grains. The removal of this outer layer of the sample is not only done in order to avoid the portion which may have been subjected to daylight, but also to avoid any significant beta dosage from the surrounding soil. This procedure works well on opaque samples such as pottery, but is of no use on transparent or translucent materials such as glass, quartz and flint. On such samples precautions taken when excavating the samples may not even be sufficient as a substantial amount of light induced TL may have occurred before burial.

Sutton and Zimmerman (1978b) proposed the use of filters to remove blue and UV on white fluorescent tubes for laboratory lighting rather than using subdued red light. This creates an illumination which more closely approximates normal white lighting, hence creating a more comfortable working environment. In our TL measurement laboratories we also use filters on white fluorescent tubes, although the filter used has superior transmission characteristics to that described by Sutton and Zimmerman (Jensen and Barbetti, 1979). The transmission characteristics of two suitable filters (manufactured by Rank Strand Electric, P.O. Box 70, Great West Road, Brentford Middlesex TW8 9 HR, U.K., and distributed worldwide) are shown in Figure 6.6. We use "Cinemoid" number 1 (yellow) with a minimum of two thicknesses wrapped around each white fluorescent tube, the ends of which are sealed with black plastic sheet and adhesive tape. Also shown in Figure 6.6 is

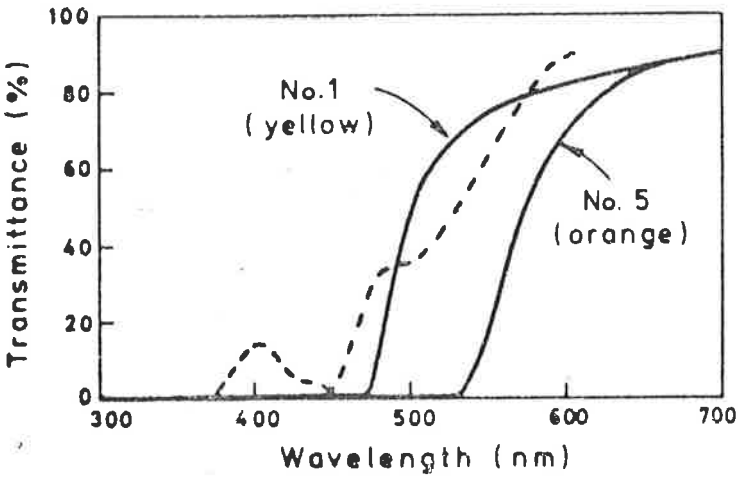

Figure 6.6 Transmission Spectra of Filters for Laboratory Illumination.

The spectra shown corresponds to the light transmission through single thicknesses of "Cinemoid" No. 1 and No. 5 colour filters (measured on Perkin Elmer and Pye Unicam Spectrophotometers, Dept. of Physical and Inorganic Chemistry, Adelaide University).

Transmittance between 350 nm and the cut-off value (475 nm for No. 1, 530 nm for No. 5) is less than 0.5%.

The dashed line is the amber filter described by Sutton and Zimmerman (1978b). Photons with wavelengths shorter than about 300 nm are not transmitted through the glass in fluorescent tubes.

the transmission characteristics of the filter described by Sutton and Zimmerman.

A significant amount of research has been done on the possible mechanisms for light induced TL (see for example, Schayes *et al*, 1967; Bailiff, 1976; Bailiff *et al*, 1977; Bowman, 1978; Sasidharan *et al*, 1978b). The generally accepted model is that proposed by Schayes *et al*. According to them, the effect of exposure to UV light is to transfer charge carriers from deep traps (referred to as "donors") into shallower traps ("acceptors"). This model certainly makes it possible for peaks from above 500°C, which is the usual maximum glow temperature, to appear below 500°C, after having subjected the sample to UV illumination. These donor traps are generally stable over archaeological time (see Section 6.2) and hence the corresponding photo-transferred peaks may well be suitable for age determinations. Bailiff *et al* (1977) found the photo-transfer technique to be suitable on the mineral quartz, in which the traps responsible for the 325°C and 375°C peaks act as donors and the more sensitive 110°C peak as the acceptor (see also Fleming, 1979). Extensive studies have also been made on the phosphor CaF_2 (MBLE) (see for example, Schayes *et al*, 1967; Okuno and Watanabe, 1972; Bailiff, 1976). Photo-transfer TL studies have also been carried out on minerals exhibiting anomalous fading. Transfer measurements carried out on samples of zircon and fluorapatite (Bailiff, 1976) indicate that anomalous fading of the donor peaks was appreciably less than that observed on conventional peaks in the 300-500°C temperature region (see also Zimmerman, 1978).

6.3.5 Supralinearity and Sensitivity Change

Up to this point it has been assumed that the TL response increases linearly with radiation dose. However, in most of the minerals studied this has been found to be only approximately true (see for example, Tite, 1966; Fleming, 1970; Thompson, 1970). Figure 6.7 shows the initial part of a typical TL growth curve as a function of beta dose. The non-linear behaviour at doses below about 300 rads is termed "supralinearity", since the response increases more rapidly than linear. From Figure 6.7, one observes that the form of a typical growth curve is such that a linear response to beta radiation is observed for TL caused by additional dosage above that corresponding to the archaeological dosage (natural TL). The obvious way around this effect would appear to plot out the growth curve of each sample after the natural TL has been drained by heating to 500°C. From this purely "artificially' induced growth curve it should then be possible to determine the correct dose received by the sample in archaeological time. However, Tite (1966) found that the TL drainage of some samples of pottery caused a significant change in TL sensitivity. This phenomenon is diagrammatically illustrated in Figures 6.8(a) and (b). This may either be associated with a transparency change associated with mineralogical alterations brought about by heating the sample, or to more fundamental effects arising from the magnitude of the radiation dose received before heating (commonly referred to as "pre-dose sensitization"). Both supralinearity and pre-dose sensitization are exhibited by some of the dosimetry phosphors including LiF (TLD-100) (Cameron *et al*, 1964), and $Li_2B_4O_7$:Mn (Schulman *et al*, 1967), however,

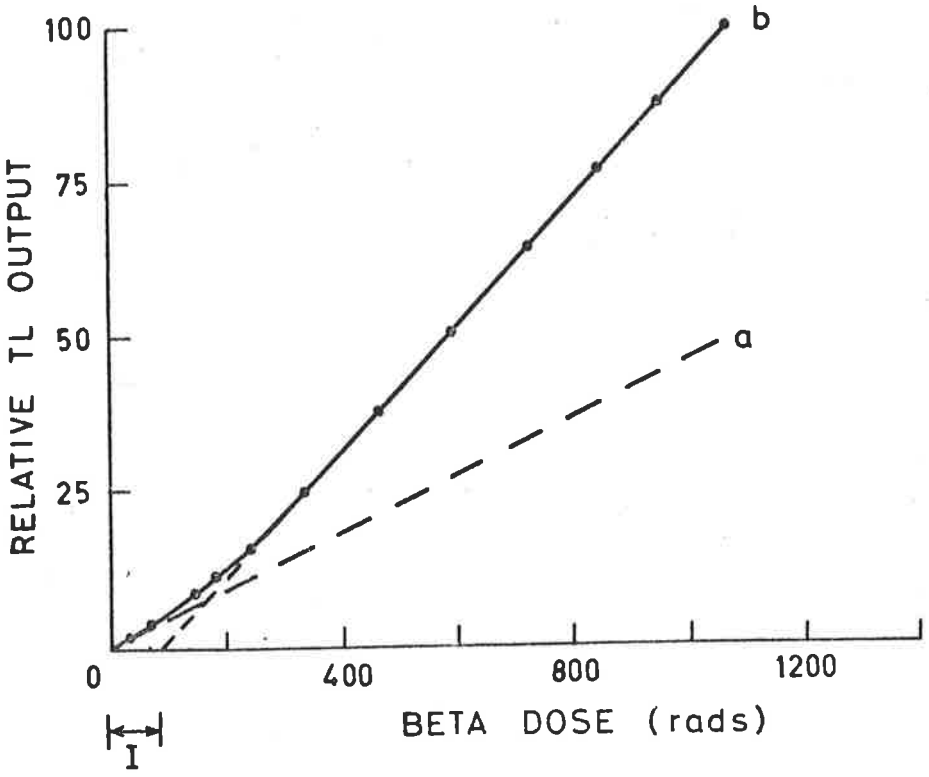

Figure 6.7 Typical TL-Growth Curve as a Function of Beta-Dose.

In this example the low dose sensitivity (curve a) is only about half the sensitivity exhibited beyond the limit of initial curvature.

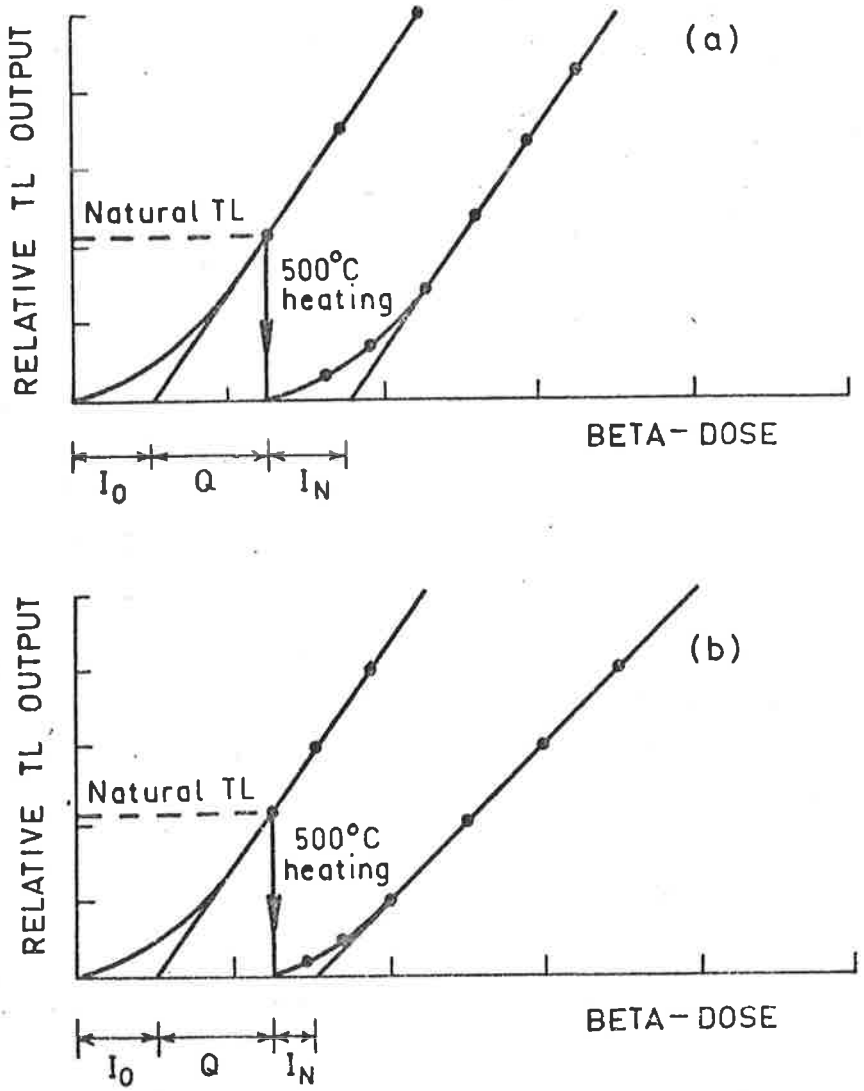

Figure 6.8

(a) High temperature TL where the sensitivity and dose-intercept remains unchanged on reheating after drainage.

(b) High temperature TL where both the sensitivity and dose-intercept is changed on reheating after drainage.

NOTE: One sometimes observes a sensitivity change (change of slope) without changing the dose-intercept (and vice-versa).

they do not present serious problems because of the availability of un-irradiated material for the establishment of a reference growth curve (Aitken and Fleming, 1972). One possible method of avoiding errors due to sensitivity change has been outlined by Aitken and Fleming, (1972). They suggest the use of three identical samples, one of which is measured without further dosage to obtain the natural TL, the other two are then given different doses of beta radiation and their natural plus induced TL individually measured. This "additive" procedure is illustrated in Figure 6.9. By using this procedure one does not avoid error due to supralinearity; however, as long as the level of the natural TL is well above the supralinear portion this error is not too serious. The magnitude of the supralinearity effect is then estimated by assuming that, although there may be a sensitivity change upon heating, the dose intercept I is left unaltered. Significant work has been done, on the accuracy of the additive procedure. Thompson (1970) found this assumption to be true for the clay-forming minerals that she studied, the addition of the intercept (I) gave more accurate TL dates for pottery fragments of known archaeological age (this corresponds to $I_0 = I_N$ in Figure 6.8(b)). Fleming (1975, 1979) mentions that he has also encountered samples in which no sensitivity change was observed, although the dose-intercept was altered. By evaluating a dose-intercept after adding a beta dose (B) on top of the natural dose (N), he found that generally I_{N+B} was less than I_N. Fleming (1975) suggests a way of correcting for this based on a linear connection between the change in supralinearity and radiation dose yields. However, the supralinearity correction, derived by studying the TL sensitive minerals of pottery fragments (fine-grain method), remains an empirical one (Aitken and Fleming, 1972).

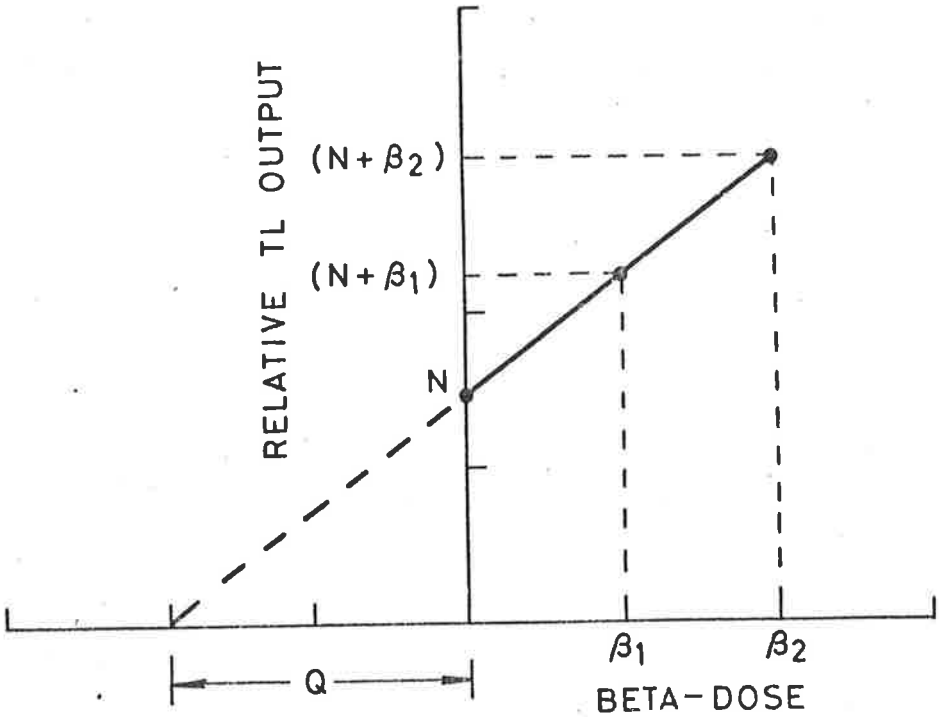

Figure 6.9 The "Additive" Procedure for determining the Linearly Extrapolated Dose Q

Graph of high temperature TL from an un-irradiated sample (N) and two identical samples given different beta doses (β_1 and β_2), extrapolated to zero TL to give Q. The response demonstrates the linear behaviour of TL above the natural, but cannot detect any non-linearity below the natural level.

For the quartz includion technique the correction for supra-linearity is on much firmer ground. Studies by Fleming (1968b, 1970 1975, 1979) shows that the 375° C ("benign") peak growth curve is not usually altered by drainage whereas the 325° C ("malign") peak growth curve is. The growth curve for the malign peak is generally, but not always, found to change both in slope and intercept after drainage. Occasionally the 375° C peak growth curve changes sensitivity after drainage, although the dose intercept remains the same. Usually both peaks contribute to the TL and it is necessary to determine at what temperature the contribution of the malign peak ceases to be important and to utilize only the glow curve above that temperature. Fleming (1979) suggests an approach which includes the measurement of glow curves corresponding to different beta doses. The benign temperature region then corresponds to the temperature range in which a dose-plateau is observed. In the extreme cases, where the 325° C tail is so far up the temperature axis that accurate measurements are spoilt by high background of incandescence, Fleming suggests the use of selective bleaching of the 325° C traps using UV light (see also Section 6.3.4).

The supralinearity phenomenon just described appears only at low beta doses. From a purely kinetic point of view one expects the growth curves to level off as all of the traps available become filled (saturation). This typically commences at about 10 krad for fine grains extracted from pottery (Tite, 1966), and at about 2 krad for quartz inclusions (Fleming, 1968b). However, in neither case does the measured growth curve completely level off. This is generally

attributed to radiation damage within the crystal structure creating defects which then can form additional TL trapping centres.

6.4 Conclusion

Among useful results that can be obtained from a glow curve is the determination for each peak of the kinetic parameters: activation energy, pre-exponential factor and trapped charge concentration. Ordinary glow curves are however, not always suitable for kinetic studies unless it can be demonstrated that the measured phototube current is proportional to the number of processes occurring per unit time. This is a requirement upon which both the first and second order kinetic theories have been derived and one which is often ignored by researchers when calculating kinetic parameters on a particular glow peak.

As far as TL dating on archaeological samples is concerned, it is apparent that it would often be advantageous to have a better understanding of the actual TL processes involved. Some of the problems include spurious-TL, anomalous fading, optical bleaching, light induced TL, supralinearity in the acquisition of TL at low levels of radiation and a change in the TL sensitivity after the archaeological TL has been removed by heating. One would hope that the availability of 3-D glow curves on archaeological samples would enable us to tackle some of these problems which must be solved before the accuracy of the dating method can be further improved.

CHAPTER VII

SENSITIVITY OF SPECTRAL TL INSTRUMENTS

7.1 Previously Constructed Spectral TL Instruments

Several instruments have so far been designed and constructed for the purpose of studying TL emission spectra. The majority of these are rapid scanning prism or grating monochromator type instruments (see for example, Halperin and Kristianpoller, 1958; Oltman *et al* 1968; Harris and Jackson 1970 and Mattern *et al* 1971). Other instruments have been constructed (see for example, Reynolds and Gruner, 1975; Tomita *et al* 1976; 1978; and Spurny and Hruska, 1976) but most of them resemble the monochromator type instruments. While such spectrometers are suitable for spectral studies of TL dosimetry phosphors, they lack the sensitivity needed for archaeological TL by at least two or three orders of magnitude. On these instruments, if spectral information is sought, it is necessary to subject the sample to relatively high doses of radiation prior to measurement. However, it is quite possible for the spectral glow-curve characteristics to change somewhat depending on the dose delivered to the sample (Bailiff, 1978). It is hence preferable to obtain the spectral information from the archaeological dose delivered to the sample rather than from a large laboratory dose.

Figure 7.1 shows some typical radiation induced TL emission spectra of a natural quartz sample obtained by the monochromator type instrument described by Mattern *et al* (1971). The plots are from Levy

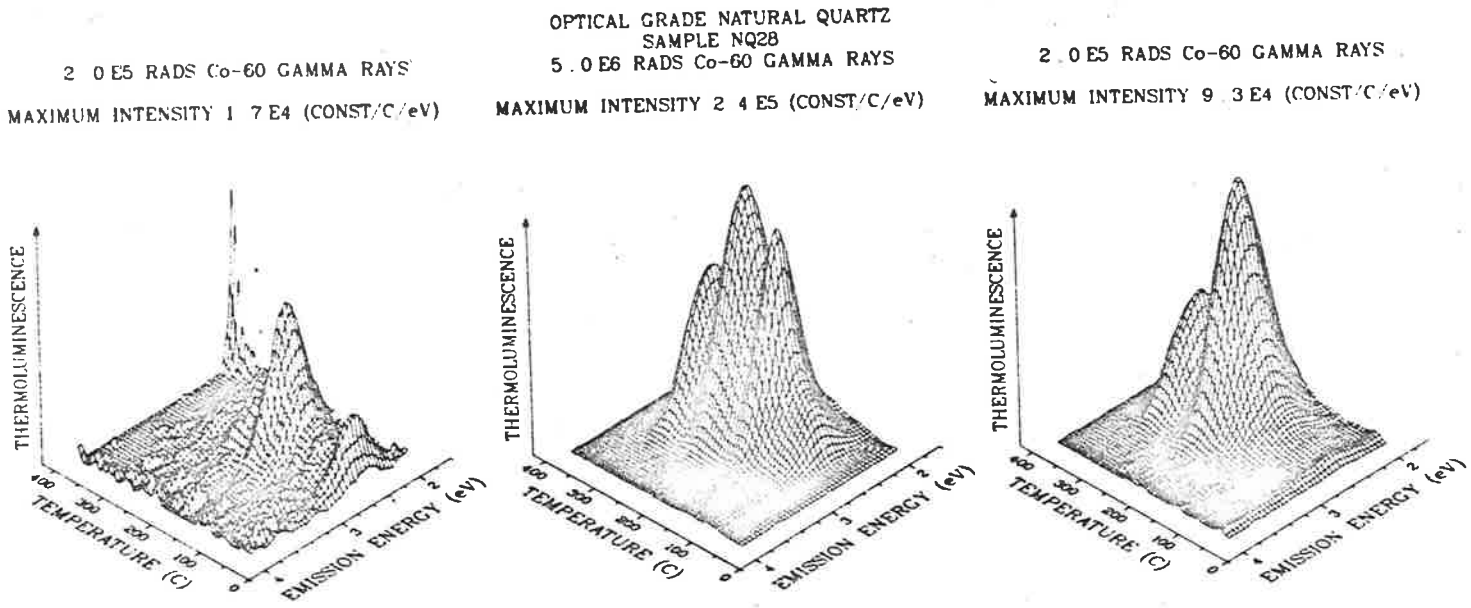

Figure 7.1 Some typical Radiation-Induced TL Emission Spectra of a Natural Quartz Sample obtained after successive ^{60}Co irradiations of 2×10^5 R, 5×10^6 R and 2×10^5 R. (from Levy, 1978).

(1978) (see also Fuller and Levy, 1977; 1978). These spectra are computer prepared 3-D plots showing the TL intensity as a function of both temperature and wavelength. In this particular case the quartz sample (Brazilian "vug" quartz) had been subjected to successive ^{60}Co irradiations above 10^5 R. Levy (1978) states the emission from quartz crystals exposed to smaller doses is usually too low in intensity to be studied conveniently using that particular instrument. One of the few instruments which were designed especially for the detection of TL emission spectra for archaeological samples is that of Bailiff *et al* (1977). They employ a rapid scanning interference filter spectrometer. Since this is probably the most efficient instrument previously constructed it is appropriate to consider its design in some detail. Figure 7.2 is a schematic diagram of the optical and mechanical parts of the Bailiff spectrometer. The instrument consists of 16 interference filters mounted on the periphery of an aluminium disc which is then rotated at a constant speed of about 8 rev s^{-1}. Each of the filters transmits a wavelength band of approximately 20 nm and the total wavelength coverage is usually chosen to be 340 - 640 nm. The optical arrangement of the spectrometer is very simple. Light emitted from a 10 mm diameter sample disc is collimated on to one of the filters by a 12 mm diameter $f/2$ lens (F_2); the filtered light is then focussed by a 25 mm diameter $f/1$ lens combination on to the photocathode of an RCA gallium arsenide photomultiplier. The scanning interval is kept short at 125 ms with the counting time for each filter being about 6 ms. If one neglects the reflection losses then the overall efficiency of the Bailiff spectrometer system is given by the relation

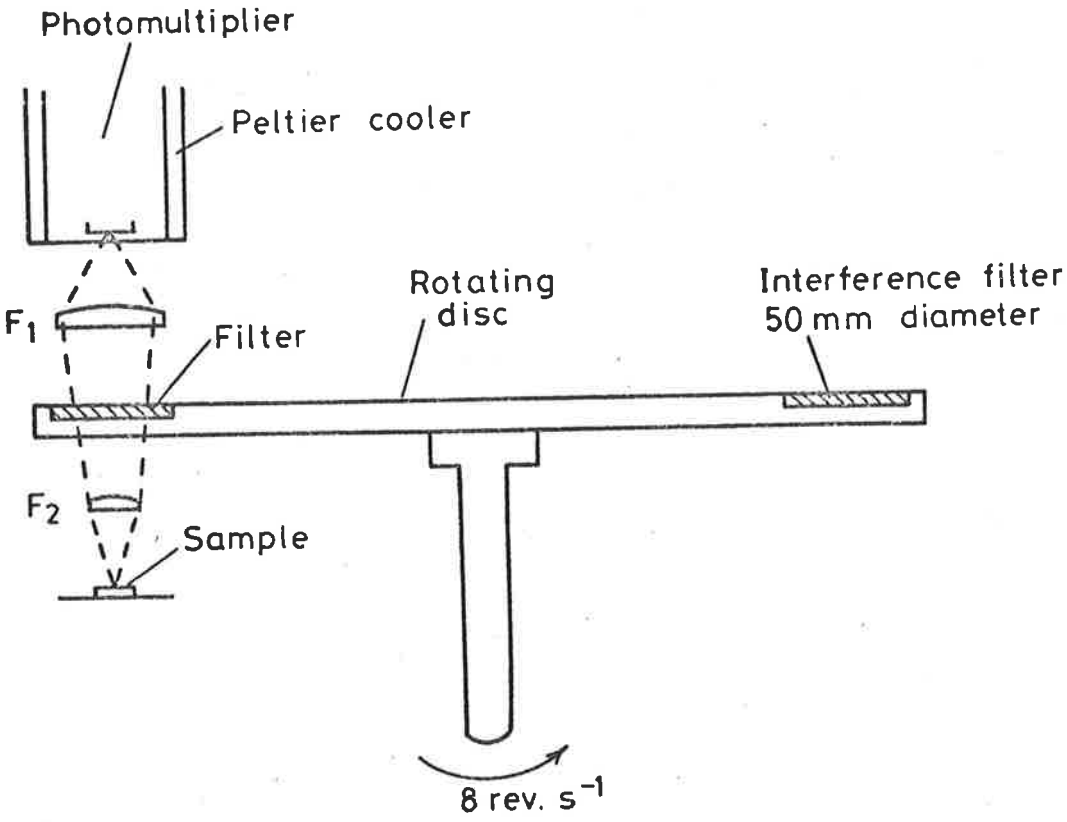

Figure 7.2 Schematic Diagram of the Optical and Mechanical Parts of the Bailiff Spectrometer.

$$E_B = K_1 K_2 K_3 K_4 K_5 \qquad (7.1)$$

where K_1 is the fraction of solid angle subtended by F_2 ($f/2$ optics), K_2 is the transmission coefficient of the filters (~ 30%), K_3 is the fraction of solid angle subtended by F_1 ($f/1$ optics), K_4 is the photocathode quantum efficiency (~ 20%) and K_5 is the scanning time efficienty. This gives a theoretical efficienty of about 1.1×10^{-5} which agrees well with a measured value of about 10^{-5} (Bailiff *et al*, 1977).

7.2 Improving the Spectral TL Instrument Sensitivity : Discussion

One of the main reasons for the lack of sensitivity of previously constructed 3-D TL instruments is the fact that they are all rapid scanning wavelength instruments. In order to illustrate this point for the monochromator-type instruments, it is useful to consider the basic working principle of a monochromator. This is shown schematically in Figure 7.3, where the main components are : an entrance slit, w_1, of adjustable width; a collimator, M_1, which may be a mirror or a lens; a dispersing element, G, which may be a prism or a grating; a lens (or a mirror), M_2, used to focus the dispersed light; and an exit slit, w_2, also of adjustable width. Different wavelengths of light leave the prism at slightly different angles and the dispersed light is focussed on to the plane VR, so that each specific wavelength present produces an image of the entrance slit at some point along VR. Hence, the exit slit, w_2, only selects a small fraction of the wavelength spectrum at any one time. The smaller the wavelength fraction, the better the wavelength resolution. This wavelength fraction depends on the width of both the entrance and exit slits. The source spectrum can be recorded by rotating the dispersing

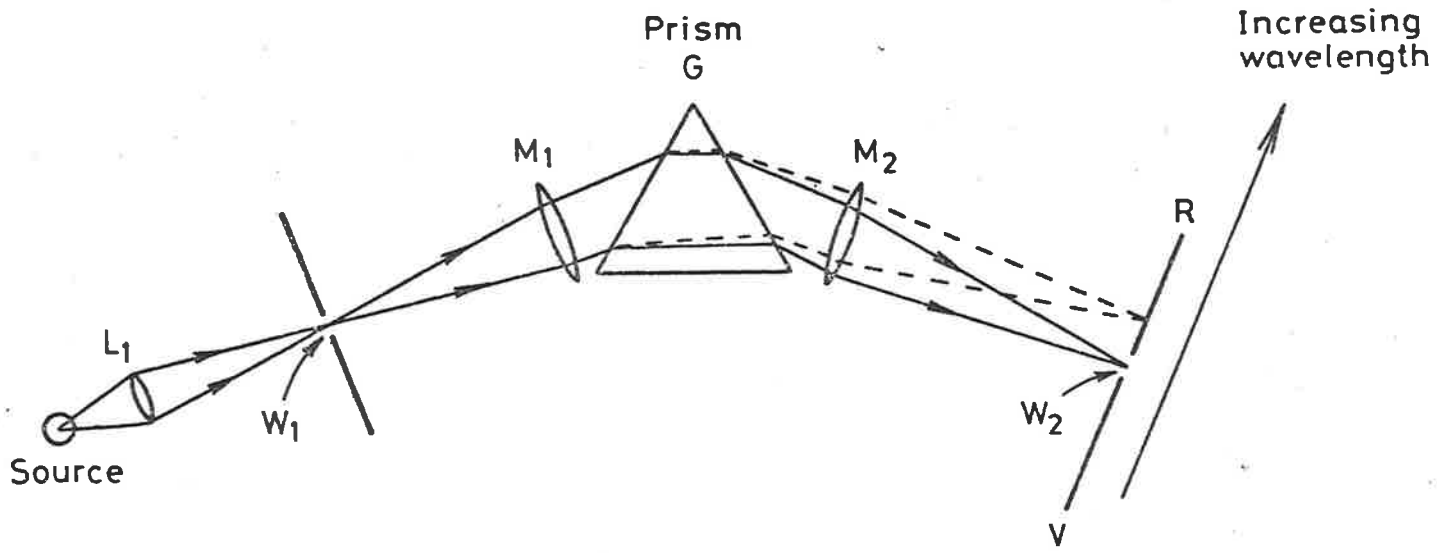

Figure 7.3 Optical Principles of a Monochromator.

element and by placing a detector in conjunction with suitable light collecting optics behind the exit slit.

The disadvantage of rapid wavelength scanning on the monochromator-type instruments could be overcome if, in the plane of the exit slit (VR), one substituted the exit slit with an array of detectors, such as light sensitive photodiodes. Such photodiode arrays are now commercially available (e.g. Reticon), and spectral instruments using these arrays are also available (e.g. Tracor Northern). The sensitivity advantage exploited here is clearly that of multiple wavelength detection. One should point out that the rapid scanning filter spectrometer mentioned in Section 7.1 (Figure 7.2) considers the spectral elements one at a time and hence does not exploit this advantage.

Another drawback of monochromator-type instruments, which leads to poor sensitivity, is the requirement of a narrow entrance slit (denoted by w_1 in Figure 7.3) which implies a small input solid angle. This is the main reason why the interference filter spectrometer is much more sensitive than the monochromator-type instruments. The interference filter accepts light from a 10 mm diameter source, via $f/2$ input optics, rather than via a narrow entrance slit.

This input deficiency of the monochromator-type instruments was first fully appreciated and investigated by Jacquinot (1954, 1958 and 1960). He proposed the use of interferometers in order to improve the throughput (as well as to utilize the phenomenon of multiple wavelength detection). In interferometry the principle of multiple

wavelength detection is generally referred to as the "multiplex advantage". This feature was first pointed out by Fellgett (1951, 1958) and hence is sometimes referred to as the "Fellgett advantage". It will be discussed in some detail in Section 8.2. The technique of interference spectroscopy, as conceived by Jacquinot and Fellgett, was first put to effective use in the study of atmospheric spectra in the infrared wavelength region (see for example, Connes, 1958; Gebbie, 1958; Connes and Gush, 1960). The device most commonly used for interference spectroscopy is the Michelson interferometer, the basic principles of which will be discussed in Section 7.3.

7.3 The Michelson Interferometer.

The first interferometer to be applied to any form of spectral analysis was the two-beam instrument that Michelson invented in 1882 (see for example, Michelson, 1891; 1892). A schematic diagram of the Michelson interferometer is shown in Figure 7.4(a). The basic optical principles are simple (see for example, Jenkins and White, 1976). The interferometer consists essentially of two plane mirrors M_1 and M_2 and a beamsplitter B. The mirrors are perpendicular to each other and one of the mirrors is movable. The beamsplitter B, which is a half-silvered mirror, splits each ray coming from an extended source into two perpendicular rays, one going toward M_1 and the other toward M_2. The two rays are reflected by M_1 and M_2 and as the latter is moved along the optical axis the resultant interference pattern can be observed with the naked eye at D. Many other variations of the Michelson interferometer have been developed in the last hundred years. Figure 7.4(b) is an optical

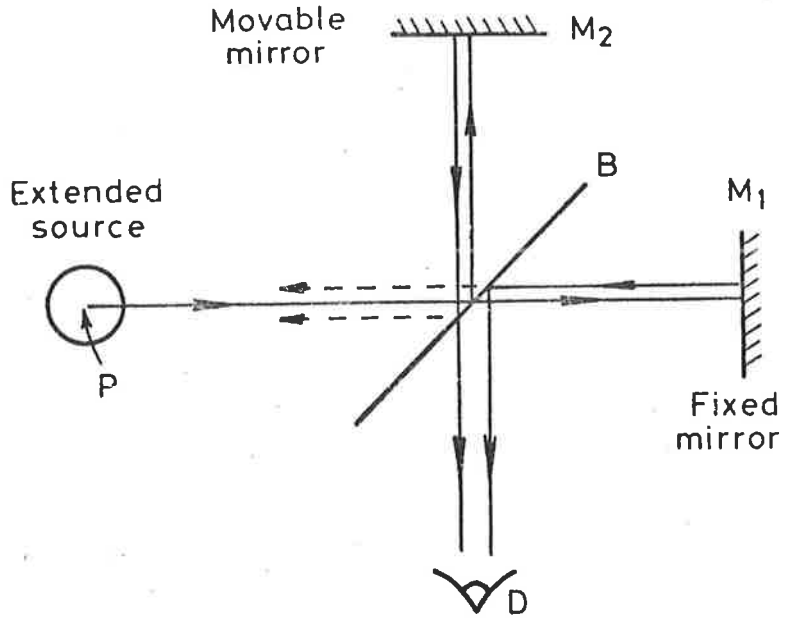

Figure 7.4(a) Optical System of the Interferometer originally constructed by Michelson in 1882.

The optical path of a particular ray originating at point P from an extended source is shown. The displacements of the beams are only for illustrative purposes.

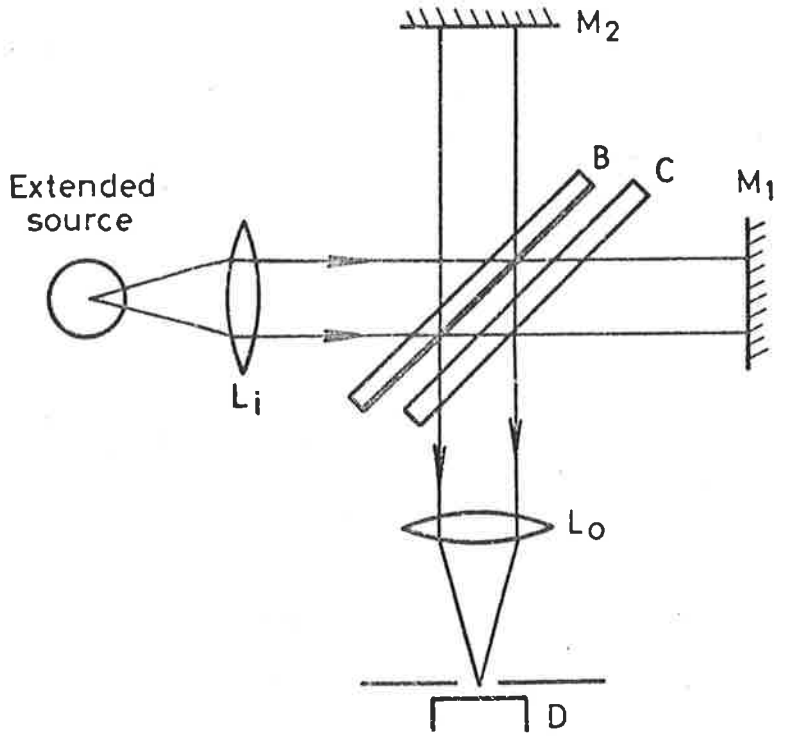

Figure 7.4(b) Optical System of a Michelson Interferometer which accepts collimated light.

For simplicity, the refraction of the light beams at the beamsplitter and compensator surfaces is not shown.

diagram of a Michelson type interferometer which accepts collimated light. In this diagram a compensating plate, C, has also been introduced in order to keep the optical paths in the two arms approximately the same. This compensating plate is only necessary if the interferometer is to be used with white light, as monochromatic fringes are visible even if it is removed. The interferometer schematically shown in Figure 7.4(b) is what today is commonly referred to as the Michelson Interferometer.

In order to understand the basic concepts of interference spectroscopy it is most convenient to consider the case of monochromatic light of wavelength λ_1(nm) as it passes through both arms of a Michelson interferometer. One can then determine the intensity of the resultant beam at the detector as a function of the different positions of the movable mirror. The optical path difference (OPD), x, or retardation, between the beams travelling to the mirrors M_1 and M_2 is given by

$$\text{OPD} \equiv x = 2(d_2 - d_1) \tag{7.6}$$

where d_2 denotes the position of the movable mirror, M_2, and d_1 denotes the position of the fixed mirror, M_1, relative to the beam splitting surface. At zero path difference (ZPD) the two beams are perfectly in phase and constructive interference results upon recombination at the beamsplitting surface; hence, the intensity observed at the detector is the sum of the contributions from each arm. If the mirror M_2 is moved a distance of $\lambda_1/4$ nm, the OPD becomes $\lambda_1/2$ which means that the two beams are 180 degrees out of phase and interfere destructively upon recombination, thus producing a minimum

in intensity at the detector. If the movable mirror is moved a further distance of $\lambda_1/4$ then the two beams are once again in phase and a maximum in intensity is again observed at the detector. The complete record of resultant intensity versus optical path difference, $I(x)$, can be expressed as

$$I(x) = \text{const} \; [\; 1 + \cos(2\pi\sigma_1 x) \;] \qquad (7.7)$$

where $\sigma_1 = 1/\lambda_1$ is the wavenumber of the monochromatic beam (see for example, Bell 1972; Martin, 1980).

In the general case of $B(\sigma)$ representing a continuous distribution of spectral intensities, the relationship between measured intensity, $I(x)$, and spectral intensity, $B(\sigma)$, is

$$[I(x) - \tfrac{1}{2}I(o) \;] = \text{const} \int_0^\infty B(\sigma) \cos(2\pi\sigma x) \, d\sigma \qquad (7.8)$$

where $I(o)$ is the intensity at ZPD. For a derivation of this general relationship, see Bell(1972). The term $[\; I(x) - \tfrac{1}{2}I(o) \;]$ is generally referred to as the interferogram. Mathematically, the interferogram is said to be the Fourier cosine transform of $B(\sigma)$, the desired spectral intensity function. Using the Fourier inversion theorem Equation (7.8) can be rewritten as

$$B(\sigma) = \text{const} \int_0^\infty [\; I(x) - \tfrac{1}{2}I(o) \;] \cos(2\pi\sigma x) \, dx \qquad (7.9)$$

That is, the intensity spectrum $B(\sigma)$ is the inverse Fourier cosine transform of the measured intensity as a function of OPD, $I(x)$, after having first subtracted half of the intensity at ZPD. This is the reason why the technique of interference spectroscopy, as conceived by Fellgett and Jacquinot, is usually referred to as Fourier transform

spectroscopy (FTS). Figure 7.5 is a diagrammatic representation of the relationship between a broad band wavelength spectrum and the observed interferogram. The broad band spectrum can be thought of as the sum of many monochromatic components of varying intensities each giving rise to cosinusoidal intensity variations at the detector (Equation 7.7). These will be in phase at ZPD, but they move out of step as the OPD is increased.

Equation (7.9) only holds for an ideal Michelson interferometer in which the two arms are completely symmetric. In this case only a one-sided interferogram need be observed, because it will be completely symmetric about ZPD. For an asymmetric interferometer the cosine Fourier transform is replaced by a complex Fourier transform (see for example, Bell 1972; Chantry, 1979) and the interferogram must be recorded on both sides of ZPD (a two-sided interferogram). In this case, Equation (7.9) becomes

$$B(\sigma) = \text{const} \int_{-\infty}^{\infty} [\, I(x) - \tfrac{1}{2}I(o) \,] \exp(-i2\pi\sigma x)\, dx \qquad (7.10)$$

The fact that the Michelson interferometer accepts light via circular apertures rather than through narrow slits means that it has a much larger throughput than the conventional monochromator-type spectrometers. This advantage is commonly referred to as the Jacquinot advantage, or the "étendue", it will be discussed in more detail in Chapter 8. It is the Jacquinot and Fellgett advantages in sensitivity of apparatus which makes FTS such a viable proposition, particularly in the infrared wavelength region (see Section 8.2).

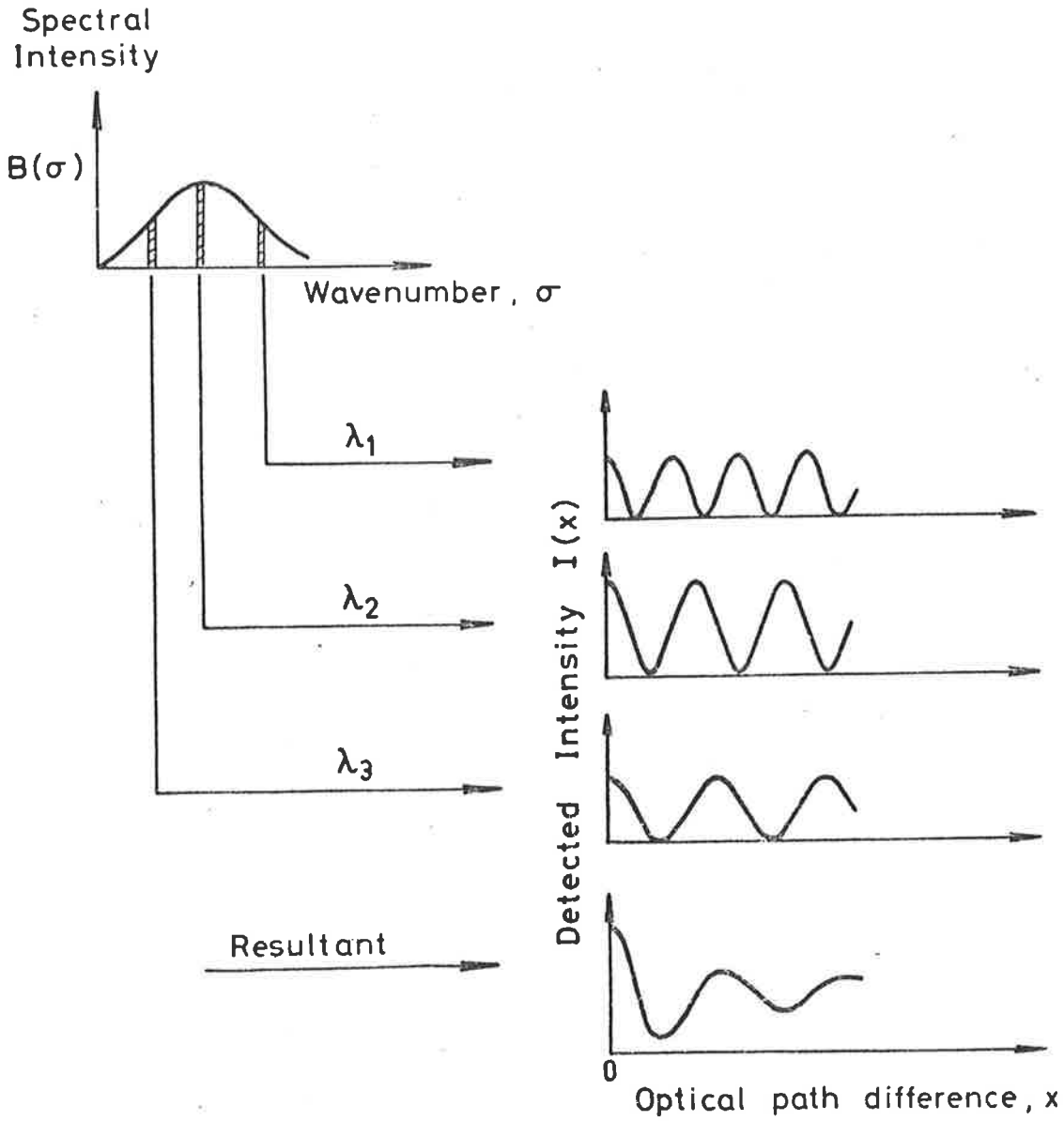

Figure 7.5 The Relationship between a Broad Band Wavelength Spectrum and the observed Interferogram.

The main disadvantage of FTS is that one needs to have access to computer facilities in order to do the Fourier transform calculations. This is however, not a strong argument against the use of interferometers as computers are now a recognized necessity in most fields of scientific research. One problem which one can foresee is that it may be difficult for an inexperienced operator to visually interpret the outcome of an experiment just by looking at the interferogram, hence a Fourier transform computation may be needed in order to judge whether or not an experiment has been completed successfully., This problem should however be overcome as the operator obtains some experience in recognizing special features of the measured interferogram.

CHAPTER VIII

THEORETICAL CONSIDERATIONS OF FOURIER TRANSFORM SPECTROSCOPY

8.1 Introduction

The purpose of this Chapter is to consider some of the theoretical aspects of using a Michelson interferometer for spectral studies. The Jacquinot and Fellgett advantages are both discussed on a quantitative basis in Section 8.2, where the throughput of the Michelson interferometer is compared with that of a conventional prism or grating monochromator-type instrument. In practice, the basic Fourier transform integral, relating the observed interferogram to the spectrum (Equation 7.10), has finite OPD limits. This means that the computed spectrum differs somewhat from the true spectrum. To correct for this the observed interferogram is usually multiplied by a function, the apodizing function, and the corrective procedure is called "apodization". The effect of having a finite OPD and the process of "apodization" will be discussed in Section 8.3. In order to design a Michelson interferometer it is necessary to consider both the resolution and sampling interval criteria; these will be outlined in Sections 8.4 and 8.5 respectively.

8.2 The Jacquinot and Fellgett Advantages

Jacquinot (1960) pointed out that although the Michelson interferometer has a much larger throughput than conventional grating or prism spectrometers, the maximum solid angle allowable is inversely proportional to the resolving power of the interferometer. For a resolving power, R_m, defined by

$$R_m = \frac{\lambda}{\Delta\lambda} \tag{8.1}$$

where λ is the wavelength and $\Delta\lambda$ is the wavelength resolution. The allowable input solid angle for the Michelson interferometer, Ω_m, is given by

$$\Omega_m = \frac{2\pi}{R_m} \tag{8.2}$$

Jacquinot also focussed attention on the fact that, in a lossless optical system, the brightness of an object equals the brightness of the image. For the Michelson interferometer he re-stated this as being equivalent to the fact that the product $\Omega_m A_m$ (A_m being the area of the collimating lens) is a constant from the source to the detector. This "throughput" product was called the "étendue" of the interferometer. Hence one obtains

$$E_m = \Omega_m A_m = \frac{2\pi A_m}{R_m} \tag{8.3}$$

where E_m is the Michelson interferometer "étendue".

A quantitative measure of the Jacquinot advantage can be obtained by estimating the "étendue" for a grating monochromator-type instrument and this has been done by many researchers (see for example, Jacquinot (1960), Bell (1972), Luc and Gerstenkorn (1978)). Bell showed that the grating spectrometer "étendue" is approximately given by

$$E_G = \left(\frac{L}{F}\right)\left(\frac{A_G}{R_G}\right) \tag{8.4}$$

where L is the height of the entrance slit and F is the focal length of the collimating lens. If one assumes that the area and focal

lengths of the collimators are the same for the two instruments working at the same resolving power, then the ratio of the interferometer and grating "étendues" becomes

$$\frac{E_m}{E_G} \simeq 2\pi \left(\frac{F}{L} \right) \tag{8.5}$$

From this relationship, Bell (1972) estimated that the throughput of a Michelson interferometer is generally about two orders of magnitude larger than even the best grating spectrometers.

The other important advantage associated with FTS is the "Fellgett advantage". In order to fully understand when this advantage exists it is necessary to consider the gain quantitatively. If one is interested in measuring a broad spectrum between the wavelengths λ_1 and λ_2 with a resolution of $\Delta\lambda$, then the number of spectral elements, M, in this band is given by

$$M = \frac{\lambda_2 - \lambda_1}{\Delta\lambda} \tag{8.6}$$

If a prism or grating instrument, such as illustrated in Figure 7.2, is being used, then each small wavelength band of width $\Delta\lambda$ can be observed for a time T/M, where T is the total time required for a scan from λ_1 to λ_2. Hence, the integrated signal received in a small band $\Delta\lambda$ is proportional to T/M. For random noise, independent of signal level, one obtains a signal/noise (S/N) ratio given by

$$(S/N)_G \propto \left(\frac{T}{M} \right)^{\frac{1}{2}} \tag{8.7}$$

For the Michelson interferometer and the modified monochromator (mentioned in Section 7.2), the situation is different because all of the wavelengths in the broad band λ_1 to λ_2 are

measured all the time. For the Michelson interferometer one can estimate the signal/noise ratio by assuming that the noise is random and independent of the signal level (Fellgett, 1958). In this case the signal is proportional to the measuring time T and the noise is proportional to $T^{\frac{1}{2}}$. Hence, the signal/noise ratio is given by

$$(S/N)_I \propto T^{\frac{1}{2}} \tag{8.8}$$

with the same proportionality constant as Equation (8.7). Comparing Equations (8.7) and (8.8), the ratio of the $(S/N)_I$ for the interferometer to the $(S/N)_G$ for a conventional grating or prism dispersive instrument is given by

$$\frac{(S/N)_I}{(S/N)_G} = M^{\frac{1}{2}} >> 1 \tag{8.9}$$

From Equations (8.3) and (8.9) one notices that for a high resolution interferometer the Fellgett advantage dominates,whereas for a low resolution instrument the Jacquinot advantage is the larger. The overall advantage for a particular Michelson interferometer is given by the product of the Fellgett and Jacquinot gains.

In the derivation of Equation (8.9) one of the assumptions was that the noise is random and independent of the signal level and, therefore, only dependent on the measuring time. While this assumption holds in the infrared wavelength region, it is generally not true in the visible wavelength region. In the infrared region the noise is generally only detector noise which is independent of the signal level, hence the full Fellgett advantage is obtained for infrared

studies. In the visible region detectors, such as photomultiplier tubes, can detect individual photons which means that the noise level is predominantly given by the Poisson fluctuation of the number of photons detected.

Kahn (1959) has shown that in the visible region the multiplex gain depends (in the case of photon noise limited FTS) on the square root of the ratio of the intensity $I(\lambda)$ of a peak to the mean intensity $\overline{I(\lambda)}$ of the whole spectrum. That is, in the visible region, Equation (8.9) becomes

$$\frac{(S/N)_I}{(S/N)_G} \simeq \left(\frac{I(\lambda)}{\overline{I(\lambda)}}\right)^{\frac{1}{2}} \tag{8.10}$$

(for a derivation of this relationship see for example, Luc and Gerstenkorn, 1978). Hence, in the visible region, the magnitude of the multiplex gain depends on the peak or line in question; it is a function of the intensity of the peak as well as the overall intensity characteristics of the rest of the spectrum. This is in marked contrast to FTS in the infrared region,where the gain is proportional to $M^{\frac{1}{2}}$ (see Equation (8.8) and independent of the intensity of the individual peaks. From Equation (8.10) one sees that for a continuous spectrum of constant intensity the multiplex gain is lost; this special case has been discussed by Bell (1972). However, in cases of actual visible wavelength spectra, the multiplex gain is not lost entirely.

The phenomenon of multiplexing is a property of the system as a whole. Merely using an interferometer does not guarantee this advantage, nor does the need to use a dispersive instrument necessarily deny it. It is mainly the Jacquinot advantage which makes the Michelson interferometer such a suitable instrument for measuring TL spectra in

the visible wavelength region. The fact that the multiplex advantage is not fully utilized for FTS in this wavelength region is not critical, as far as archaeological TL spectral measurements are concerned, because TL emission spectra are relatively broad band and high resolution is not essential. One should point out that the interference filter spectrometer (Bailiff *et al*, 1977) considers only sixteen spectral bands in the wavelength range from about 340 to about 640 nm; which corresponds to a resolution of approximately 20 nm. Hence, a Michelson interferometer is ideally suited for the detection of archaeological TL emission spectra, the main reason being the rather low levels of light involved. If one wants to study the spectral characteristics of dosimetry phosphors, or geological samples, in which the light levels are much higher, then one can tolerate a much higher resolution and hence a dispersive instrument would be suitable.

8.3 Apodization

In the previous Chapter it was shown that, in the general case, the interferogram observed in a Michelson interferometer is related to the spectrum by the inverse Fourier transform relationship

$$B(\sigma) = \text{const} \int_{\infty}^{\infty} [\, I(x) - \tfrac{1}{2} I(o) \,] \exp(- i2\pi\sigma x) \, dx \qquad (8.11)$$

However, in practice, $I(x)$ cannot be observed out to $x = \pm \infty$ as required by Equation (8.11). It must be truncated at $x = \pm L$, which corresponds to the maximum OPD between the two beams. The result of this practical limitation is that the spectrum calculated by Equation (8.11) differs somewhat from the true physical spectrum. For a truncated two-sided interferogram Equation (8.11) becomes

$$B(\sigma) = \int_{-L}^{L} [\, I(x) - \tfrac{1}{2} I(o) \,] \exp(- i2\pi\sigma x) \, dx \qquad (8.12)$$

where the constant of proportionality has been set to unity.

Mathematically, the truncation of the interferogram is equivalent to multiplying an interferogram of infinite length by a rectangular boxcar function of height unity for $-L \leqslant x \leqslant L$ and zero elsewhere. That is, Equation (8.12) may be rewritten as

$$B(\sigma) = \int_{-\infty}^{\infty} A(x) \left[I(x) - \tfrac{1}{2} I(o) \right] \exp(-i2\pi\sigma x)\, dx \qquad (8.13)$$

with $$A(x) = \begin{cases} 1 & -L \leqslant x \leqslant L \\ 0 & \text{elsewhere,} \end{cases}$$

where $A(x)$ is in general referred to as an "apodization" function, and the particular case referred to in Equation (8.13) is usually termed the boxcar or square wave function (see for example, Chantry, 1979). The effect of multiplying the interferogram by an "apodixation" function can be understood with the aid of the convolution theorem, which states that the Fourier transform of a product of two functions is equal to the convolution of the separate Fourier transforms (Bracewell, 1965). Mathematically, the convolution of two functions $f(x)$ and $g(x)$ is defined as

$$f(x) * g(x) = \int_{-\infty}^{\infty} f(u)\, g(x-u)\, du \qquad (8.14)$$

The Fourier transform of the truncated interferogram will therefore, be the convolution of the Fourier transform of the infinite interferogram, that is the spectrum undistorted by instrumental limitations, with the Fourier transform of the boxcar function. Thus

$$B(\sigma) = F \left[A(x) \right] * F \left[I(x) - \tfrac{1}{2} I(o) \right] \qquad (8.15)$$

where F denotes the Fourier transform and the asterisk indicates convolution. In order to discuss the consequences of truncation, it is again convenient to consider the case of a monochromatic source. We have already seen that the interferogram observed from a monochromatic source is a cosine wave (Equation 7.7). The Fourier transform of a cosine wave is simply a delta function pair (see for example, Bracewell, 1965). This means that the spectrum observed for a monochromatic source is the Fourier transform of the "apodization" function A(x). The Fourier transform of the boxcar function is the sinc function $2L\,[\sin(2\pi\sigma L)]/2\pi\sigma L$, and this is the counterpart in interferometric spectrometry of the scanning function in dispersive spectrometry (Bell, 1972). It is often referred to as the instrumental line-shape (ILS), because it is the shape of a monochromatic input line as observed by an interferometric spectrometer. The same ILS function can be obtained by simply substituting the interferogram function $2\cos(2\pi\sigma_1\delta)$ into Equation (8.12) (see for example, Bell, 1972). By this method, one obtains a spectrum given by

$$B(\sigma) \approx 2L\,\frac{(\sin z)}{z} \equiv 2L\ \mathrm{sinc}\ z \qquad (8.14)$$

where $z \equiv 2\pi(\sigma_1 - \sigma)L$

In Figure 8.1(a) the shape of the sinc function is compared with the spectrum of a monochromatic source as L approaches infinity (the "delta" function). The important features of the ILS function are a fairly broad central maximum and several subsidiary positive and negative "sidelobes" or "feet" which have up to 22% of the peak-to-peak intensity of the central maximum (Bell, 1972). Whereas the central peak can be tolerated as an approximation to the monochromatic source

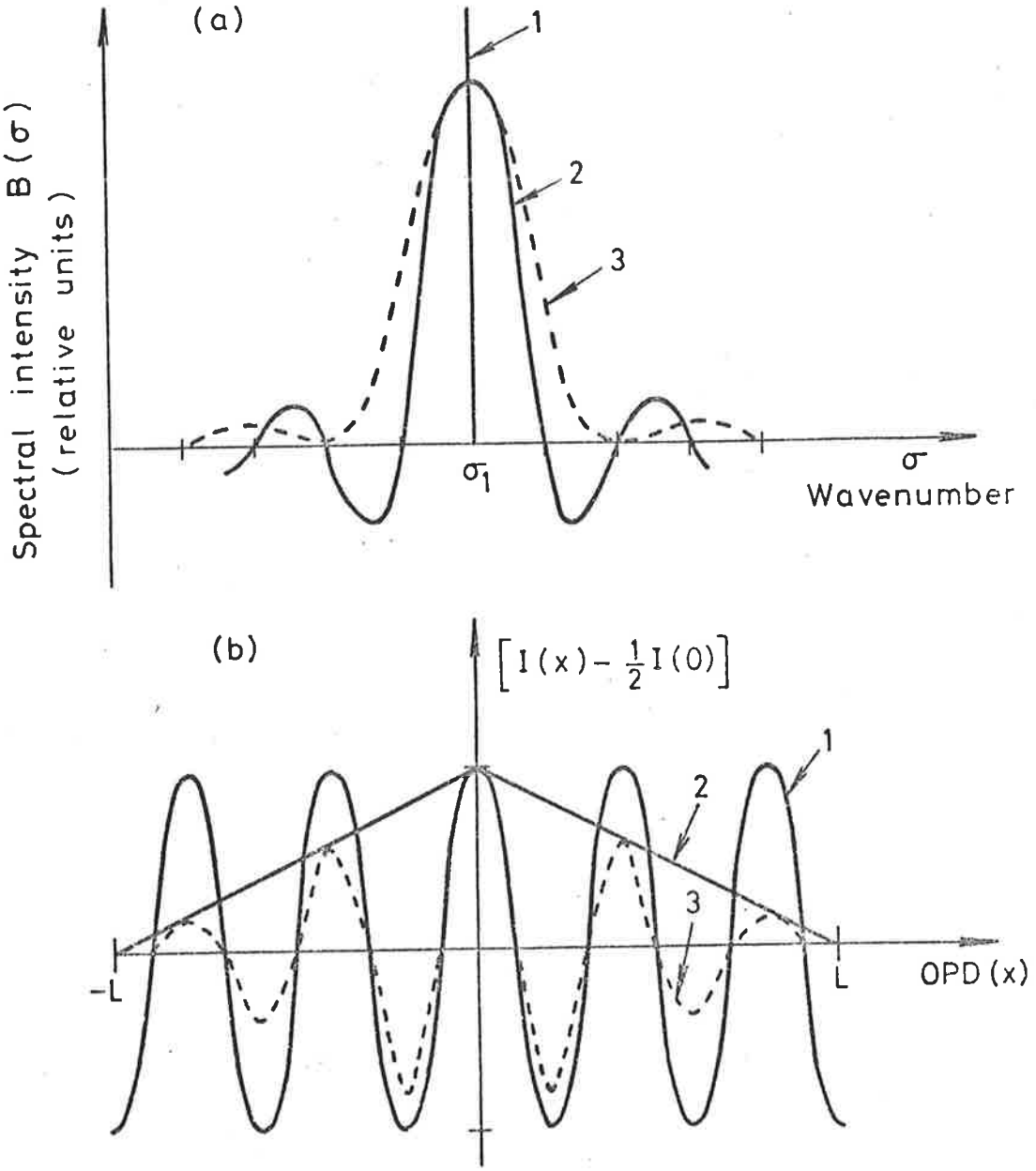

Figure 8.1(a) The spectra of (1) the monochromatic source if L approaches infinity (the "delta" function); (2) the same source if L is finite ("boxcar apodization"); (3) the same as (2) with triangular apodization.

(b) Interferogram for (1) a monochromatic source and (2) the same source after triangular apodization, and (3) the triangular apodizing function.

spectrum, the "feet" would appear as false sources of energy at nearby wavelengths. In order to reduce the size of the "feet" one can multiply the interferogram with an appropriate "apodization" function. The boxcar "apodization" function is only a consequence of truncating the interferogram integral. Bell (1972) has discussed the use of a triangular function given by

$$A(x) = \left(1 - \frac{|x|}{L} \right) \tag{8.15}$$

This results in a spectrum given by

$$B(\sigma) = L \, \mathrm{sinc}^2 (z/2) \tag{8.16}$$

where z is defined in Equation (8.14). This spectral function is also shown in Figure 8.1(a). The effect of triangular apodization on the interferogram of a monochromatic source is shown diagrammatically in Figure 8.1(b). By using triangular apodization the size of the "feet" are reduced by a factor of about four. The width of the central peak is increased somewhat; however, the loss in resolution is not serious (see Section 8.4). Thus, by apodizing the interferogram with an appropriate function, one obtains a spectrum which is a much more acceptable approximation to the perfect monochromatic source spectrum. The general Fourier transform Equation can then be rewritten as

$$B_A(\sigma) = \int_{-L}^{L} A(x) \, [\, I(x) - \tfrac{1}{2} I(o) \,] \exp(- i2\pi\sigma x) \, dx \tag{8.17}$$

where $B_A(\sigma)$ is the corrected or apodized spectrum. The term apodization is generally used to describe the elimination of strong sidelobes by

means of a convolution in the spectral domain; hence, the boxcar function is not generally referred to as an apodization function. Spectra obtained by using only a boxcar function are hence labelled unapodized spectra. Triangular apodixation has been considered here for easy understanding. Numerous other apodization functions have been used in the field of interferometric spectroscopy (see for example, Bell, 1972), some of these will be discussed in Chapter 10.

8.4 The Resolution of a Michelson Interferometer

The question of deciding resolution limits in FTS is rather more complicated than the corresponding problem in normal dispersive spectrometry. We have already seen that the throughput of a Michelson interferometer is limited by the Jacquinot relationship (Equation 8.2).

$$\Omega_m = \frac{2\pi}{R_m} = \frac{2\pi\Delta\lambda}{\lambda} \qquad (8.18)$$

where Ω_m is the input solid angle and R_m is the resolving power of the instrument. Another restriction on the resolution of a Michelson interferometer is that it depends on the maximum OPD between the two beams (see for example, Bell, 1972; Chantry and Fleming, 1976; Chamberlain, 1979; Chantry, 1979). The most commonly used resolution criterion is the Rayleigh criterion, which states that two peaks of equal intensity are resolved if the maximum intensity of one of the peaks coincides with the first zero intensity of the other. Chantry and Fleming (1976) have shown that, by using the Rayleigh criterion in the spectral domain, the resolution of unapodized spectra is limited by

$$\Delta\sigma \simeq \frac{0.7}{L} \qquad (8.19)$$

where $\Delta\sigma$ is the wavenumber resolution (cm^{-1}) and L is the maximum OPD. In the previous section it was shown that in the case of triangular apodization there was a broadening of the central peak. In this particular case it can be shown that the resolution is given by

$$\Delta\sigma_A \simeq \frac{0.9}{L} \qquad (8.20)$$

(see for example, Chantry and Fleming, 1976; Chamberlain, 1979). There are, as already mentioned, many weighting functions which may be applied to the interferogram in order to produce apodized spectra. Chantry and Fleming (1976) have pointed out that, although the spectral line shapes depend on the form of the apodization function, the resolution limit is generally given by Equation (8.20). They have shown that in the case of one peak being twice as intense as the other the resolution of an apodized spectrum is given by

$$\Delta\sigma_A \simeq \frac{1}{L} \qquad (8.21)$$

This is the restriction which is generally quoted as the resolution of a Michelson interferometer. Whichever criterion is used, the general result is that the resolution varies inversely as the maximum OPD. Hence, in order to increase the resolution by a factor of two it is necessary to double the maximum OPD between the two beams and subsequently take twice as long to retain the same signal/noise ratio. The ultimate resolution limit is, however, given by Equation (8.18). By combining Equations (8.18) and (8.21) one obtains an estimate of the maximum OPD beyond which no improvement in the resolution is obtained.

That is, in the case of apodized spectra L must satisfy the relation

$$L \lesssim \frac{2\pi\lambda}{\Omega_m} = \lambda R_m \qquad (8.22)$$

8.5 The Sampling Interval

In order to compute the spectrum, via a Fourier transform computation on the interferogram, it is necessary to sample the interferogram at discrete intervals. That is, the Fourier transform computation becomes discrete rather than continuous. The experimental details of this operation will be discussed in Chapter 10, it is only mentioned here in order to develop some theoretical consequences. If the interferogram is recorded at equally spaced intervals, then the general Fourier integral Equation (Equation 8.17) becomes

$$B_{S,A}(\sigma) = \sum_{j=-\frac{N}{2}}^{(\frac{N}{2})-1} A(j\Delta x)\,[J(j\Delta x) - \tfrac{1}{2} I(o)]\,\exp(-i2\pi\sigma j\Delta x) \qquad (8.23)$$

where Δx is the increment in OPD, N is the total number of data points in the two-sided interferogram, and $B_{S,A}(\sigma)$ is the spectrum obtained from a sampled interferogram which has been apodized. In this Equation the continuous interferogram function has been replaced by its ordinates at regularly spaced values of the OPD and an integration up to the maximum OPD has been replaced by a summation. By recording the interferogram in equal intervals, one is able to use the Cooley-Tukey algorithm for the Fourier computation. This algorithm can significantly reduce computation time; however, one of

the requirements for its use is that the interferogram data must be recorded in equal increments. The Cooley-Tukey algorithm will be discussed in Chapter 10 and Appendix E.

If the interferogram is sampled at intervals of Δx then it can be shown that the corresponding sampled spectrum is related to the complete spectrum by the relationship

$$B_S(\sigma) = \sum_{n=-\infty}^{\infty} B_C [\, \sigma - n\,(\sigma_2 - \sigma_1)\,] \qquad (8.24)$$

where $\sigma_2 - \sigma_1 = \frac{1}{\Delta x}$ (8.25)

(see for example, Bell, 1972; Chamberlain, 1979). That is, if one computes a sampled spectrum from a sampled interferogram (as given by Equation 8.23), then one obtains the complete spectrum every time σ equals $n\,(\sigma_2 - \sigma_1)$ for all integers n, where $(\sigma_2 - \sigma_1)$ is the wavenumber bandwidth. This repetition phenomenon, commonly referred to as "aliasing", is illustrated diagrammatically in Figure 8.2. In order to obtain the true spectrum it is important that none of the "aliases" overlap. Whether or not overlapping occurs depends on the magnitude of the wavenumber bandwidth $(\sigma_2 - \sigma_1)$. If this bandwidth is large enough, which corresponds to the sampling interval being small enough, then no overlapping occurs. The phenomenon of "aliasing", as related to interferometric spectroscopy, has been discussed extensively in the literature (see for example, Chantry, 1971; Bell, 1972). The condition for no overlapping is that

$$\Delta x \leqslant \frac{1}{2\sigma_{max}} = \tfrac{1}{2}\,\lambda_{min} \qquad (8.26)$$

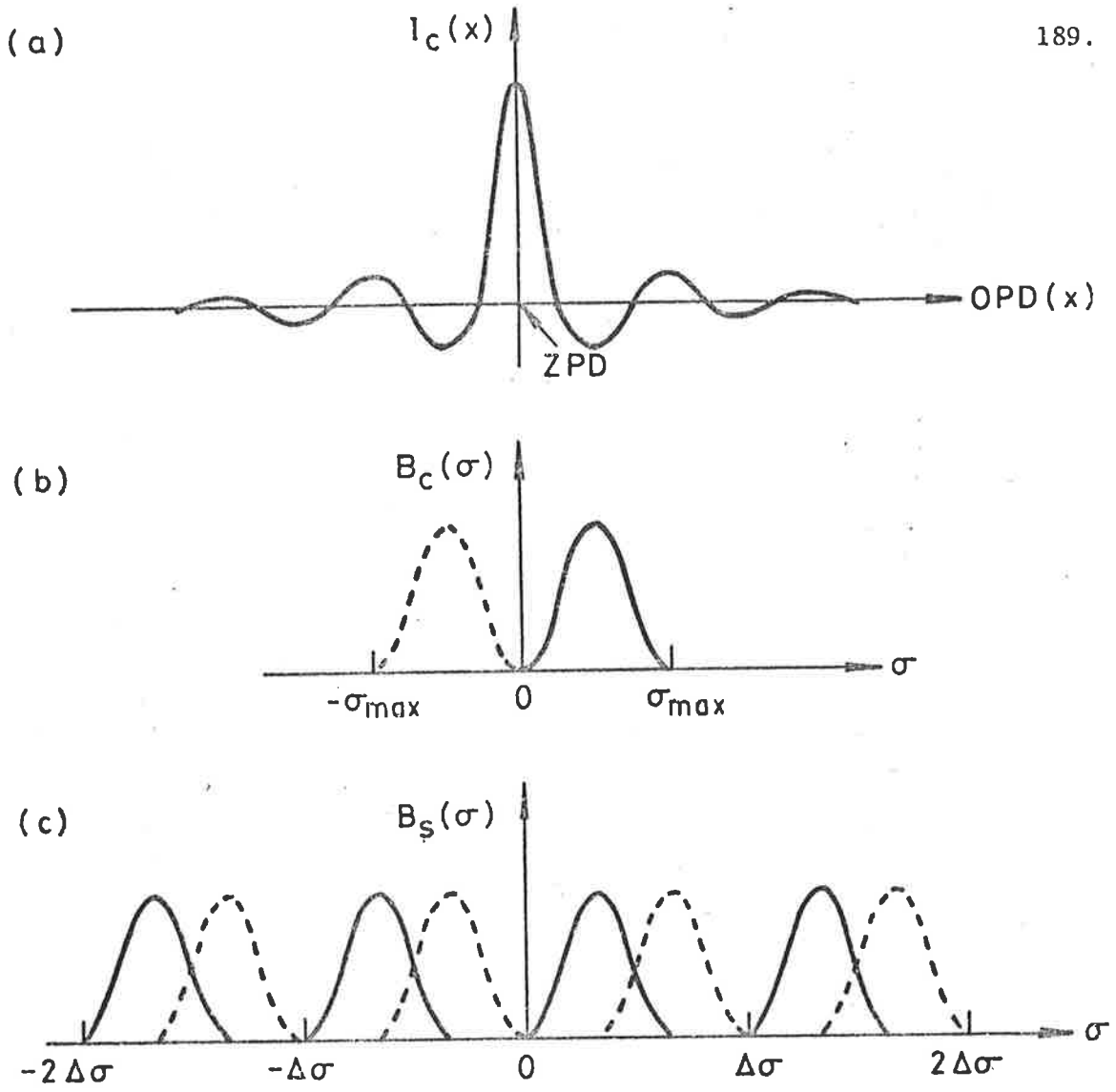

Figure 8.2 An Illustration of the Replication of the Spectrum from the Sampling of the Interferogram

(a) The complete interferogram.

(b) The corresponding complete spectrum. The Fourier transform calculation of the interferogram yields a spectrum containing both positive (solid line) and negative frequency values (dashed line).

(c) Shows the repetition of spectra and the overlapping of the negative and positive spectrum when sampling interval is too long.

That is, the sampling interval, when recording an interferogram, has to have an upper bound of half the smallest wavelength present in the spectrum if overlapping is to be avoided. This requirement is generally referred to as the sampling theorem.

CHAPTER IX

THE DESIGN AND SETTING UP OF THE SPECTRAL TL INTERFEROMETER

9.1 Introduction

Having considered the basic theory of FTS, it was decided to design and construct a Michelson-type interferometer for the measurement of TL emission spectra. The overall performance sought was to cover the spectral range 300-650 nm with a wavelength resolution of about 20 nm. One of the design requirements is that the interferometer needs to be interfaced to a conventional TL oven. This means that suitable input and light gathering optics must be incorporated in order to efficiently collect the TL emitted by a standard 10 mm diameter sample disc. It must also be possible to use the TL oven for conventional measurements.

9.2 The Optical Design of the Instrument

The optical principles of the Michelson interferometer have already been discussed in Section 7.3. Figure 9.1 is a schematic diagram of the optics for the interferometer, as designed for the purpose of measuring TL emission spectra. The basic components are a beam splitter and compensator, denoted collectively by B, which are identical plates of glass (measuring 76.2 x 54.0 x 6.4 mm), together with two 30 mm diameter (10 mm thick) aluminium coated mirrors. The semi-transparent beamsplitter coating is also aluminium. These optical components were made by Cole Precision Optics, Adelaide (now a division of Quentron Optics, Adelaide). The design includes input, light gathering and output optics (lenses denoted by L_1, L_2, L_3 and L_4 and a front surface mirror M) necessary in order efficiently to collect the

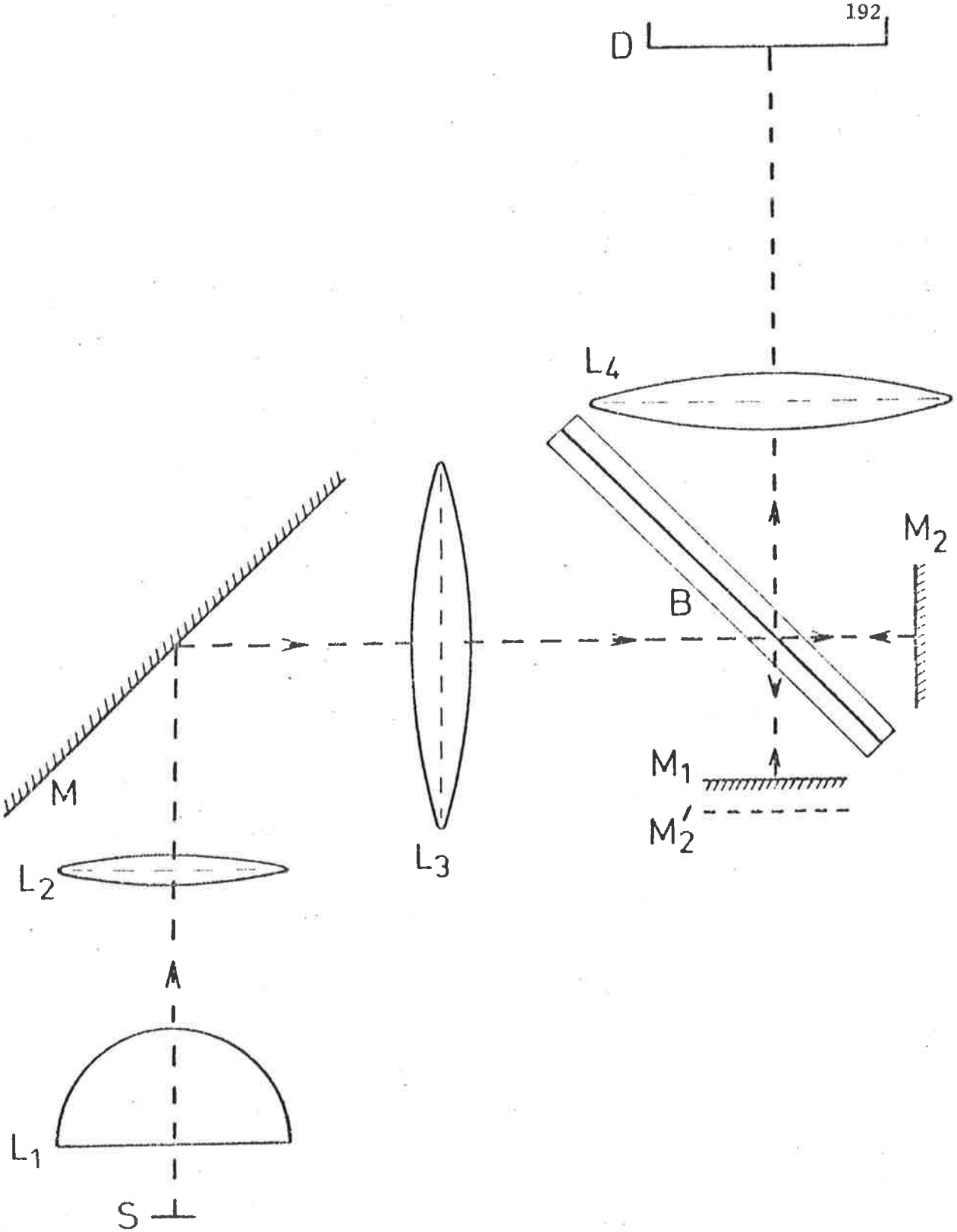

Figure 9.1 Schematic Diagram of the Optical Components of the Michelson Interferometer designed for spectral TL studies.

light from a 10 mm diameter sample disc, S.

A ray diagram of the input optical arrangement is shown schematically in Figure 9.2(a). L_1 is a 50 mm diameter aspheric lens (33 mm focal length) ($f/0.67$), which collects about 50% of the light emitted in the forward direction by the source. L_2 is a 50 mm diameter field lens (200 mm focal length) positioned in the focal plane of L_3, which is an 81 mm diameter Fresnel lens (101.6 mm focal length). The mirror M (Figure 9.1) is included so that the plane of the instrument can be horizontal and mounted on a rigid base. Using this input optical arrangement, an image of the source is obtained in the focal plane of L_3, the magnification being about 3. The purpose of the field stop is to restrict the input solid angle to give the desired instrument resolving power (see Section 8.2, Equation 8.2). Equation 8.2 can be re-written as

$$\frac{\theta}{\delta} = \frac{1}{R_m} \qquad (9.1)$$

where θ is the angular diameter observed at the mirror (see Figure 9.2(a)) and R_m is the instrument resolving power. For this instrument θ is limited to 0.48 radians, which corresponds to a resolving power of about 35. This is equivalent to an étendue (see Equation 8.3) of 40.5π mm^2 sr.. The output optics consists of a two identical 81 mm diameter Fresnel lenses (focal length 71.1 mm), separated by a distance of 4 mm (effective focal length 36.5 mm), this combination is denoted by L_4 in Figure 9.1. The purpose of this Fresnel lens combination is to direct the light reflected by the mirrors M_1 and M_2 on to the detector D, this is illustrated diagrammatically in Figure 9.2(b).

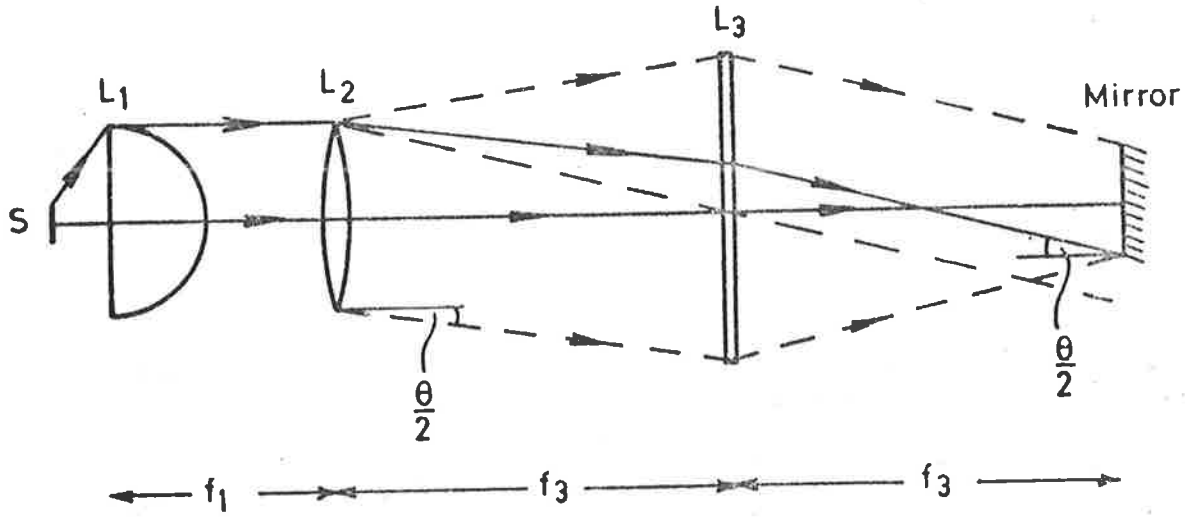

Figure 9.2(a) Schematic Diagram of the Interferometer Input Optics

For simplicity, only the extreme rays acceptable to the mirror are shown and the beamsplitter-compensator combination has been left out.

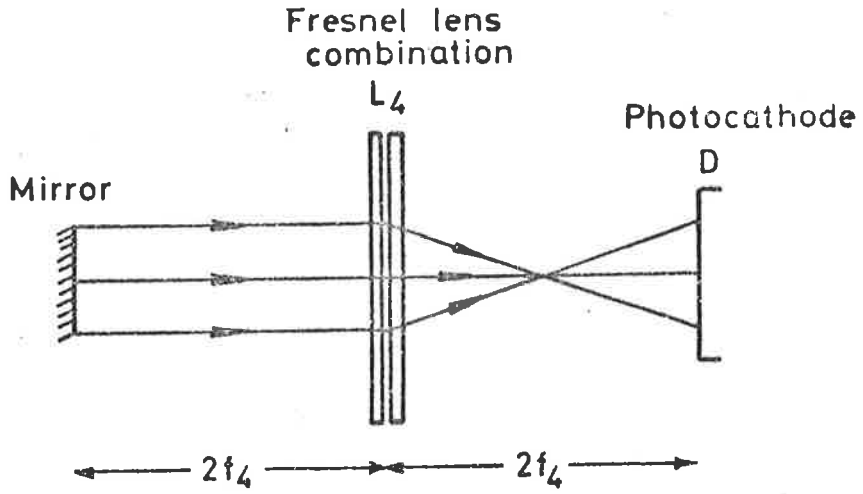

Figure 9.2(b) Schematic Diagram of the Interferometer Output Optics

For simplicity the beamsplitter-compensator combination has been left out.

The interferometer optics is somewhat more complicated than shown in Figure 9.2(a). One of the complications is that the rays are refracted at the beamsplitter and compensator surfaces, which means that the optical axis is displaced. This is illustrated diagrammatically in Figure 9.3(a). For this particular beamsplitter and compensator the optical axis displacement is about 4 mm. A further complication is that of multiple reflections of optical rays within the beamsplitter-compensator combination. This phenomenon is illustrated in Figure 9.3(b); it will be further discussed in Section 9.4.

Spectral transmission curves for the various interferometer optical components are shown in Figure 9.4(a). The Fresnel lenses are manufactured from optical grade acrylic, whereas the remaining components (including the beamsplitter and compensator) are of boro-silicate crown glass (BSC-BK-7). Also shown in Figure 9.4(a) is a typical reflection curve for an aluminium mirror coating.

The detector used is an EMI-9635 QA photomultiplier, used in the photon counting mode and cooled by a Products for Research TE 104 cooling unit. This tube was chosen because of its high quantum efficiency in the blue-green region of the visible spectrum. It also offers an effective reduction of the red background incandescence (Fleming, 1979). The spectral response for this photomultiplier is shown in Figure 9.4(b); also shown is the instrument response corrected for the transmission of the optical components of the interferometer.

Also incorporated in the apparatus design is the facility to measure conventional 2-D TL glow-curves. The detector used for this is also an EMI-9635 QA photomultiplier. The optical arrangement is

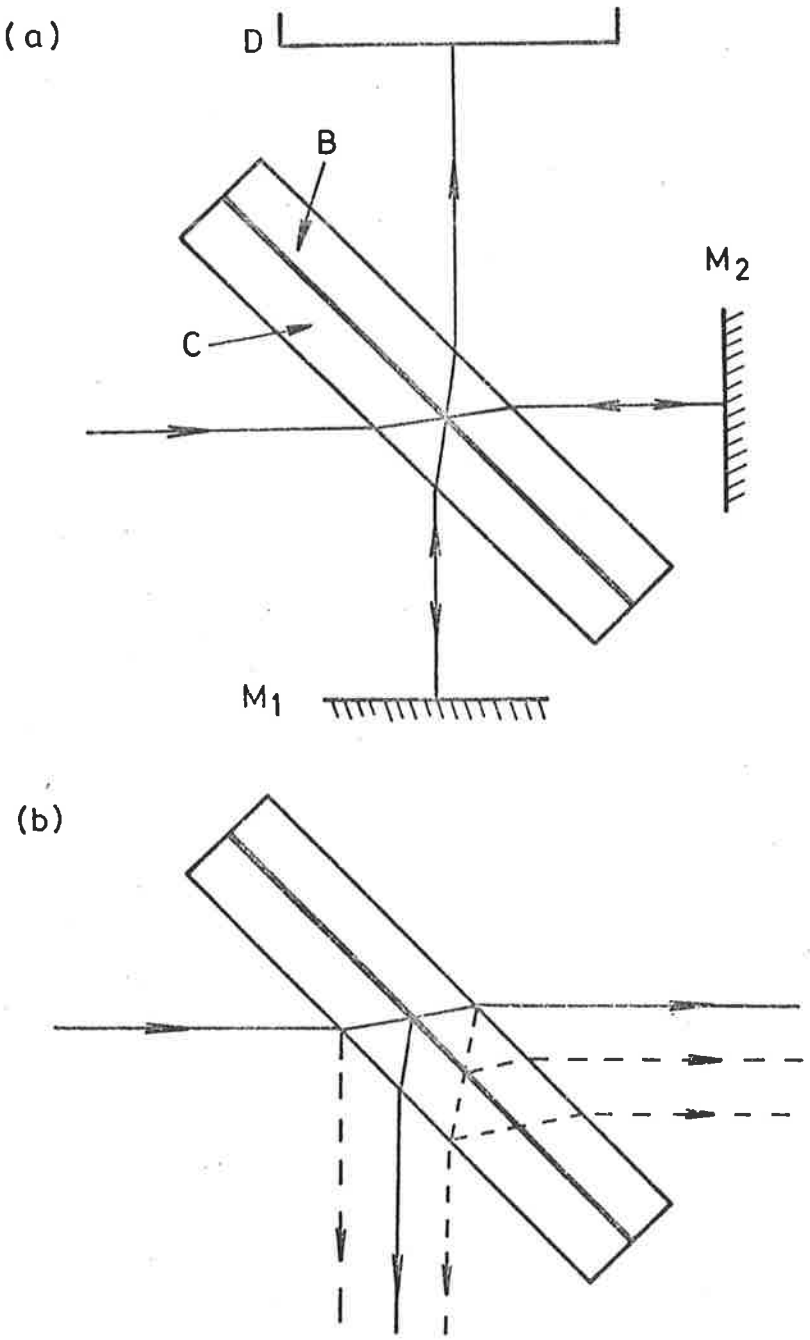

Figure 9.3 Ray Paths through the Beamsplitter and Compensating Plates

(a) Ray diagram showing the deviation due to refraction at the beamsplitter (B) and compensator (C) surfaces.

(b) Some of the multiple reflections in the beamsplitter and compensator.

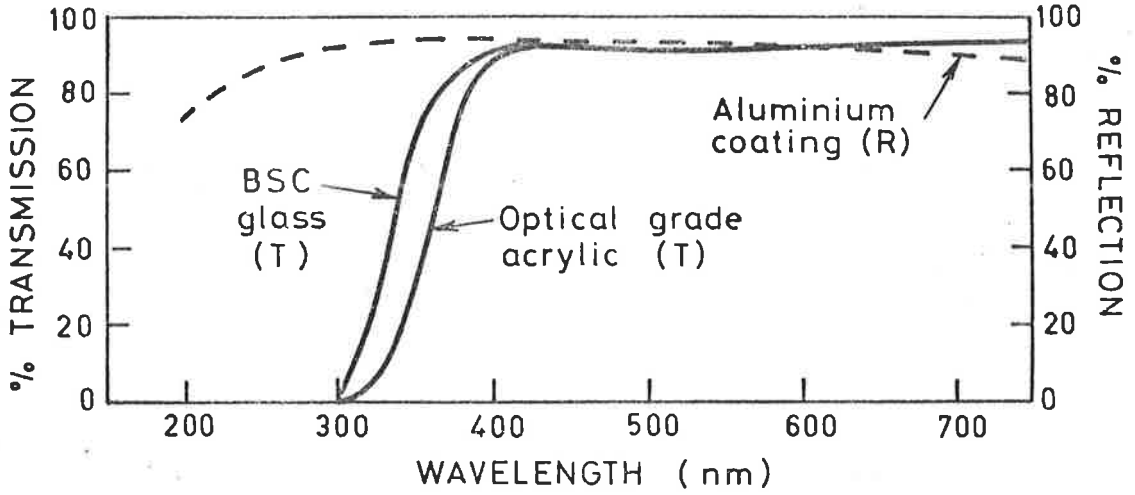

Figure 9.4(a) Typical Spectral Transmission Characteristics of Borosilicate Crown Glass and Optical Grade Acrylic (5 mm thickness)

Also shown is a typical reflection curve for an aluminium coating.

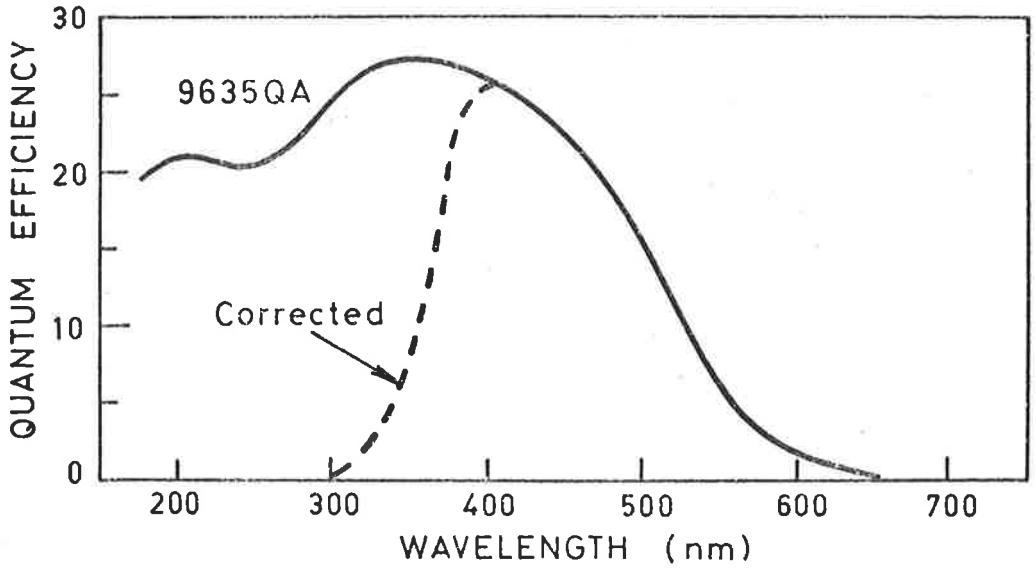

Figure 9.4(b) Spectral Response of the EMI-9635QA Photomultiplier Tube

Also shown is the response corrected for the transmission of the optical components of the interferometer.

illustrated in Figure 9.5(a). Interposed between the sample disc and the detector is a combination of filters, which gives an even better rejection of the incandescent signal, and a quartz light guide. Fleming (1979) has suggested two possible filter combinations: (1) Corning filter (7-59) (4 mm thickness) plus a Chance Pilkington heat reflecting filter (HA-3) (3 mm thickness). (2) Corning filter (5-58) (2.5 mm thickness). The spectral transmission characteristics of these filters and the quartz light guide are shown in Figure 9.5(b). The spectral response of filter (7-59) is much broader than that of the (5-58) which means that combination (1) is about 40% more effective in TL detection. This is the reason why this is often the preferred filter combination. Fleming points out that the second filter combination reduces the background incandescence to less than 20% of that obtained from the first combination. Hence, the second filter combination is often used when studying high temperature glow peaks, where the background incandescence often dominates. Both of these filter combinations also help to subdue any "spurious" TL present, as its emission has been found to lie in the yellow-red region of the spectrum (see Section 6.3.2).

9.3 The Mechanical Construction

The 10 mm diameter sample disc rests on a 60 x 29 mm water cooled nichrome heating strip; this forms the basis of what is generally referred to as the TL oven. The TL oven design is much the same as that manufactured by the Littlemore Scientific Engineering Co., Oxford, England. Figure 9.6 is a diagram of the mounting arrangement

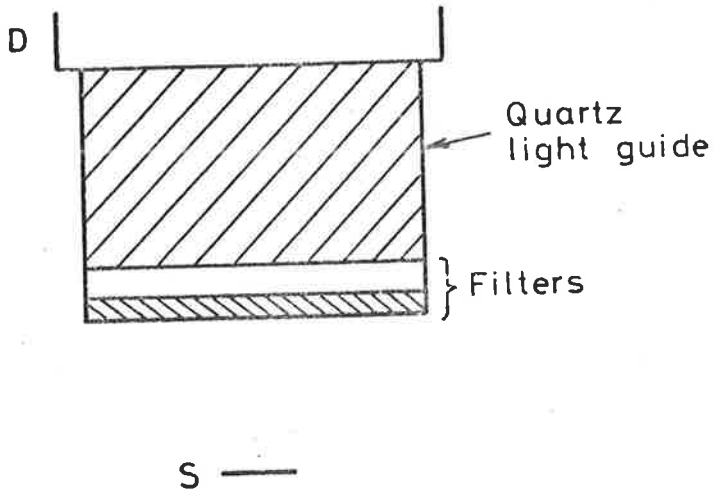

Figure 9.5(a) Schematic Diagram of the Optics used for conventional TL Measurements (2-D)

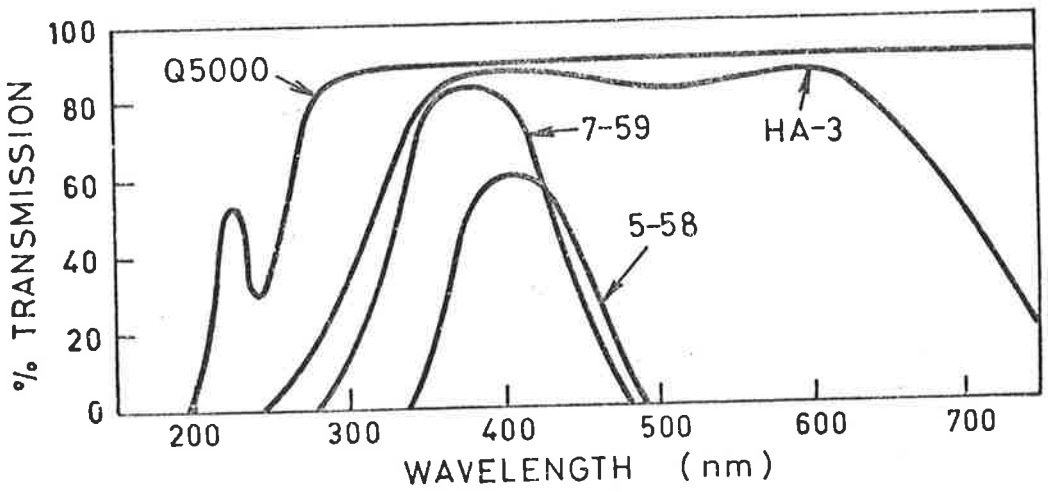

Figure 9.5(b) Spectral Transmission Characteristics of Filters and Quartz Light Guide.

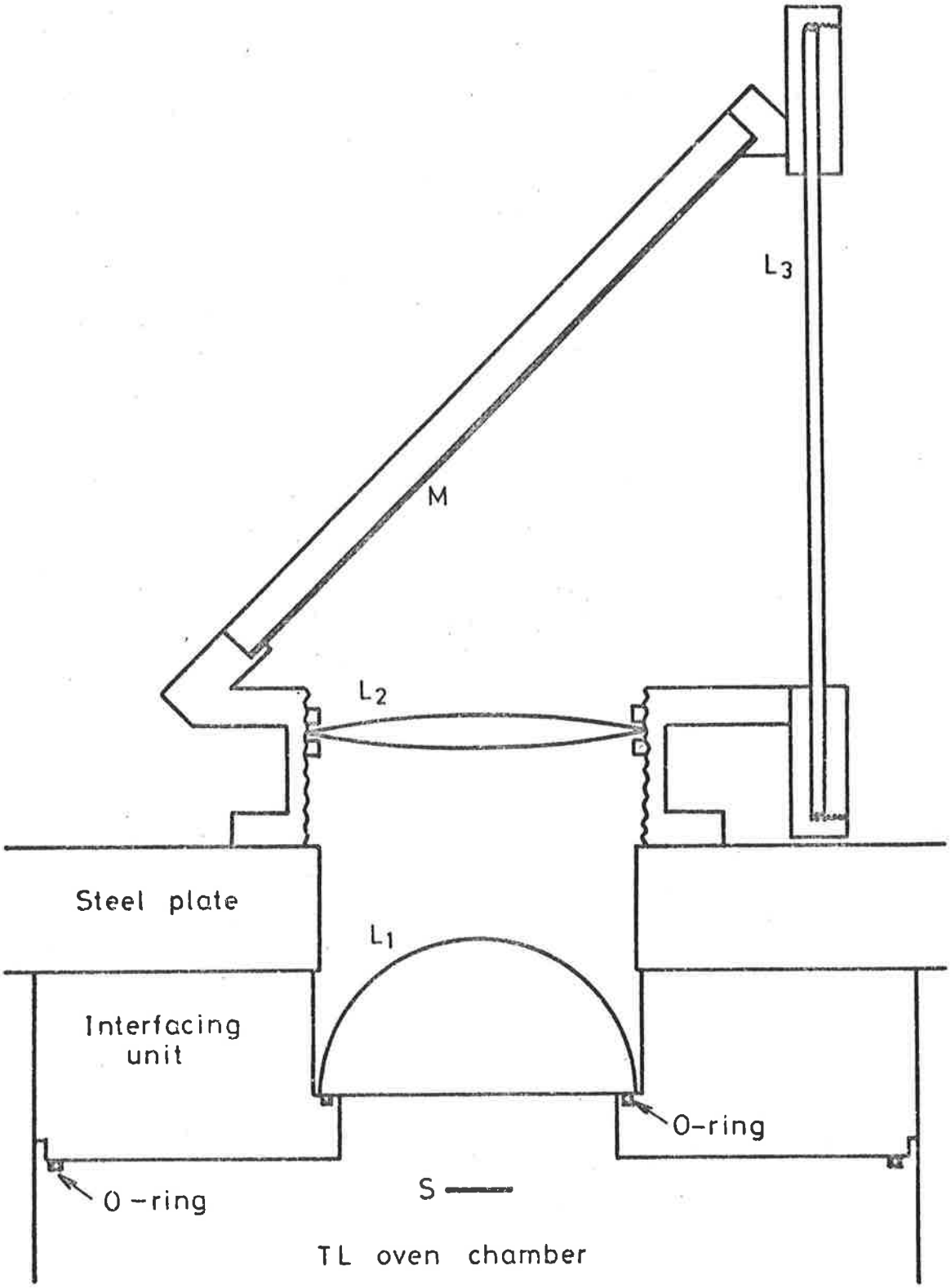

Figure 9.6 Schematic Diagram of the Mounting Arrangement for the Interferometer Input Optics.

for the interferometer input optics. The basic interferometer components, including the detector, are mounted on a 47 x 47 x 2 cm steel base plate, which is mounted on a solid table. Figure 9.7 is a photograph of the interferometer. Mounted below the base plate is an interfacing unit which houses the aspheric lens L_1 (see Figure 9.6) and couples the TL oven to the base plate. The TL oven is mounted on a sliding rail and spring loaded cam arrangement, which enables it to be positioned either in contact with the interferometer interfacing unit or in a position where conventional 2-D TL measurements can be made.

It is important to make sure that the beamsplitter-compensator combination and the two mirrors are mounted so that the appropriate adjustments can be made easily without causing any strain on the optical components. The mounting arrangement for the beamsplitter and compensator combination is shown diagrammatically in Figure 9.8. The combination is mounted in a steel frame which is mounted directly on the base plate so that it makes an angle of 45 degrees with the optical axis. The fine adjustment of this angle is then done via a rotating pivot. On one side of the frame the compensator makes contact at the top and the bottom via thin paper pads which ensures that there is no strain. On the other side the contact is made via two phosphor bronze leaf springs which are shaped to form a three-point kinematic mount, thin paper pads were also inserted at the contact points.

For the two interferometer mirrors it is important that adjustments can be made so that the mirror surfaces are strictly perpendicular to the optical axis. It is also important to make sure that the motion of the moveable mirror is strictly perpendicular to

Figure 9.7 Photograph of the Michelson-Type Interferometer.

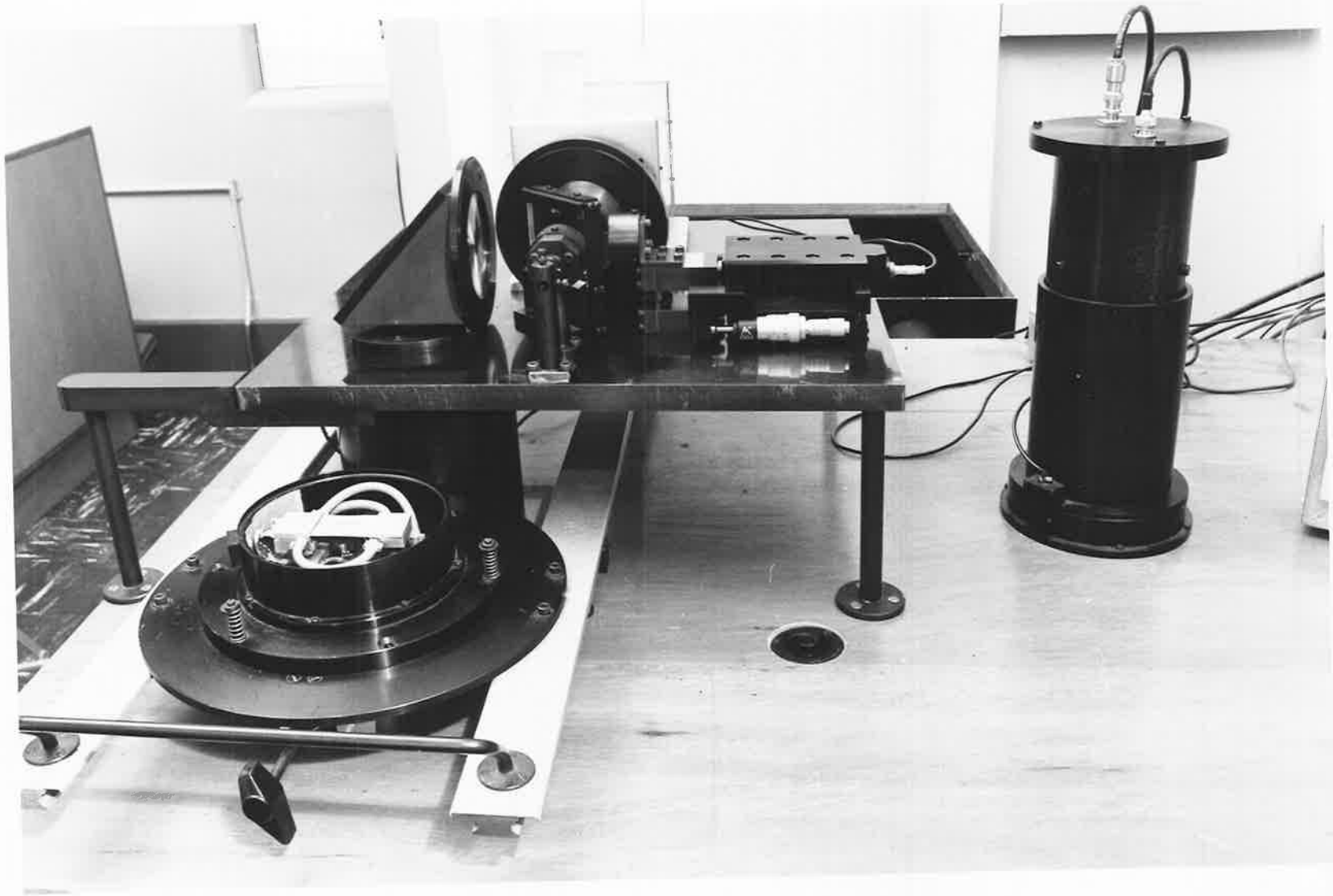

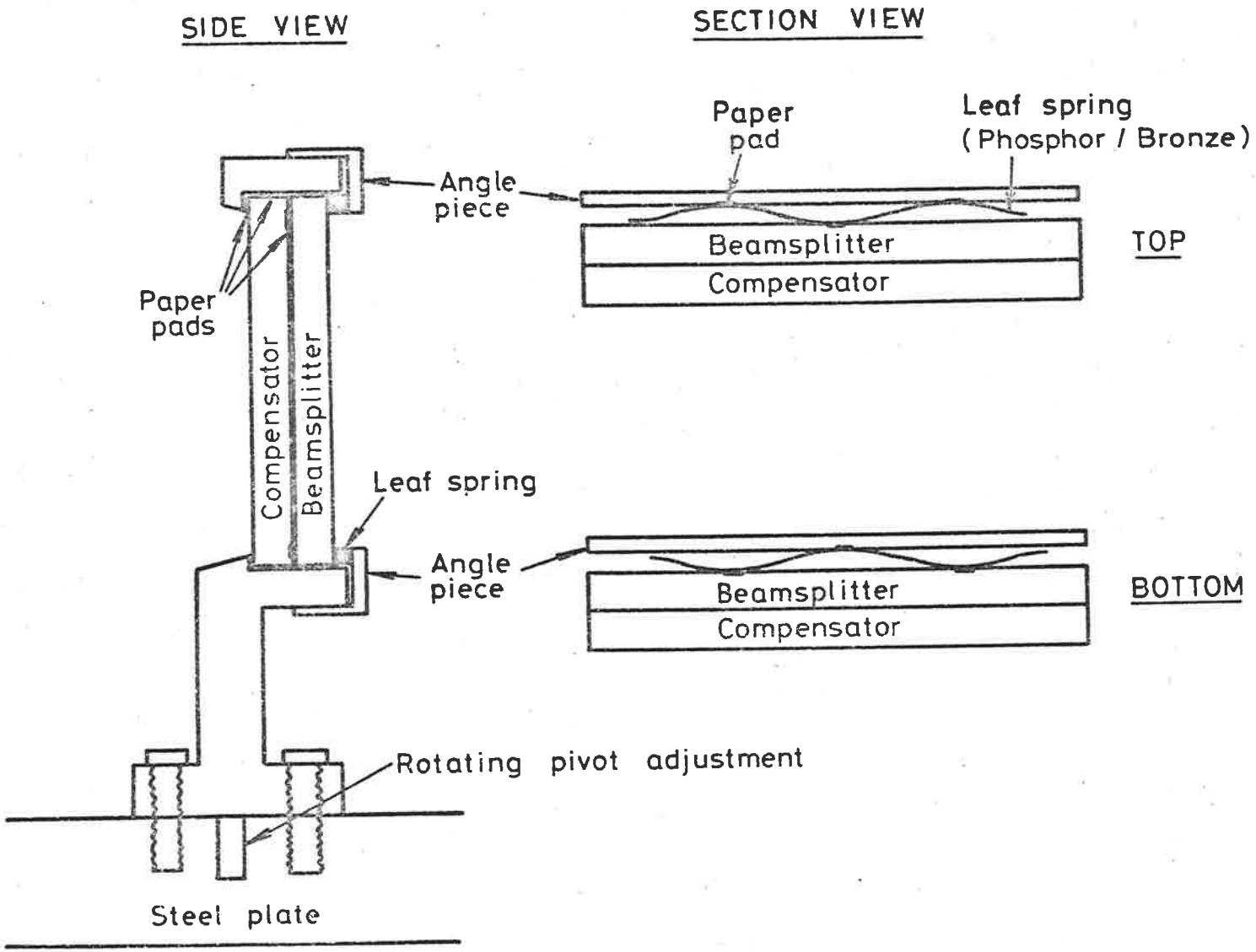

Figure 9.8 Schematic Diagram of the Mounting Arrangement for the Beamsplitter and Compensator combination.

the optical axis over the entire scanning range and that ZPD is well defined within this range (see Section 7.3). The optical alignment of the interferometer will be discussed in Section 9.4 and the moveable mirror scanning mechanism will be discussed in Section 9.6. The mounting arrangement for the fixed mirror is shown diagrammatically in Figure 9.9. The mirror is mounted in a vertical position with the back surface resting on a three-point contact phosphor bronze disc. The coarse adjustment is done at the front surface via three M2 grub screws, thin paper pads were inserted at all the contact points. The moveable mirror is mounted in an identical manner to this. A fine adjustment is also provided on the fixed mirror. This is done by supplying a downward or sideways force at the end of a 4 cm long lever, which is attached to the mirror mount.

The photomultiplier is cooled by a Products for Research Inc. cooling unit (Model No. TE-104TS), which is mounted directly on the base plate. All of the optical components of the interferometer are mounted so that the optical axis is a distance of 66.5 mm above the top of this plate. A light tight cover which fits over the assembly is also incorporated.

Also visible in Figure 9.7 is a "calibration/test light source" chamber which fits onto the interferometer interfacing unit in place of the TL oven. Figure 9.10 is a detailed diagram of this unit. It consists basically of a 14 mm diameter input lens (69 mm focal length), a 25.4 x 25.4 mm front surface mirror positioned at 45 degrees to the input lens, and a 10 mm diameter diffusing screen. By placing a steady (constant intensity) point source (such as a laser beam) at

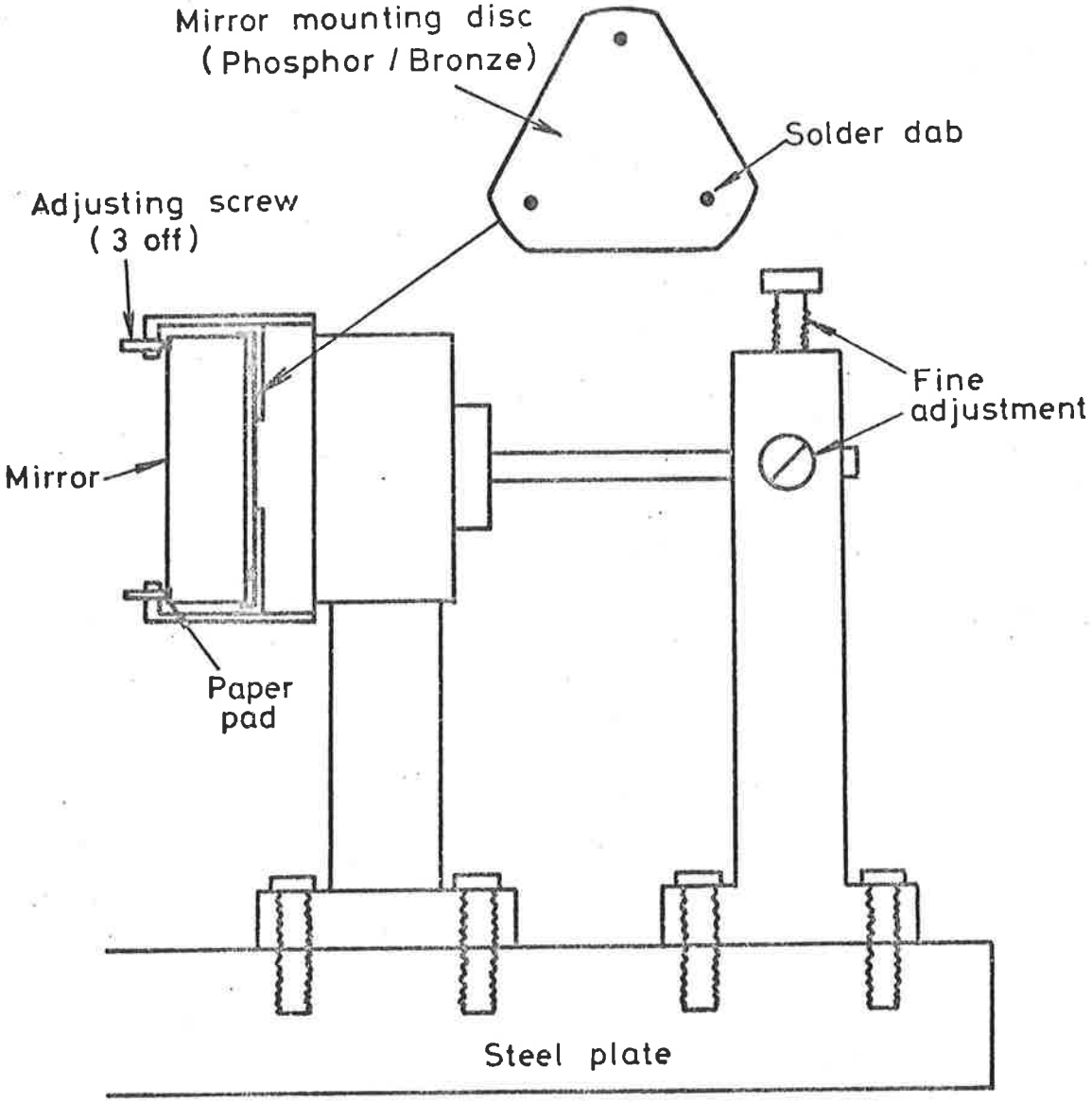

Figure 9.9 Schematic Diagram of the Mounting Arrangement for the Fixed Mirror.

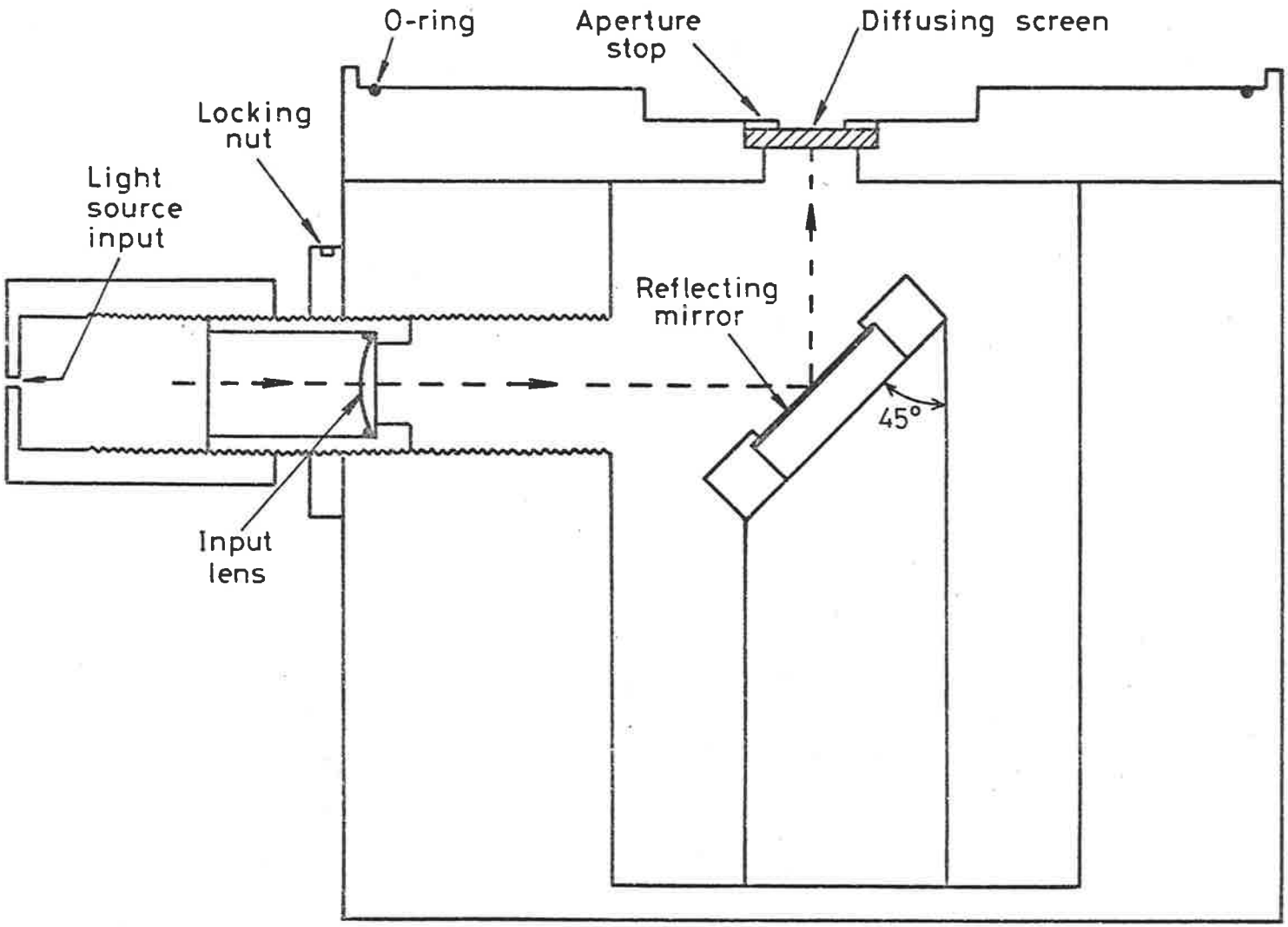

Figure 9.10 Schematic Diagram of the "calibration/test light source" chamber.

the focal point of the input lens, one obtains a uniformly illuminated source. That is, the sample disc source which is normally placed on the heater plate of the TL oven is being simulated by the uniformly illuminated constant intensity light source.

The photomultiplier housing, used in the conventional 2-D TL mode of operation can also be seen in Figure 9.7. It is shown resting on a "dummy" oven which contains a solid state light source used for photomultiplier calibration purposes (see Appendix D) .

Not shown in Figure 9.7 is the vacuum system which enables the TL oven to be evacuated prior to taking TL measurements. Figure 9.11 is a schematic diagram of the vacuum system. It is situated below the table top and consists of a Dynavac 4 two-stage vacuum pump fitted with a vapour trap (phosphorus pentoxide), an Edwards air admittance valve, a Veeco co-axial trap (Model No. VS-120), an Edwards isolation valve, an Edwards pirani head (Model No. PR-10-S) and a pressure release valve. The vacuum system is coupled to the TL oven via a flexible rubber tubing which enables the oven to be moved from the 2-D TL to the 3-D TL configurations. The rubber tubing also ensures that no significant vacuum pump vibrations are translated to the interferometer. Using this vacuum system it is possible to evacuate the TL oven to below 5×10^{-2} torr within a couple of minutes. The actual heating of the sample is carried out in an atmosphere of ultra high purity nitrogen at an appropriate rate of flow in the region 1-5 L min^{-1} .

9.4 Optical Alignment of Interferometer

Before discussing the various stages of optical alignment (coarse, intermediate and fine), it is necessary to first consider the

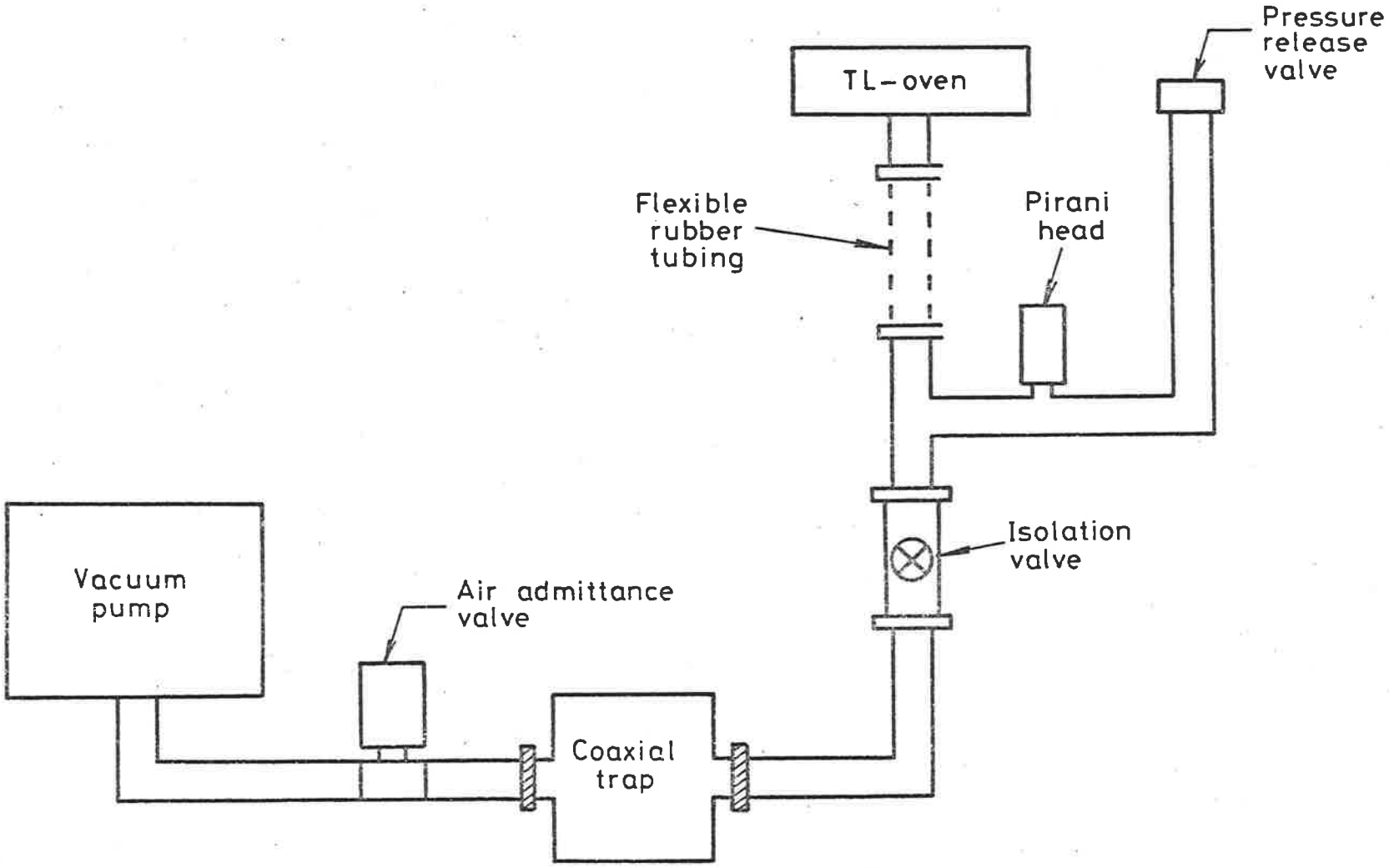

Figure 9.11 Schematic Diagram of the Vacuum System.

nature of the various types of fringes which can be observed using different optical configurations of the Michelson interferometer. Figure 9.12 is a diagram of the equivalent optical system of a Michelson interferometer which accepts light from an extended source. Shown is an optical ray incident and reflected from the fixed and moveable mirrors. Rays, such as those reflected at A and B, interfere when they are recombined at the detector. The OPD between the two reflected rays depends on both the mirror separation d and the angle which the incident ray makes with the optical axis. If the angle of incidence is α, then the OPD, x_α, is given by

$$x_\alpha = (AB + BC) - AD = 2d\cos\alpha \qquad (9.2)$$

where d is the separation of the two mirrors. At the detector the rays will reinforce each other to produce maxima for those angles α satisfying the relation

$$2d\cos\alpha = m\lambda \qquad (9.3)$$

where λ is the wavelength and m the order of interference. Hence, for a monochromatic source the maxima will lie on concentric circles centred about the optical axis. These fringes are generally referred to as fringes of equal inclination or Haidinger's fringes. The spacing between these fringes increases as the OPD is decreased, at ZPD the central fringe covers the entire field of view. If the mirrors M_2' and M_1 are not strictly flat and parallel then Equation (9.2) is no longer obeyed, and the fringes are not circular. If the space between the mirrors is wedge-shaped, then the fringes observed are

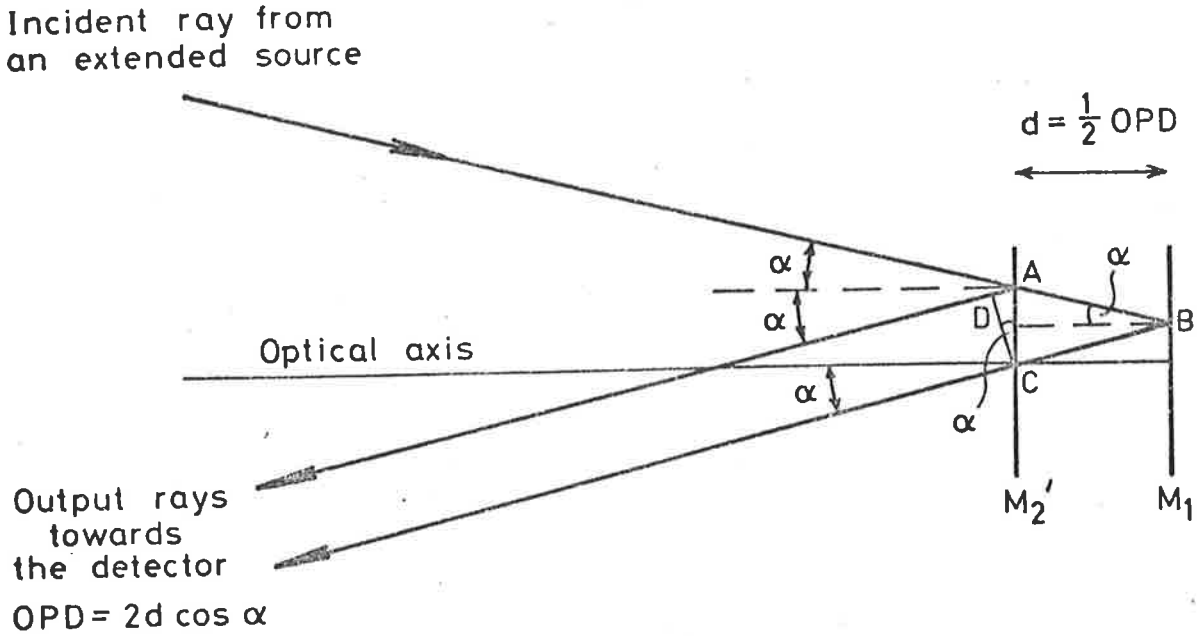

Figure 9.12 Equivalent Optical System of the Michelson Interferometer.

Showing the image of the moveable mirror M_2' in front of the fixed mirror by a distance d.

curved and they are always convex toward the thin edge of the wedge. These type of fringes are generally referred to as localized fringes (Jenkins and White, 1976, p. 244). They can be very useful in obtaining a rough estimate of the position of ZPD since, for a given mirror tilt, the curvature is opposite on either side of ZPD. At ZPD intersection the localized fringes become straight lines.

Another type of fringe can be observed by using the Michelson interferometer in what is often referred to as the "Twyman-Green" configuration. In this mode of operation the interferometer is illuminated with strictly parallel light, produced by a monochromatic point source at the principal focus of a well corrected input lens. The fringe pattern is then observed at the principal focus of a well corrected output lens (Candler, 1951; Wood, 1967). In this case all of the incident rays are parallel to the optical axis and there is no variation of angle of incidence. If the mirrors M_1 and M_2' are strictly flat and parallel and the two uniting wave-fronts at the detector are both truly plane, then the whole field of view will have uniform intensity. By producing a slight tilt on one of the mirrors, the fringes becomes straight lines equally spaced across the field of view. These fringes are generally called fringes of equal thickness. The orientation of these fringes can be altered by changing the direction of the mirror tilt. Also, the larger the mirror tilt the closer the spacing between fringes. The Twyman-Green optical configuration of the Michelson interferometer is a very powerful instrument for testing the perfection of optical components,including those of the present instrument. If one places the component to be tested in one of the optical arms of the interferometer, then the "straightness" (and

variation in separation) of the observed fringes gives a direct measure of the flatness and/or parallelism of the optical component.

In both the extended and point source configurations the fringes produced by a monochromatic source are visible for very large path differences, the limit being set only by the fact that no actual source gives perfectly monochromatic light. If a white light source is used instead, then no fringes will be seen at all except for path differences which are within a few wavelengths of ZPD.

Before any fringes can be observed, it is important that both the mirrors are mounted so that only slight adjustments are required to make them perpendicular to the optical axis. It is also important that the beamsplitter-compensator combination is mounted so that it makes an angle of as close to 45° to the optical axis as possible. Furthermore, one should aim to mount the optical components so that one is as close to ZPD as possible. The following alignment procedure was used for the initial setting up of the interferometer (coarse adjustment):

1. Locate the optical axis.

2. Mount an alignment collimator (auto-collimator, with illuminated cross) on the optical axis. Mount the moveable mirror and use its coarse adjustment to position it perpendicular to the optical axis.

3. Insert the beamsplitter-compensator combination and use the rotating pivot adjustment to ensure that it makes an angle of 45° with the optical axis.

   This was done by carefully mounting a 45° front surface reflecting prism (45°, 45°, 90°) on to the input side of the beamsplitter-compensator combination. The prism reflecting surface is then made perpendicular to the optical axis by use of the alignment collimator.

4. Mount the fixed mirror and block off the the optical beam to the moveable mirror. The coarse adjustment screws on the fixed mirror are then used to ensure that it is also perpendicular to the optical axis.

Having completed the initial set-up of the optical components, no more adjustments need to be made on either the moveable mirror or the beamsplitter-compensator combination. The next stage of adjustment (intermediate) is to use an extended monochromatic light source and obtain the circular fringes. This was done by placing a sodium lamp so that its optical rays were directed along the input optical axis. A small object such as a pin-hole in a card was inserted in front of this source. On looking into the instrument along the output optical axis, two overlapping images of the small object were observed. Other much less intense images can also be seen on either side of the main image, these are due to multiple reflections at the beamsplitter-compensator surfaces (see Figure 9.3(b)). It is quite probable that no fringes will appear when the two images of the small object seem to have been brought into coincidence. This is because the eye cannot judge with sufficient accuracy for this purpose when the two images are really superimposed. To locate the fringes it is only necessary to move the fine adjustment on the fixed mirror back and forth. Having found the fringes using an extended monochromatic light source one can vary the fine adjustment to produce at will the various forms of fringes. In order to locate the fringes in white light (fine adjustment) the monochromatic fringes were first made arcs of circles. By stepping the moveable mirror (see Section 9.6) the fringes were seen to change curvature. A region was found where the localized fringes were straight. Having now located, within rather narrow limits, the position of ZPD, the sodium light source was replaced by a white light source. The

white light fringes were then found by stepping slowly through this region. ZPD was seen to correspond to a central bright fringe, bordered on either side by about ten coloured fringes. An excellent reproduction in colour of such white light fringes is given by Michelson (1907). The final stage of adjustment is then to position the central bright fringe so that it intersects the optical axis, then use the fine adjustment to ensure that this fringe covers the whole field of view.

Prior to making the final adjustments the interferometer was set up in the "Twyman-Green" configuration. This was done with the aid of a 50 mm diameter input lens (152.4 mm focal length) and a 50 mm diameter output lens (101.6 mm focal length), both mounted on the input and output optical axis respectively. The fringes of equal thickness were observed by placing a sodium pin-hole source at the focus of the input lens and the eye at the focus of the output lens. The fringes were found to be straight to within $\lambda/10$ in both the vertical and horizontal positions, which is rather better than required. The Rayleigh criterion states that the image will be very little inferior to that produced by a perfect system, if the difference between the shortest and longest optical paths does not exceed one quarter of a wavelength (see for example, Candler, 1951). This measurement corresponds to the resultant flatness of the interferometer. It also gives a measure of the flatness and parallelism of the beamsplitter-compensator combination as the two mirrors were specified by the manufacturers to be flat to better than $\lambda/20$.

9.5 Electronics

In concept, the electronics of the TL apparatus is straightforward. This can be seen by reference to Figures 9.13-15. A linear ramp signal is compared with a thermocouple signal in a servo system which produces a linear temperature rise depending on the difference between these two signals. The light output is simultaneously recorded.

The temperature ramp control is digital, which means that it is easily interfaced for computer operations. A PET Commodore Computer (32K RAM) is used to control the running of both the 2-D and 3-D TL experiments, as well as to collect the data. Simplified block diagrams of the apparatus used for the 2-D and 3-D TL measurements are shown in Figures 9.13 and 9.14 respectively. The same electronics is used for both the 2-D and 3-D configurations, the only difference being the fact that in the 3-D configuration it is necessary to provide the appropriate signals to the moveable mirror stepping mechanism (see Section 9.6). Figure 9.15 is a block diagram of the electronic system. The photon counting system is contained in the top of the diagram and the electronics associated with the temperature ramp is contained in the bottom half. A more detailed block diagram of the digital ramp generator is given in Figure 9.16.

A precision ten turn potentiometer H is used to adjust the frequency (heating rate) of a voltage controlled oscillator (VCO, XR-2206). The VCO is adjusted so that the potentiometer varies the frequency of pulses from 20 Hz to 2 kHz over ten turns, this corresponds to heating rates from $1^{\circ}c\ s^{-1}$ to $100^{\circ}c\ s^{-1}$. This heating rate is

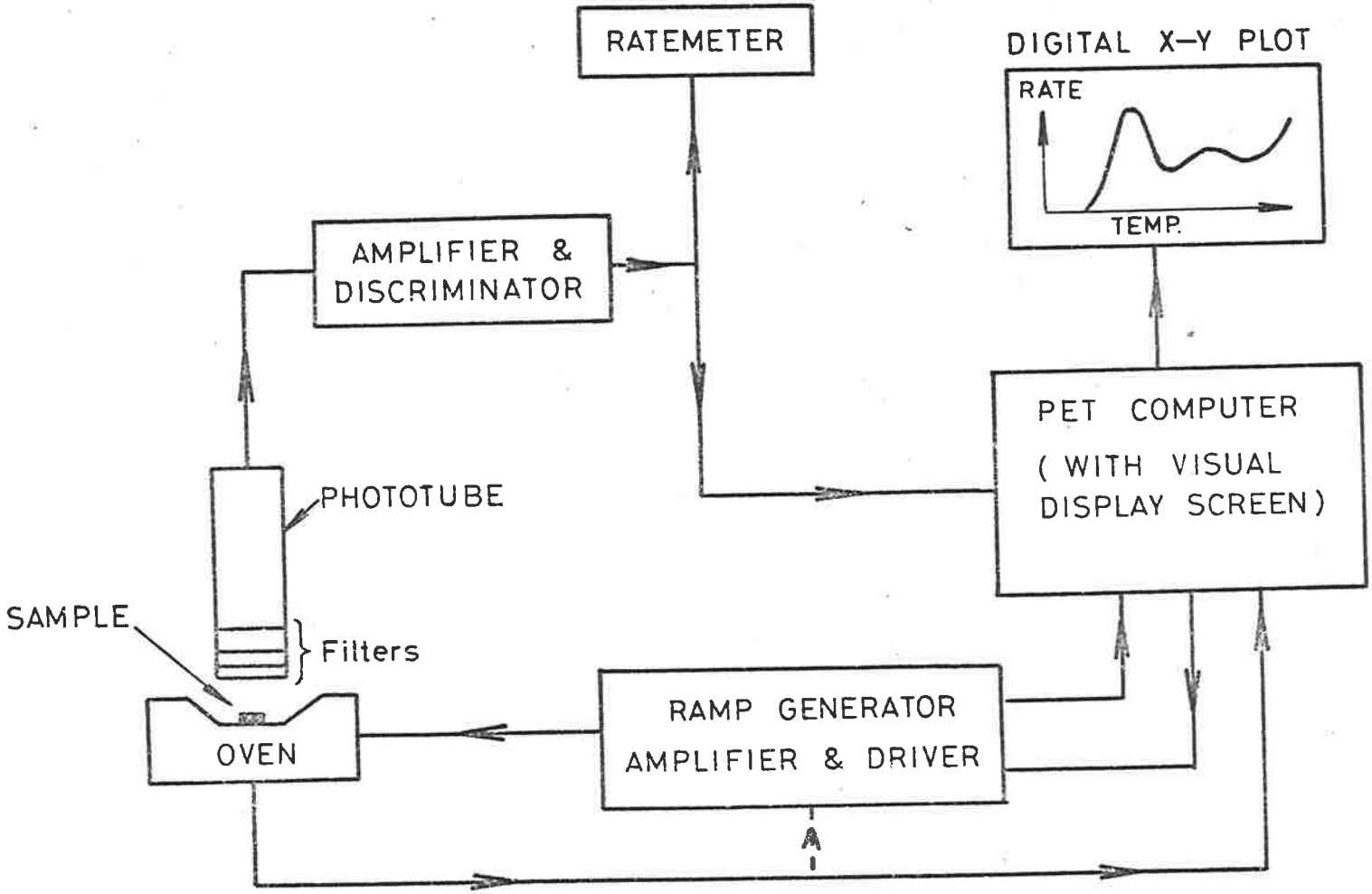

Figure 9.13 Simplified Block Diagram of the 2-D TL Apparatus.

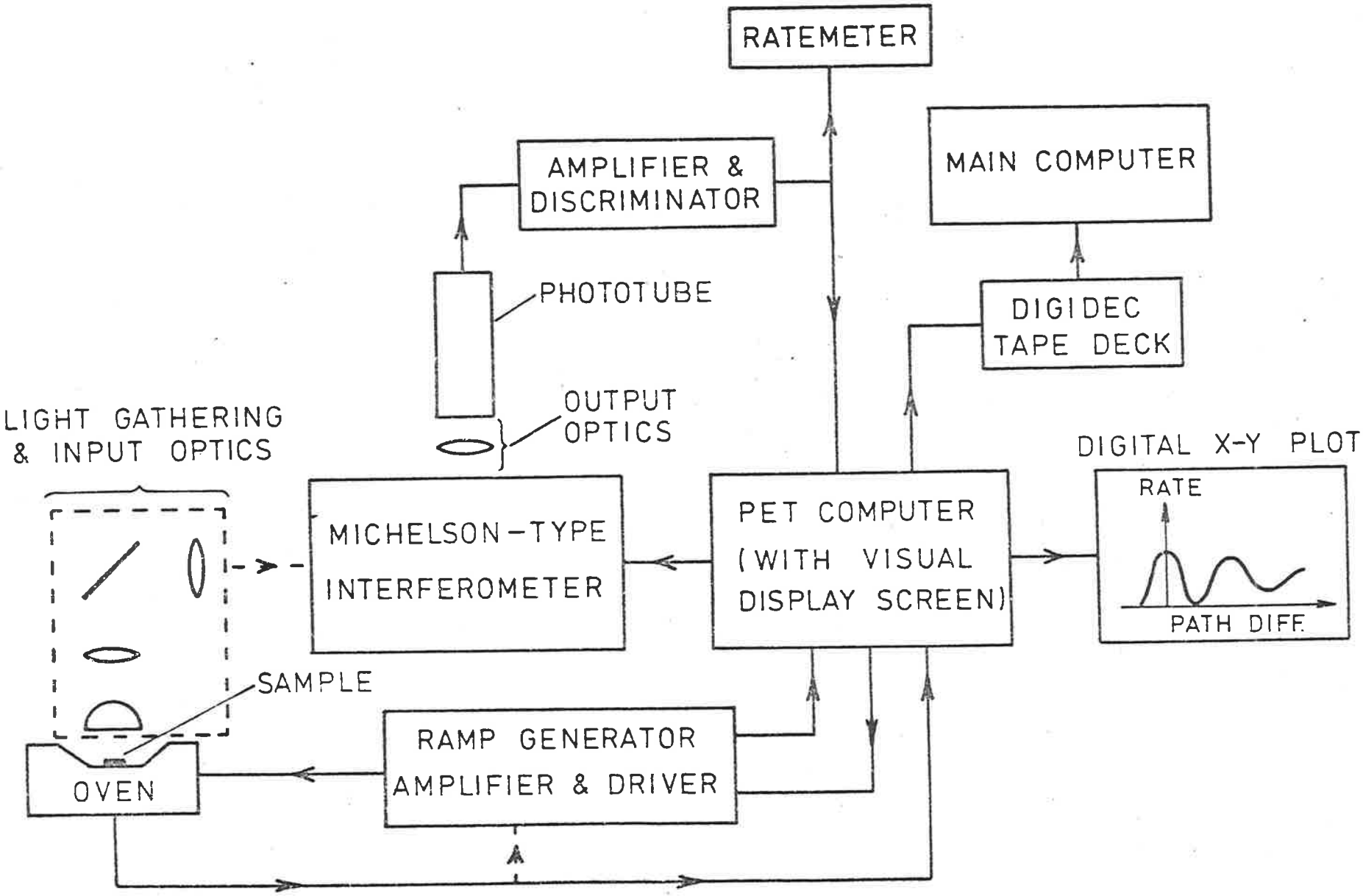

Figure 9.14 Simplified Block Diagram of the 3-D TL Apparatus.

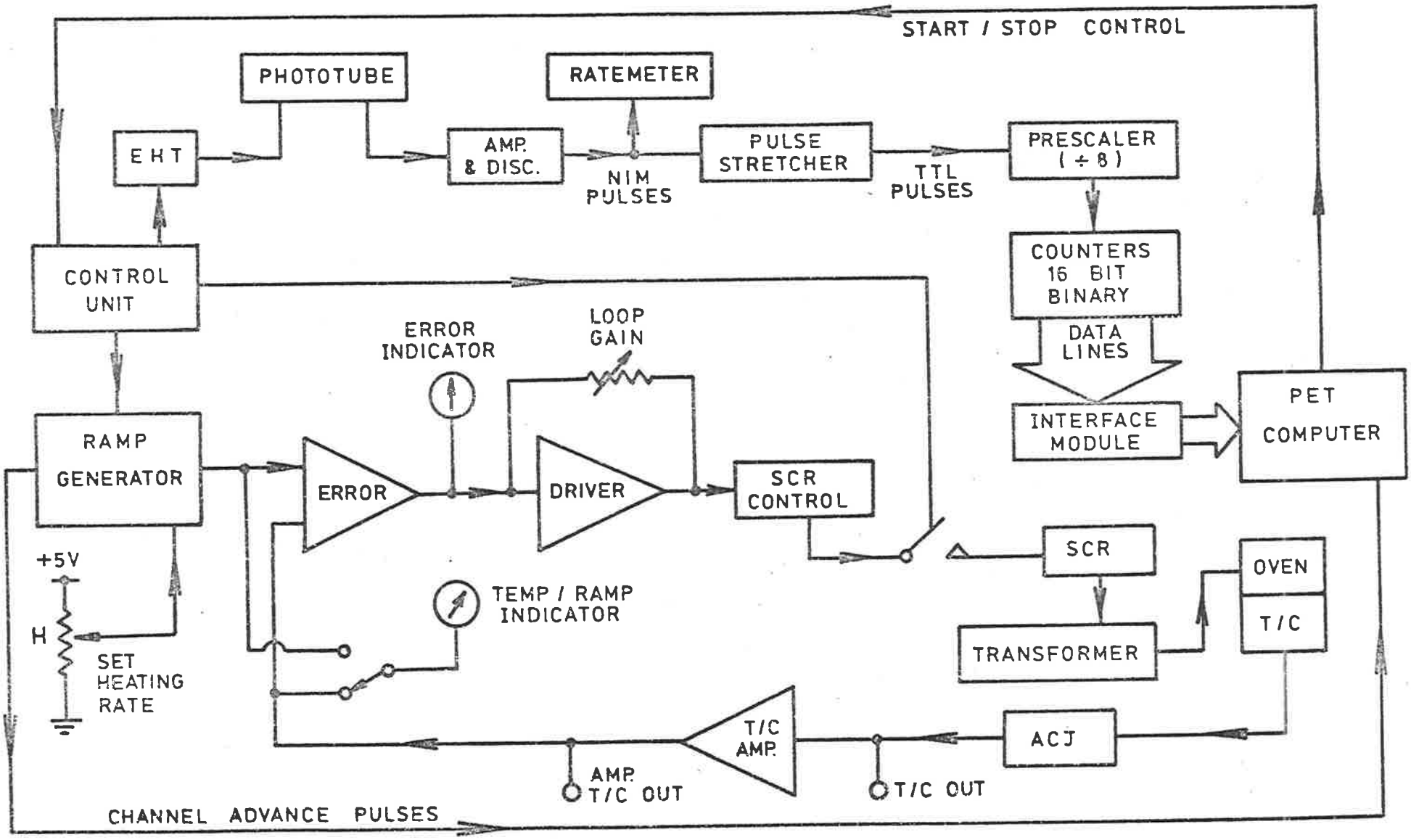

Figure 9.15 Simplified Block Diagram of TL System

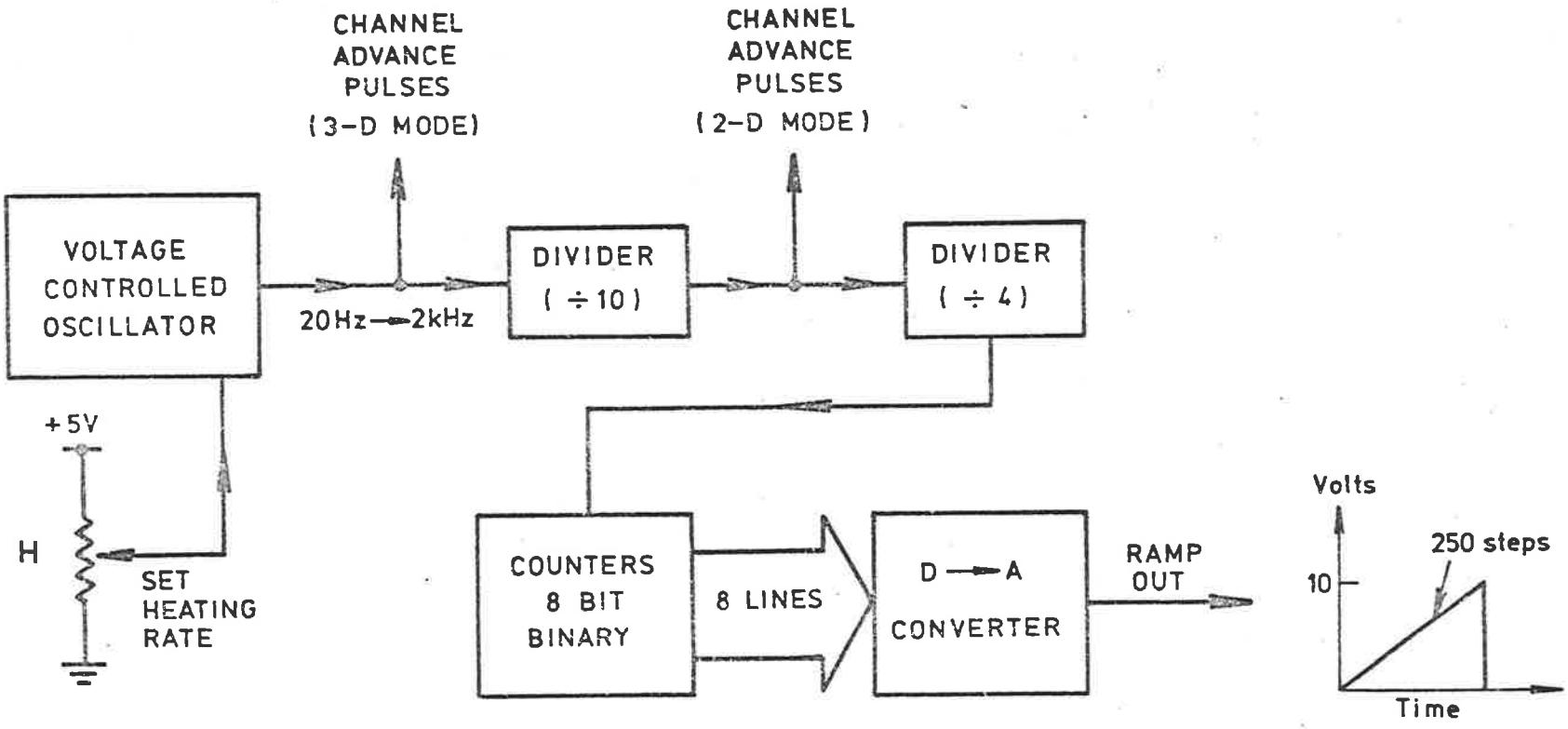

Figure 9.16 Block Diagram of Digital Ramp Generator.

reproducible to within ± 1%. The pulses are then divided by ten to provide channel advance pulses for the 2-D configuration. They are then divided by four and passed to an eight-bit binary counter, the output of which is fed to an eight-bit digital-to-analogue converter. The output of the digital-to-analogue converter is a ramp signal adjusted so that 10.24 volts amplitude corresponds to 10240 channel advance pulses (given out by the VCO). The slope of the ramp is determined by the frequency of the VCO.

Attached to the nichrome heating strip, which is situated in the oven, is a chromel-alumel thermocouple which monitors the temperature. Incorporated is an automatic cold junction (ACJ-2, supplied by Ancom Limited, Cheltenham, England), this provides an equivalent ice-point reference for the thermocouple cold-junction. The amplified thermocouple and ramp signals are compared with each other in a servo system, which drives the oven depending on the difference between the two signals. The output of the VCO is also fed directly to the PET for experimental control purposes. That is, the commencement and completion of a particular run is controlled by the PET. The oscillator pulses are also used to drive the moveable mirror scanning mechanism, when operating in the 3-D configuration and are therefore synchronised to the heater ramp and hence the temperature. The maximum temperature of 512° C corresponds to 10240 channel advance pulses in the 3-D mode of operation, whereas it only corresponds to 1024 channel advance pulses in the 2-D mode.

The output from the photomultiplier is fed to a pulse amplifier and discriminator (Ortec 9302), the output of which are NIM pulses (typical width of 5 ns, maximum frequency 100 MHz). The NIM pulses

are converted to TTL and stretched to a width of 50 ns, which limits the maximum frequency to about 20 MHz. These pulses are then prescaled by a factor of eight before being fed to a sixteen-bit binary counting chip (8253), which consists of three individual counters. Two of these are used alternately to count the input pulses; while one is counting the other is being read by the PET. Also incorporated is a photon ratemeter (Ortec 9349), which gives a visual indication of the rate while the experiment is actually running.

The data is stored in the PET in the form of digital glow-curves or interferograms, depending on whether one is operating, in the 2-D or 3-D mode; these can be visually displayed on the computer screen monitor. From there the data can be displayed on a digital X-Y plotter (Hewlett Packard Model 7225A). The interferograms can also be output on cassette tape (Digidec Model PI 70) which can be read by a larger computer, where the fast Fourier transform or other computational processes can be completed. A transform based on the Cooley-Tukey algorithm has also been written in the PET computer language, namely BASIC (see Chapter 10, Appendix E). This enables the PET to complete the spectral calculations without the need for a larger computer, albeit slowly and one at a time.

9.6 The Moveable Mirror Scanning Mechanism

One of the most important aspects of the interferometer design is the moveable mirror scanning mechanism. Having completed the interferometer optical alignment, it is important that accurate parallelism is maintained between the fixed and moveable mirrors. That is, the moveable mirror must be kept parallel to itself while moving from ZPD to maximum displacement; too much tilting will result in false

spectral features (see for example, Vanessa and Sakai, 1967). Murty (1960) has shown that the maximum permissible angular error in parallelism, $\Delta\theta$, is given by the Equation

$$\Delta\theta \sim \frac{\lambda_{min}}{20d} \qquad (9.4)$$

where d is the mirror diameter and λ_{min} is the shortest wavelength present in the spectrum. From Equation (9.4) it can be seen that a precise mirror drive is essential and this is particularly so in the visible wavelength region. For our instrument, where d is 30 mm and λ_{min} is about 300 nm, $\Delta\theta$ is about 5×10^{-7} radians. Using Equation (8.22) one can estimate the maximum OPD, beyond which no improvement in resolution is obtained. For a resolution of 20 nm this gives us a maximum OPD of about 21.1 μm at a wavelength of 650 nm (or about 10.5 μm at 300 nm), which corresponds to a maximum mirror travel of about 10.6 μm (for a one-sided interferogram). Another important requirement is that the incremental step size in OPD must be smaller than half the smallest wavelength present in the spectrum, if "aliasing" is to be avoided (see Section 8.5). This means that, for a minimum wavelength of 300 nm, the increments in mirror travel must be smaller than 75 nm. It is also important that this step size is constant and accurately known if meaningful spectra are to be obtained.

In order to achieve these rather strict requirements, the moveable mirror mount is mounted on a parallel leaf spring arrangement as shown schematically in Figure 9.17. This consists of two identical phosphor/bronze leaf springs (50.5 mm length, 40.0 mm width, 0.7 mm thickness) clamped between two identical parallel steel blocks (36.0 mm length, 40.0 mm width, 18.0 mm thickness), the bottom one of which is fixed to the interferometer base plate. A movement which is very close

to parallel mirror translation is then obtained by applying a horizontal force to the top platform. This type of parallel spring movement is often used to move optical components a distance of up to several millimetres, with the degree of cantilever bending being quite small (see for example, James and Sternberg, 1969). Jones and Young (1956) have discussed the accuracy of this type of spring movement. They state that the angle of cantilever bending is approximately given by the relationship

$$\Delta\theta = \left(\frac{2t^2}{b^2 \ell}\right) x \qquad (9.5)$$

where $\Delta\theta$ is the angle of bending of the top platform relative to the bottom platform, t is the thickness of the springs, ℓ is the length of the springs, b is the length of platform between springs and x is the horizontal displacement of the top platform. From Equation 9.5 one can see that the amount of cantilever bending depends on the square of the spring thickness, thus making it desirable to use springs as thin as possible. However, the springs have to carry a load which means that some sort of compromise in thickness is necessary. This is especially so since the spring strength is proportional to the cube of the thickness, whereas it is only proportional to the first power of the width. For a mirror displacement of 20 μm, which is about the maximum travel required for a complete two-sided interferogram, the amount of cantilever bending can be estimated (using Equation 9.5) to be about 1.5×10^{-7} radians. This is about a factor of three smaller than the calculated permissible amount of cantilever bending.

An attempt was made to drive the parallel spring arrangement with the aid of a differential screw turned by a computer controlled

stepping motor. The principle of this scanning mechanism is schematically illustrated in Figure 9.17. The differential screw itself consists of two overlapping fine threads of slightly different pitch, the effective displacement for each turn corresponding to the difference in pitch. Several differential screws were constructed, varying in effective pitch from about 6 μm to 8 μm. A stepping motor providing 96 steps rev^{-1} should then produce individual mirror displacement steps in the range 62.5 nm to about 83.3 nm, the exact step size depending on the effective pitch.

A good measure of the linearity of the scanning mechanism can be obtained by applying a small tilt to the fixed mirror and visually observing the relative displacement of the straight line fringes, produced by a monochromatic source, as they move across the field of view (see Section 9.4). An even better measure is obtained by considering the actual interferogram produced by a monochromatic source. Using a He-Ne laser (632.8 nm) one expects the interferogram to be a cosine function, with the mirror displacement between successive maxima being 316.4 nm. Although the differential screw principle is a plausible concept in theory, it was found that the effective forward mirror displacement was too irregular to be of any use. It was at first thought that the irregularities in the scanning motion could be due to random variations in the motor steps. However, this was discounted as the irregularities were still present as the differential screw was turned manually. Furthermore, a damping dashpot mounted on the stepping motor shaft produced no significant improvement.

As an alternative, the differential screw was replaced by a differential spring and micrometer head driving mechanism. This scanning

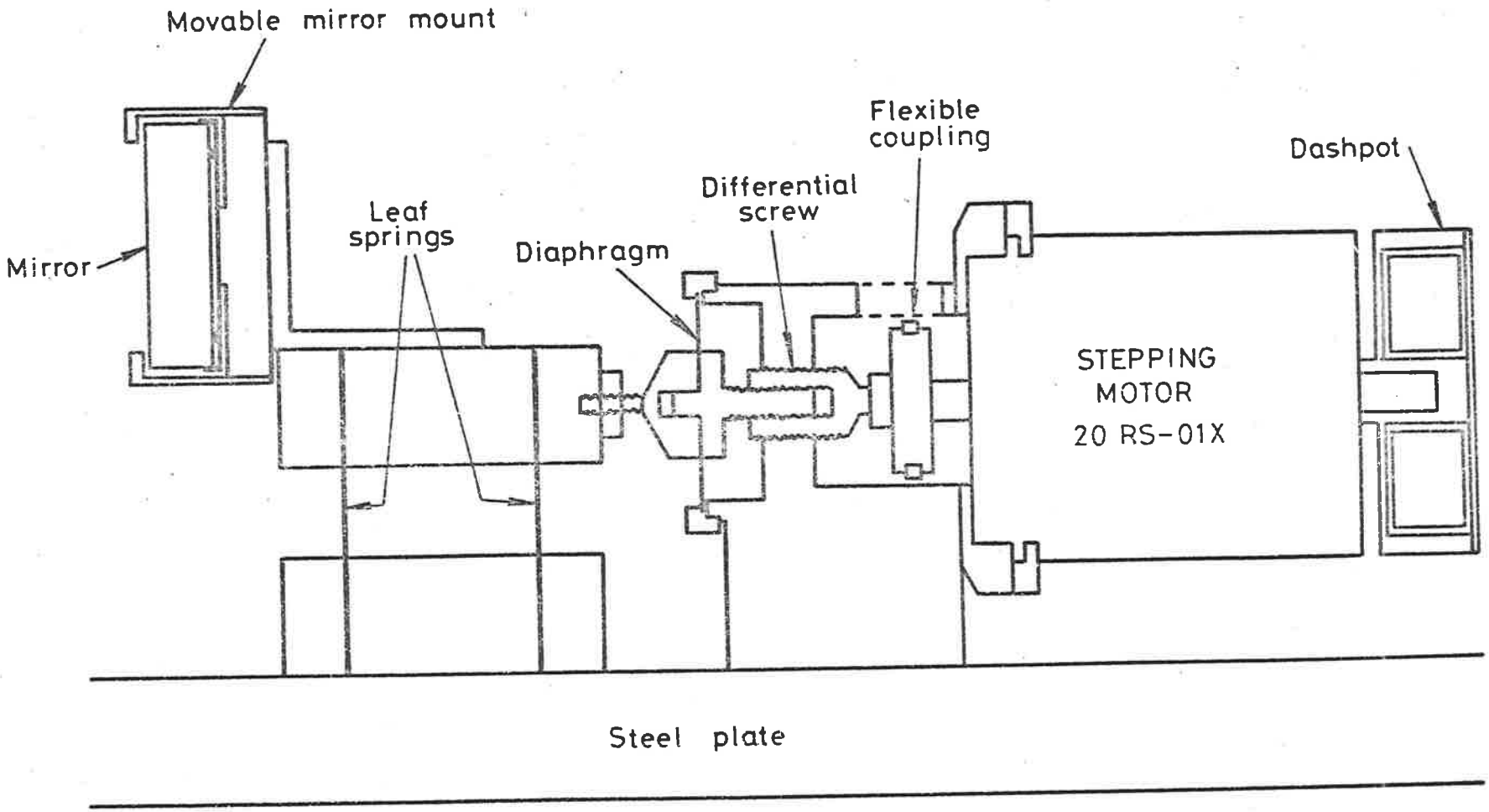

Figure 9.17 Schematic Diagram of the Differential Screw Driving mechanism for the moveable mirror.

mechanism is illustrated schematically in Figure 9.18. It relies on the differential deflection of two leaf springs of different stiffness and is a common device for achieving small displacements inexpensively. In this case the parallel leaf spring combination shown in Figure 9.17 was used as the stiff spring and a narrower leaf spring, mounted between the stiff spring and the micrometer head, was used as the "thin" spring. The effective pitch of the scanning mechanism is given by the pitch of the micrometer (0.5 mm) multiplied by the spring stiffness demagnification factor. A demagnification factor of about 150 was obtained by using a "thin" phosphor/bronze leaf spring measuring 60 mm in length, 13.5 mm in width and 0.7 mm in thickness. Using a stepping motor supplying 46 steps rev^{-1}, a resultant mirror displacement of about 69.4 nm $step^{-1}$ was obtained. This type of scanning mechanism was found to be much better than that of the differential screw. The interferograms produced at sampling rates of up to about 1 Hz were quite good. However, at higher scanning rates the quality of the interferograms were found to deteriorate significantly. The main problem being the high frequency oscillations produced on the "thin" leaf spring while stepping. Although the incorporation of a damping dashpot (see Figure 9.17) produced some improvement, the Q of the system remained too high and the differential spring type scanning mechanism was also rejected.

Having discarded both the differential screw and differential spring scanning mechanisms, it was decided to consider the use of piezo-electric translator devices. A scanning mechanism using a Burleigh PZ-44 piezo-electric translator was constructed. The design

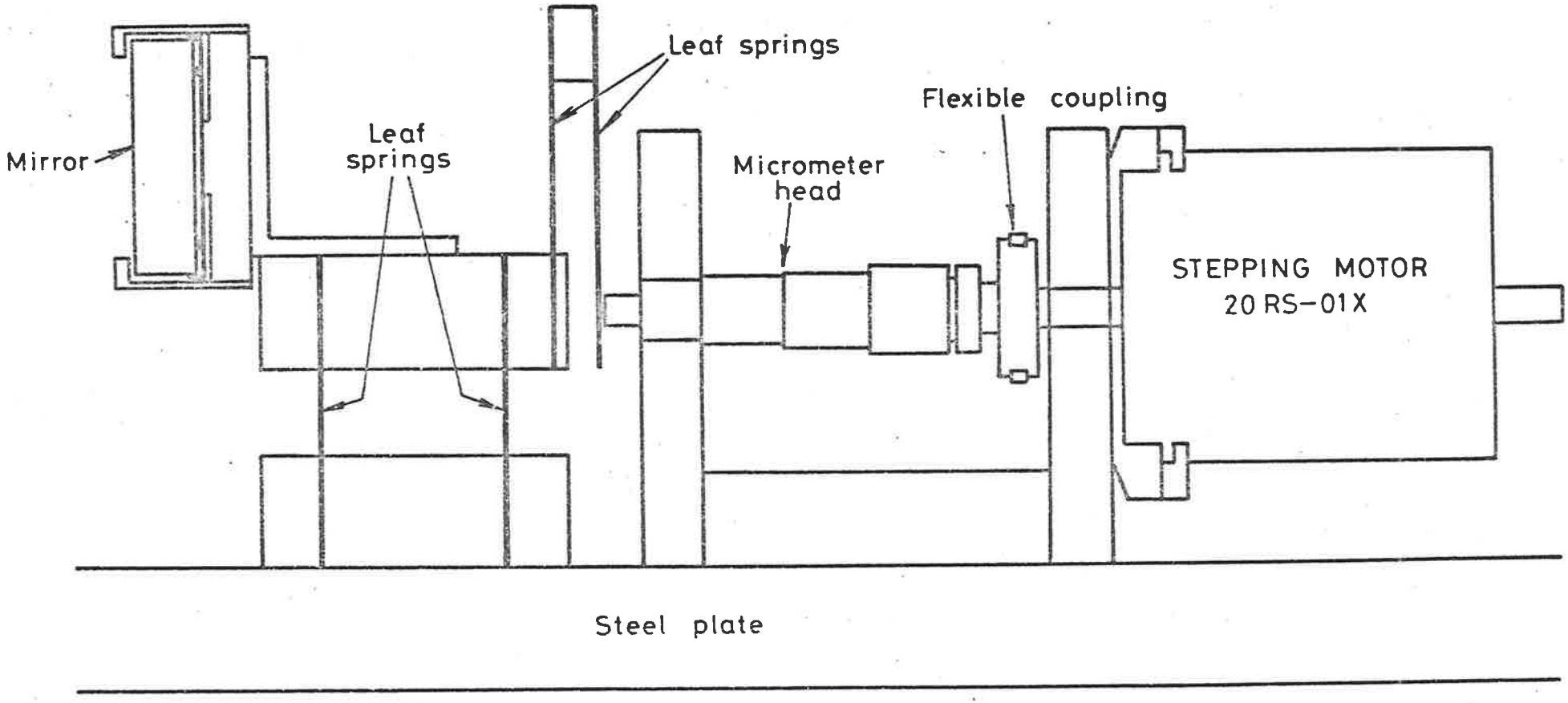

Figure 9.18 Schematic Diagram of the Differential Spring and Micrometer Driving Mechanism for the moveable mirror.

is schematically illustrated in Figure 9.19. The active element of the PZ-44 pusher is a piezo-electric transducer (PZT) that contracts when a voltage is applied. A maximum voltage of 1000V produces a displacement of about 40 μm, which is longer than we actually require. Attached to the PZT is a spring loaded ceramic cap, which provides the motion as the voltage is applied to the PZT. This cap is spring loaded for two important reasons. First, it assures that all the motion of the PZT is transferred to the ceramic cap. Second, it reduces the possibility of creep often found in piezo-electric devices of this type. The vibration problem encountered with the differential spring driving mechanism should be eliminated, as the ceramic cap of the PZ-44 is in direct contact with the top platform of the parallel spring assembly. Furthermore, the manufacturers claims that the PZ-44 has a flat frequency response to about 2 kHz which is much better than actually required. The PZ-44 is mounted on a Newport Research Corporation (NRC) translation stage (Model 430-1). Also incorporated is a differential micrometer (NRC, DM-13), the fine adjustment of which is used for the initial setting up of the interferometer (see Section 9.4). A photograph which includes this scanning mechanism has already been shown (see Figure 9.7). The PZ-44 is driven by a Burleigh RC-44 programmable ramp generator, which provides a variable ramp of amplitude up to 1000V. The incremental step size of the PZ-44 is limited by the smallest incremental voltage which can be supplied, as well as by the noise and ripple on the power supply. Using the RC-44 one can easily resolve 1 volt out of 1000. This corresponds to a lower limit incremental step size of about 40 nm, which is smaller than actually required. Included on the RC-44 is a digital display which reads the ramp voltage to the nearest volt.

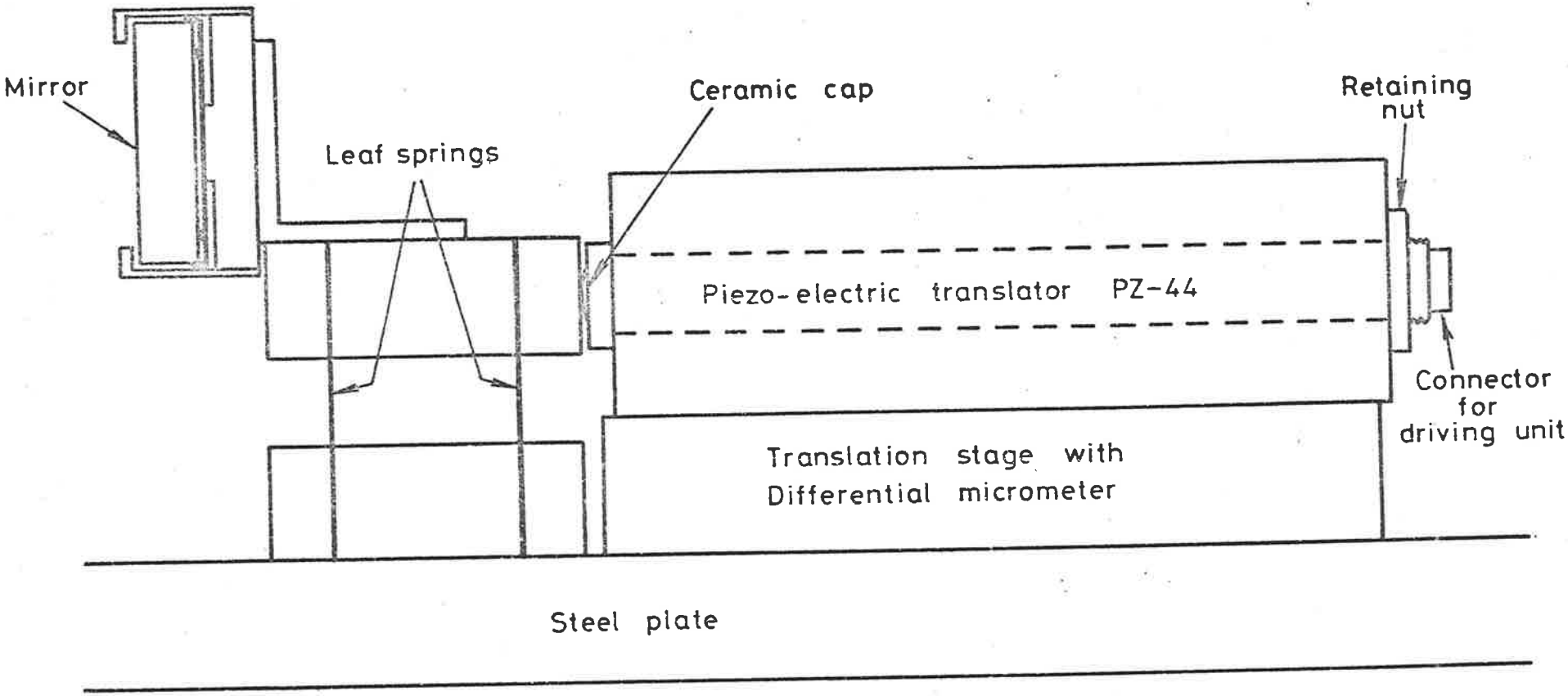

Figure 9.19 Schematic Diagram of the Piezo-electric Translation Driving Mechanism for the moveable mirror.

Figure 9.20 is a block diagram of the electronics which actually drives the PZ-44. The temperature ramp channel advance pulses (see Figure 9.16) are used to provide the drive for the PZ-44, rather than using the RC-44 directly. Included in the driving circuitry is the facility to have both an adjustable bias level and an adjustable incremental step size. These are varied using precision ten turn potentiometers both located on the interface and control unit. The other stepping parameters are all controlled by the PET computer, determined by the instructions given via the keyboard; these include : the rate of stepping (heating rate), the number of steps per scan and the total number of scans required for a particular 3-D TL glow-curve. Also incorporated is the facility to manually step the PZ-44 translator. This is very useful for setting up purposes as one can manually one-step the translator either forward or backward while visually observing fringe shifts.

The piezo-electric driving mechanism was found to be appreciably better than that of the differential spring. Figure 9.21 shows a typical interferogram produced with a He-Ne laser beam placed at the input of the artificial "steady light source" chamber (see Figure 9.10). A neutral density filter was inserted at the input in order to reduce the intensity. In this case the incremental step size was about 40 nm and the total number of steps was 128. The time taken was 25.6s, which corresponds to a sampling rate of 5 Hz. Similar interferograms were also observed at sampling rates up to 20 Hz without any appreciable degradation in quality. However, the piezo-electric drive system does suffer from hysteresis effects and this is illustrated in Figure 9.22. This shows typical forward and reverse scan interferograms produced by

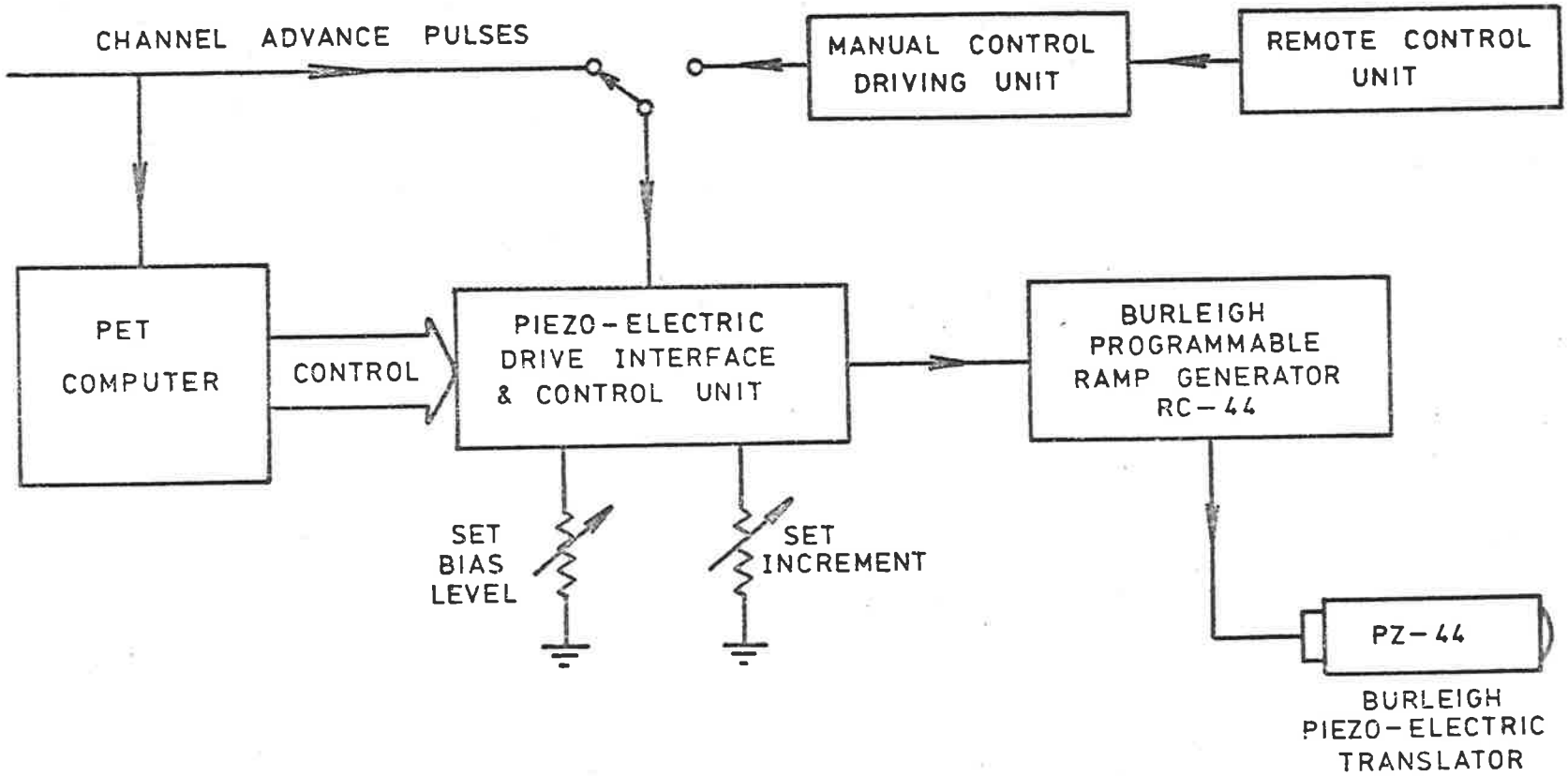

Figure 9.20 Block Diagram of the Electronic Driving Circuitry for the Piezo-Electric Translator.

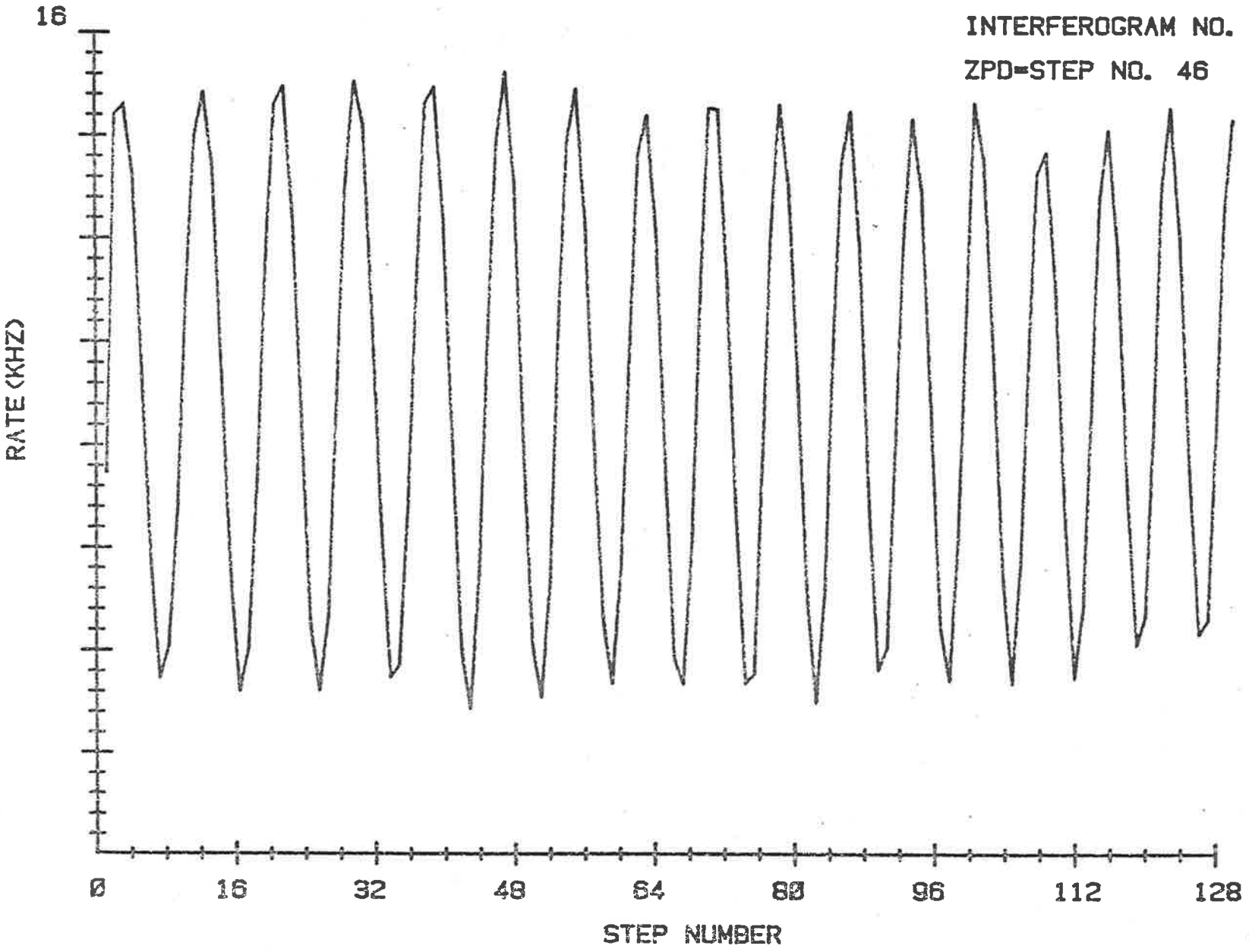

Figure 9.21 Interferogram produced by a He-Ne Laser Source

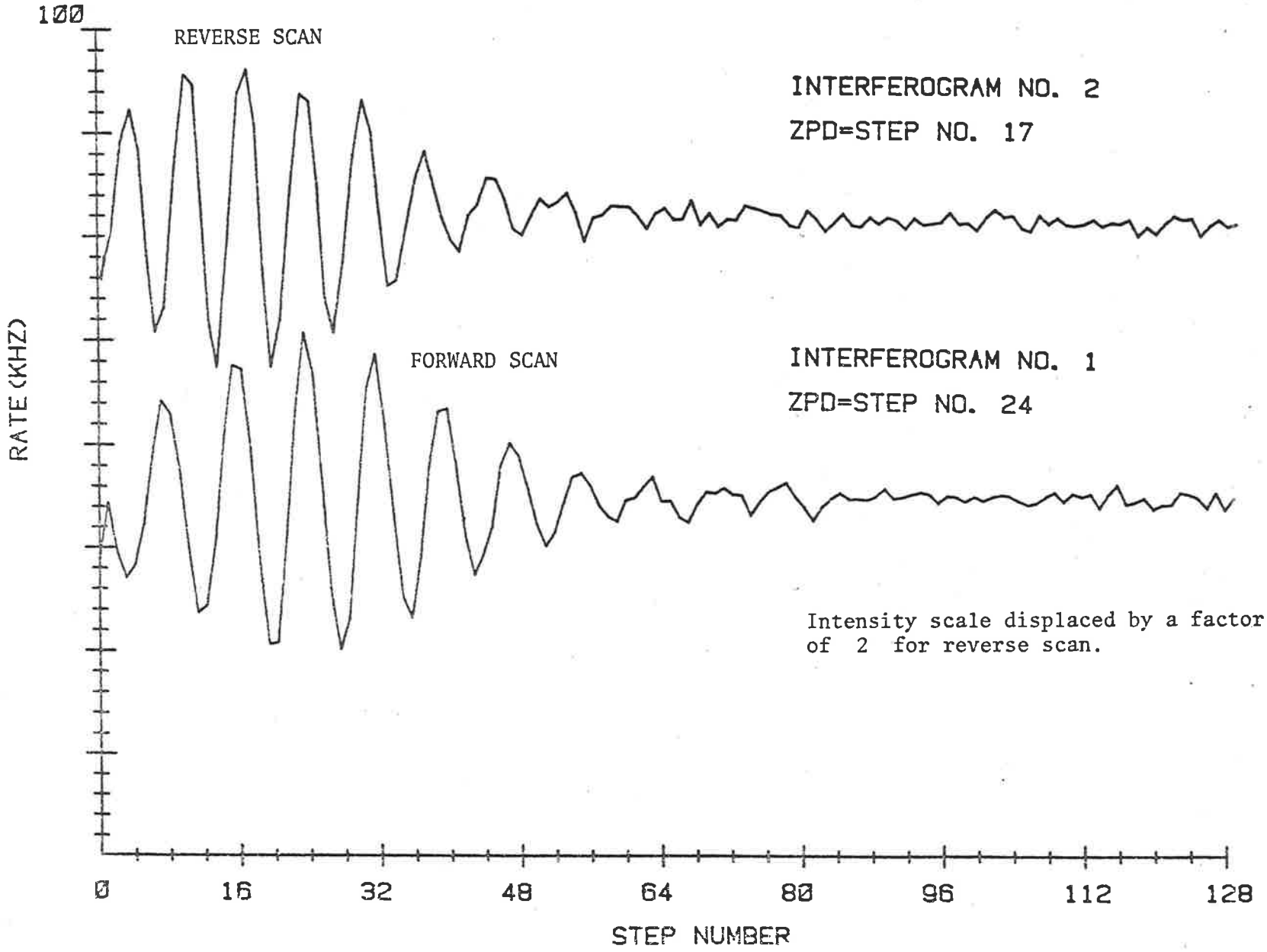

Figure 9.22 Forward and Reverse Scan Interferograms produced by a White Light Source

placing a miniature "white light" source in place of the laser beam. Using such a broad-band wavelength light source one obtains an interferogram which consists only of a few peaks which are symmetric about the ZPD intensity maximum. This type of light source is hence ideal for detecting any shifts in the ZPD position. In this particular case the incremental step size was 40 nm and the ZPD displacement between the forward and reverse scan interferograms was about 7 steps. At present, this hysteresis effect is allowed for by working the system into a "cyclic" state before data is recorded (by repeated cycling) and by allowing for the differences between forward and reverse scans in the analysis. Once the system is in a cyclic state, ZPD is reproducible from one run to the next. Consideration is being given to changing the operation to a slow forward scan (during which the interferogram would be recorded) followed by a fast return so that all actual interferograms would have the same ZPD, but this is not part of the system reported here.

Figure 9.23 is a photograph of the overall TL apparatus.

Figure 9.23 Photograph of the Overall TL Apparatus.


PET
CBM

CHAPTER X

THE COMPUTATION OF SPECTRA : RESULTS

10.1 Introduction

Thic Chapter is concerned with the computational aspects involved with obtaining spectra and a discussion of some preliminary results. The procedure used for computing spectra from the observed interferograms is discussed in Section 10.2 and the various functions of the main computer program are outlined in Section 10.3.

The interferometer was tested using a variety of constant intensity light sources and the results obtained are discussed in Section 10.4.

In summary, an evaluation of the existing system and suggestions for further improvements are given in Section 10.5.

10.2 The Computation of Spectra

It has already been shown that, for a Michelson interferometer, the resolution varies inversely as the maximum OPD (Equation 8.21) and that for an extended source the ultimate resolution limit depends on the input solid angle (Equation 8.18). For an extended source, the result of the beam divergence is that there is a spread in the computed wavenumber (wavelength) spectrum. Equation 8.18 can be re-written as

$$\Delta\sigma = \sigma \left(\frac{\Omega_m}{2\pi} \right) \qquad (10.1)$$

where $\Delta\sigma$ corresponds to the difference in spectral wavenumbers of the central and extreme off-axis optical rays. It can be shown the spread

in the computed spectrum is entirely on the low-wavenumber side of the source wavenumber (see for example, Bell, 1972). This means that for a monochromatic source of wavenumber σ_0, the computed spectrum is spread between the wavenumbers σ_1 and σ_2, where

$$\sigma_1 = \sigma_0 \left[1 - \frac{\Omega_m}{2\pi} \right] \tag{10.2}$$

and $\sigma_2 = \sigma_0$

Hence, the mean wavenumber of the spectrum is given by

$$\overline{\sigma} = \frac{\sigma_1 + \sigma_2}{2} = \sigma_0 \left[1 - \frac{\Omega_m}{4\pi} \right] \tag{10.3}$$

In the infrared wavelength region, this spread is quite small and often ignored. However, for a large throughput interferometer operating in the visible, the wavenumber shift must be taken into account if accurate spectra are to be obtained. For our instrument the mean wavenumber of the computed spectrum is about 20% lower than the source wavenumber.

The quality of the computed spectrum is also affected by the optical alignment of the interferometer. After being reflected by the mirrors the images formed from the two optical beams must be accurately superimposed on the detector if maximum modulation in the interferogram is to be achieved. There are two types of misalignment which cause a degradation in the interferogram and hence in the computed spectrum. The possibility of misalignment of the movable mirror resulting from a retardation-dependent tilt, produced by the drive mechanism has already been discussed in Section 9.6. The result of such a mirror tilt is to produce a variation in OPD over the

aperture of the mirrors. The effect on the resolution of the computed spectrum is thus similar to that produced by the effects of beam divergence due to having an extended source. The other possibility of misalignment is that of a constant mirror tilt of one mirror with respect to the other, which does not change with mirror motion, this was discussed in Section 9.4.

Bell (1972) shows that for a perfectly aligned interferometer, which utilizes a (constant intensity) point source (collimated light), the interferogram intensity at large path differences $I(\infty)$, which corresponds to incoherent interference between the two beams, equals half the intensity at ZPD. This means that one can write the interferogram as

$$[\, I(x) - \tfrac{1}{2}\, I(o) \,] = [I(x) - I(\infty) \,] \qquad (10.4)$$

which shows that for a point source, the interferogram is the variation of the resultant intensity about the incoherent signal level found at large path differences. However, for an extended source Equation (10.4) is no longer valid. In this case there will be an additional constant component of intensity, ΔI, reaching the detector, which is independent of OPD. Equation (10.4) can then be re-written as

$$[I(x) - I(\infty)] = [(I(x) + \Delta I) - (I(\infty) + (\Delta I))\,] \qquad (10.5)$$

This equation indicates that for an extended source, the true interferogram may be re-defined as the magnitude of the intensity variation $(I(x) + \Delta I)$ about the large OPD intensity $(I(\infty) + \Delta I)$. It should be pointed out that a small but constant mirror tilt

mis-alignment would also produce a constant intensity reaching the detector, which is independent of OPD. Hence, a small variation in OPD across the aperture of the mirrors, caused by either beam divergence or constant mirror tilt, can be allowed for by simply redefining the DC level of the measured interferogram. This result is important as far as the computation of spectra from a constant intensity source are concerned. The general relationship between a sampled two-sided interferogram, and the computed spectrum (Equation 8.23) becomes

$$B_{s,A}(\sigma) = \sum_{j=-\frac{N}{2}}^{(\frac{N}{2})-1} S(j) \exp(-i\, 2\pi\sigma j\Delta x)$$

where $S(j) \equiv A(j\Delta x)\,[\, I(j\Delta x) - I(\infty)\,]$ (10.6)

The first step in the spectrum computation process is to compute the interferogram by subtracting $I(\infty)$ from each of the measured intensity values $I(j\Delta x)$. $I(\infty)$ can be determined by calculating the average of the last few points of the interferogram. Alternatively, it can be determined by calculating the average value of all the points in the interferogram. In this case $I(\infty)$ is given by

$$I(\infty) \simeq \frac{1}{N} \sum_{j=-\frac{N}{2}}^{(\frac{N}{2})-1} I(j\Delta x) \qquad (10.7)$$

where N is the total number of data points. Equation (10.7) is a good approximation for $I(\infty)$ because the interferogram contains as many constructive as destructive interference points.

However, when measuring interferograms produced by TL emission, the source intensity varies as a function of temperature and hence OPD. This means that the baseline correction intensity (incoherent signal) is no longer constant, and hence the above correction procedure is not valid. This TL intensity variation is a problem

which to some extent can be overcome by measuring the interferograms over small variations in temperature. This is a requirement in the present application since the wavelength characteristics of the TL signal may well change as a function of temperature (see Section 6.2). The problem therefore largely takes care of itself. The baseline intensity of a given interferogram can be separately determined by measuring another interferogram of the same source, in which the movable mirror is fixed at some large OPD. This is of course what is measured in the conventional 2-D TL configuration. Alternatively, the baseline correction may be done on a computer by fitting a polynomial function to the measured interferogram, so that the integral of the entire interferogram remains zero. All spectral computations reported here will assume that the baseline intensity is constant and the approximation given by Equation (10.7) will be used. The consequence of using this rather crude approximation is that false spectral features appear in the low-wavenumber region of the computed spectrum. However, this is not a serious problem, as these false features are well separated from the true spectral features (see Section 10.4). It should also be pointed out that the consequence of completely omitting this baseline correction is that a spike will appear in the first data point of the computed spectrum (zero frequency), as this corresponds to the DC term of the interferogram (see Appendix E).

The next step in the computation process is to locate the position of ZPD. For a perfectly aligned interferometer, the measured interferogram is symmetric about ZPD (even function) and hence one need only carry out a cosine Fourier transform for one side of the

interferogram. However, in practice it may not be easy to arrange for a digital sample to be taken at exactly ZPD. This means that the digitized interferogram will not necessarily reflect the symmetry of the analogue interferogram and the digitized signal will not be completely symmetric about ZPD. Asymmetry in the interferogram can also be caused by faults in the interferometer itself, such as poor optical alignment. The presence of asymmetry in the measured interferogram is equivalent to a phase error being introduced. Phase errors cause sinusoidal components to be added to the cosine transform of the interferogram leading to severe distortions in the computed spectrum. A number of authors have proposed ways in which phase errors may be corrected (see for example, Foreman *et al*, 1966; Mertz, 1967). If the phase error ϕ is solely due to mis-sampling the position of ZPD by a distance β, then the computed spectrum $B_c(\sigma)$ is related to the true spectrum $B(\sigma)$ by the relationship

$$B_c(\sigma) = B(\sigma) \exp(-i\phi)$$

$$\text{where } \phi = 2\pi\sigma\beta \qquad (10.8)$$

In this case, the true spectrum can be obtained by computing the square root of the sum of the squares of the real and imaginary parts of the computed spectrum (power spectrum) for a two-sided interferogram. That is, the phase error is removed by computing

$$| B_c(\sigma) | = [(P_c(\sigma))^2 + (Q_c(\sigma))^2]^{\frac{1}{2}} = |B(\sigma)| \qquad (10.9)$$

where $P_c(\sigma)$ is the real part (cosine transform) and $Q_c(\sigma)$ is the imaginary part (sine transform) of the computed spectrum. Bell (1972) points out that by using this method it is possible to remove any

linear phase error in wavenumber, without having a precise knowledge of the ZPD position. However, there are disadvantages in using Equation (10.9). The most obvious is that for a given wavelength resolution, it takes twice as long to record a two-sided interferogram compared with the one-sided interferogram. Furthermore, the process of obtaining the absolute value by the square root of the sum of the squares is non-linear. This means that the noise in the computed spectrum is changed from a function randomly fluctuating around zero to one that fluctuates around some positive value .

An alternative phase correction method is to calculate the phase error function from a short two-sided interferogram (Mertz, 1967). It It can be shown that as long as the phase error $\phi(\sigma)$ is a slowly varying function of wavenumber, it can be eliminated by computing $P_c(\sigma)$ and $Q_c(\sigma)$ from a short two-sided region and using

$$\phi(\sigma) = \arctan \left[\frac{Q_c(\sigma)}{P_c(\sigma)} \right] \qquad (10.10)$$

(see for example, Bell, 1972). A power spectrum of the entire interferogram is then calculated with reference to the largest signal as ZPD. The phase correction is then made on the computed spectrum by multiplying each frequency by the cosine of the difference of the reference phase and the phase error given by Equation (10.10). Using this method one obtains a phase corrected spectrum in which the noise is randomly positive and negative.

The method used for locating the ZPD position is to measure a short two-sided (or a complete two-sided) interferogram and then choose ZPD to correspond to the maximum intensity. A visual check can

then also be made for symmetry about ZPD. While this method works very well for interferograms produced by constant intensity light sources (i.e. constant baseline intensity), it is not always suitable when measuring interferograms produced by TL emission. This aspect will be further discussed in Section 10.4.

Prior to computing the spectrum it may be necessary to apodize the interferogram data in order to reduce the size of the sidelobes in the spectrum, caused by truncating the interferogram data. The effects of triangular apodization have already been discussed in Section 8.3. Many other window functions are commonly used in the field of FTS (see for example, Childers and Durling, 1975; Chamberlain, 1979; Rabolt and Bellar, 1981). The particular apodizing function chosen depends on the data and the circumstances at hand. A very popular apodizing function is one suggested by Tukey (see Childers and Durling), which is a raised cosine wave applied to the first and last ten percent of the data (for a two-sided interferogram) with a weight of unity applied in between. In this case the interferogram values are multiplied by $A(j\Delta x)$ where

$$
\begin{aligned}
A(j\Delta x) &= \frac{\sin^2 \pi j}{0.2N} = \tfrac{1}{2}\left[\, 1-\cos \frac{\pi j}{0.1N} \,\right], && 0 \leqslant j \leqslant 0.1N \\
&= \frac{\sin^2 \pi (N-j)}{0.2N} = \tfrac{1}{2}\left[\, 1-\cos \frac{\pi (N-j)}{0.1N} \,\right], && 0.9N \leqslant j \leqslant N \\
&= 1 && , \; 0.1N \leqslant j \leqslant 0.9N \\
&= 0 && , \text{ elsewhere}
\end{aligned}
\qquad (10.11)
$$

Another popular trigonometric function is that attributed to Happ and Genzel (1961), which is of the form

$$A(j\Delta x) = 0.54 + 0.46 \cos \frac{\pi}{2} \frac{|j-z|}{N-Z}, \quad 0 \leq j \leq N$$

$$= 0 \qquad \text{, elsewhere} \qquad (10.12)$$

where Z corresponds to the ZPD position.
BASIC subroutines have been written for both the Tukey and the Happ-Genzel apodization procedures, and they are listed in Appendix F.

In order to compute the spectrum from the apodized interferogram (Equation 10.6) one can use the fast Fourier transform (FFT) algorithm, proposed by Cooley and Tukey (1965). This algorithm requires that all of the interferometric data is available at the start of computation and that all the spectral output data points are computed simultaneously. By using the Cooley-Tukey algorithm one achieves a significant saving in computation time, compared with the conventional Fourier transform computational technique. However, one of its basic requirements is that the number of data points to be transformed must be of the form $N = 2^n$ (for some positive inter n). Furthermore, it is essential that these data points are equally spaced, otherwise false features may appear in the computed spectrum. The savings in computation time are achieved by clever choice of the output sampling points. Numerous authors have outlined the basic principles of the Cooley-Tukey algorithm so these will not be discussed here, (see for example, Bell, 1972). A FFT subroutine based on the Cooley-Tukey algorithm was written for the PET computer

and this is presented with a test program and a brief explanation in Appendix E. One of the properties of the FFT is that the spacing of the data points in wavenumber (and hence wavelength) space depends on the total number of data points in Fourier transform space. That is, the sampling interval used in the interferogram domain completely determines the sampling interval in the spectral domain. For a one-sided interferogram consisting of N points, sampled at OPD intervals of Δx satisfying the sampling theorem (Equation 8.26), the spectral wavenumber sampling interval $\Delta\sigma$ will be given by

$$\Delta\sigma = \frac{1}{N\Delta x} \tag{10.13}$$

The general method of computing the spectrum from the recorded intensity signal versus OPD can be summarized as follows:

1. Measure $I(j\Delta x)$ values by recording the signal versus OPD,

2. Determines the baseline intensity as a function of OPD and subtract this from the measured intensity values. For a constant intensity source the base-line intensity is constant and the interferogram is given by $[I(j\Delta x) - I(\infty)]$.

3. Determine the position of ZPD. For a one-sided interferogram $I(o)$ must correspond to the first data point, whereas for a two-sided interferogram it must be situated somewhere in the middle of the scan.

4. Multiply the interferogram by the apodizing function $A(j\Delta x)$ to give the apodized interferogram values $S(j)$.

5. Compute the spectrum via the Cooley-Tukey algorithm. The obtained spectrum is then wave-number shifted, due to having an extended source.

A spectrum obtained from the measurement of a short two-sided interferogram may also be corrected for any possible phase errors. The spectrum must then be corrected for instrumental wavelength response.

10.3 The Main Computer Program

The recording and subsequent data analysis and displays of both the 2-D TL glow-curves and 3-D TL interferograms (and spectra) are done via the same computer program, which is stored on cassette tape. A listing of this program is given in Appendix G. A machine language subroutine is used to start the temperature ramp, read the counters and decide when the maximum temperature has been reached (see Section 9.5). The remaining part of the program is written in BASIC. After the machine language subroutine has been written into memory a subroutine is automatically run to check whether the required electronic interfaces and oven controls are all present. One is then presented with two alternatives :

1. Run 2-D TL configuration,
2. Run 3-D TL configuration.

For the 2-D configuration, one must specify the required heating rate (1 to 100° C s^{-1}) and maximum temperature (maximum value of 512° C) of the glow-curve. At the completion of a 2-D run, one is faced with

the following alternatives :

1. Run a new 2-D TL configuration,
2. Run 3-D TL configuration,
3. Graph the current 2-D TL glow-curve on the computer display screen (specifying which temperature region is to be displayed),
4. Plot the current 2-D TL glow-curve on digital X-Y plotter.

For the 3-D configuration, one must specify the following parameters :

(a) The heating rate, which must be in the range 1 - 100°C s^{-1} (in multiples of 0.5°C s^{-1}),

(b) The temperature increment per movable mirror step, A1, which must be either 0.1 or 0.2°C,

(c) The number of sampling points per interferogram, A2. One has a choice of either 64, 128 or 256 steps,

(d) The number of interferograms required, which must be a multiple of two. The maximum number available depends on the temperature increment per step, the number of steps per interferogram and the maximum temperature. For a maximum temperature of 512°C the number of interferograms available is variable from 10 (A1 = 0.2°C, A2 = 256) to 80 (A1 = 0.1°C, A2 = 64), which corresponds to temperature intervals variable from 51.2°C down to 6.4°C.

Having completed a 3-D run one is faced with the following alternatives:

1. Run 2-D TL configuration,

2. Run a new 3-D TL configuration,

5. Graph a current 3-D TL interferogram on the computer display screen (specifying the number of the interferogram that is to be displayed).

6. Plot a current 3-D TL interferogram on the digital X-Y plotter (specifying which number interferogram is to be plotted).

7. Compute the spectrum of a particular interferogram. The ordinates of both the real and imaginary parts of the spectrum are then displayed on the computer screen and the corrected spectrum is plotted on the digital X-Y plotter.

10.4 Testing and Preliminary Results

Tests of the operation of the interferometer are reported in this Section.

Prior to the commencement of a particular run, the usual procedure is accurately to locate the ZPD position by measuring the interferogram produced by a miniature white-light source. A good quality white-light source interferogram (short two-sided) is shown in Figure 10.1. In this case the incremental step size was 40 nm and the total number of steps 64.

It has already been mentioned that the piezo-electric mirror drive system suffers from hysteresis effects (see Figure 9.22).

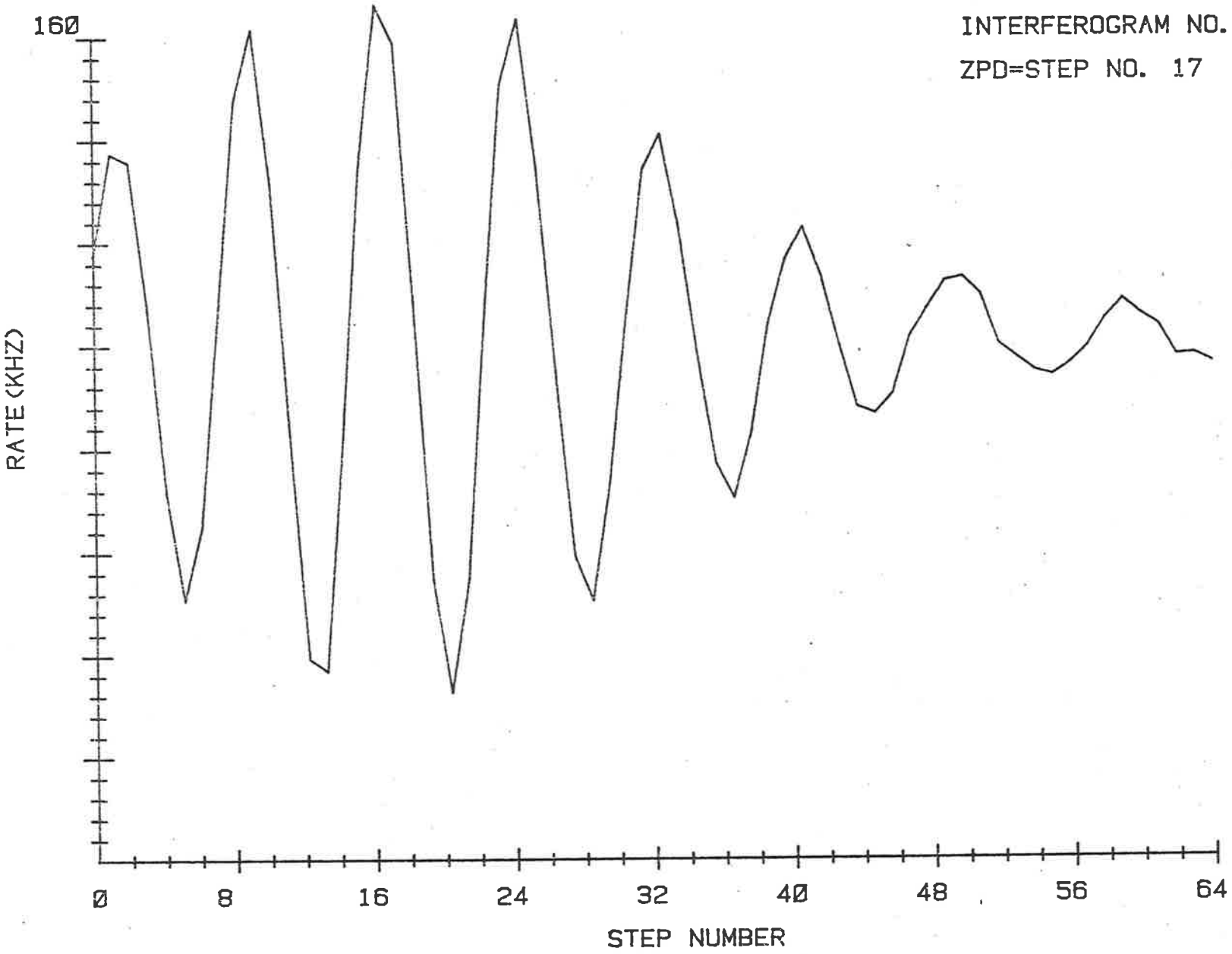

Figure 10.1 A short two-sided interferogram produced by miniature White-light source.

For this reason, it is important to check on the reproducibility of the mirror drive system once it has been worked into a "cyclic" state. An example of the reproducibility is illustrated in Figure 10.2, which is a plot of ten successive (forward scan) white-light source interferograms. One can see that the reproducibility is within a fraction of a step, the incremental step size being 40 nm.

Although the ZPD position is reproducible from one scan to the next (once in a "cyclic" state), one is still faced with a non-linear mirror drive system. While this is not a severe problem in the present case, it may well become so if improved performance is desired and some comments on this are to be found in Section 10.5.

It will be recalled that the interferogram produced by a monochromatic (i.e. He-Ne laser) source is a cosine function. Such an interferogram was shown in Figure 9.21. Figure 10.3 shows the Fourier transform (spectrum)as computed from a one-sided interferogram produced by the laser source (632.8 nm). In this particular case, the power spectrum is plotted as a function of wavenumber increments (see Equation 10.3). As expected, the recovered spectrum is sharply peaked at around 640 nm, the resolution being about 40 nm. The fact that the Fourier transform is symmetric means that only half the transform values are actually required in order to obtain the complete spectrum; this phenomenon is discussed in Appendix E. Some "false detail" is also seen in the spectrum, the reasons for which have already been outlined in detail. In the present case, it is due mostly to the truncation of the interferogram.

In order to test the overall performance of the system, a variety of constant intensity light sources was used. Interferograms

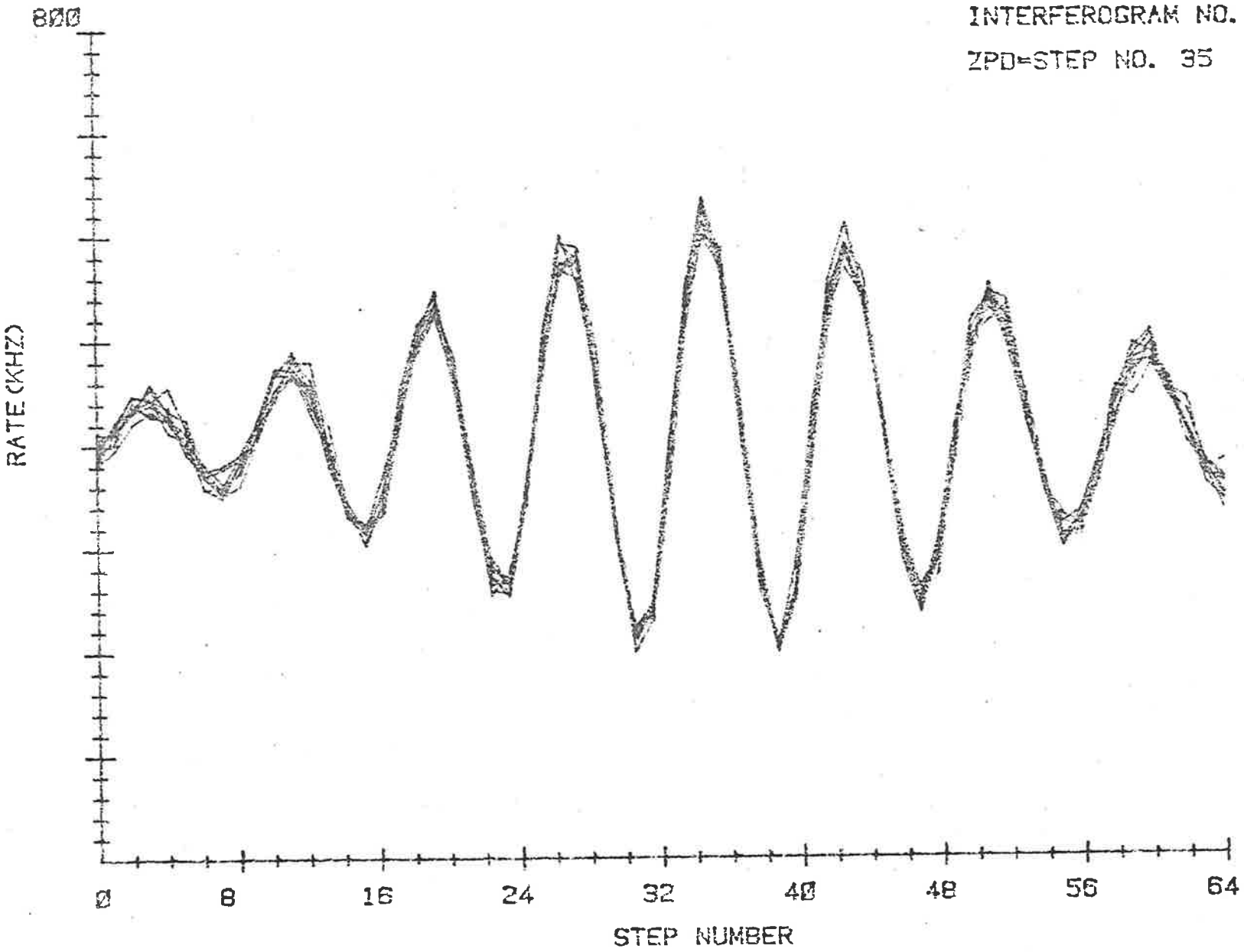

Figure 10.2 Plot of ten successive (Forward scan) White-light source interferograms.

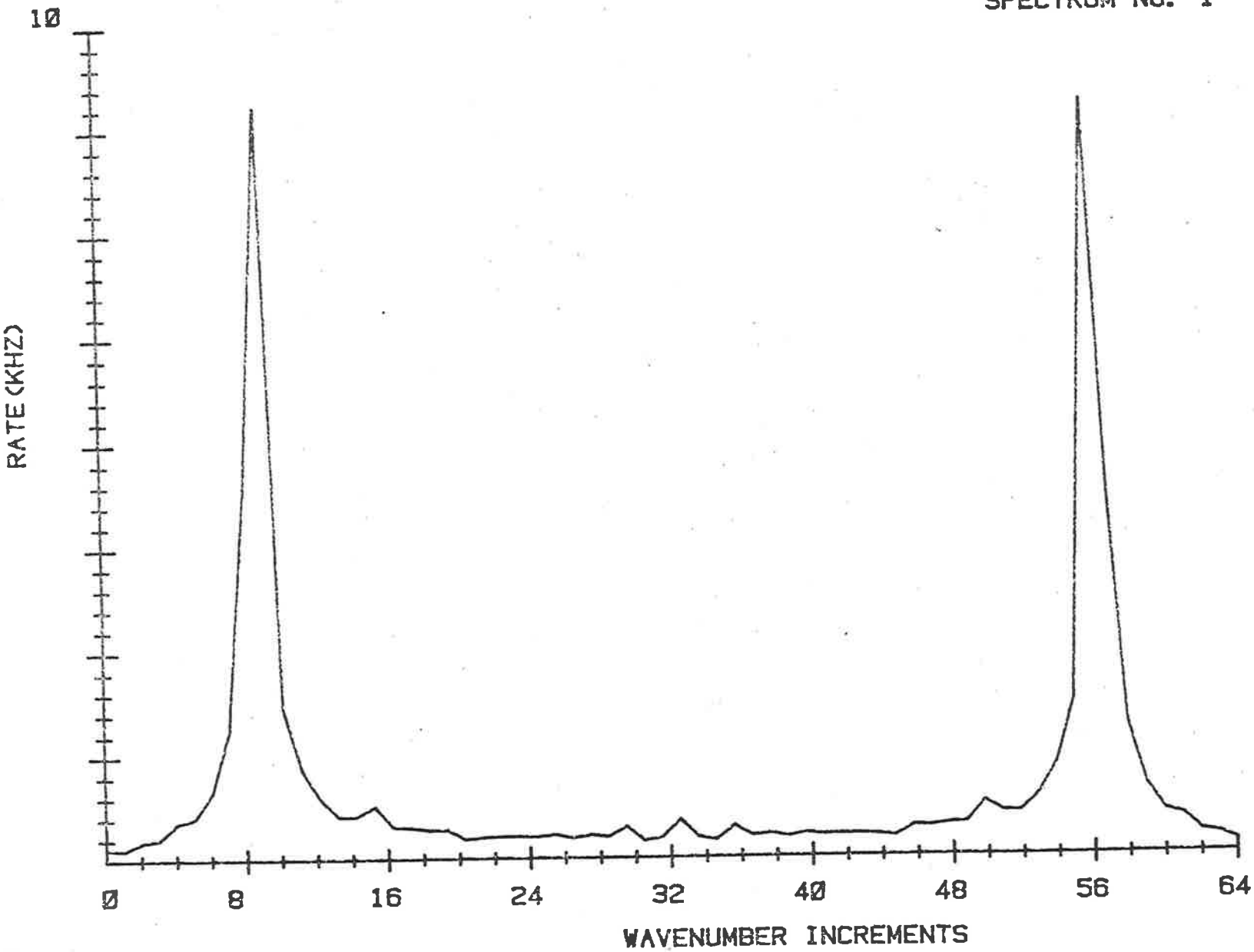

Figure 10.3 Spectrum computed from a one-sided interferogram produced by the laser source.

were measured by placing different coloured light emitting diodes (LED's) at the input of the artificial "steady light source" chamber (see Figure 9.10). Some typical short two-sided interferograms produced by blue, green, yellow and red LED's are shown in Figures 10.4, 10.5, 10.6 and 10.7 respectively. The corresponding emission spectra, supplied by the manufacturers, are shown in Figure 10.8(a). The green, yellow and red LED's have relatively narrow spectral bandwidths (typical half-intensity bandwidths of 30 to 40 nm), with their peak emissions being at about 565 nm, 585 nm and 635 nm respectively. The blue LED has a much broader emission spectrum (half-intensity bandwidth of about 90 nm), with the peak emission being at about 480 nm. The measured interferograms nicely show the characteristic features to be expected. Firstly, the OPD between successive interferogram maxima increases as the wavelength increases. Secondly, for the narrow spectral bandwidth LED's, the amplitude of oscillations (about the DC level) decreases more slowly as one moves away from the ZPD position, as compared with the broad band spectrum.

The spectrum computation procedure outlined in Section 10.2 was used to compute spectra from the interferograms shown in Figures 10.4 - 10.7.

The Fourier transform computation results in an "apparent" spectrum. In order to obtain the true spectra it is necessary to correct the computed spectra for the instrumental response. That is, one needs an accurate measure of the relative efficiency of the instrument as a function of wavelength. An absolute intensity light source, calibrated for spectral irradiance over the entire visible wavelength range, has been on order from the Australian Measurement Laboratories for more than six months, but it had not arrived at the time of

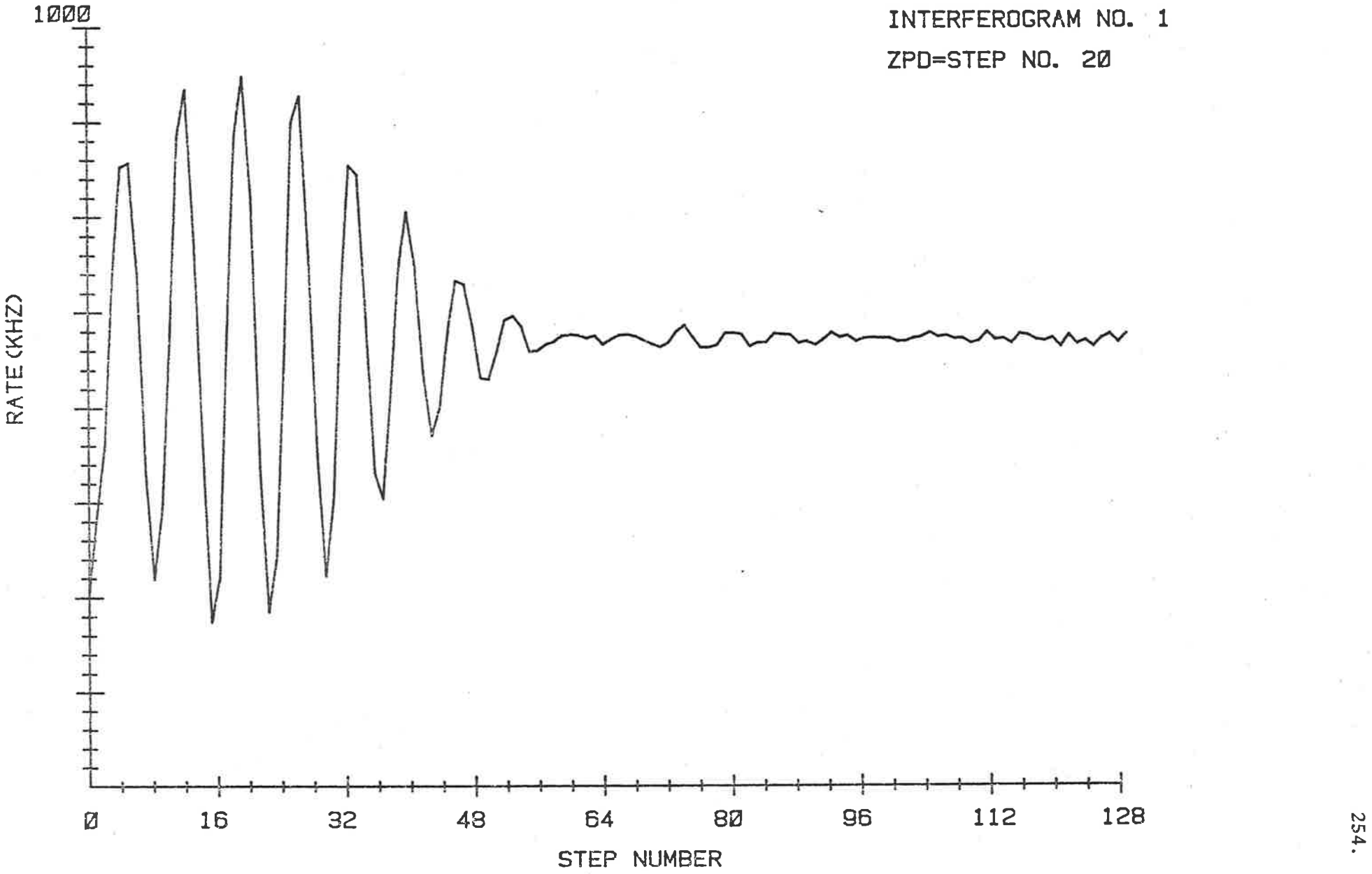

Figure 10.4 Short two-sided interferogram produced by Blue LED.

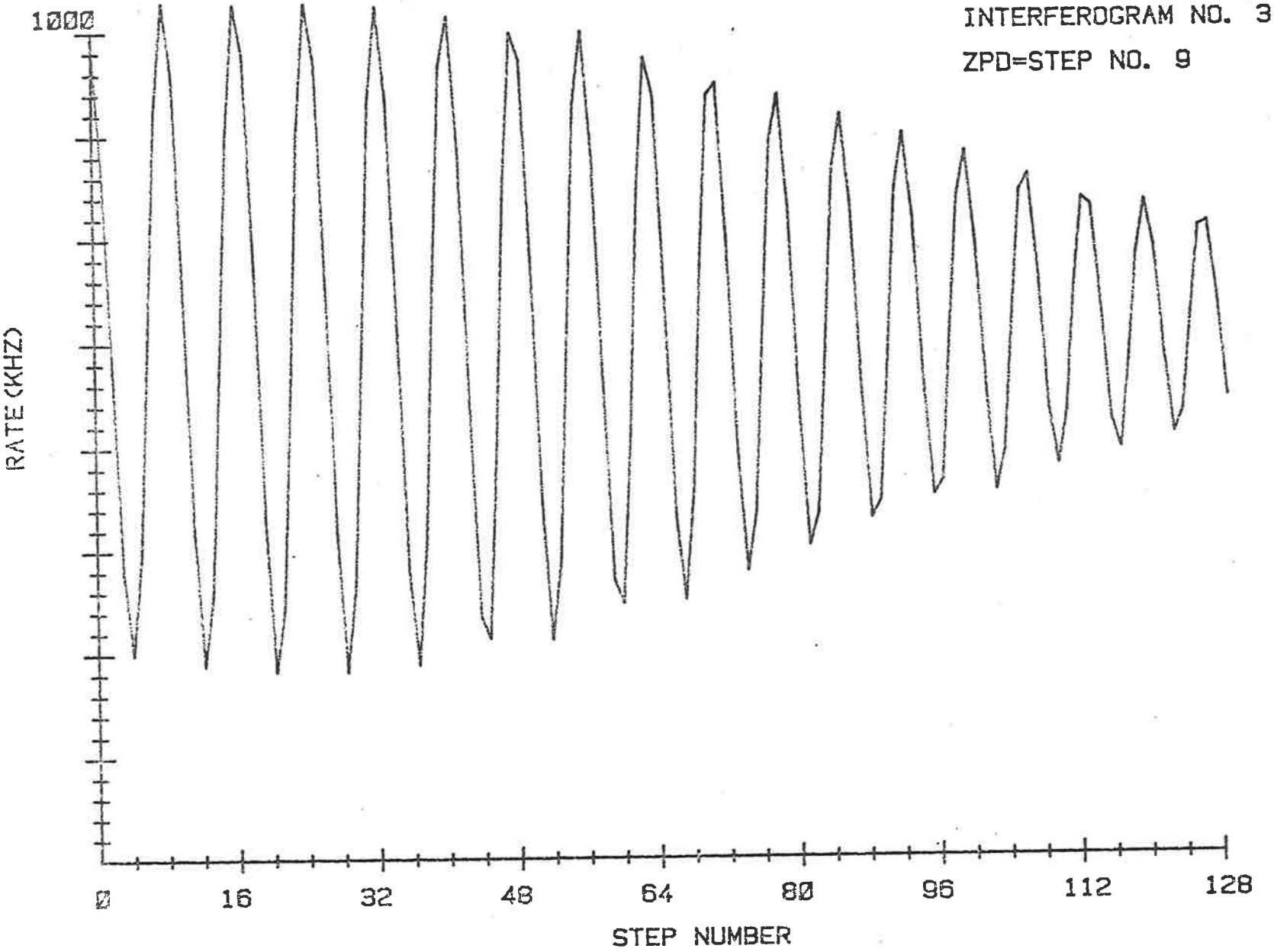

Figure 10.5 Short two-sided interferogram produced by Green LED.

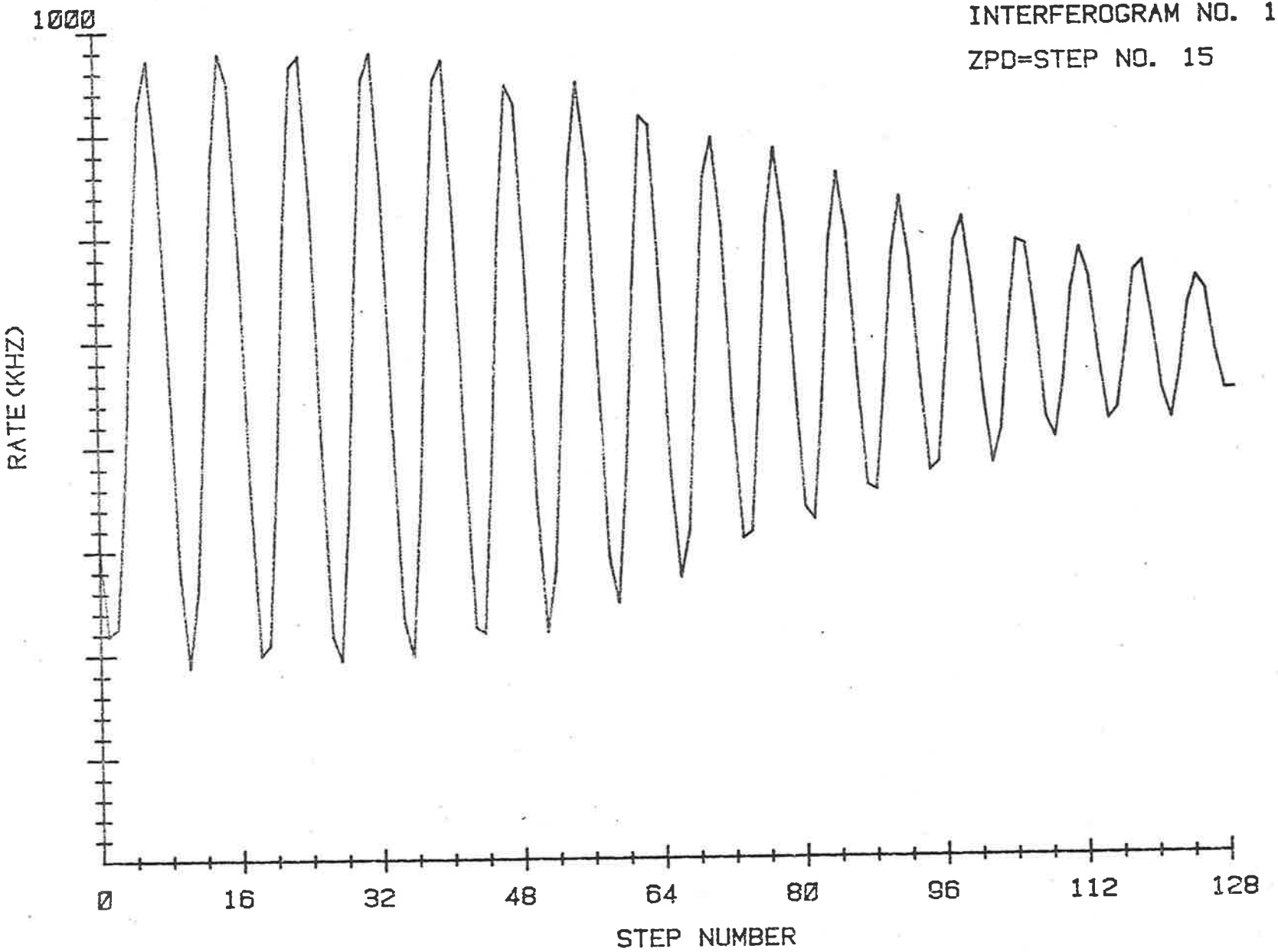

Figure 10.6 Short two-sided interferogram produced by Yellow LED.

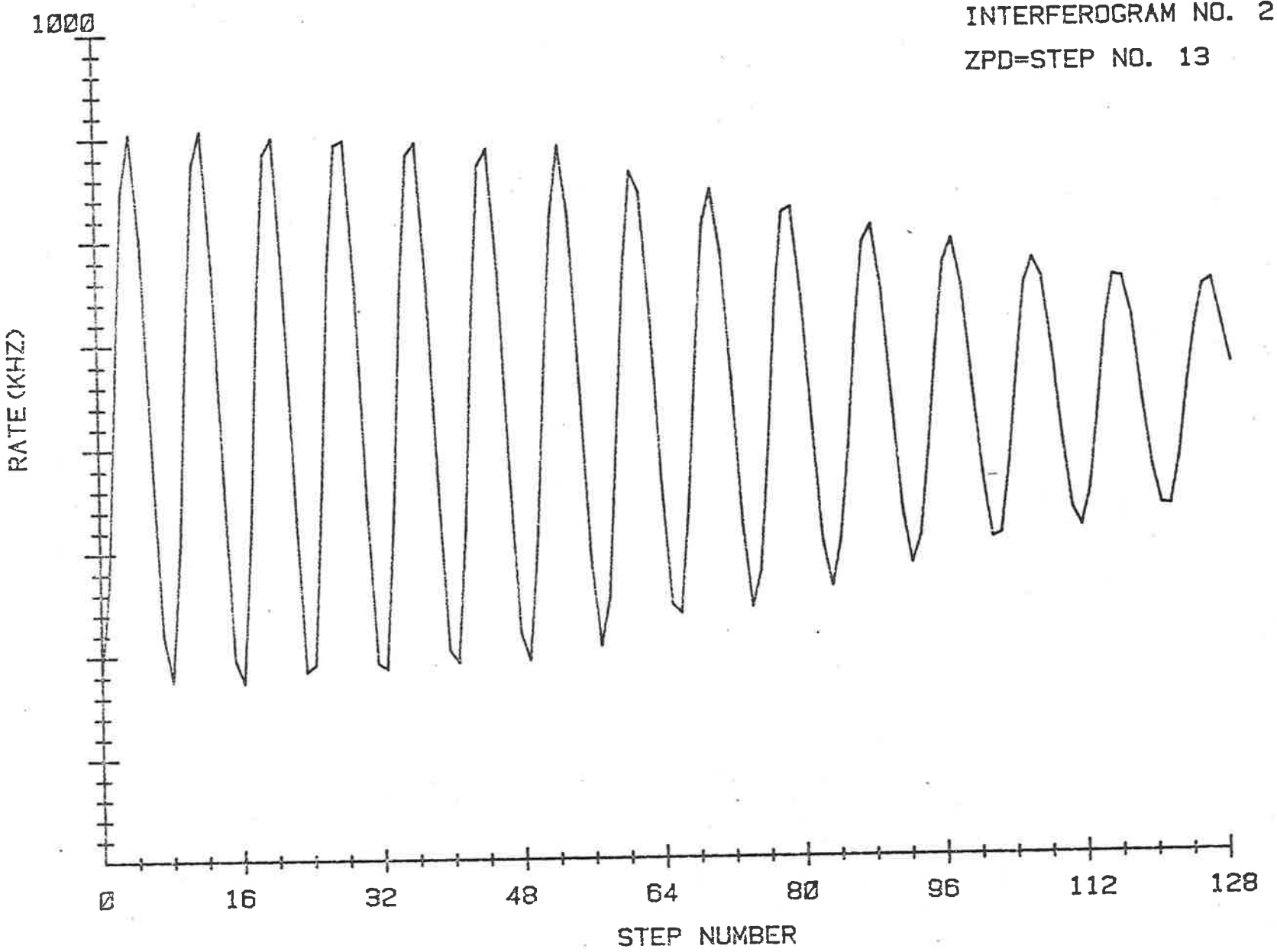

Figure 10.7 Short two-sided interferogram produced by Red LED.

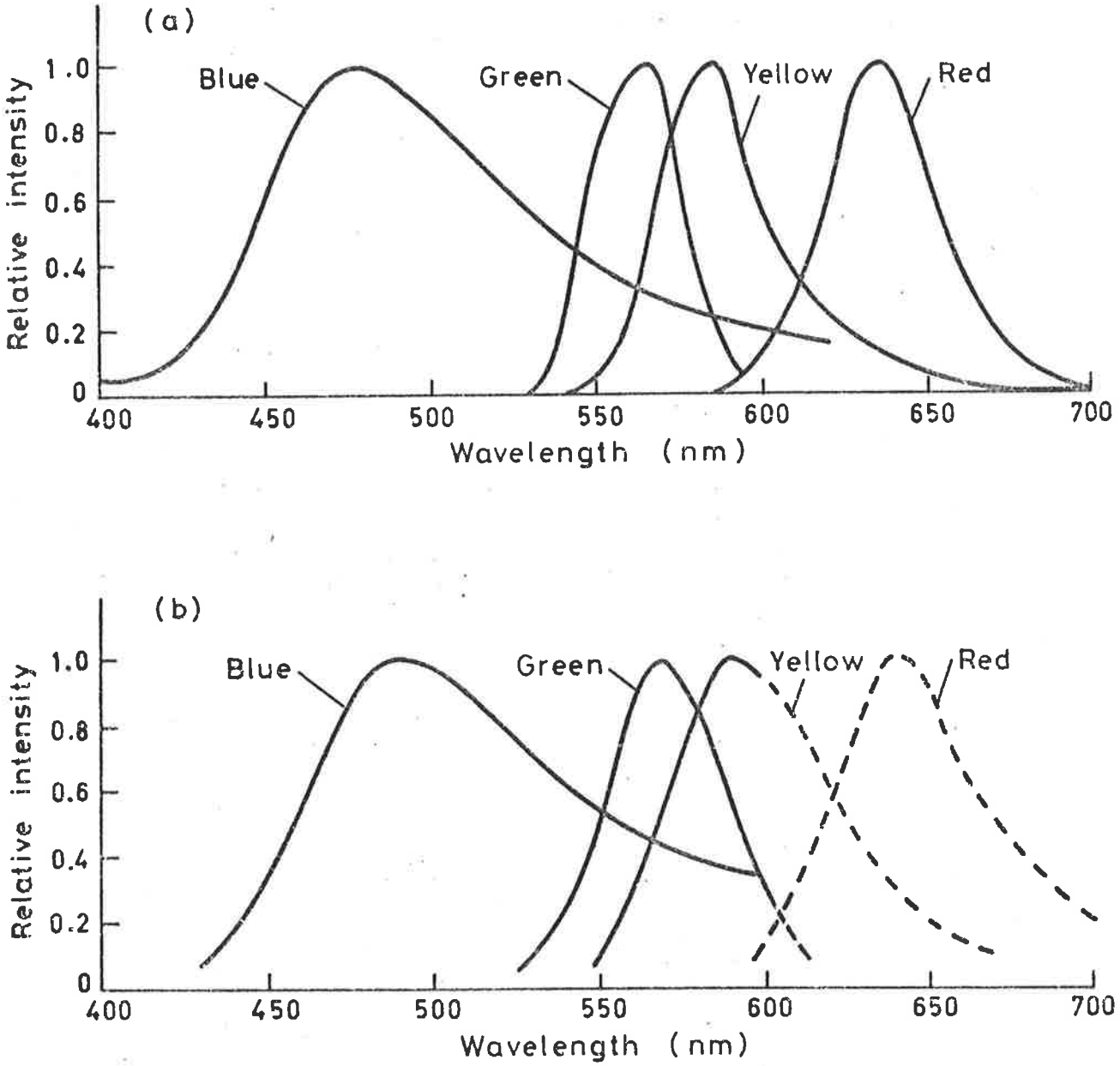

Figure 10.8 Spectra for Light Emitting Diodes

(a) As given by the manufacturers. See Hewlett-Packard Optoelectronics Designer's Catalogue, 1980, p. 124, for details on the green, yellow and red LED's and Siemens data sheets for details on the blue LED.

(b) As computed from the measured interferograms (see Figures 10.4 - 10.7). The dashed part of the curves indicates that no correction has been made for instrumental spectral response.

writing. Hence the spectra reported here have been corrected using the instrumental response shown in Figure 9.4(b), which is largely that of the photomultiplier, as published by the manufacturers, but also includes an estimate of the effects of the optical components. However, corrections have not been continued for wavelengths over 600 nm, as the quantum efficiency of the photomultiplier is low and uncertain in this wavelength region. The computed spectra are shown in Figure 10.8(b). The spectra have been normalized to unity at maximum intensity and some minor false detail has been omitted. Although the spectral resolution was low (about 40 nm), the spectra obtained agree well with those supplied by the manufacturers, which are shown in Figure 10.8(a).

Interferograms produced by the miniature white-light source have already been shown in Figures 9.22, 10.1 and 10.2. This broad-band light source was actually rather "yellow-reddish" because the intensity was kept low by operating it at a low current. The spacing between successive maxima is consistent with a "yellow-reddish" source as can be seen by comparison with the interferograms produced by the yellow and red LED's (see Figures 10.6 and 10.7). The apparent spectrum shown in Figure 10.9 is limited on the low wavelength side by the colour temperature of the source and on the high side by response of the photomultiplier. The "true" spectrum corrected for instrumental response is indicated by the dashed curve, but a full correction above 600 nm is not practicable. However, it is not unreasonably to suggest that the "true" spectrum is consistent with that of a black-body, which is what one expects from such a light source.

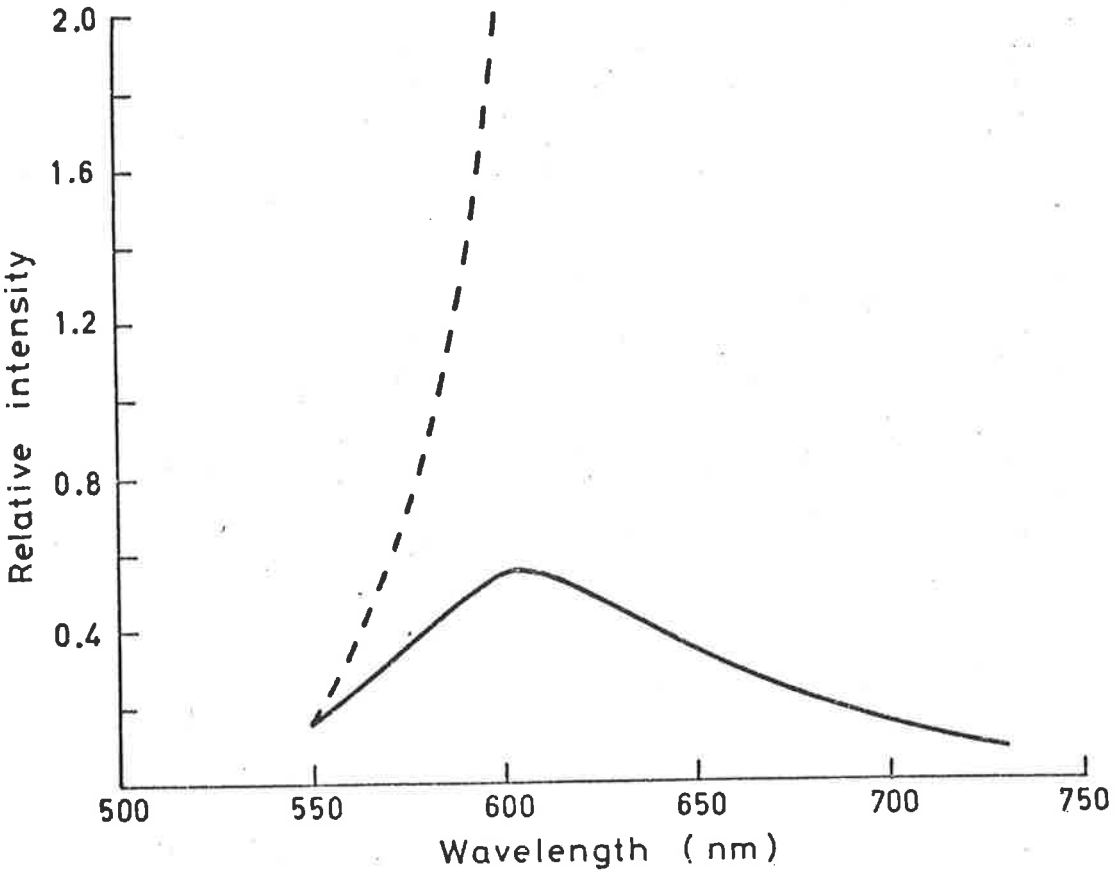

Figure 10.9 Spectrum Obtained from Miniature White-Light Source

Solid curve has not been corrected for instrumental response; whereas dashed curve has (up to 600 nm).

Preliminary results on TL emission spectra have also been obtained and these are reported here to further demonstrate the working of the apparatus. Figure 10.10 shows a conventional 2-D TL glow-curve obtained from a fine-grain pottery sample (Baginton, LRF-73-F314, see Section 5.4), which had been subjected to a beta dose of about 3.4×10^3 rads. The maximum temperature was about 485°C and the heating rate $1°C\ s^{-1}$. Figures 10.11, 10.12 and 10.13 show interferograms corresponding to the temperature regions 434.3-447.1°C, 447.1-459.9°C and 459.9-472.7°C. The reason for choosing this particular sample is that the glow-curve intensity is fairly constant with temperature, particularly so in the temperature region 430-480°C. This means that the ZPD intensity is likely to correspond to the maximum signal intensity, which is an essential requirement for the present spectral computation procedure (see Section 10.2). Figure 10.11 is an example of an interferogram in which the maximum intensity position (step number 127) does not correspond to that of ZPD (step number 32). In Figures 10.12 and 10.13 there is adequate symmetry about the respective maximum intensity positions. The corresponding computed spectra, with a resolution of about 40 nm, are shown in Figure 10.14 (curves a and b respectively). Again it is difficult to make accurate corrections for instrumental response as the emission is broad-band and mainly above 550 nm.

10.5 Evaluation of the Existing System : Suggestions for Further Improvements.

The original objective was to develop an instrument for measuring both conventional 2-D TL glow-curves and 3-D TL emission

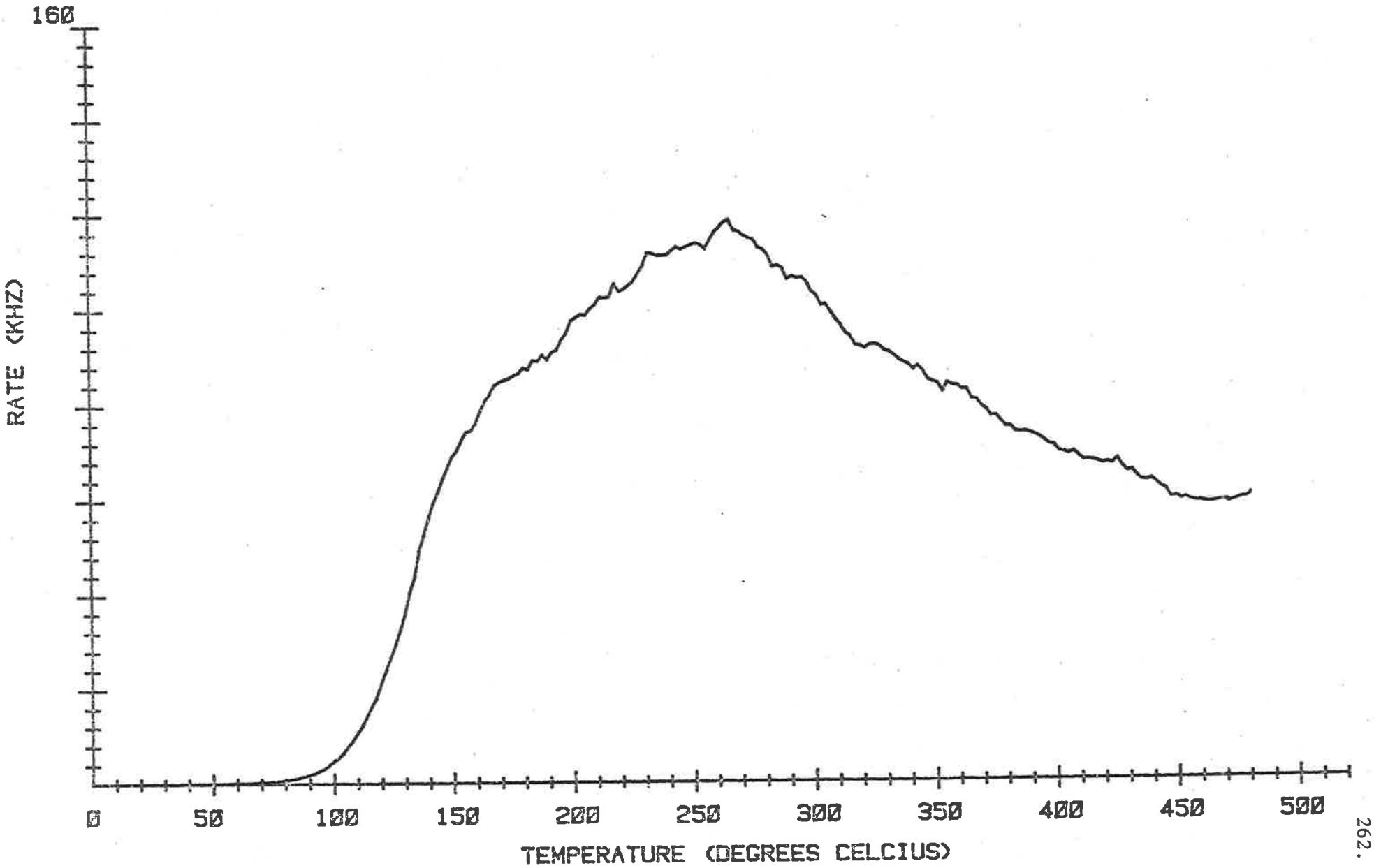

Figure 10.10 Conventional 2-D TL glow-curve obtained from a fine-grain Baginton Pottery Sample Disc, which had been subjected to a Beta Dose of about 3.4×10^3 rads.

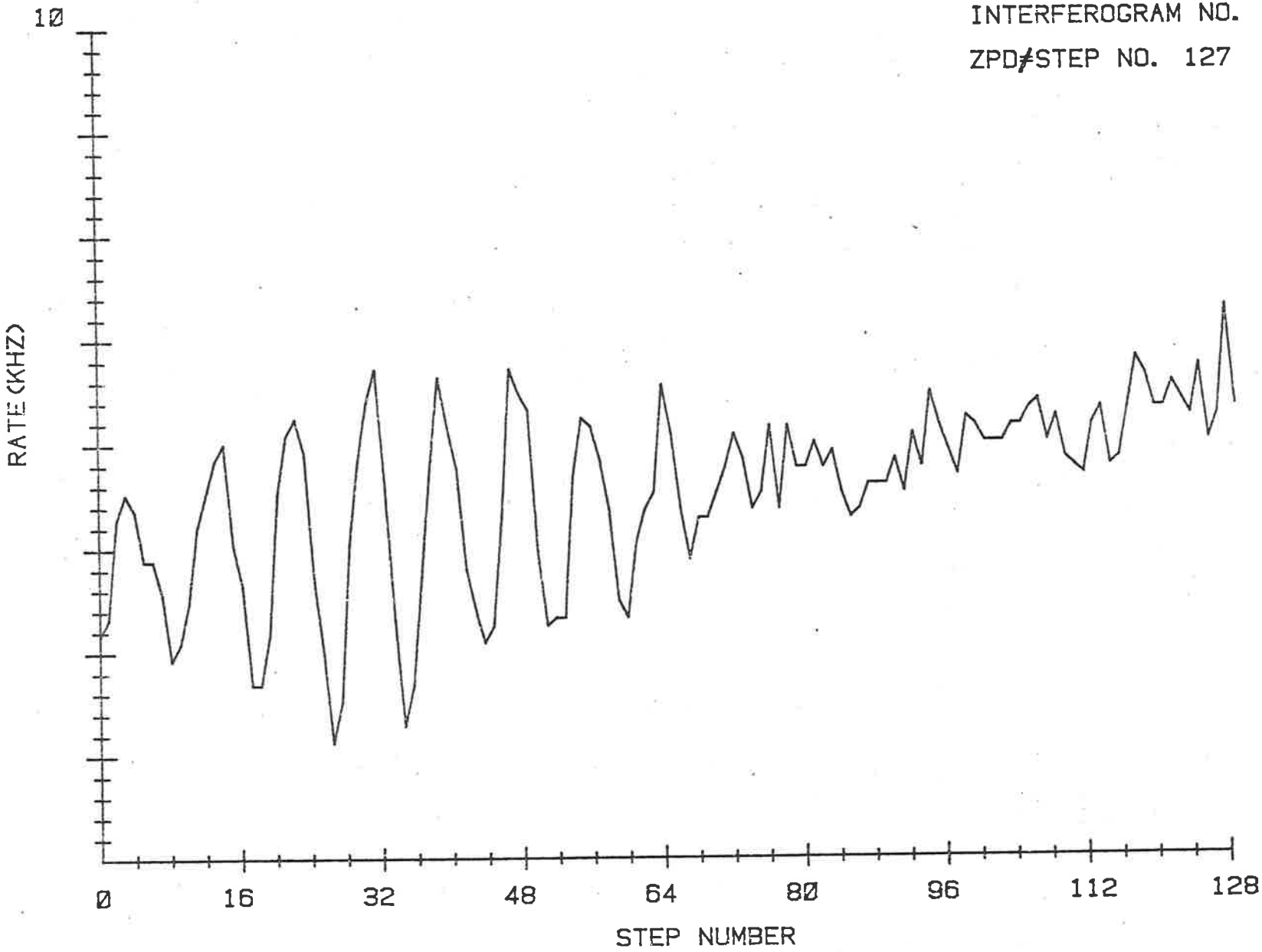

Figure 10.11 Short two-sided TL interferogram corresponding to the temperature region 434.3-447.1°C of the glow-curve shown in Figure 10.10.

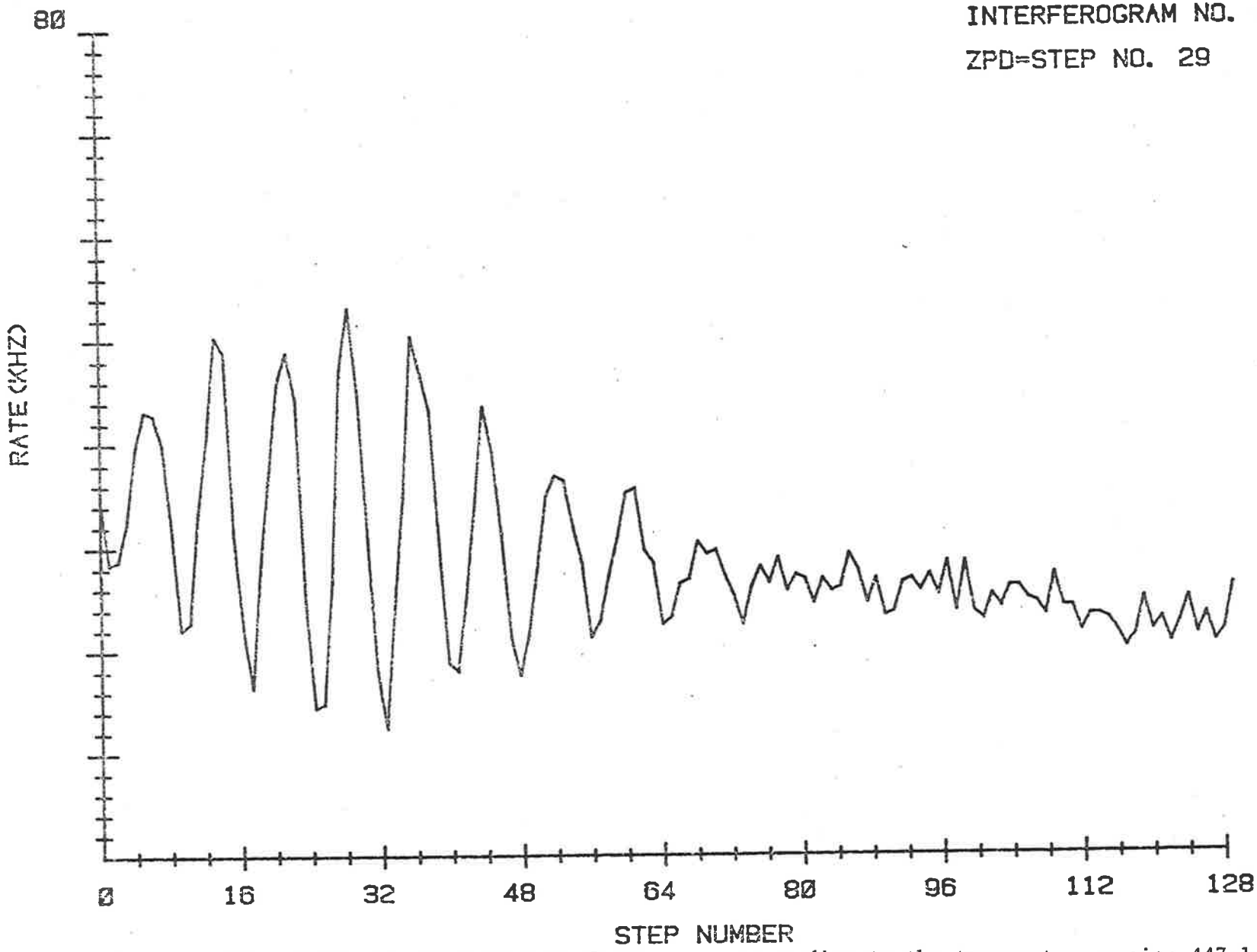

Figure 10.12 Short two-sided TL interferogram corresponding to the temperature region 447.1-459.9°C of the glow-curve shown in Figure 10.10.

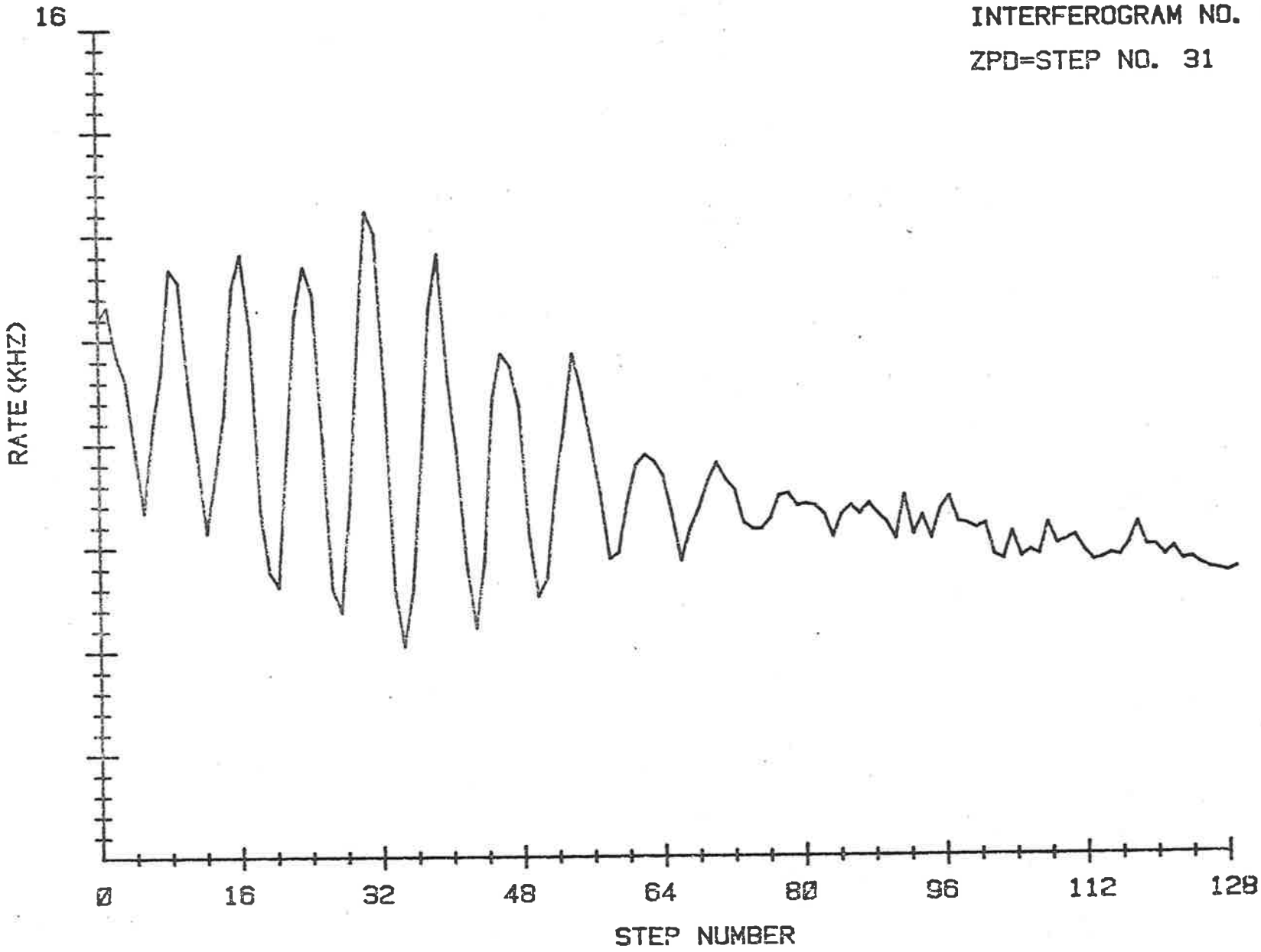

Figure 10.13 Short two-sided TL interferogram corresponding to the temperature region 459.9-472.7°C of the glow-curve shown in Figure 10.10.

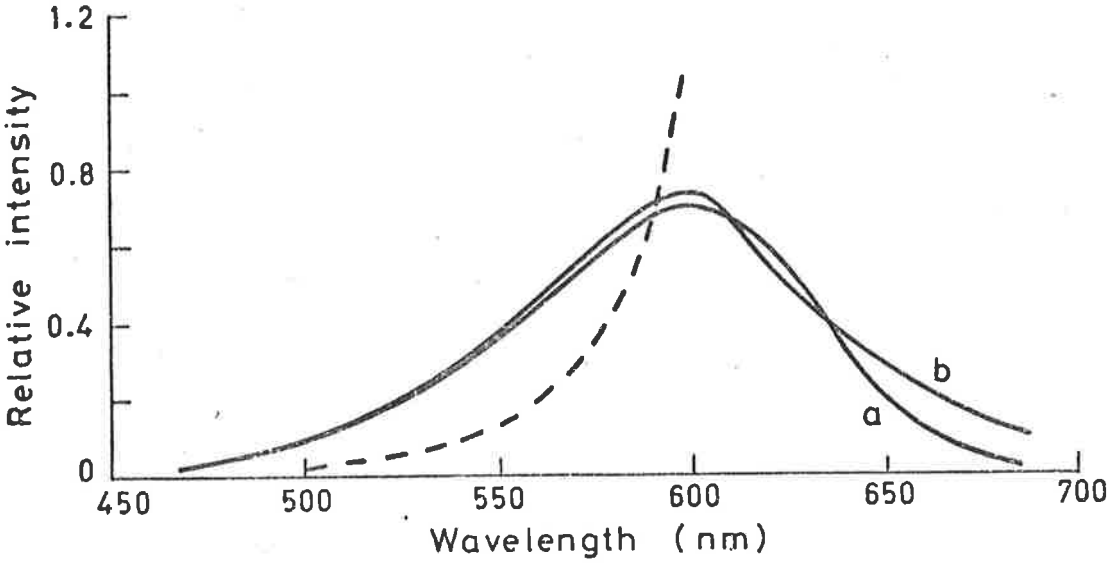

Figure 10.14 Spectra obtained from Baginton Pottery Sample.

Curves a and b have been computed from the interferograms shown in Figures 10.12 and 10.13, respectively. Solid curves have not been corrected for instrumental response; whereas dashed curve has (up to 600 nm). For the dashed curve the relative intensity has been reduced by a factor of 5.

spectra. Although the present instrument can be used for the routine measurements of 2-D TL glow-curves, several design modifications are desirable before the interferometer can be used for fully routine measurements of TL emission spectra.

There is no doubt that the development of the Michelson interferometer has been far more troublesome than was first envisaged. Although Michelson interferometers have been used extensively for low light level spectral measurements, they have predominantly been used in the infrared spectral region, where the multiplex advantage is the greatest (see Section 8.2). Not a great deal of research has previously been done on its use in the visible spectral region. The main problems encountered at shorter wavelengths include those of optical mounting, optical alignment, constancy of sampling interval and instrument stability. Although the problems of optical mounting and alignment have been overcome on the existing system, some design modifications are still desirable.

One of the problems with the existing interferometer is that minor optical adjustments are often required in order to obtain maximum amplitude of the oscillations in the observed interferograms. That is, after having completed the final stage of optical alignment (see Section 9.4), slight adjustments are often required in order to maintain perfect alignment. This is quite a severe problem with the present design, as this re-alignment can only be carried out by removing the interferometer cover and manually making the adjustment, while visually observing the fringes produced by a white-light source. Although the final optical alignment procedure is straightforward, the design should be modified so that any minor optical re-alignment can be carried out without having to remove the interferometer cover. A

possible design modification is to mount the fixed mirror on a piezo-electric aligner consisting of three individual piezo-electric transducers. The final alignment and any subsequent minor tilt corrections can then be done electronically by appropriately adjusting the bias voltages on the three piezo-electric transducers while observing the interferogram oscillations produced by a white-light source.

Another problem is that long-term drift in the location of ZPD has been observed, which is thought to be caused by temperature variations. For this reason it is important to maintain as close to a constant temperature as is possible. Minor long-term drifts are not a serious problem as they can be corrected for by appropriately adjusting the bias voltage on the piezo-electric transducer, but it is nevertheless a nuisance to keep track of.

The problem of a non-linear mirror drive system was mentioned in Section 10.4. In the existing system, the slight non-linearity is not a severe problem. However, the degree of non-linearity increases as does the OPD. This means that if one wants to increase the resolution, by increasing the maximum OPD and reducing the optical acceptance angle (see Section 8.4), it will be necessary to correct for this non-linearity. This is because one of the requirements of the FFT algorithm is that the recorded data points must be equally spaced. A possible method for doing this is to independently measure the non-linearity and then correct for it by supplying the piezo-electric translator with a corrected ramp signal, thus making the effective mirror displacement linear. This is a

special feature available on the RC-44 ramp generator, which could be computer controlled. One method of measuring the effective displacement of the moveable mirror would be to incorporate a small subsidiary referencing interferometer, which shares the common moveable mirror. In this way, the OPD could be independently monitored by observing the fringes produced by an inbuilt monochromatic source. An alternative method would be to mount a capacitance displacement transducer on the moveable mirror, having a fixed reference such as the interferometer base plate.

It may also be advantageous to carry out the Fourier transform computations on a larger computer. One of the disadvantages with the Cooley-Tukey algorithm is that the spectrum is computed for all wavenumbers σ, with a constant wavenumber increment. It would be satisfactory to evaluate the Fourier transform integral for some chosen σ values (in the visible range) rather than the entire spectrum. A number of other software refinements, such as automatic computer search for ZPD, correction for phase errors and apodization routines would also be more easily accomplished on a larger computer.

There may also be some advantages in extending the wavelength range of the interferometer further towards the UV region. This can be done by replacing the crown glass optical components with those of quartz.

APPENDIX A

THE ALPHA DECAY OF THE URANIUM AND THORIUM DECAY SERIES

In order to fully appreciate the various aspects of thick source alpha particle counting, it is necessary to consider the decay series of the three parent alpha emitters U-238, U-235 and Th-232. The relevant data for these decay chains are summarized in Tables A1, A2 and A3 respectively. These tables have been compiled using the data supplied by Diamond and Gindler (1963), Bell (1976, 1977) and Rytz (1979). From the tables one can see that the energy of the alpha particles emitted vary from 4.00 MeV (Th-232) to 8.78 MeV (Po-212), with an average energy of 5.36 MeV for the U-238 decay chain, 5.96 for the U-235 decay chain and 5.98 for the Th-232 decay chain.

TABLE A.1 THE URANIUM-238 ALPHA DECAY SERIES

(Natural abundance 99.28%)

Isotope and emitted radiation	Half-life	α-Energy (MeV)
U-238		
↓ α	4.49×10^9 yrs	4.186
Th-234		
↓ β	24.1 days	-
Pa-234		
↓ β	1.17 mins	-
U-234		
↓ α	2.48×10^5 yrs	4.760
Th-230		
↓ α	7.7×10^4 yrs	4.671
Ra-226		
↓ α	1.6×10^3 yrs	4.774
Rn-222		
↓ α	3.82 days	5.490
Po-218		
↓ α	3.05 mins	6.002
Pb-214		
↓ β	26.8 mins	-
Bi-214		
↓ β	19.8 mins	-
Po-214		
↓ α	1.62×10^{-4} secs	7.687
Pb-210		
↓ β	21.3 yrs	-
Bi-210		
↓ β	5.01 days	-
Po-210		
↓ α	138.4 days	5.304
Pb-206		

TABLE A.2 THE URANIUM-235 ALPHA DECAY SERIES

(Natural abundance 0.72%)

Isotope and emitted radiation	half-life	α-Energy (MeV)
U-235		
↓α	7.1 x 10^8 yrs	4.390
Th-231		
↓β	25.52 hrs	-
Pa-231		
↓α	3.25 x 10^4 yrs	4.923
Ac-227		
↓β	21.77 yrs	-
Th-227		
↓α	18.2 days	5.840
Ra-223		
↓α	11.43 days	5.822
Rn-219		
↓α	3.96 secs	6.759
Po-215		
↓α	1.78 x 10^{-3} secs	7.386
Pb-211		
↓β	36.1 mins	-
Bi-211		
↓α	2.15 mins	6.568
Tℓ-207		
↓β	4.79 mins	-
Pb-207		

TABLE A.3 THE THORIUM-232 ALPHA DECAY SERIES

Isotope and emitted radiation	Half-life	α-Energy (MeV)
Th-232		
↓α	1.40 x 10^{10} yrs	4.000
Ra-228		
↓β	5.75 yrs	-
Ac-228		
↓β	6.13 hrs	-
Th-228		
↓α	1.91 yrs	5.369
Ra-224		
↓α	3.64 days	5.674
Rn-220		
↓α	55.3 secs	6.288
Po-216		
↓α	0.145 secs	6.778
Pb-212		
↓β	10.64 hrs	-
Bi-212		
(64%) ↙	60.60 mins	-
Po-212 β	60.60 mins	5.620 (64% of 8.784)
↓α		
(36%) ↓α	3.0 x 10^{-7} secs	2.182 (36% of 6.060)
Tℓ-208		
↓β	3.07 mins	-
Pb-208		
Pb-208		

APPENDIX B

THEORETICAL DERIVATION OF THE PAIRS FRACTION FORMULA IN ALPHA COUNTING

Consider a layer of sample to be alpha counted, thickness d, emitting alpha particles uniformly from throughout its volume and resting on a plane of ZnS scintillator. In Figure B.1 this situation is illustrated diagrammatically. From simple geometry one can evaluate the solid angle of the cone whose circular area cross section is AB and whose height is h, call this Ω'.

$$\Omega' = 2\pi (1 - \cos \theta) \qquad (B.1)$$

The solid angle of the total sphere is 4π thus making the fraction of solid angle seen across AB $\Omega'/4\pi$, this then represents the probability of an alpha particle from the unit volume reaching the ZnS screen. The total number of alpha particles emerging per unit area of sample per unit time is hence given by

$$\alpha_A = \frac{N}{2} \int_{h=0}^{h=d} (1 - h/R)dh = \frac{NR}{4}, \qquad (B.2)$$

$$[\, d >> R \,]$$

where N is the number of alpha particles emitted per unit volume of active material per unit time, R is the effective range of an alpha particle in the active medium and h is the height of the unit volume above the ZnS (see for example, Turner *et al*, 1958). Any possible edge effects can be ignored as the diameter of the counting area is more than three orders of magnitude larger than the alpha particle ranges.

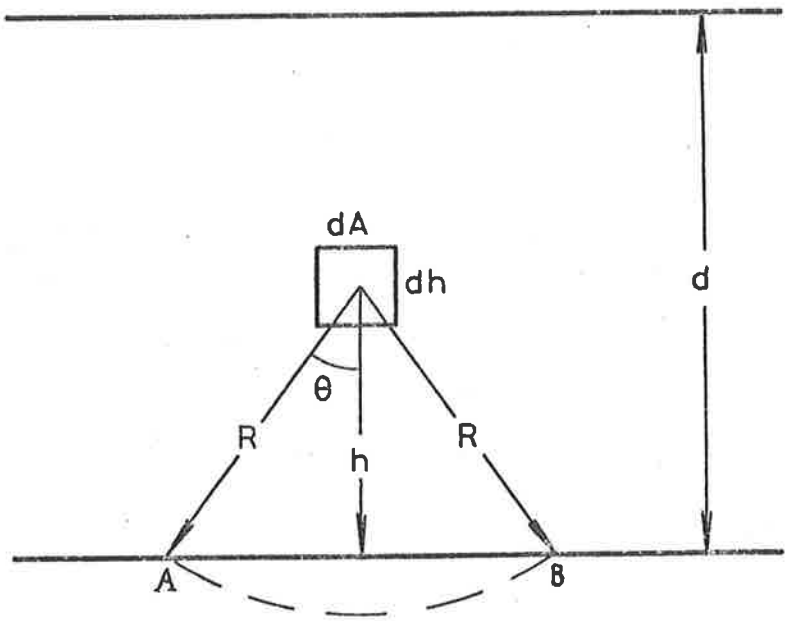

Figure B.1 Diagrammatic Illustration of the Alpha Counting Geometry.

Similarly, the same geometric argument can be used to calculate the probability of a pair reaching the ZnS screen. The fraction of double disintegrations occurring in the same unit volume dAdh resulting in two alphas emitted within the given solid angle is thus given by

$$P_{dAdh} = \frac{1}{4}\left(1 - \frac{h}{R_1}\right)\left(1 - \frac{h}{R_2}\right), \qquad (B.3)$$

where R_1 and R_2 are the respective ranges of the two alpha's concerned (they are actually the maximum distances travelled in $g.cm^{-2}$ after which they will still be detected by the ZnS screen). The total number of pairs emerging per unit area of sample is then given by

$$P_A = \frac{n}{4}\int_0^{R_1}\left(1 - \frac{h}{R_1}\right)\left(1 - \frac{h}{R_2}\right)dh, \qquad (B.4)$$

$$[\, R_1 < R_2 \;;\; d >> R_1, R_2 \,]$$

where n is the number of double disintegrations in the unit volume per unit time. Now using the convention of Bell (1978), one can define a new variable s as the number of alpha particles emitted per unit mass per unit time. Then s equals N/ρ where ρ is the density of the active material. Thus one obtains

$$\alpha_A = \frac{1}{4}\, s\rho R, \qquad (B.5)$$

and similarly

$$n_A = \frac{1}{12}\, s\rho R_1 \left[\, 1 + \frac{R_2 - R_1}{2\,R_2} \,\right], \qquad (B.6)$$

where n_A is the total number of pairs emerging per unit area of sample per unit time. Now recalling that the threshold is set so that

15% of the alpha's from the thorium standard are not actually counted one obtains

$$\alpha_A = \frac{1}{4} s\rho \, (R - \delta R) \qquad (B.7)$$

and

$$n_A = \frac{1}{12} s\rho \, (R_1 - \delta R) \, [\, 1 + \frac{R_2 - R_1}{2(R_2 - \delta R)} \,], \qquad (B.8)$$

where δR is the alpha particle range corresponding to the threshold setting. The counting area (A) is 13.85 cm^2, hence one has

$$\alpha_{total} = \alpha_A \times A = \frac{13.85}{4} \, [\, s_1(R_1\rho - \delta R\rho) + s_2(R_1\rho - \delta R\rho) \ldots .$$

$$+ \, s_1(R_i\rho - \delta R\rho) + \ldots . \,], \qquad (B.9)$$

where s_i and R_i refers to the individual alpha emitters. Assuming equilibrium conditions one has

$S_{parent} = s_1 = s_2 = \ldots . = s_i$, which then gives us

$$\alpha_{total} = 3.463 \, [\sum_1 s_i \, (R_i\rho - \delta R\rho) \,] \qquad (B.10)$$

Similarly, for the pairs one obtains

$$P_\alpha = \frac{13.85}{12} \, s_{Th\text{-}232} \, [\, R_1\rho - \delta R\rho \,] \, [\, 1 + \frac{R_2\rho - R_1\rho}{2(R_2\rho - \delta R\rho)} \,]$$

$$[\, 1 - \exp \, (- \lambda\tau) \,] \qquad (B.11)$$

where the term $[\, 1 - \exp(- \lambda\tau) \,]$ is the half-life correction factor, λ is the decay constant of the second member of the pair and τ is the gating time for the pairs coincidence counter.

There is a total of 6 alpha's emitted in the thorium chain. The average value of $R_i\rho$ in the chain as estimated by Aitken and Bowman (1975), assuming equilibrium, is 6.94 $mg.cm^{-2}$, hence

$$\alpha_{Thorium} = 3.463\ (5.90 \times 6 \times S_i) \times 10^{-3}$$

$$\alpha_{Thorium} = 0.1226\ S_i = 0.1226\ S_{Th\text{-}232} \qquad (B.12)$$

Using the range energy data of Bowman (1976) one obtains $R_1\rho = 7.32\ mg.cm^{-2}$ and $R_2\rho = 8.195\ mg.cm^{-2}$, this gives one

$$P_\alpha = 7.689\ [\ 1 - \exp(-\lambda\tau)\ ]\ S_{Th\text{-}232} \times 10^{-3} \qquad (B.13)$$

Now combining Equations (B.13) and (B.12) one obtains for the pairs fraction formula

$$(P/\alpha)_{Thorium} = 0.0627\ [\ 1 - \exp(-\ln 2\ (\tau/\tau_{\frac{1}{2}}))\ ] \qquad (B.14)$$

APPENDIX C

ESTIMATING THE RELATIVE ERROR IN Th/U RATIOS WHEN EMPLOYING THE ALPHA -PAIRS COUNTING METHOD

The alpha-pairs counting method has already been discussed in some detail in Section 2.4.1. Huntley and Wintle (1978, 1981) have already discussed how the relative error in the alpha pairs count can be minimized by suitable choices of gating time and counting area.

Suppose one counts a sample for a period of T kiloseconds, let α be the total number of alpha's counted, p' the total number of pairs counted and C the total number of calculated random coincidence pairs (recalling that $C \propto \alpha^2$). Assuming that the variables α, p' and C all follow a poisson distribution, one can estimate the relative uncertainty in the true pairs count. If one denotes the total true pairs count by P then it follows that the relative uncertainty in this count as calculated at one standard deviation is given by

$$\frac{\delta P}{P} = \frac{\delta (p'-C)}{(p'-C)} = \frac{\sqrt{p'+C}}{(p'-C)} \qquad (C.1)$$

This of course assumes that the total number of alpha's counted, α, is so high that the uncertainty in converting from the alpha count rate to the random coincidence pairs rate is negligible (see Equation 2.3) compared to the overall uncertainty. When this is not the case one also has to add twice the relative error in the total alpha count since $C \propto \alpha^2$.

Having obtained the true pairs count rate, one is in a position to split α into its two components, namely, α_U (uranium) and α_{Th} (thorium). The general procedure is to calculate α_{Th} from the pairs fraction formula (Equation 2.6) and then determine α_U by subtracting α_{Th} from α. If one assumes that the relative uncertainties in the random coincidence pairs formula, the pairs fraction formula and the total alpha count are all small compared with the overall uncertainty, then the relative uncertainty in the Th/U ratio estimated at one standard deviation is given by

$$\frac{\delta(Th/U)}{(Th/U)} = \frac{2\sqrt{p'+C}}{(p'-C)} \qquad (C.2)$$

The factor of 2 is there because the Th/U ratio is proportional to α_{Th}/α_U and both α_U and α_{Th} have approximately the same relative uncertainty.

APPENDIX D

SELECTION OF PHOTOMULTIPLIERS FOR PHOTON COUNTING

The overall photon counting system has already been described in Chapter 9. The photon detectors used for both the 2-D and 3-D counting configurations are EMI-9635QA photomultipliers operating in the single photon counting mode. These are specially selected to have a low dark current, which is an essential requirement for the photon counting system.

The best method for determining the operating voltage for a given photomultiplier tube is the so-called "plateau" test. In this test the photomultiplier is exposed to a constant intensity light source and the observed photon count rate is plotted as a function of applied EHT (for a given amplifier gain and discriminator threshold setting). The operating voltage is then chosen to be somewhere at the beginning of the plateau. Figure D.1 is such a plot for a selection of four different EMI-9635QA photomultiplier tubes, the light source used being a solid state source supplied by D.A. Pitman Limited, Surrey England, (Facey, 1966). Figure D.2 is a plot of the photomultiplier dark count as a function of applied EHT for four of the tubes tested. From Figures D.1 and D.2, one can see that the main reason for choosing the onset of the plateau as the operating voltage is that it corresponds to an optimum signal/noise ratio. The problem which now arises is that the dark current determined in the factory is a DC measurement usually measured at an anode sensitivity of 2000 A/L, whereas the measurement required is the dark counts at the optimum operating conditions which might well be very much different. This is

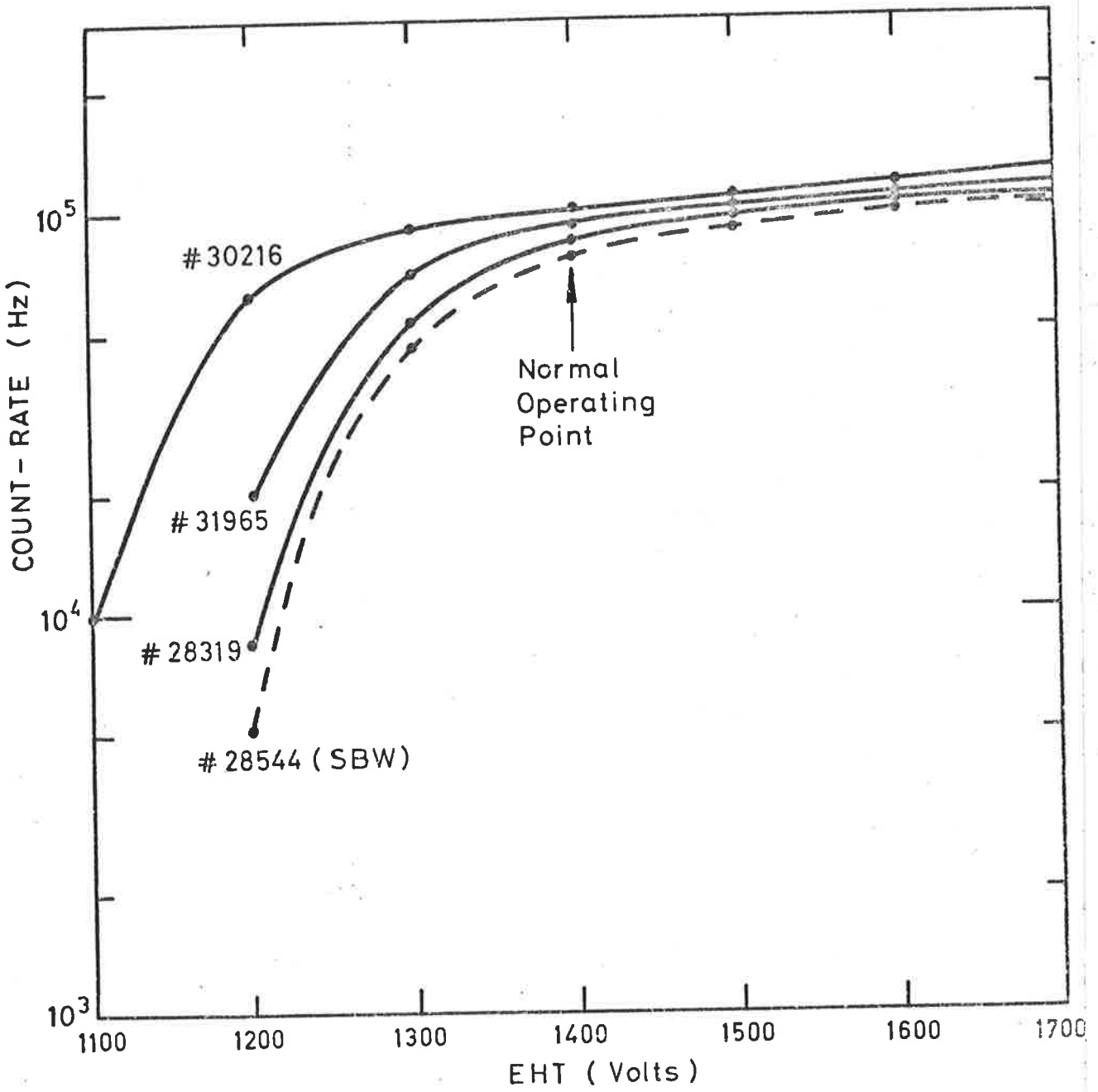

Figure D.1 Plot of Photon Count-Rate versus EHT for Several EMI 9635QA Photomultiplier Tubes : The Plateau Test.

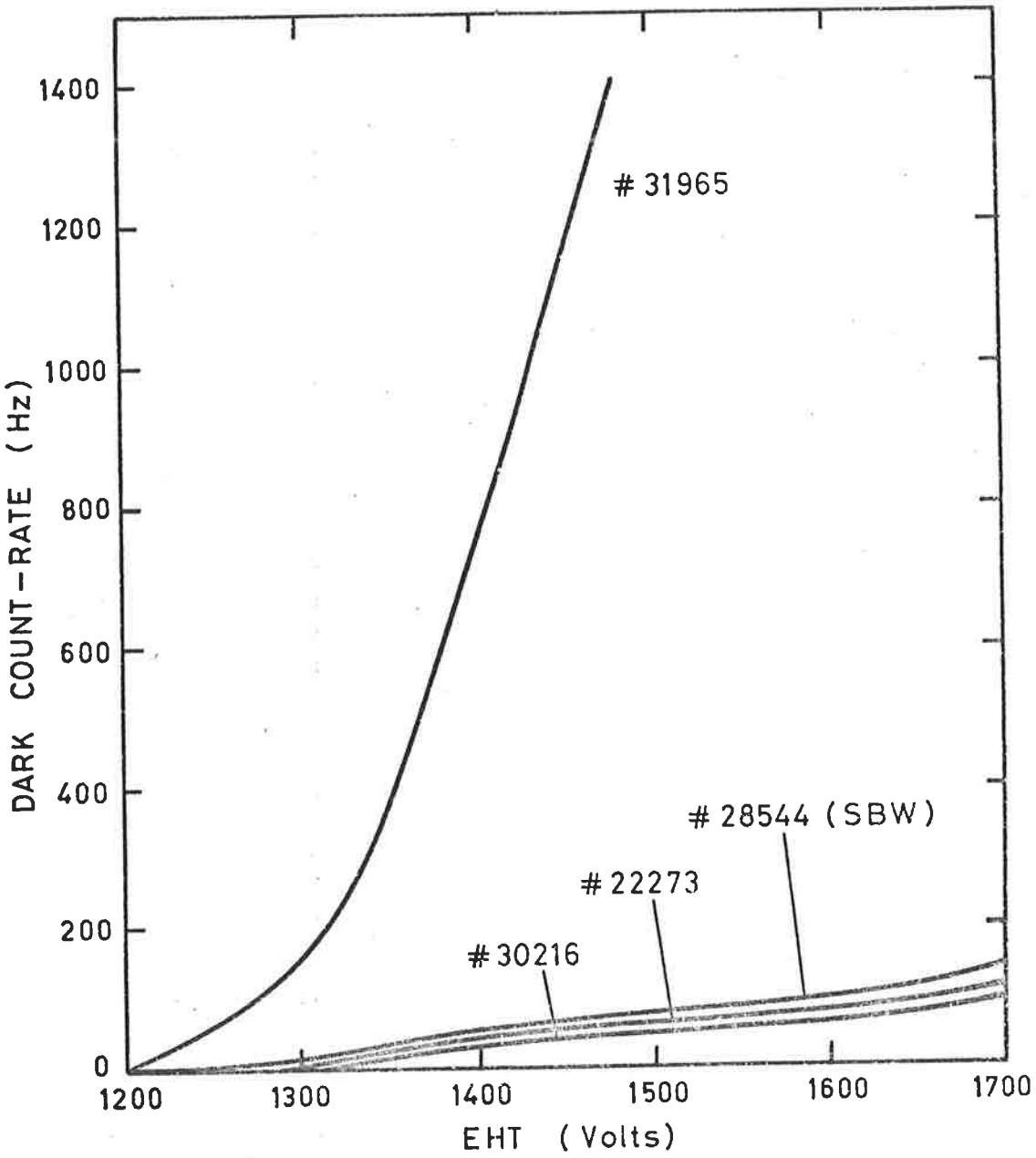

Figure D.2 Photomultiplier Dark Noise as a Function of Applied EHT for a Variety of EMI 9635QA Tubes.

clearly the case for tube ǂ 31965 where the optimum operating voltage is about 1400V and the DC dark current had been measured at about 1100V. While the DC measurement is correct there is for this tube, unlike that observed on other tubes, a dramatic increase in the dark noise as the EHT is increased (Figure D.2). The dark noise at 1400V is about 10-15 times higher than that observed on other tubes (25-50 Hz), clearly making it unsuitable for low level photon counting. Another abnormal behaviour of tube ǂ 31965 is that the dark noise (at 1400V) is very large (about 10 kHz) immediately after switching the EHT on, it then decays away with a time constant of the order of about 100s. Prescott (private communication) has suggested that this unusual behaviour could be due to charging and discharging of some internal structure through an inadequate or non-existent contact. A third abnormal feature of tube ǂ 31965 is a hysteresis effect. With a completely dark-adapted tube to which the EHT has been continuously applied, the dark count depends on the immediately preceding history of the tube. After having exposed the tube to a light source, the dark noise measured immediately after removal of the source was found to be enhanced by as much as 30%, depending on the strength of the source. This effect also slowly decays away with time.

Abnormal behaviour of photomultiplier dark counts is evidently not uncommon: Of six tubes tested, only three were found to be suitable for low level photon counting. For one of these (ǂ 28319) the dark count was found to increase with time after switching the EHT on. This is illustrated in Figure D.3 where one can see that the dark count immediately after switching on the EHT is quite low (about 10 Hz

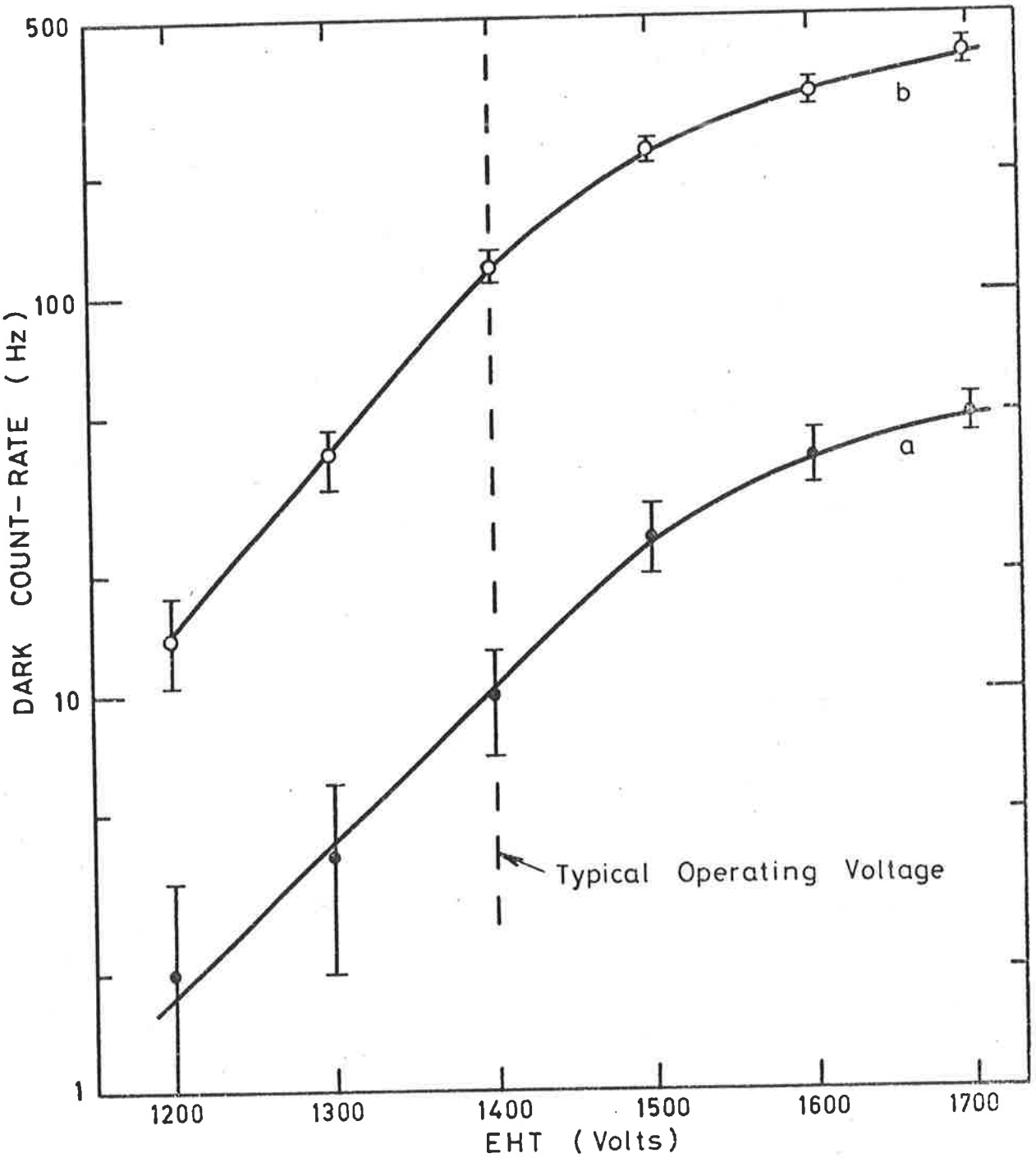

Figure D.3 Plot of Photomultiplier Dark Noise as a Function of Applied EHT for Tube 9635QA, Serial No: 28319.

(a) obtained immediately after switching EHT on

(b) obtained 1 hour after switching EHT on

at 1400V), this then increases by a factor of about 10 within 1 hour.

One of the well behaved tubes is ǂ 28544 this was supplied with a sand blasted window (SBW) which, the manufacturers claim, enhances the counting efficiency. Although this tube was found to be suitable for photon counting, no improvement in efficiency was noticeable (see Figures D.1 and D.2).

At optimum operating conditions the lowest dark count was exhibited by tube ǂ 30216 (25-35 Hz at 1400V). Hence, this tube was selected for the 3-D photon counting system. Operating the cooling unit at - 20°C resulted in the dark noise for tube ǂ 30216 being reduced by a factor of about 2 (10-15 Hz); this was furthermore found to be fairly well independent of EHT in the region 1300 to 1700V.

From the observations described in this Appendix, one can see that it is not advisable to select a photomultiplier tube on the basis of its DC dark current alone. That is, a low DC dark current does not necessarily mean that the tube will be suitable for photon counting. The manufacturers state that one should specify that the tube must be specially selected for low level photon counting.

APPENDIX E

THE FAST FOURIER TRANSFORM ALGORITHM

This Appendix presents an FFT algorithm in the form of a BASIC subroutine (written for the PET minicomputer). A simple test program and its results are also presented to verify the operation of the subroutine. The FFT subroutine is based on the Cooley-Tukey algorithm (Cooley and Tukey, 1965). In order to write a FFT subroutine it is necessary to understand the basic principles of this algorithm; however, these have already been outlined elsewhere (see for example, Bergland 1969, Bell 1972, Stanley and Peterson 1978) and hence will not be discussed here.

The FFT subroutine is presented in Figure E.1. It should be pointed out that the number of data points to be transformed must be of the form $N = 2^n$, where n is a positive integer. The subroutine enables one to calculate both the DFT (ID = 1) and the inverse DFT (ID = 2) of any input function. Figure E.2 is a listing of a simple FFT test program which uses a cosine wave as the input function. This is a suitable input function, as far as FTS is concerned, as it corresponds to the interferogram observed for a monochromatic source (see Section 8.3). In this test program the forward DFT of the cosine wave is followed by the inverse DFT of its Fourier transform. That is, one ends up with the original cosine wave input function. The input and output data are displayed on the visual display unit of the PET computer. The time taken for the FFT is also calculated using the internal clock of the PET, for a 64-point transform this is about 20s. For the example given, the cosine wave generated represents an assumed frequency of 100 Hz with a sampling interval of 1.5624 ms. If the

```
100 REM FFT SUB. WRITTEN BY HANS JENSEN
105 REM COOLEY-TUKEY ALGORITHM IN BASIC
110 REM NO. OF DATA POINTS (N) MUST BE OF THE FORM N=2↑M
115 REM X IS AN ARRAY CONTAINING THE REAL PART OF THE DATA
116 REM Y CONTAINS THE IMAGINARY PART
120 PI=π
130 FORL=1TOM
140 LE=2↑(M+1-L)
150 LP=LE/2
160 U1=1.0:U2=0.0
170 AG=PI/LP
180 C=COS(AG)
181 REM ID=1 WHEN USING THE DFT
182 REM ID=2 WHEN USING THE INVERSE DFT
190 S=(-1)↑ID*SIN(AG)
200 FORJ=1TOLP
210 FORI=JTONSTEPLE
220 IP=I+LP
230 T1=X(I)+X(IP)
240 T2=Y(I)+Y(IP)
250 T3=X(I)-X(IP)
260 T4=Y(I)-Y(IP)
270 X(IP)=T3*U1-T4*U2
280 Y(IP)=T4*U1+T3*U2
290 X(I)=T1
300 Y(I)=T2
310 NEXTI
320 U3=U1*C-U2*S
330 U2=U2*C+U1*S
335 U1=U3
340 NEXTJ:NEXTL
341 REM PERFORMING BIT REVERSAL
350 N2=N/2:N1=N-1:J=1
360 FORI=1TON1
370 IF(I>=J)GOTO410
380 T1=X(J):T2=Y(J)
390 X(J)=X(I):Y(J)=Y(I)
400 X(I)=T1:Y(I)=T2
410 K=N/2
420 IF(K>=J)GOTO450
430 J=J-K:K=K/2
440 GOTO420
450 J=J+K
455 NEXTI
460 RETURN
```

Figure E.1 Listing of FFT subroutine written in Basic for the PET Computer.

```
5 REM TEST PROGRAM FOR FFT SUBROUTINE
8 N=64:M=6
12 DIMX(N),Y(N)
15 PRINTTAB(10);"TEST FUNCTION"
16 PRINT"N-VAL.";TAB(10);"REAL";
17 PRINTTAB(20);"IMAG"
20 T=0
25 REM COSINE TEST FUNCTION
29 T=0
30 FORK=1TON
40 X(K)=COS(2*π*100*T)
41 Y(K)=0
45 T=T+1.5624E-3
46 REM FREQ.RESOLUTION(F.R)=1/(1.5624E-3*N)
54 X(K)=INT(X(K)*10↑2+.5)/(10↑2)
55 PRINTK,X(K),Y(K)
65 NEXTK
66 REM CALLING THE FFT SUB. (ID=1)
67 TA=TI:ID=1
68 GOSUB120
69 TB=TI:TT=(TB-TA)/60
70 PRINT"TIME TAKEN FOR FFT="TT"SEC"
71 PRINT"HARM";TAB(9);"REAL";TAB(20);"IMAG"
72 FORK=1TON
73 X(K)=X(K)/(N/2):Y(K)=Y(K)/(N/2)
74 X(K)=INT(X(K)*10↑2+.5)/(10↑2)
75 Y(K)=INT(Y(K)*10↑2+.5)/(10↑2)
76 IFABS(X(K))<10↑(-2)THENX(K)=0
77 IFABS(Y(K))<10↑(-2)THENY(K)=0
81 K1=K-1
82 PRINTK1,X(K),Y(K)
85 NEXTK
86 REM CALLING THE INVERSE FFT SUB. (ID=2)
87 TA=TI
88 ID=2:GOSUB120
89 TB=TI
90 TT=(TB-TA)/60
91 PRINT"TIME TAKEN FOR FFT="TT"SEC"
93 FOR K=1TON
94 X(K)=X(K)/2:Y(K)=Y(K)/2
95 X(K)=INT(X(K)*10↑2+.5)/(10↑2)
96 Y(K)=INT(Y(K)*10↑2+.5)/(10↑2)
97 PRINTK,X(K),Y(K)
98 NEXTK
99 END
```

Figure E.2 Listing of Basic Test Program for FFT Subroutine.

total time duration of the input function is t_i, then the spectral components are spaced apart in frequency by $F = 1/t_i$. This means that for the example given (N=64), the frequency resolution is 10 Hz. The monochromatic output (delta function) is hence observed at the 10th harmonic, which is equivalent to the 11th data point (the first data point corresponds to the zeroth harmonic or DC component). In this particular example, the input is a real, even function which means that there are only N/2 meaningful spectral components. That is, the spectral function obtained is symmetric about N=32. This is illustrated in Figure E.3 where both the cosine wave and its Fourier transform power spectrum are plotted. It should be pointed out that, for the example given, the frequency of the cosine wave (100 Hz) corresponds exactly to one of the harmonic numbers, which is the reason why only a single spectral frequency appears. If for example, the frequency of the cosine wave were changed to 145 Hz, while keeping the frequency resolution at 10 Hz, then the spectral component would theoretically appear half-way between the 14th and 15th harmonics. What actually happens is that the signal is not restricted only to the 14th and 15th harmonics, but appears also in several of the neighbouring harmonics. This particular example is also illustrated in Figure E.3. This phenomenon is usually referred to as "leakage". It is an imperfection of the DFT which can be reduced by smoothing the data to be transformed with certain "window functions" (or apodizing functions) before computing the FFT (see Section 8.3).

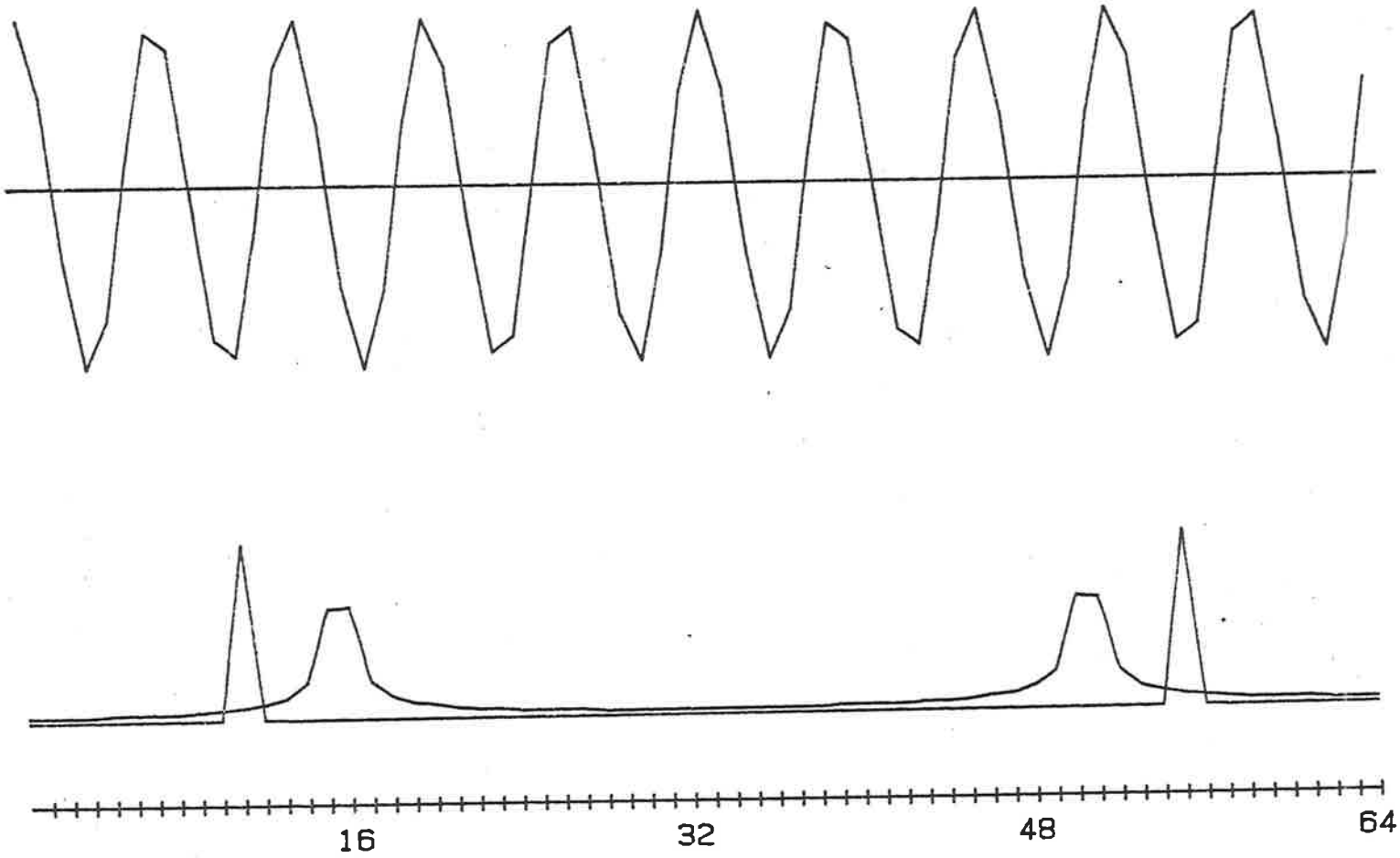

Figure E.3 Plot of Cosine Test Function and its corresponding Fourier Transform Power Spectrum.

APPENDIX F

BASIC SUBROUTINES FOR THE HAPP-GENZEL AND TUKEY APODIZATION PROCEDURES

```
10 REM HAPP-GENZEL APODIZING ROUTINE
20 REM FOR A ONE-SIDED INTERFEROGRAM
30 REM CONSISTING OF N DATA POINTS
40 DIMX(N),A(N)
50 FORI=1TON
60 A(I)=0.54+0.46*COS(π/2*(I-1)/N)
70 X(I)=X(I)*A(I):X(I)=INT(X(I))
80 NEXTI
90 RETURN
```

```
100 REM TUKEY APODIZING ROUTINE
110 REM FOR A TWO-SIDED INTERFEROGRAM
120 REM CONSISTING OF N DATA POINTS
130 DIMX(N),A(N)
140 T=N/10:X(1)=0:X(N)=0:F=π/T
150 FORJ=2TOT
160 A(J)=(1-COS(F*(J-1)))/2
170 X(J)=X(J)*A(J)
180 X(N-J+1)=X(N-J+1)*A(J)
190 NEXTJ
200 FORI=1TON
210 X(I)=INT(X(I))
220 NEXTI
230 RETURN
```

APPENDIX G

A LISTING OF THE MAIN COMPUTER PROGRAM.

```
20 GOSUB3010
25 DATA 169,0,168,173,0,176,41,208,141,0,176,76,69,3,104
26 DATA168,104,104,173,0,176
27 DATA 41,1,170,169,16,176,73,255,145,1,200,189,16,176
28 DATA73,255,145,1,200,208
29 DATA 2,230,2,169,0,197,2,208,4,192,0,240,46,169,255
30 DATA157,20,176,157,20,176
31 DATA 44,0,176,48,32,112,14,173,0,176,73,80,141,0,176
32 DATA169,0,133,6,240,16
33 DATA 230,6,165,6,197,4,208,8,169,176,45,0,176,141,0
34 DATA176,64,132,1,104,104
35 DATA 104,169,224,141,0,176,169,127,141,14,176,96
40 FORI=1TO116:READA:POKE(825+I),A:NEXTI
45 DIMX(256),Y(256),Z(256)
50 GOSUB2000
55 POKEN,224:POKEN+3,7:POKEN+2,240
60 GOSUB2200
75 GETA$:A=VAL(A$):IFA=1GOTO155
80 IFA=2THENGOSUB5000
85 IF(A=3)AND(L=2)GOTO990
90 IF(A=4)AND(L=2)GOTO6500
95 IF(A=5)AND(L=3)GOTO6000
96 IF(A=6)AND(L=3)GOTO7200
97 IF(A=7)AND(L=3)GOTO8000
100 GOTO75
155 IFL=2GOTO190
171 GOSUB3000
172 E1=0:GOSUB2300
173 IFE1=1GOTO171
175 PRINT"■SPECIFY MAX.TEMP":INPUT"(0 TO 511)";A$:U1=VAL(A$)
177 U0=2*U1+2:IFINT(U1)<>U1OR(U1<00RU1>511)GOTO171
190 GOSUB3000
192 GOSUB2400
193 PRINT"■■OKAY (Y/N) ?"
194 GETA$:IFA$="N"GOTO171
195 IFA$<>"Y"GOTO194
200 GOSUB3050
218 GOSUB3000
220 PRINT"■1. RUNNING 2-D TL GLOWCURVE EXPERIMENT"
221 L=2:A1=0.5
225 GOSUB3150
230 GOTO55:PI=π
990 GOSUB3000
1000 GOSUB3080
1010 PRINT"■■SPECIFY START TEMP. OF CURVE";SPC(12);"(DEG.C)"
1020 INPUT"(0 TO 472) ";A$:S=VAL(A$)
1030 IFS<0ORS>472OR(S=0ANDASC(A$)<>48)ORS<>INT(S)GOTO990
1040 PRINT"■■SPECIFY INCREMENTS OF TEMP.(MULT.OF 0.5 DEGREE)"
1050 W=INT((511-S)/36)/2:PRINT"(.5 TO";W;"■)"
1060 INPUT"■■■■■■■■■■■■■■■■";A$:T=VAL(A$)
1070 IFT*2<>INT(T*2)ORT<0.5ORT>WGOTO990
1080 A2=S+72*T:A6=229:A7=0:A8=0:A9=S:GOSUB3300
1270 Z=Y+4*(S+78*T)-1
1280 Y=17408:P=Y+2*S/A1:J=2*T/A1:B=0:R=256:I=J/2:B1=4*A2-J
1285 Z1=INT((PEEK(1)+256*PEEK(2)-J)/J)*J:IFZ>Z1THENZ=Z1
1286 IF(A=6)AND(L=3)GOTO6536
1290 GOSUB3450
```

```
1331 IFB<3001THENXX=10:GOTO1335
1332 IFB<30001THENXX=1:GOTO1335
1333 IFB<300001THENXX=.1:GOTO1335
1334 XX=.01:D=6/XX
1336 IFB*XX<6000GOTO1339
1337 IFB*XX<12000THEND=D*2:GOTO1339
1338 D=D*5:GOTO1360
1360 POKE225,127:POKE224,255:PRINTSTR$(D)
1370 Q=1:O=46*U/T/1000/D
1376 IFZ<PTHENC=0:Q=1:GOTO1575
1379 B1=4*A2-J
1380 FORA=PTOZSTEPJ
1390 GOSUB1650
1400 E=INT(C*O+.5)/2
1410 A=A+J
1420 GOSUB1650
1430 C=INT(C*O+.5)/2
1440 IFINT(E)=EGOTO1480
1450 IFC=ETHENF=98:GOTO1530
1460 IFC=E+.5THENF=255:GOTO1530
1470 F=123:GOTO1510
1480 IFC=ETHENF=226:GOTO1530
1490 IFC=E-.5THENF=127:GOTO1530
1500 F=126
1510 IFINT(C)=CTHENG=124:GOTO1540
1520 G=108:GOTO1540:G=F
1540 IFE=0ANDC=.5THENG=108
1550 IFC=0ANDE=.5THENF=123
1551 IFE=0GOTO1553
1552 POKEN+Q-40*INT(E-.5),F
1553 IFC=0GOTO1560
1554 POKEN+Q-40*INT(C-.5),G
1560 Q=Q+1:NEXTA
1575 IFQ>39THENQ=Q-1
1576 POKEN+Q-40*(INT(C-.5)+1),42
1580 GETA$:IFA$=""GOTO1580
1585 IFL=3GOTO1610
1590 PRINT"■■■DO YOU WANT ANOTHER GLOWCURVE (Y/N) ?"
1595 GETA$:IFA$="Y"GOTO990
1600 IFA$="N"GOTO55
1605 GOTO1595
1610 PRINT"■■■DO YOU WANT ANOTHER INTERFEROGRAM (Y/N)?"
1615 GETA$:IFA$="Y"GOTO6000
1620 IFA$="N"GOTO55
1625 GOTO1615
1650 C=0
1651 IFL=2GOTO1660
1652 H4=G4/2:IF(INT(H4)=H4)GOTO1695
1660 FORK=1 TO J STEP2
1670 C=C+8*(PEEK(A+K-1)+R*PEEK(A+K))
1686 NEXTK
1690 RETURN
1695 C=0
1700 FORK=1 TO J STEP2
1705 C=C+8*(PEEK(A+K+B1-1)+R*PEEK(A+K+B1))
1714 NEXTK
1715 B1=B1-2*J:RETURN
```

```
2000 N=45056:B=0:L=1:POKEN+2,0:Y=17408
2005 IFPEEK(N)>239GOTO2025
2010 PRINT"■■INTERFACE NOT PRESENT RESET PET & RELOAD."
2015 GOTO2015
2025 IFPEEK(N)AND8THENRETURN
2030 IFB=1GOTO2025
2040 PRINT"■■      OVEN CONTROLLER NOT PRESENT":B=1:GOTO2025
2200 GOSUB3010
2210 PRINT"■TO PERFORM DESIRED FUNCTION KEY IN"
2215 PRINT"CORRESPONDING FUNCTION NUMBER."
2220 PRINT"■1. RUN 2-D TL GLOWCURVE EXPERIMENT"
2225 PRINT"■2. RUN 3-D TL INTERFEROGRAM EXPERIMENT"
2226 IFL=1THEN RETURN
2229 L=3
2230 IFL=2THENPRINT"■3. GRAPH 2-D TL GLOWCURVE OF LAST RUN"
2232 IFL=2THENPRINT"■4. PLOT 2-D TL GLOWCURVE OF LAST RUN"
2235 IFL=3THENPRINT"■5.GRAPH INTERFEROGRAM OF LAST RUN"
2236 IFL=3THENPRINT"■6.PLOT INTERFEROGRAM OF LAST RUN"
2237 IFL=3THENPRINT"■7. PLOT 3-D TL SPECTRUM OF LAST RUN"
2240 RETURN
2300 PRINT"■■SPECIFY HEATING RATE";SPC(20);"(MULT.OF 0.5)"
2305 INPUT"(1 TO 100)";A$:U=VAL(A$)
2310 IF2*U<>INT(U*2)OR1>UOR100<UTHENE1=1
2315 RETURN
2400 PRINT"■■HEATING RATE (DEGREES PER SECOND) =";U
2405 PRINT"■MAXIMUM TEMPERATURE =";U1:RETURN
3000 PRINT"■";SPC(11);"2-D TL GLOWCURVE"
3002 PRINTSPC(11);"──────────────────"
3004 RETURN
3010 PRINT"■     THERMOLUMINESCENCE EXPERIMENT"
3020 PRINT"     ──────────────────────────────────"
3030 RETURN
3040 PRINT"■";SPC(9);"3-D TL INTERFEROGRAM"
3045 PRINTSPC(9);"──────────────────────":RETURN
3050 IF(PEEK(N)AND2)=0THENRETURN
3060 IFB=3GOTO3050
3065 GOSUB3010
3070 PRINT"■■      EHT AND/OR SCR NOT PRESENT":B=3:GOTO3050
3080 PRINT"■■HEATING RATE (DEGREES PER SECOND) =";U:RETURN
3090 PRINT"■5. PLOTTING 2-D GLOWCURVE":RETURN
3095 PRINT"■6. PLOTTING 3-D TL INTERFEROGRAM":RETURN
3150 POKE144,178:POKE145,5
3155 U3=68:U2=2*U0
3160 IFU2>255THENU2=U2-256:U3=U3+1:GOTO3160
3165 POKE871,U3:POKE877,U2
3170 FORI=1TO14
3175 READA,B:POKEA,B
3180 NEXTI
3185 DATA 45079,48,45076,255,45076,255,45079,112,45077,0
3186 DATA45077,0,1,0,2,68,45070,127
3190 DATA 45068,0,59411,60,537,72,538,3,45070,144
3195 SYS(826)
3200 FORI=1TO4
3205 READA,B:POKEA,B
3210 NEXTI
3215 DATA 537,133,538,230,59411,61,45057,0
3220 RETURN
```

```
3300 N=33688+A8:I=40:PRINT"□"
3305 FORX=0TO20STEP4
3310 FORA=XTOX+2
3315 POKEN-I*A,103
3320 NEXTA
3325 POKEN-I*A,80
3330 FORV=5TO39-A7STEP8
3335 POKEN-I*A+V,79
3340 POKEN-I*A+V-1,99
3345 NEXTV:NEXTX
3355 FORX=1TOI-A7STEP4
3360 FORA=XTOX+2
3365 POKEN+I+A,99
3370 NEXTA
3375 POKEN+I+A,80
3380 NEXTX
3385 POKE225,131:POKE224,192+A8:PRINTA9
3390 POKE225,131:POKE224,A6:PRINTMID$(STR$(A2),2)
3395 POKEN,48:RETURN
3450 FORA=PTOZSTEPJ:GOSUB1650
3460 IFC>BTHENB=C
3465 NEXTA:B=B*U/T:RETURN
4000 FORI=0TO2000STEP2
4010 PRINTI/4,PEEK(17408+I),PEEK(17409+I)
4020 NEXTI:STOP
5000 IFL=3GOTO5070:GOSUB3040
5003 E1=0:GOSUB2300:IFE1=1GOTO5002
5005 PRINT"□□SPECIFY TEMPERATURE INCREMENT PER STEP"
5010 INPUT"(1.0, 2.0 DEGREES) ";A$:A1=VAL(A$)
5015 IF(A1=1.0)OR(A1=2.0)GOTO5025
5020 GOTO5002
5025 PRINT"□□SPECIFY NO. OF STEPS PER INTERFEROGRAM"
5030 INPUT"(64, 128, 256 STEPS) ";A$:A2=VAL(A$)
5034 PRINT"□□NOTE THAT EACH SCAN CORRES.TO 2 INTERFEROGRAMS"
5035 IF(A2=64)OR(A2=128)OR(A2=256)GOTO5045
5040 GOTO5002
5045 PRINT"□□SPECIFY NUMBER OF SCANS"
5050 PRINT"(MAXIMUM ";256/A1/A2;"■)":INPUT"□■■■■";A$
5055 A3=VAL(A$):IFINT(A3)<>A3GOTO5002
5060 IF(A3<1)OR(A3>512/A1/A3)GOTO5002
5065 U1=2*A1*A2*A3-A1:U0=U1/A1+1
5066 B2=0:IFA1=1.0THEN B2=1
5067 IFA2=128THENB2=B2+2
5068 IFA2=256THENB2=B2+4
5070 GOSUB3040:GOSUG2400
5080 PRINT"□TEMPERATURE INCREMENT PER STEP =";A1
5085 PRINT"□NUMBER OF STEPS PER SCAN =";A2
5088 G3=2*A3
5089 PRINT"□□NUMBER OF INTERFEROGRAMS=";G3
5090 PRINT"□NUMBER OF SCANS=";A3
5091 PRINT"□□  CHECK THAT EHT AND SCR BOTH "
5092 PRINT"   PRESENT BEFORE PRESSING Y"
5095 PRINT"□□OKAY (Y/N) ?"
5100 GETA$:IFA$="N"GOTO5002
5105 IFA$<>"Y"GOTO5100
5110 GOSUB3040
```

```
5115 PRINT"■2. RUNNING 3-D TL INTERFEROGRAM EXP."
5120 POKE4,A2-1:POKE6,0:POKE45056,112:POKE45057,B2
5125 L=3:GOTO225
6000 GOSUB3040
6010 GOSUB3080
6014 PRINT"■■NUMBER OF SCANS SAVED IS";A3
6015 PRINT"■■NUMBER OF INTERFEROGRAMS SAVED IS";G3
6020 PRINT"COVERING THE RANGE 0 TO";U1;"DEGREES"
6025 INPUT"■WHICH NO. INTERFEROGRAM IS TO BE DISPLAYED";A$
6030 G4=VAL(A$):IFINT(G4)<>G4ORG4<1ORG4>G3GOTO6000
6032 A4=INT((G4+1)/2)
6035 T=A1*A2/64:S=2*A2*A1*(A4-1):Z=Y+A2*4*A4-2*A2-1
6040 A5=S+2*A1*A2:A6=227:A7=8:A8=2:A9=0
6045 GOSUB3300
6050 GOTO1280
6500 GOSUB3000
6505 GOSUB3090
6534 T=2.0:B=0:R=256
6535 P=Y:J=8:Z=INT((PEEK(1)+256*PEEK(2))/J)*J-1:B$="KHZ"
6536 GOSUB3450
6540 IFB<1001THENX1=10:GOTO6565
6545 IFB<10001THENX1=1:GOTO6565
6550 IFB<100001THENX1=.1:GOTO6565
6555 IFB<1000001THENX1=.01:GOTO6565
6560 X1=.001:B$="MHZ"
6565 B=B*X1:IFB<2001THENB=10:X1=X1*5:GOTO6576
6570 IFB<5001THENB=25:X1=X1*2:GOTO6576
6575 B=100:B=B/X1
6580 IFL=3GOTO7230
6581 PRINT"■DO YOU WANT AXES PLOTTED (Y/N) ?"
6582 GETA$:IFA$="Y"THENGOSUB7000
6583 IFA$="Y"GOTO6585
6584 IFA$<>"N"GOTO6582
6585 A=P:GOSUB1650
6586 POKE59411,60:A=PEEK(59460):I=1:OPEN6,6
6587 PRINT#6,"PA1000,";STR$(INT(C*X1*.7*U/T)+800);";PD"
6588 I=1
6590 FORA=YTOZSTEPJ
6595 GOSUB1650
6597 CR=C*X1*.7*U/T
6600 PRINT#6,"PA";STR$(1000+36*I);",";STR$(INT(CR)+800)
6601 I=I+1
6605 NEXTA
6610 PRINT#6,"IN":CLOSE6:POKE59411,61
6612 IFL=3THENGOTO1610
6615 GOTO55
6700 XM=0:W=1
6710 FORA=PTOZSTEPJ
6715 L=3
6725 GOSUB1650
6730 X(W)=C
6740 IFX(W)>XMTHENXM=X(W):ZP=W
6750 W=W+1
6760 NEXTA
6761 PRINTZP,XM
6770 RETURN
```

```
7000 POKE59522,1:POKE59520,0:A=PEEK(59460):POKE59411,60
7001 IFB$="MHZ"THENB=B/1000
7005 OPEN6,6
7010 PRINT#6,"PA1000,800;PD"
7015 FORI=2TO53
7020 PRINT#6,"PR180,0;XT;TL
7025 IFINT(I/L)=I/5THENPRINT#6,"TL1,1"
7030 NEXTI
7035 PRINT#6,"PU;PA1000,800;PD"
7040 FORI=2TO51
7045 PRINT#6,"PR0,140;YT;TL"
7050 IFINT(I/5)=I/5THENPRINT#6,"TL1,1"
7055 NEXTI
7060 PRINT#6,"PU;PA850,500"
7065 FORI=0TO500STEP50
7070 PRINT#6,"LB";STR$(I);CHR$(3);"PA";STR$(1650+18*I);",500"
7071 NEXTI
7075 PRINT#6,"PA4200,200;LBTEMPERATURE (DEG.CELCIUS)";CHR$(3)
7080 PRINT#6,"PA500,7900;LB";STR$(B);CHR$(3)
7081 PRINT#6,"PA500,3500;DI0,1;LBRATE(";B$;")"
7085 PRINT#6,CHR$(3):POKE59411,61:CLOSE6:RETURN
7200 GOSUB3040
7201 GOSUB3095
7210 PRINT"■■NO OF INTERFEROGRAMS SAVED IS";G3
7212 PRINT"COVERING THE RANGE 0 TO";U1;"DEGREES"
7213 PRINT"■■SPECIFY WHICH NO INTERFEROGRAM TO BE PLOTTED"
7214 INPUT"      ";A$
7215 G4=VAL(A$):Y=17408
7217 A4=INT((G4+1)/2)
7218 T=A1*A2/64:S=2*A1*A2*(A4-1):Z=Y+A2*4*A4-2*A2-1
7219 P=Y+2*S/A1:J=2
7221 B=0:R=256:B1=4*A2-J:B$="KHZ"
7222 PRINT"■WAIT FOR PET TO COMPUTE POSITION OF ZPD"
7223 L=3
7224 GOSUB3450
7225 B1=4*A2-J
7226 GOSUB6700
7227 GOTO6540
7230 PRINT"■ DO YOU WANT AXES PLOTTED (Y/N)?"
7232 GETA$
7234 IFA$="Y"THENGOSUB7500
7236 IFA$="Y"GOTO7242
7238 IFA$<>"N"GOTO7232
7242 B1=4*A2-J:A=P:GOSUB1650
7245 TT=1
7249 OPEN6,6
7250 PRINT#6,"PA1000,";STR$(INT(C*X1*.7*U/T)+800);";PD
7255 I=1:P=P+2
7260 FORA=PTOZSTEPJ
7270 GOSUB1650
7275 CP=C*X1*.7*U/T
7280 PRINT#6,"PA";STR$(1000+122*I*64/A2);","STR$(INT(CP)+800)
7290 I=I+1:NEXTA
7295 PRINT#6,"IN":CLOSE6
7296 PRINT"■■■DO YOU WANT TO PLOT ANOTHER INTERFEROGRAM (Y/N)?"
7297 INPUT"     ";A$:IFA$="Y"GOTO7200
7298 IFA$="N"GOTO55
```

```
7500 POKE59411,60
7502 IFB$="MHZ"THENB=B/1000
7505 OPEN6,6
7520 PRINT#6,"PA1000,800;PD"
7530 FORI=2TO33
7540 PRINT#6,"PR240,0;XT;TL"
7550 IFINT(I/4)=I/4THENPRINT#6,"TL1,1"
7560 NEXTI
7570 PRINT#6,"PU;PA1000,800;PD"
7580 FORI=2TO51
7590 PRINT#6,"PR0,140;YT;TL"
7600 IFINT(I/5)=I/5THENPRINT#6,"TL1,1"
7610 NEXTI
7620 PRINT#6,"PU;PA4500,200;DI;LBSTEP NUMBER";CHR$(3)
7630 PRINT#6,"PU;PA850,500"
7635 H=A2
7640 FORI=0TOHSTEP(H/8)
7650 PRINT#6,"LB";STR$(I);CHR$(3)
7655 PRINT#6,"PA";STR$(750+((60*128)/H)*(I+(H/8)));",500
7660 NEXTI
7661 PRINT#6,"PA500,7900;LB";STR$(B);CHR$(3)
7662 PRINT#6,"PA500,3500;DI0,1;LBRATE(";B$;")";CHR$(3)
7663 PRINT#6,"PU;PA7000,7900;DI;LBINTERFEROGRAM NO.";G4
7664 PRINT#6,CHR$(3)
7665 PRINT#6,"PU;PA7000,7600;DI;LBZPD=STEP NO.";ZP;CHR$(3)
7669 POKE59411,61
7670 CLOSE6:RETURN
8000 GOSUB3040
8010 PRINT"■7.PLOTTING 3-D SPECTRA"
8020 PRINT"■■NO OF INTERFEROGRAMS SAVED IS";G3
8050 PRINT"■■WHICH NO SPECTRUM WOULD YOU LIKE TO COMPUTE"
8060 INPUT"      ";A$
8065 G4=VAL(A$)
8070 A4=INT((G4+1)/2):Y=17408
8080 T=A1*A2/64:Z=Y+A2*4*A4-2*A2-1:J=2
8090 B1=4*A2-J
8100 SX=0:G=1:R=256:M=5
8101 S=2*A1*A2*(A4-1)
8102 P=Y+2*S/A1:B=0:B$="KHZ"
8103 PRINTA2,A1,T,B1,P,Z,J
8133 IFA2=128THENM=M+1
8134 IFA2=256THENM=M+2
8135 ID=2:J=2
8142 B1=4*A2-J
8144 PRINTB1,J,A2,M
8145 GOSUB6700
8146 I=ZP:D=A2/2:SX=0
8148 FORL=1TOD
8150 X(L)=X(I):Y(L)=0
8151 SX=SX+X(L)
8152 PRINTL,I,X(L),Y(L)
8154 I=I+1
8156 NEXTL
8160 FORK=1TOD
8161 Y(K)=0
8162 CT=INT(SX/D):X(K)=X(K)-CT
8163 PRINTK,INT(X(K)),INT(Y(K)),CT
8164 NEXTK
```

```
8166 FORI=1TOD
8167 A=.54+.46*COS(π/2*(I-1)/D)
8168 X(I)=X(I)*A:X(I)=INT(X(I))
8170 NEXTI
8171 FORK=1TOD
8172 PRINTK,X(K)
8173 NEXTK
8175 PRINT"▒▒PET IS NOW COMPUTING FFT"
8176 PRINT"▒▒WAIT FOR DATA TO APPEAR ON SCREEN"
8177 TA=TI
8178 GOSUB8319:TB=TI
8180 FORK=1TOD
8181 TT=(TB-TA)/60
8182 PRINT"▒▒TIME TAKEN FOR FFT WAS";TT"SEC"
8184 FORK=1TOD
8185 X(K)=X(K)/(D/2) :Y(K)=Y(K)/(D/2)
8186 Z(K)=SQR(X(K)↑2+Y(K)↑2)
8190 PRINTK;INT(X(K));INT(Y(K));INT(Z(K))
8191 NEXTK
8193 FORK=1TOD
8195 CC=Z(K)
8197 IFCC>BTHENB=CC
8199 NEXTK:B=B*U/T
8200 IFB<1001THENX1=10:GOTO8205
8201 IFB<10001THENX1=1:GOTO8205
8202 IFB<100001THENX1=.1:GOTO8205
8203 IFB<1000001THENX1=.01:GOTO8205
8204 X1=.001:B$="MHZ"
8205 B=B*X1:IFB<2001THENB=10:X1=X1*5:GOTO 8208
8206 IFB<5001THENB=25:X1=X1*2:GOTO8208
8207 B=100:B=B/X1
8209 PRINT"▒DO YOU WANT AXES PLOTTED (Y/N)?"
8210 GETA$
8215 IFA$="Y"THENGOSUB9000
8216 IFA$="Y"GOTO8224
8220 IFA$="N"GOTO8224
8222 IFA$<>"N"GOTO8210
8224 C1=Z(1)
8225 OPEN6,6
8226 PRINT#6,"PA1000,";STR$(INT(C1*X1*.7*U/T)+800);";PD
8227 I=1:F=D/4
8228 FORK=2TOF
8229 CN=Z(K)
8230 CL=CN*X1*.7*U/T
8231 PRINT#6,"PA";STR$(1000+122*I*64/F);","STR$(INT(CL)+800)
8232 I=I+1:NEXTK
8236 PRINT#6,"IN":CLOSE6
8290 PRINT"▒▒DO YOU WANT TO PLOT ANOTHER SPECTRUM (Y/N)?"
8291 INPUT"       ";A$
8292 IFA$="Y"GOTO8010
8293 IFA$="N"GOTO55
8294 GOTO8290
```

```
8319 PI=π:N=64:M=6
8320 FORV=1TOM
8325 LE=2↑(M+1-V)
8330 LP=LE/2
8340 H1=1.0:H2=0.0
8350 AG=PI/LP
8360 CS=COS(AG)
8370 SN=(-1)↑ID*SIN(AG)
8380 FORW=1TOLP
8390 FORI=WTON STEPLE
8400 IP=I+LP
8410 T1=X(I)+X(IP)
8420 T2=Y(I)+Y(IP)
8430 T3=X(I)-X(IP)
8440 T4=Y(I)-Y(IP)
8450 X(IP)=T3*H1-T4*H2
8460 Y(IP)=T4*H1+T3*H2
8470 X(I)=T1
8480 Y(I)=T2
8490 NEXTI
8500 H3=H1*CS-H2*SN
8510 H2=H2*CS+H1*SN
8520 H1=H3
8530 NEXTW
8535 NEXTV
8550 N2=N/2:N1=N-1:W=1
8560 FORI=1TON1
8570 IF(I>=W)GOTO8610
8580 T1=X(W):T2=Y(W)
8590 X(W)=X(I):Y(W)=Y(I)
8600 X(I)=T1:Y(I)=T2:K=N/2
8620 IF(K>=W)GOTO8650
8630 W=W-K:K=K/2
8640 GOTO8620
8650 W=W+K
8660 NEXTI
8670 RETURN
9000 IFB$="MHZ"THENB=B/1000
9005 OPEN6,6
9010 PRINT#6,"PA1000,800;PD"
9015 FORI=2TO33
9020 PRINT#6,"PR240,0;XT;TL"
9025 IFINT(I/4)=I/4THENPRINT#6,"TL1,1"
9030 NEXTI
9035 PRINT#6,"PU;PA1000,800;PD"
9040 FORI=2TO51
9045 PRINT#6,"PR0,140;YT;TL"
9050 IFINT(I/5)=I/5THENPRINT#6,"TL1,1"
9055 NEXTI
9060 PRINT#6,"PU;PA4500,200;DI;LBWAVELENGTH";CHR$(3)
9065 PRINT#6,"PA500,7900;LB";STR$(B);CHR$(3)
9066 PRINT#6,"PA500,3500;DIO,1;LBRATE(";B$;")"
9070 PRINT#6,CHR$(3)
9075 PRINT#6,"PU;PA7000,7900;DI;LB SPECTRUM NO.";G4;CHR$(3)
9080 CLOSE6:RETURN
```

BIBLIOGRAPHY

Aitken, M.J., Tite, M.S. and Reid, J. (1963) "Thermoluminescent dating : progress report". Archaeometry 6, p. 65.

Aitken, M.J., Reid, J., Tite, M.S. and Fleming, S.J. (1967) "Quenching of spurious thermoluminescence by nitrogen" In "Luminescence Dosimetry" (F.H. Attix, Ed.), p. 236, USAEC, CONF-65037, Washington D.C.

Aitken, M.J. (1968) "Thermoluminescent dating in archaeology : introductory review". In "Thermoluminescence of Geological Materials" (D.J. McDougall, Ed.), p. 368, Academic Press, London and New York.

Aitken, M.J., Fleming, S.J., Reid, J and Tite, M.S. (1968) "Elimination of spurious thermoluminescence". In Thermoluminescence of Geological Materials" (D.J. McDougall, Ed.), p. 133, Academic Press, London and New York.

Aitken, M.J. and Alldred, J.C. (1972) "The assessment and error limits in thermoluminescent dating" Archaeometry 14, p. 257.

Aitken, M.J. and Fleming, S.J. (1972) "Thermoluminescence dosimetry in archaeological dating" In "Topics in Radiation Dosimetry (supplement I)" (F.H. Attix, Ed.), Academic Press, New York.

Aitken, M.J. (1974) "Physics and Archaeology", (2nd edition), Clarendon Press, Oxford.

Aitken, M.J. and Bowman, S.G.E. (1975) "Thermoluminescent dating : assessment of alpha particle contribution" Archaeometry, 17, p. 132.

Aitken, M.J. (1976) "TL age evaluation and assessment of error limits : Revised system". Archaeometry, 18, p. 233.

Aitken, M.J. (1978) "Radon loss evaluation by alpha counting" PACT Journal, Council of Europe, p. 104.

Bailiff, I.K. (1976) "Use of phototransfer for the anomalous fading of thermoluminescence". Nature, 264, p. 531.

Bailiff, I.K., Bowman, S.G.E., Mobbs, S.F. and Aitken, M.J. (1977) "The phototransfer technique and its use in thermoluminescence dating". J. Electrostat, 3, p. 269.

Bailiff, I.K., Morris, D.A. and Aitken, M.J. (1977) "A rapid-scanning interference spectrometer : application to low-level thermoluminescence emission" J. Phys. E : Sci. Instrum. 10, p. 1156.

Bailiff, I.K. (1978) "TL colour : high versus low dose measurements and the pre-dose mechanism". Ancient TL. No. 2, p. 6.

Beharrell, J. (1949) "Absorption of alpha rays in thick sources" Am. Geophys. Union (Trans) 30, p. 333.

Bell, J.R. (1972) "Introductory Fourier Transform Spectroscopy" Academic Press, London.

Bell, W.T. (1976) "The assessment of the radiation dose-rate for thermoluminescent dating" Archaeometry, 18, p. 107.

Bell, W.T. (1977) "Thermoluminescent dating : radiation dose-rate data" Archaeometry, 19, p.99.

Bell, W.T. (1978) "Studies in thermoluminescent dating in Australia" Unpublished Ph.D thesis, Australian National University, Canberra, Australia.

Bell, W.T. (1979) "Thermoluminescent dating : radiation dose-rate data" Archaeometry, 21, p. 243.

Bergland, G.D. (1969) "A guided tour of the fast Fourier transform" IEEE Spectrum, 6, p. 41.

Bettinali, C. and Ferraresso, G. (1968) "Adsorption thermoluminescence of $CaCO_3$". In "Thermoluminescence of Geological Materials" (D.J. McDougall, Ed.) p. 125, Academic Press, London and New York.

Binney, S.E. and Scherpelz, R.I. (1975) "A review of the delayed fission neutron technique" Nucl. Instrum. Methods. 154, p. 413.

Bowman, S.G.E. (1976) "Thermoluminescent dating : the evaluation of radiation dosage" Unpublished D. Phil. thesis, Oxford University, Oxford England.

Bowman, S.G.E. (1978) "Photransferred TL in quartz" PACT Journal, Council of Europe, p. 381.

Boyle, R. (1663) "Experiments and considerations upon colours with observations on a diamond that shines in the dark". Henry Herringham, London (Publ. 1664). Alternative, see Boyle, R. (1964) "Experiments and considerations touching colours : a facsimile of 1664 edition" (M.B. Hall, Ed.), Johnson Reprint Corporation, p. 413.

Bracewell, R. (1965) "The Fourier Transform and its applications" McGraw-Hill, New York.

Bragg, W.H. and Kleeman, R. (1905) "Alpha particles of radium and their loss of range passing through various atoms and molecules:. Phil. Mag. 10, p. 318.

Bräunlich, P. (1967) "Comment on the initial rise method for determining trap depths". J. Appl. Phys., 38, p. 2516.

Cameron, J.R., Zimmerman, D.W., Kennedy, G., Buch, G.N., Bland, R. and Grant, R. (1964) "Thermoluminescent radiation dosimetry utilizing LiF" Health Phys. 10, p. 25.

Candler, C. (1951) "Modern Interferometers". Published by Hilger and Watts Ltd., printed in Great Britain by R. Maclehose and Co. Ltd., University Press, Glasgow.

Chamberlain, J. (1979) "The Principles of Interferometric Spectroscopy" (G.W. Chantry and N.W.B. Stone, Eds.), Wiley, New York.

Chantry, G.W. (1971) "Submillimetre Spectroscopy" Academic Press, London.

Chantry, G.W. and Fleming, J.W. (1976) "Resolution limits in Fourier transform spectrometry" Infrared Phys. 16, p. 655.

Chantry, G.W. (1979) "Modern Aspects of Microwave Spectroscopy" Academic Press, London.

Charalambous, S. and Papastefanou, C. (1977) "On the radioactivity of fossil bones" Nucl. Instrum. Methods., 142, p. 581.

Charalambous, S. and Papastefanou, C. (1978) "Radium leaching from fossil bones" Nucl. Instrum. Methods, 151, p. 599.

Chen, R. (1969) "On the calculation of activation energies and frequency factors from glow-curves" J. Appl. Phys. 40, p. 570.

Chen, R. (1976) "Review : methods for kinetic analysis of thermally stimulated processes" J. Mat. Sci., 11, p. 1521.

Cherry, R.D. (1963) "The determination of thorium and uranium in geological samples by an alpha-counting technique" Geochim. et Cosmochim. Acta., 27, p. 183.

Cherry, R.D. (1965) "Alpha particle detection techniques applicable to the measurement of samples from the natural environment" In "The Natural Radiation Environment" (Adams and Lowder, Eds.)

Childers, D.G. and Durling, A. (1975) "Digital filtering and signal processing" St. Paul, Minn., West Publishing Co.

Clayton, E., Duerden, P. and Cohen, D.D. (1978) "Theoretical interpretation of PIXE spectra" Proc. Second Australian Conf. on Nuclear Techniques of Analysis, Lucas Heights, Sydney. p. 70.

Cohen, D.D. and Duerden, P. (1978) "Proton induced X-ray emission (PIXE) analysis at Lucas Heights" Aust. Atom. Energy Comm. Rep. No. E453.

Cohen, D.D., Duerden, P., Clayton. E. and Wall, T. (1980) :The use of PIXE for the measurement of thorium and uranium at $\mu g g^{-1}$ levels in thick ore samples" Nucl. Instrum. Methods. 168, p. 523.

Connes, J. (1958) "Spectromètre interferentiel a sélection par l'amplitude de modulation" J. Phys. Rad. 19, p. 215.

Connes, J. and Gush, H.P. (1960) "Étude du ciel nocturne dans le proche infra-rouge" J. Phys. Rad. 21, p. 645.

Cooley, J.W. and Tukey, J.W. (1965) "An algorithm for the machine calculation of complex Fourier series" Maths. of Comp. 19, p. 297.

Curie, D. (1963) "Luminescence in Crystals" (G.F.J. Garlick, transl). Methuen, London; Wiley, New York.

Daniels, F., Boyd, C.A. and Saunders, D.F. (1953) "Thermoluminescence as a research tool" Science. 117, p. 343.

Debenham, N.C. (1978) "More hints on spurious reduction" Ancient TL. No. 5, p. 3.

Desai, V.S. and Aitken, M.J. (1974) "Radon escape from pottery : effect of wetness". Archaeometry, 16, p. 95.

Diamond, H. and Gindler, J.E. (1963) "Alpha half-lives of Po-216, At-217 and Rn-218" J. Inorg. Nucl. Chem. 25, p. 143.

Duerden, P., Bird, J.R., Scott, M.D., Clayton, E., Russell, L.H. and Cohen, D.D. (1980) "PIXE-PIGME studies of artifacts" Nucl. Instrum. Methods. 168, p. 447.

Evans, R.D. (1955) "The Atomic Nucleus" McGraw-Hill, New York.

Facey, R.A. (1966) "A substandard light source of very low intensity" J. Sci. Instrum. 43, p. 658.

Fairchild, R.G., Mattern, P.L., Lengweiler, K. and Levy, P.W. (1974) "Thermoluminescence of LiF TLD-100 dosimeter crystals" IEEE Trans. Nucl. Sci. NS-21.

Fellgett, P. (1951) Unpublished thesis, Cambridge University, England.

Fellgett, P. (1958) "A propos de la théorie du spectrometre interférentiel multiplex". J. Phys. Rad. 19, p. 187.

Finney, G.D. and Evans, R.D. (1935) "The radioactivity of solids determined by alpha-ray counting" Phys. Rev. 48, p. 503.

Fisenne, I.M. and Keller, H.W. (1981) "A short history of ZnS on mylar as on alpha scintillation detector" Health Phys. 40, p. 739.

Fleming, S.J. (1966) "Study of thermoluminescence of crystalline extracts from pottery" Archaeometry. 9, p. 170.

Fleming, S.J. (1968a) "The colour of spurious thermoluminescence in dosimetry phosphors" In "Proc. of Second Int. Conf. on Luminescence Dosimetry" Gatlinburg, Tennessee, USAEC, Conf - 680920, p. 266.

Fleming, S.J. (1968b) "Thermoluminescent age studies on mineral inclusions separated from ancient pottery" In "Thermoluminescence of Geological Materials" (D.J. McDougall, Ed.), p. 431, Academic Press, London and New York.

Fleming, S.J. (1969) "The acquisition of radioluminescence by ancient ceramics". Unpublished D. Phil. thesis, Oxford University, Oxford, England.

Fleming, S.J. (1970) "Thermoluminescent dating : refinement of the quartz inclusion method" Archaeometry, 12, p. 133.

Fleming, S.J. (1973) "The pre-dose technique : a new thermoluminescent dating method" Archaeometry, 15, p. 13.

Fleming, S.J. and Stoneham, D. (1973) "The subtraction technique of thermoluminescent dating" Atchaeometry, 15, p. 229.

Fleming, S.J. (1975) "Supralinearity corrections in fine-grain thermoluminescence dating " a re-appraisal". Archaeometry, 17, p. 122

Fleming, S.J. (1979) "Thermoluminescence Techniques in Archaeology" Clarendon Press, Oxford.

Folkmann, F. (1975) "Analytical use of ion-induced X-rays" J. Phys. E : Scient. Instrum. 8, p. 429.

Forman, M.L., Steel, W.H. and Vanessa, G.A. (1966) "Correction of asymmetric interferograms obtained in Fourier spectroscopy" J. Opt. Soc. Amer. 56, p. 59.

Fremlin, J.H. and Srirath, S. (1964) "Thermoluminescent dating examples of non-uniformity of luminescence" Archaeometry, 7, p. 58.

Fuller, G.E. and Levy, P.W. (1977) "Thermoluminescence measurements on gamma-ray irradiated crystalline quartz (abstract)" Bull. Amer. Phys. Soc. 22, p. 329.

Fuller, G.E. and Levy, P.W. (1978) "Thermoluminescence of natural quartz (abstract)" Bull. Amer. Phys. Soc. 23, p. 324.

Garlick, G.F.J. and Gibson, A.F. (1948) "The electron trap mechanism of luminescence in sulphide and silicate phosphors". Proc. Phys. Soc. Ser. A. 60, p. 574.

Gebbie, H.A. (1958) "Spectres d'absorption atmosphérique dans l'infra-rouge lointain par interférometrie a deux ondes" J. Phys. Rad. 19, p. 230.

Glasson, J.L. (1922) "Stopping power and atomic number" Phil. Mag. 43, p. 477.

Göksu, H.Y. and Fremlin, J.H. (1972) "Thermoluminescence from un-irradiated flints : regeneration thermoluminescence". Archaeometry, 14, p. 217.

Graves, J.D. and Dyson, J.P. (1949) "A scintillation counter for laboratory counting of alpha particles". Rev. Sci. Instrum. 20, p. 560.

Grögler, N, and Stauffer, H. (1959) "Eine besondere thermoluminiszenz-ersheinung". Helv. Phys. Acta. 32, p. 129.

Halperin, A. and Kristianpoller, N. (1958) "Thermoluminescence spectra of X-ray coloured KCℓ crystals". J. Opt. Soc. Amer. 48, p. 996.

Halperin, A. and Braner, A.A. (1960) "Evaluation of thermal activation energies from glow-curves". Phys. Rev., 117, p. 408.

Happ, H. and Genzel, L. (1961) "Interferenz-modulation mit monochromatischen millimeter-wellen". Infrared Phys., 1, p. 39.

Harris, A.M. and Jackson, J.H. (1970) "A rapid scanning spectrometer for the region 200-800 nm : application to thermoluminescent emission spectra". J. Phys. E : Sci. Instrum., 3, p. 374.

Hewlett-Packard. (1980) "Optoelectronics Designer's Catalogue" April, p. 124.

Houtermans, F.G., Jäger, E., Schön, M. and Stauffer, H. (1957). "Messungen der thermolumineszenz als mittel zür untersuchung der thermischen und der strahlungsgeschichte von natürlichen mineralien und gesteinen". Annalen der Physik. (6 Folge) 20, p. 283.

Huntley, D.J. (1977) "Experiences with an alpha counter". Ancient TL, No. 1. p. 3.

Huntley, D.J. (1978) "The effect of sample reflectance in alpha counting:. Ancient TL. No. 4, p. 2.

Huntley, D.J. and Wintle, A.G. (1978) "Some aspects of alpha counting". PACT Journal, Council of Europe, p. 115.

Huntley, D.J. and Wintle, A.G. (1981) "The use of alpha scintillation counting for measuring Th-230 and Pa-231 contents of ocean sediments" Can. J. Earth Sci. 18, p. 419.

Hurley, P.M. (1950) "Distribution of radioactivity in granites and possible relation to helium age measurement" Bull. Geol. Soc. Amer., 61, p. 1.

Hurley, P.M. and Shorey, R.R. (1952) "Discrimination of thoron alpha activity in presence of radon". Amer. Geophys. Union. (Trans) 33, p. 722.

Hurley, P.M. (1956) "Direct radiometric measurement by gamma-ray scintillation spectrometer. Part I : Uranium and thorium series in equilibrium". Bull. Geol. Soc. Amer. 67, p. 395.

Hütt, G., Smirnov, A. and Tale, I. (1979) "On the application of TL of natural quartz to the study of geochronology of sedimental deposits". PACT Journal, Council of Europe, p. 362.

Huxtable, J., Hedges, J.W., Renfrew, A.C. and Aitken, M.J. (1976). "Dating a settlement pattern by thermoluminescence : the burnt mounds of Orkney". Archaeometry, 18, p. 5.

Huxtable, J.H. (1978) "Fine grain dating". PACT Journal, Council of Europe, p. 7.

Jacquinot, P. (1954) "The luminosity of spectrometers with prisms, gratings, or Fabry-Perot etalons". J. Opt. Soc. Amer. 44, p. 761.

Jacquinot, P. (1958) "Caractères communs auxnouvelles méthodes de spectroscopie interférentielle; facteur de mérite". J. Phys. Rad. 19, p. 223.

Jacquinot, P. (1960) "New developments in interference spectroscopy". Rep Prog. Phys., 23, p. 268.

James, J.F. and Sternberg, R.S. (1969). "The design of optical spectrometers". Chapman and Hall, London.

Jenkins, F.A. and White, H.E. (1976) "Fundamentals of Optics" (4th Ed.) McGraw-Hill, New York.

Jensen, H.E. and Barbetti, M.F. (1979) "More on filters for laboratory illumination". Ancient TL. No. 7, p. 10.

Jensen, H.E. and Prescott, J.R. (1979) "Reduction of spurious TL in reducing atmospheres". Ancient TL. No. 7, p. 8.

Johansson, S.A.E. and Johansson, T.B. (1976) "Analytical application of particle-induced X-ray emission". Nucl. Instrum. Methods. 137, p. 473.

Jones, R.V. and Young, I.R. (1956) "Some parasitic deflections in parallel spring movements". J. Sci. Instrum. 33, p. 11.

Kahn, F.D. (1959) "The signal to noise ratio of a suggested spectral analyzer" Astrophys. J. 129, p. 518.

Keevil, N.B. and Grasham, W.E. (1943) "Theory of alpha-ray counting from solid sources". Can. J. Res. 21(A), p. 21.

Kennedy, G. and Knopff, L. (1960) "Dating by thermoluminescence (editorial note)". Archaeology, 13, p. 147.

Kulp, J.L., Holland, H.D. and Volchok, H.L. (1952) "Scintillation alpha counting of rocks and minerals". Amer. Geophys. Union (Trans) 33, p. 101.

Levy, P.W., Mattern, P.L. and Lengweiler, K. (1971) "Three-dimensional thermoluminescent analysis of minerals". Mod. Geol. 2, p. 295.

Levy. P.W. (1978) "Thermoluminescence studies having applications to geology and archaeometry". PACT Journal, Council of Europe, p. 466.

Lewis, D.R. (1968) "Effect of grinding on thermoluminescence of dolomite, calcite and halite" In "Thermoluminescence of Geological Materials" (D.J. McDougall, Ed.), p. 125. Academic Press, London and New York.

Lewis, T. (1974) "Heat production measurements in rocks using a gamma-ray spectrometer with a solid state detector" Can. J. Earth Sci., 11, p. 256.

Lioutas, N. (1981) "Measurement of very low levels of radio-activity". Unpublished Honours thesis, Adelaide University, Australia.

Luc, P. and Gerstenkorn, S. (1978) "Fourier transform Spectroscopy in the visible and ultraviolet range". Appl. Optics, 17, p. 1327.

Lushchik, C.B. (1955) Dokl. Akad. Nauk. S.S.S.R. 101, p. 641.

Martin, A.E. (1980) "Infrared Interferometric Spectrometers". (J.R. Durig, Ed.), Elsevier Scientific Publishing Co. Amsterdam.

Mattern, P.L., Lengweiler, K. and Levy. P.W. (1971) "Apparatus for the simultaneous determination of thermoluminescent intensity and spectral distribution". Mod. Geol. 2, p. 293.

May, C.E. and Partridge, J.A. (1964) "Thermoluminescent kinetics of alpha-irradiated alkali halides". J. Chem. Phys. 40, p. 1401.

McKeever, S.W.S. (1979) "A note on the plateau test as used in thermoluminescence dating". Ancient TL. No. 6, p. 13.

McKeever, S.W.S. (1980) "The analysis of thermoluminescence glow-curves from meteorites". Mod. Geol. 7, p. 105.

Meakins, R.L., Dickson, B.L. and Kelly, J.C. (1978) "The effect on thermoluminescent dating of disequilibrium in the uranium decay chain". PACT Journal, Council of Europe, p. 97.

Meakins, R.L., Dickson, B.L. and Kelly, J.C. (1979). "Gamma ray analysis of K, U and Th for dose-rate estimation in thermoluminescent dating". Archaeometry, 21, p. 79.

Mejdahl, V. (1969) "Thermoluminescence dating of ancient Danish ceramics". Archaeometry, 11, p. 99.

Megumi, K. (1979) "Radioactive disequilibrium of uranium and actinium series nuclides in soil". J. Geophys. Res. 84, (B7), p. 3677.

Mertz, L. (1967) "Auxiliary computation for Fourier spectrometry" Infrared Phys., 7, p. 17.

Michelson, A.A. (1891) "Visibility of interference-fringes in the focus of a telescope" Phil. Mag. 31, p. 256.

Michelson, A.A. (1892) "On the application of interference methods to spectroscopic measurements". Phil. Mag. 34, p. 280.

Michelson, A.A. (1907) "Light waves and their uses". (Plate II). The Decennial Publications of the University of Chicago.

Moseley, H.G.J. and Fajans, K. (1911) "Radioactive products of short life" Phil. Mag. 22, p. 629.

Murray, A.S. (1980) "Discrepancies in the alpha counting of known activity samples". PACT Journal, Council of Europe, (in press).

Murray, A.S. and Aitken, M.J. (1980) "The measurement and importance of radioactive disequilibria in TL samples" PACT Journal, Council of Europe (in press).

Murty, M.V.R.K. (1960) "Some more aspects of the Michelson interferometer with cube corners". J. Opt. Soc. Amer. 50, p. 7.

Nash, A.E., Attix, F.H. and Schulman, J.H. (1967) "Spurious thermoluminescence of CaF_2 : Mn and LiF (TLD-100)" In "Luminescence Dosimetry" (F.H. Attix, Ed.) p. 244, USAEC, Washington, D.C.

Nogami, H.H. and Hurley, P.M. (1948) "The absorption factor in counting alpha rays from thick mineral sources". Amer. Geophys. Union (Trans.) 29, p. 335.

Northcliffe, L.C. and Schilling, R.F. (1970) "Range and stopping power tables for heavy ions". Nucl. Data Tables A7, p. 257.

Norrish, K. and Hutton, J.T. (1964) "Preparation of samples for analysis by X-ray fluorescent spectrography". Div. Rep. Div. Soils, CSIRO (Adelaide), 3/64.

Norrish, K. and Hutton, J.T. (1969) "An accurate X-ray spectrographic method for the analysis of a wide range of geological samples". Geochim. Cosmochim. Acta. 33, p. 431.

Okuno, E. and Watanabe, S. (1972) "Ultraviolet induced thermoluminescence on natural calcium fluoride". Health Phys. 23, p. 377.

Oltman, B.G., Kastner, J. and Paden, C. (1968) "Spectral analysis of thermoluminescence glow curves" In "Proc. of Second Int. Conf. on Luminescence Dosimetry", Gatlinburg, Tennessee, p. 623.

Prescott, J.R. (private communication), University of Adelaide, Australia.

Prescott, J.R., Robertson, G.B. and Green, R.C. (1982) "Thermoluminescent dating of pacific island pottery - successes and failures". Archaeology in Oceania (in press).

Rabolt, J.H. and Bellar, R. (1981) "The nature of apodization in Fourier transform spectroscopy". Appl. Spectroscopy, 35, p. 132

Randall, J.T. and Wilkins, M.H.F. (1945) "Phosphorescence and electron traps". Proc. Roy. Soc. Ser. A. A184, p. 366.

Reynolds, G.T. and Gruner, S. (1975) "A high gain image intensifier-spectroscope system for *in vivo* spectral studies of bioluminescence". IEEE Trans. on Nucl. Sci., NS-22.

Rosholt, J.N. (1959) "Natural radioactive disequilibrium of the uranium series" Geological Survey Bulletin, 1084-A, p. 1, United States Government Printing Office, Washington, D.C.

Rytz, A. (1979) "New catalogue of recommended alpha energy and intensity values". Atomic Data and Nuclear Data Tables, 23, p. 507.

Sasidharan, R., Sunta, C.M. and Nambi, K.S.V. (1978a) "TL dating : error implications in case of undertermined U-Th concentration ratio in pottery samples". Ancient TL. No. 2, p. 8.

Sasidharan, R., Sunta, C.M. and Nambi, K.S.V. (1978b) "Phototransfer method of determining archaeological dose of pottery sherds" PACT Journal, Council of Europe, p. 401.

Schayes, R., Brooke, C., Kozlowitz, I. and Lheureux, M. (1967) "Thermoluminescent properties of natural calcium fluoride". In "Luminescence Dosimetry" (F.H. Attix, Ed.), p. 138, USAEC, Conf-65037, Washington, D.C.

Schulman, J.H., Attix, F.H., West, E.H. and Ginther, R.J. (1960) New thermoluminescent dosimeter". Rev. Sci. Instrum. 31, p. 1236.

Schulman, J.H., Kirk, R.D. and West, E.J. (1967) "Use of lithium borate for thermoluminescence dosimetry" In "Luminescence Dosimetry" (F.H. Attix, Ed.), p. 113, USAEC, Conf-65037, Washington, D.C.

Shalgaonkar, C.S. and Narlikar, A.V. (1972) "Review : a review of the recent methods for determining trap depth from glow curves". J. Mat. Sci. 7, p. 1465.

Siemens Aktiengensellschaft. "Data sheets for blue-emitting diode", Munich, West Germany.

Singhvi, A.K. and Zimmerman, D.W. (1978) "The luminescent minerals in fine-grain samples from archaeological ceramics". PACT Journal Council of Europe, p. 12.

Singhvi, A.K. and Zimmerman, D.W. (1979) "The luminescent minerals in fine-grain samples from archaeological ceramics". Archaeometry, 21, p. 73.

Singhvi, A.K. (1981) "A possible correlation between the alpha efficiency and the anomalous fading characteristics". Ancient TL. No. 14, p. 11.

Spock, L.E. (1961) "Guide to the study of rocks". p. 100, Harpers and Bros. New York.

Spurny, Z. and Hruska, J. (1976) "A method for estimation of thermoluminescence emission spectra". Phys. Med. Biol. 21, p. 439.

Stanley, W.D. and Peterson, S.J. (1978) "Fast Fourier transforms on your home computer". Byte, Dec., p. 14.

Sunta, C.M. and Kathuria, S.P. (1978) "Factor influencing the kinetics of glow-peaks". PACT Journal, Council of Europe, p. 185.

Sutton, S.R. and Zimmerman, D.W. (1977) "Hints for the reduction of spurious TL". Ancient TL. No. 1, p. 7.

Sutton S.R. and Zimmerman, D.W. (1978a) "Attempts to circumvent anomalous fading". Ancient TL. No. 3, p. 10.

Sutton, S.R. and Zimmerman, D.W. (1978b) "A blue-UV absorbing filter for laboratory illumination". Ancient TL. No. 5, p. 5.

Svarcer, V. and Fowler, J.F. (1967) "Spurious thermoluminescence and triboluminescence in lithium fluoride dosimetry powder". In "Luminescence Dosimetry" (F.H. Attix, Ed.), p. 227, USAEC, Conf-65037, Washington, D.C.

Szöghy, I.M. and Kish, L. (1978) "Determination of radioactive disequilibrium in uranium bearing rocks". Can. J. Earth Sci. 15, p. 33.

Thompson, J. (1970) "The influence of previous irradiation on thermoluminescence sensitivity". Unpublished D. Phil. thesis, Oxford University, Oxford England.

Tite, M.S. and Waine, J. (1962) "Thermoluminescent dating : a re-appraisal". Archaeometry, 5, p. 53.

Tite, M.S. (1966) "Thermoluminescent dating of ancient ceramics : a re-assessment". Archaeometry, 9, p. 155.

Tomita, A., Hirai, N. and Tsutsumi, K. (1976) "Correlation between thermally stimulated exo-electron emission and thermoluminescence of pure LiF single crystal". Jap. J. Appl. Phys. 15, p. 1899.

Tomita, A. and Tsutsumi, K. (1978) "Emission spectra of thermoluminescence in $CaSO_4$". Jap. J. Appl. Phys., 17, p. 453.

Turner, R.E., Radley, J.M. and Mayneord, W.V. (1958) "The alpha-ray activity of human tissues". Brit. J. Radiol. 31, p. 397.

Urbach, F. (1930) Wiener Ber. IIa, 139, p. 363.

Urbach, F. (1946) "Storage and release of light by phosphors" Cornell Symposium, p. 132, Wiley, New York.

Vanessa, G.A. and Sakai, H. (1967) "Fourier spectroscopy". Prog. Opt. 6, p. 261.

Wall, T. (1979) "The AAEC uranium service". Atom. Energy Aust. 22, No. 3, p. 2.

Ward, A.G. (1942) "A new method for determining half-value periods from observations with a single geiger counter". Proc. Roy. Soc. 181(A) , p. 183.

Warren, S.E. (1978) "Thermoluminescence dating of pottery: on assessment of the dose-rate from rubidium". Archaeometry, 20, p. 69.

Whaling, W. (1958) "The energy loss of charged particles in matter". Handbuch der Physik (S. Flugge, Ed.) 34, p. 193.

Whittle, E.H. and Arnaud, J.M. (1975) "Anomalous fading of thermoluminescence in fine-grain samples". Archaeometry, 17, p. 22.

Williamson, C.F., Boujot, J.P. and Picard, J. (1966). "Tables of range and stopping power of chemical elements for charged particles of energy 0.05 to 500 MeV". Rapport CEA-R3042, Centre D'etudes Nucleaires de Saclay, France.

Wintle, A.G., Aitken, M.J. and Huxtable, J. (1971) "Abnormal thermoluminescence fading characteristics". In "Proc. Third Int. Conf. on Luminescence Dosimetry". (V. Mejdahl, Ed.), Riso, DAEC Rep. No. 240, P. 105.

Wintle, A.G. (1973) "Anomalous fading of thermoluminescence in mineral samples". Nature, 245, p. 143.

Wintle, A.G. (1974) "Factors determining the thermoluminescence of chronologically significant materials". Unpublished D. Phil. thesis, Oxford University, Oxford, England.

Wintle, A.G. and Aitken, M.J. (1973) "Thermoluminescence dating of burnt flint : application to a lower palaeolithic site, Terra Amata". Archaeometry, 19, p. 111.

Wintle, A.G. (1978) "Anomalous fading" PACT Journal, Council of Europe, p. 240.

Wintle, A.G. and Huntley, D.J. (1979) "Thermoluminescence of a deep-see ocean core". Nature, 274, p. 710.

Wintle, A.G. (1980) "Thermoluminescent dating : a review of recent applications to non-pottery materials". Archaeometry, 22, p. 113.

Wintle, A.G. and Huntley, D.J. (1980) "Thermoluminescence dating of ocean sediments". Can. J. Earth Sci. 17, p. 348.

Wintle, A.G. and Huntley, D.J. (1982) "Thermoluminescence dating of sediments". Quart. Sci. Rev. 1, p. 31.

Woldseth, R. (1973) "All you ever wanted to know about XES". Keevex Corp., Burlingame, California.

Wood, R.W. (1967) "Physical Optics". Dover, New York.

Ziegler, J.F. (1977) "Helium : stopping powers and ranges in all elemental matter". Pergamon Press, New York.

Zimmerman, D.W. (1967) "Thermoluminescence from fine-grains from ancient pottery". Archaeometry, 10, p. 26.

Zimmerman, D.W. (1971) "Uranium distributions in archaeological ceramics : dating of radioactive inclusions". Science, 74, p. 818.

Zimmerman, D.W. (1978) "Radiative recombination and anomalous fading (abstract)". PACT Journal, Council of Europe, p. 257.